

**SOIL PHYSICAL PROPERTIES IN LANDSLIDES
AT VOLCANIC AREA**

A Doctoral Thesis
Integrated Graduate School of Medicine, Engineering and Agricultural Science
University of Yamanashi

MARCH 2021

**G18DTK06
MEGA LIA ISTIYANTI**

ACKNOWLEDGEMENT

All praises and thanks to Allah swt, the Almighty, for His showers of blessings throughout my research work to complete the research.

First of all, my deep and sincere gratitude is for my research supervisor, Associate Professor Satoshi Goto, for his guidance and great efforts in helping me throughout this research. It was a great privilege and honor to work and study under his guidance, since I was able to get a lot of experience from a lot of field works, and a lot of chance to meet other member of the project.

I sincerely thank to all the member which I met in the field, Dr. Takashi Kimura, Professor Go Sato, Professor Shintaro Hayashi, Professor Akihiko Wakai, Professor Daisuke Higaki, Dr. Shoji Doshida, Dr. Hiroataka Ochiai, Dr. Kazuyuki Sakaguchi, and Dr. Nobuyuki Shibasaki, for a lot of advices in my research. I extend my sincere thanks to all my colleagues in Geotechnical laboratory for a lot of discussion, a lot of good memories, and support throughout my study.

I am extremely grateful to my parents, my husband, and my siblings for their love, prayers, and caring on me in every situation and condition. I am very much thankful to my friends in University of Yamanashi, for their support throughout my study.

I sincerely praise my gratitude; their support will not be forgotten.

SUMMARY

Occurrence of the landslides in the mountain area of tephra materials are recorded higher either during heavy rainfall or earthquake. Tephra materials are unconsolidated pyroclastic materials from volcanic eruptions which becoming an important research in recent times. This study observed parameters of sliding layer in tephra materials by considering characteristics of physical properties and clay minerals. Less research has been conducted by physical properties in tephra materials on landslide. Parameter of sliding layer has a role on research field of landslides in volcanic area, and it is important for volcanic hazard prediction and risk management.

Tephra deposits are highly susceptible to landslide and have been responsible for catastrophic landslides (Kluger et al. 2020). Characteristics features of pyroclastic fall deposits are mantle-bedding, which are slope-parallel bedding, and interlayering of weathered, weak beds and relatively intact beds (Chigira and Suzuki 2016), moreover, unconsolidated superficial tephra deposits that cover the volcanic edifices have great potential for generating serious landslides (Miyabuchi et al. 2015).

This study focuses on tephra materials at heavy rainfall-induced landslides and earthquake-induced landslides in volcanic area. This study observed the heavy rainfall-induced landslides at Takadake area in Aso mountain, Kyushu caused by heavy rainfall 2012 and at Izu Oshima in Tokyo caused by heavy rainfall 2013. Furthermore, earthquake-induced landslides at Takanodai area in Aso mountain, Kyushu caused by earthquake 2016 and at Eastern Iburi Region in Hokkaido caused by earthquake 2018 are also observed. Beside tephra materials, this study also investigates the physical properties and clay minerals at diverse landslide mechanisms in Oita Prefecture, Kyushu which

consist of tuff breccia and andesite materials.

Field measurements and laboratory tests were performed in this study. Soil stratigraphic analysis and soil hardness measurements were performed in the field measurements. Furthermore, laboratory tests were performed to observe physical properties, saturated permeability properties, and the content of clay minerals on soil materials.

Each research areas on this study consist of tephra materials deposits which produced from the eruption activity in the difference of period. The oldest tephra material on this study is Kusasenrigahama from Takanodai area which erupted from 30 ka years ago, and the youngest tephra material on this study is Younger group Oshima from Izu Oshima area which erupted at AD 1400–1800. This study observed classification of tephra materials based on the age of tephra materials using the plasticity chart. Young tephra materials have lower plasticity index and liquid limit values, rather than old tephra materials.

In addition, characteristics of sliding layer are also observed on this study. Characteristics of sliding layer in heavy rainfall-induced landslides at Takadake area has low soil hardness, high plasticity index, high fine fraction content (less than 0.075 mm), low density of soil particles, high water content, high void ratio, and low dry density. Physical properties on sliding layer showed that sliding layer has loose structure with low strength and active soil.

Furthermore, characteristics of sliding layer in earthquake-induced landslides at Takanodai, Towa, and Mizuho landslides are non-plastic soil with low density of soil particles, high void ratio, and low dry density. Sliding layer on earthquake-induced landslides also has halloysite which could have been influenced the layer during an

earthquake since halloysite represents a potential weak and occurred the shrinkage cracks (Moon et al. 2015a).

Sliding layer in tephra materials at heavy rainfall-induced landslides and in earthquake-induced landslides has high void ratio and low dry density. High void ratio and low dry density showed the loose structure in sliding layer.

This study also observed the estimation of the activity value in tephra materials using the relation between plasticity index and clay content (% 0.002 mm), and between plasticity index and fine fraction content (% 0.075 mm). The activity value was divided into four groups; 0–1 is *inactive*, 1–5 is *normal activity*, 6–10 is *active*, and >10 is *very active*. The sliding layers on this study are *normal* to *very active* soil; sliding layer in Takadake 1 landslide is *very active* soil, in Takadake 2 and Yabakei landslides are *active* soil, and in Ohtsuru and Ono landslides are *normal activity* soil. Activity value is related with soil plasticity and sliding layer in earthquake-induced landslides is non-plastic soil, because of that, activity value on sliding layer in earthquake-induced landslides is not observed.

On the other hand, characteristics of physical properties on sliding layer in tuff breccia and andesite materials at diverse landslide mechanisms are not observed. An obvious dissimilarity on the soil hardness is observed between tuff breccia and the upper layer in Ohtsuru and Ono landslides, and characteristics of sliding layer on other physical properties are not observed. Moreover, weathering process in Yabakei landslide formed the highly weathered tuff breccia which has higher fine fraction content (less than 0.075 mm), plasticity index, *active* soil, and lower soil hardness rather than soil materials from Ohtsuru and Ono landslides.

TABLE OF CONTENTS

ACKNOWLEDGMENT	ii
SUMMARY	iii
TABLE OF CONTENT	vi
LIST OF FIGURES	x
LIST OF PHOTOS	xvii
LIST OF TABLE	xix
1 INTRODUCTION	
1.1 Background.....	1
1.2 Objectives.....	2
1.3 Scope of the study.....	3
1.4 Structure of the study.....	3
2 LITERATURE REVIEW	
2.1 Tephra.....	5
2.2 Landslides on tephra materials.....	5
2.2.1 Heavy rainfall-induced landslides on tephra materials.....	7
2.2.2 Earthquake-induced landslides on tephra materials.....	8
2.3 Occurrence of clay minerals in soils.....	9
2.3.1 Kaolinite in soils.....	9
2.3.2 Halloysite in soils.....	9
2.3.3 Illite in soils.....	11

2.3.4 Vermiculite in soils	12
2.3.5 Smectite in soils	13
2.3.6 Palygorskite and sepiolite in soils	14
2.4 Clay minerals influence landslides on tephra materials	14
3 RESEARCH METHODS	
3.1 Field measurements.....	17
3.2 Physical properties tests	18
3.2.1 Liquid limit and plastic limit	18
3.2.2 Particle size distribution	22
3.2.3 Density of soil particles.....	31
3.2.4 Saturated permeability of soils	33
3.2.5 X-Ray Powder Diffraction	36
4 RESEARCH AREAS	
4.1 Research area consisting of tephra materials	42
4.1.1 Aso volcanic mountains in Kumamoto	42
4.1.2 Izu Oshima in Tokyo.....	46
4.1.3 Iburi Region in Hokkaido.....	49
4.2 Research area consisting of tuff breccia and andesite	53
5 CASE STUDIES OF LANDSLIDES AT VOLCANIC AREA	
5.1 Takadake landslides caused by heavy rainfall 2012.....	58
5.2 Izu Oshima landslide caused by heavy rainfall 2013	65
5.3 Takanodai landslide caused by earthquake 2016	69
5.4 Towa and Mizuho landslides caused by Hokkaido Eastern Iburi Earthquake 2018.....	72
5.5 Diverse mechanisms of landslides in Oita Prefecture, Kyushu, Japan.....	79

6 SOIL PHYSICAL PROPERTIES IN LANDSLIDES AT VOLCANIC AREA	
6.1 Soil hardness measurements	86
6.1.1 Soil hardness measurements on tephra materials.....	86
6.1.2 Soil hardness measurements on tuff breccia and andesite materials	88
6.2 Plasticity index.....	89
6.2.1 Plasticity index on tephra materials	90
6.2.2 Plasticity index on tuff breccia and andesite materials	92
6.3 Particle size distribution	93
6.3.1 Particle size distribution on tephra materials.....	93
6.3.2 Particle size distribution on tuff breccia and andesite materials	95
6.4 Activity of soil materials.....	95
6.5 Density of soil particles	98
6.5.1 Density of soil particles on tephra materials.....	98
6.5.2 Density of soil particles on tuff breccia and andesite materials.....	98
6.6 Saturated permeability of soils.....	100
6.6.1 Characteristics on saturated permeability in tephra materials	101
6.6.2 Characteristics on saturated permeability in tuff breccia and andesite materials	107
6.7 Content of clay minerals.....	112
7 CHARACTERISTICS OF SOIL PHYSICAL PROPERTIES ON SLIDING LAYER IN HEAVY RAINFALL-INDUCED LANDSLIDES AND IN EARTHQUAKE-INDUCED LANDSLIDES AT VOLCANIC AREA	
7.1 Heavy rainfall-induced landslides on tephra materials.....	115
7.2 Earthquake-induced landslides on tephra materials	115

7.3 Characteristics of tuff breccia-andesite in diverse mechanisms of landslides	116
8 CONCLUSIONS	119
REFERENCES	xxii
LIST OF PUBLICATIONS	xxxii
LIST OF CONFERENCES	xxxii
APPENDIX	xxxiv

LIST OF FIGURES

Figure 1.1 Map location of major source volcanoes of Quaternary tephras in and around Japan (1: large caldera with diameter of more than 10 km; 2: caldera volcanoes with diameters of less than 10 km often associated with composite stratovolcanoes; 3: stratovolcanoes; 4: central cones within calderas; 5: buried caldera; 6: trench and trough axis (plate boundary)) (Machida 2002).....	2
Figure 1.2 Research areas and sampling locations on this study are located in Takadake areas and Takanodai at Aso volcanic mountains, Izu Oshima, Towa and Abira Town at Hokkaido, and in Oita Prefecture	4
Figure 2.1 Isopach maps on tephra materials at research areas (OJS scoria (Miyabuchi et al. 2004); Kpfa (Miyabuchi et al. 2003; Ta-d and En-a (Furukawa and Nakagawa 2010; Y0.8-Y5.0 (Koyama and Hayakawa 1996).....	6
Figure 2.2 Structure of kaolinite (Lancellota 2009).....	9
Figure 2.3 Structure of illite (Lancellota 2009)	12
Figure 2.4 Structure of montmorillonite (Lancellota 2009)	13
Figure 2.5 Schematic sketch showing the successions including halloysite-rich zone, in which a sliding layer was made (Chigira and Suzuki 2016)	16
Figure 3.1 Plasticity chart (Casagrande 1948).....	21
Figure 3.2 Soil permeability measuring instrument (DIK-4012).....	34
Figure 3.3 Simplified sketch of one possible configuration of the X-ray source (X-ray tube), the X-ray detector, and the sample during an X-ray scan. In this configuration, the X-ray tube and the detector both move through the angle theta (θ) and the samples remains	

stationary.....	41
Figure 4.1 Schematic stratigraphy of fallout tephra deposits from post-caldera central cones of Aso volcano (Miyabuchi 2009).....	42
Figure 4.2 Landslides in Aso volcanic mountains (Google Earth)	43
Figure 4.3 Main landslide on the western part of Izu Oshima island (Google Earth 2020)	46
Figure 4.4 Stratigraphic relations of tephra fallout layers and lava on the western slope of Izu Oshima volcano (Miyabuchi et al. 2015).....	47
Figure 4.5 Schematic stratigraphy of fallout tephra deposits in Iburi Region at Hokkaido (GSJ 2020)	49
Figure 4.6 Landslides in Iburi Region at Hokkaido (Google Earth 2020)	50
Figure 4.7 Precipitation data in Hita City and Nakatsu City, Oita Prefecture (JMA 2020).....	54
Figure 4.8 Geological map of landslides consisting of tuff breccia and andesite in Hita Prefecture (Google Earth and GSJ 2020)	54
Figure 5.1 Soil stratigraphy in Takadake; black dotted lines indicate sliding layer by field observation.....	59
Figure 5.2 Particle size distribution curves of Takadake materials.....	60
Figure 5.3 Fine fraction content (% 0.075 mm) on Takadake landslides shows the dissimilarity between kuroboku and scoria layers	60
Figure 5.4 Physical properties and saturated permeability properties of soil in Takadake landslides; black dotted lines indicated location of sliding layer by field observation	61
Figure 5.5 Plasticity chart shows the dissimilarity between kuroboku and scoria layers.....	62
Figure 5.6 Correlation between fine fraction content (% 0.075 mm)-plasticity index shows dissimilarity between kuroboku and scoria.....	63

Figure 5.7 Clay minerals on tephra materials from Takadake landslides (Red lines indicated sliding layers)	64
Figure 5.8 Soil stratigraphy by field observation in Izu Oshima	65
Figure 5.9 Particle size distribution curves of Izu Oshima materials.....	66
Figure 5.10 Fine fraction content (% 0.075 mm) on Izu Oshima	66
Figure 5.11 Physical properties and saturated permeability properties of soil in Izu Oshima.....	67
Figure 5.12 Plasticity chart on tephra layers from Izu Oshima	68
Figure 5.13 Clay minerals on tephra materials from Izu Oshima (Red lines indicated sliding layers)	68
Figure 5.14 Soil stratigraphy by field observation in Takanodai; black dotted lines indicated location of sliding layer by field observation	69
Figure 5.15 Particle size distribution curves of Takanodai materials.....	70
Figure 5.16 Fine fraction content (% 0.075 mm) on Takanodai landslides	70
Figure 5.17 Physical properties and saturated permeability properties of soil in Takanodai landslide; black dotted lines indicated location of sliding layer by field observation	71
Figure 5.18 Clay minerals on tephra materials from Takanodai landslide (Red lines indicated sliding layers)	71
Figure 5.19 Soil stratigraphy in Towa and Mizuho landslides; black dotted lines indicate sliding layer by field observation.....	73
Figure 5.20 Particle size distribution curves of Towa and Mizuho materials.....	74
Figure 5.21 Fine fraction content (% 0.075 mm) on Towa and Mizuho landslides	74
Figure 5.22 Physical properties and saturated permeability properties of soil in Towa and Mizuho landslides; black dotted lines indicated location of sliding layer by field observation	

.....	76
Figure 5.23 Plasticity chart on tephra layers at Towa and Mizuho landslides shows the group of Ta-d layers.....	77
Figure 5.24 Clay minerals on tephra materials from Towa and Mizuho landslides (Red lines indicated sliding layers).....	78
Figure 5.25 Soil stratigraphy in Ohtsuru (a) and Ono (b) landslides	80
Figure 5.26 Field observation and soil hardness measurement in Yabakei landslide	81
Figure 5.27 Particle size distribution curves of soil materials.....	81
Figure 5.28 Fine fraction content (% 0.075 mm) on soil materials	82
Figure 5.29 Physical properties and saturated permeability properties of soil in Ohtsuru (a), Ono (b), and Yabakei (c) landslides	83
Figure 5.30 Plasticity chart shows the dissimilarity characteristics on highly weathered tuff breccia.....	84
Figure 5.31 Clay minerals on tuff breccia and andesite materials in Ohtsuru (a), Ono (b), and Yabakei (c) landslides (Red lines indicated sliding layers).....	85
Figure 6.1 Stratigraphic and soil hardness profiles at landslide areas which consisting of tephra materials; black dotted lines indicated location of sliding layer by field observation	87
Figure 6.2 Stratigraphic and soil hardness profiles at Ohtsuru and Yabakei landslides which consisting of tuff breccia and andesite; black dotted lines indicated location of sliding layer by field observation	89
Figure 6.3 Stratigraphic and soil hardness profiles at Ono landslide which consisting of tuff breccia and andesite; black dotted lines indicated location of sliding layer by field observation	89

Figure 6.4 Plotted data of soil materials on plasticity chart	90
Figure 6.5 Plotted data of tephra materials on plasticity chart	91
Figure 6.6 Plotted data of tuff breccia and andesite materials on plasticity chart.....	92
Figure 6.7 Particle size distribution curves of soil materials	94
Figure 6.8 Estimate the degree of expansiveness of some clay soils from Nata, South Africa using the activity chart (Bell and Maud 1995)	95
Figure 6.9 Relation between plasticity index and clay content (% 0.002 mm) show the active value on soil materials.....	96
Figure 6.10 Relation between plasticity index and fine fraction content (% 0.075 mm) show the active value on soil materials	97
Figure 6.11 Stratigraphic and density of soil particles profiles at landslide areas which consisting of tephra materials; black dotted lines indicated location of sliding layer by field observation	99
Figure 6.12 Stratigraphic and density of soil particles profiles at Ohtsuru and Yabakei landslides which consisting of tuff breccia and andesite; black dotted lines indicated location of sliding layer by field observation	100
Figure 6.13 Stratigraphic and density of soil particles profiles at Ono landslide which consisting of tuff breccia and andesite; black dotted lines indicated location of sliding layer by field observation	100
Figure 6.14 Relation between coefficient of permeability and type of soil.....	101
Figure 6.15 Stratigraphic and water content profiles at landslide areas which consisting of tephra materials; black dotted lines indicated location of sliding layer by field observation	103
Figure 6.16 Stratigraphic and coefficient of saturated permeability profiles at landslide areas	

which consisting of tephra materials; black dotted lines indicated location of sliding layer by field observation.....	104
Figure 6.17 Stratigraphic and void ratio profiles at landslide areas which consisting of tephra materials; black dotted lines indicated location of sliding layer by field observation	105
Figure 6.18 Stratigraphic and dry density profiles at landslide areas which consisting of tephra materials; black dotted lines indicated location of sliding layer by field observation	106
Figure 6.19 Stratigraphic and water content profiles at Ohtsuru and Yabakei landslides which consisting of tuff breccia and andesite; black dotted lines indicated location of sliding layer by field observation.....	107
Figure 6.20 Stratigraphic and water content profiles at Ono landslide which consisting of tuff breccia and andesite; black dotted lines indicated location of sliding layer by field observation	107
Figure 6.21 Stratigraphic and coefficient of saturated permeability profiles at Ohtsuru and Yabakei landslides which consisting of tuff breccia and andesite; black dotted lines indicated location of sliding layer by field observation	108
Figure 6.22 Stratigraphic and coefficient of saturated permeability profiles at Ono landslide which consisting of tuff breccia and andesite; black dotted lines indicated location of sliding layer by field observation.....	108
Figure 6.23 Stratigraphic and degree of saturation profiles at Ohtsuru and Yabakei landslides which consisting of tuff breccia and andesite; black dotted lines indicated location of sliding layer by field observation	109
Figure 6.24 Stratigraphic and degree of saturation profiles at Ono landslide which consisting of	

tuff breccia and andesite; black dotted lines indicated location of sliding layer by field observation.....	109
Figure 6.25 Stratigraphic and void ratio profiles at Ohtsuru and Yabakei landslides which consisting of tuff breccia and andesite; black dotted lines indicated location of sliding layer by field observation.....	110
Figure 6.26 Stratigraphic and void ratio profiles at Ono landslide which consisting of tuff breccia and andesite; black dotted lines indicated location of sliding layer by field observation	110
Figure 6.27 Correlation between coefficient of saturated permeability (m/s) and void ratio on (a) tuff breccia materials and (b) andesite materials	111
Figure 6.28 Stratigraphic and content of clay minerals on sliding layers at landslide areas which consisting of tephra materials; black dotted lines indicated location of sliding layer by field observation	113
Figure 6.29 Stratigraphic and content of clay minerals on sliding layers at landslide areas which consisting of tuff breccia and andesite; black dotted lines indicated location of sliding layer by field observation.....	114

LIST OF PHOTOS

Photo 2.1 SEM images showing various morphologies of halloysite: (a) lamellar particles; (b) tubular or club-like particles; (c) needle-like or fibrous particles; (d) parallel clusters of single tubular halloysite crystals; (e) growth of fibrous halloysite on the edge of platy rectorite; (f) contact twins of halloysite (Hong and Mi 2006)	10
Photo 3.1 Separating tephra layers using colored toothpicks and measuring depth of tephra layers using scale in field measurements	17
Photo 3.2 Measuring soil hardness using a Yamanaka-type soil hardness meter	17
Photo 3.3 Equipment for liquid limit test	18
Photo 3.4 Particle size distribution test method: (a) Sieve analysis; (b) Sedimentation analysis	23
Photo 3.5 Equipment for liquid limit test	32
Photo 3.6 Saturated hydraulic conductivity test (Constant water level test)	35
Photo 3.7 Oriented powder in sample holder	37
Photo 3.8 Method on ethylene glycol vapour treatment	38
Photo 4.1 Takadake 1 and tephra stratigraphy in the landslide (Taken on October 2016)	44
Photo 4.2 Takadake 2 and tephra stratigraphy in the landslide (Taken on October 2016)	44
Photo 4.3 Takanodai and tephra stratigraphy in the landslide (Taken on October 2016).....	45
Photo 4.4 Tephra stratigraphy in Izu Oshima (Taken on November 2016)	48
Photo 4.5 Tephra layers from Ta-a until Spfa-1 which located nearby the research area (Taken on September 2019).....	51
Photo 4.6 (a) Towa landslide and (b) Mizuho landslide, and tephra stratigraphy in the landslides	

(Taken on September 2019)	52
Photo 4.7 Ohtsuru landslide and soil materials in the landslide (Taken on July 2017).....	55
Photo 4.8 Ono landslide and soil materials in the landslide (Taken on July 2017)	56
Photo 4.9 Yabakei landslide and soil material in the landslide (Taken on July 2018)	56
Photo 5.1 Two collapses in Ono landslide (Photo taken on July 2018)	79
Photo 7.1 Condition of Ohtsuru landslide (Photo taken on July 2018).....	117
Photo 7.2 Condition of Ono landslide (Photo taken on July 2017)	117
Photo 7.3 Condition of Yabakei landslide (Photo taken on July 2018).....	118

LIST OF TABLES

Table 3.1 Classes of activity value (Skempton 1953).....	22
Table A.1 Soil hardness in Takadake 1, Aso volcanic mountain	xxxiv
Table A.2 Soil hardness in Takadake 2, Aso volcanic mountain	xxxv
Table A.3 Soil hardness in Izu Oshima, Tokyo.....	xxxvi
Table A.4 Soil hardness in Takanodai, Aso volcanic mountain	xxxvi
Table A.5 Soil hardness in Towa, Hokkaido.....	xxxvii
Table A.6 Soil hardness in Mizuho, Hokkaido.....	xxxix
Table A.7 Soil hardness in Ohtsuru, Oita Prefecture	xli
Table A.8 Soil hardness in Ono, Oita Prefecture.....	xli
Table A.9 Soil hardness in Yabakei, Oita Prefecture.....	xlii
Table B.1 Plasticity index and activity values in Takadake 1, Aso volcanic mountain.....	xliii
Table B.2 Plasticity index and activity values in Takadake 2, Aso volcanic mountain.....	xliii
Table B.3 Plasticity index and activity values in Izu Oshima, Tokyo	xliii
Table B.4 Plasticity index and activity values in Takanodai, Aso volcanic mountain	xliii
Table B.5 Plasticity index and activity values in Towa, Hokkaido	xliv
Table B.6 Plasticity index and activity values in Mizuho, Hokkaido	xliv
Table B.7 Plasticity index and activity values in Ohtsuru, Oita Prefecture.....	xliv
Table B.8 Plasticity index and activity values in Ono, Oita Prefecture	xliv
Table B.9 Plasticity index and activity values in Yabakei, Oita Prefecture.....	xliv

Table C.1 Grain size distribution properties in Takadake 1, Aso volcanic mountain.....	xlvi
Table C.2 Grain size distribution properties in Takadake 2, Aso volcanic mountain.....	xlvi
Table C.3 Grain size distribution properties in Izu Oshima, Tokyo	xlvi
Table C.4 Grain size distribution properties in Takanodai, Aso volcanic mountain	xlvi
Table C.5 Grain size distribution properties in Towa, Hokkaido	xlvi
Table C.6 Grain size distribution properties in Mizuho, Hokkaido	xlvi
Table C.7 Grain size distribution properties in Ohtsuru, Oita Prefecture	xlvi
Table C.8 Grain size distribution properties in Ono, Oita Prefecture	xlvi
Table C.9 Grain size distribution properties in Yabakei, Oita Prefecture	xlvi
Table D.1 Density of soil particles in Takadake 1, Aso volcanic mountain.....	xlix
Table D.2 Density of soil particles in Takadake 2, Aso volcanic mountain.....	xlix
Table D.3 Density of soil particles in Izu Oshima, Tokyo	xlix
Table D.4 Density of soil particles in Takanodai, Aso volcanic mountain	xlix
Table D.5 Density of soil particles in Towa, Hokkaido.....	xlix
Table D.6 Density of soil particles in Mizuho, Hokkaido.....	l
Table D.7 Density of soil particles in Ohtsuru, Oita Prefecture	l
Table D.8 Density of soil particles in Ono, Oita Prefecture.....	l
Table D.9 Density of soil particles in Yabakei, Oita Prefecture.....	l
Table E.1 Saturated permeability properties in Takadake 1, Aso volcanic mountain	li
Table E.2 Saturated permeability properties in Takadake 2, Aso volcanic mountain	li

Table E.3 Saturated permeability properties in Izu Oshima, Tokyo	lii
Table E.4 Saturated permeability properties in Takanodai, Aso volcanic mountain	lii
Table E.5 Saturated permeability properties in Towa, Hokkaido	liii
Table E.6 Saturated permeability properties in Mizuho, Hokkaido	liii
Table E.7 Saturated permeability properties in Ohtsuru, Oita Prefecture	liv
Table E.8 Saturated permeability properties in Ono, Oita Prefecture	liv
Table E.9 Saturated permeability properties in Yabakei, Oita Prefecture	lv

Chapter 1

Introduction

1.1 Background

One of the famous volcanic countries in the world is Japan. The center of volcanic in and around Japan occur in two zones accompanying plate subduction along the Japan island arcs and Korean areas west of the Sea of Japan (Fig. 1.1) (Machida 2002). There are 111 active volcanoes in Japan (JMA 2020) and large explosive eruptions may substantially transform landscapes by burying topography under thick layers of tephra (Korup 2017).

Tephra deposits consist of numerous layer and that are an important source of information about eruption because most of which can be used to reconstruct records of past volcanic activity, correlated with specific explosions, and to infer the characteristics of the eruptions that produced them (Alfano 2011; Biass and Bonadonna 2011; Bonadonna and Houghton 2005; Cutler 2020; Shane 2000). The characteristics which show an abrupt change in grain size distribution, suggest that they may be related to two different explosive events (Alfano et al. 2011). Furthermore, tephra deposits can be used to establish time-space relationships of volcanism and insight into petrogenesis (Wilson and Hildreth 1997; Smith et al. 2005, 2006; Oladottir et al. 2008), and for volcanic hazard prediction and risk management (Hurst and Smith 2004; Jenkins et al. 2007; Lindsay et al. 2009; Turner et al. 2008, 2009).

Moreover, occurrence of the landslides in the mountain area of tephra materials are recorded higher either during heavy rainfall or earthquake. Occurrence of the landslides in mountain area and the number of volcanoes in Japan, are one of the background of this study. This study also has implication for geotechnical engineering, especially on the field of landslides. Heavy rainfall-induced landslides on tephra materials were occurred at Takadake area in Aso mountain and at Izu Oshima in Tokyo, and earthquakes-induced landslides were occurred at Takanodai area in Aso mountain and at Iburi Region in Hokkaido.

Generally, research on landslides in tephra materials were conducted by mechanical properties, and less research has been conducted by physical properties. Therefore, this

study aiming to relate characteristics of physical properties on sliding layer in tephra materials at heavy rainfall-induced landslides and at earthquake-induced landslides.

1.2 Objectives

General objective

- Observe parameters of sliding layer in tephra materials by considering characteristics of physical properties.

Specific objective

- Field observation to observe the mechanical properties using soil hardness testing on sliding layer and other tephra layers at landslide.



Figure 1.1 Map location of major source volcanoes of Quaternary tephras in and around Japan (1: large caldera with diameter of more than 10 km; 2: caldera volcanoes with diameters of less than 10 km often associated with composite stratovolcanoes; 3: stratovolcanoes; 4: central cones within calderas; 5: buried caldera; 6: trench and trough axis (plate boundary)) (Machida 2002)

- Field observation to observe the stratigraphy on tephra layers at landslide.
- Observe the physical properties on sliding layer and other tephra layers at landslide.
- Observe the saturated permeability properties on sliding layer and other tephra layers at landslide.
- Observe the content of clay minerals on sliding layer and other tephra layers at landslide.
- Classify the tephra materials.
- Observe the landslides on tuff breccia and andesite materials.

1.3 Scope of the study

The study covers the investigation of tephra materials on heavy rainfall-induced landslides and on earthquake-induced landslides. Research areas and sampling locations are located in Aso volcanic mountains at Kumamoto, in Izu Oshima at Tokyo, in Towa and Abira Town at Hokkaido, and in Hita and Nakatsu City at Oita Prefecture (Fig. 1.2). This study focuses on tephra materials at landslides to relate the characteristics of physical properties on sliding layer. Furthermore, this study also focuses on identification, classification, and relation of tephra materials based on the common field observation and laboratory tests. This study has implication for geotechnical engineering, especially on field of landslides. This study also observed the landslides on tuff breccia and andesite materials which are also the products of volcanic, as a comparison.

This study performed the field observation, soil physical properties, saturated permeability properties, and X-ray diffraction (XRD) test on each layer at tephra materials. The methods of this study are the basic methods which are applicable in all over the world to perform the analysis on landslides in tephra materials.

1.4 Structure of the study

This dissertation is divided into eight chapters. Chapter 1 is an introduction chapter which include the background of research, objectives, scope of the study, and structure of the study. Chapter 2 deals with a brief literature review which related to this research. Furthermore, chapter 3 includes the detailed explanation of research methodology in this study, both on field observation and laboratory tests. Chapter 4 presents the research areas, including information on geology of the area and the landslide which was occurred. Chapter 5 explain the case studies of landslides at volcanic area, soil physical properties

in landslides at volcanic area are explained in chapter 6, and characteristics of physical properties on sliding layers in landslides at volcanic area are done in chapter 7. Finally, conclusions and recommendations drawn from this study will explain at chapter 8.

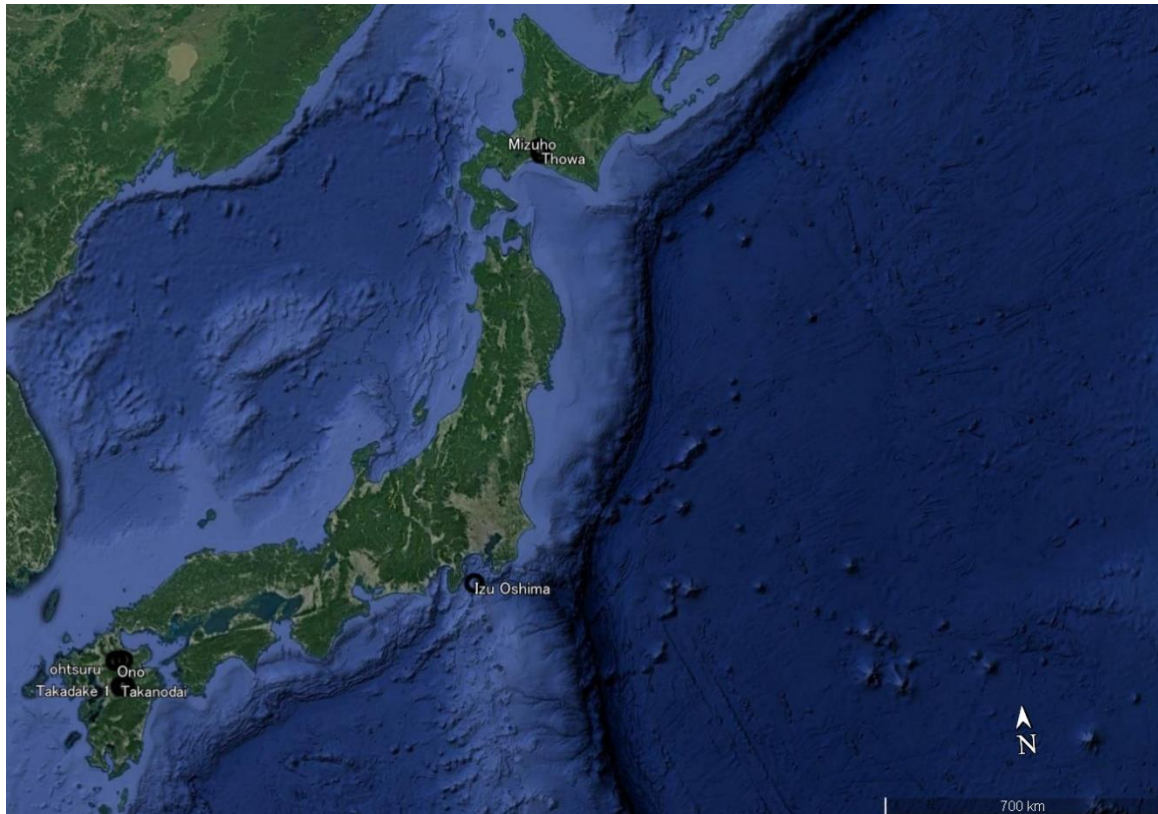


Figure 1.2 Research areas and sampling locations on this study are located in Takadake areas and Takanodai at Aso volcanic mountains, Izu Oshima, Towa and Abira Town at Hokkaido, and in Oita Prefecture

Chapter 2

Literature Review

2.1 Tephra

Large explosive eruptions may substantially transform landscapes by deposit of thick layers of tephra (Korup 2017). Tephra, from the Greek word meaning ‘ashes’, comprise all the explosively-erupted, unconsolidated pyroclastic (fragmental) products of volcanic eruptions (Lowe 2011). Tephra beds are deposits of nonconsolidated pyroclastic ejecta that can be dispersed up to thousands of kilometers from their source volcano (Shane 2000). The term tephra applies to all volcanological grain sizes: ash (grains <2 mm in diameter), lapillus or lapilli (2-64 mm), and blocks (angular) or bombs (subrounded) (>64 mm) (Lowe 2011).

Nowadays, tephra studies have become increasingly important in Quaternary research to arrange high-resolution paleo-environmental or archaeological records, and to synchronize and date such records, further, it has become an urgent focus in a range of globally important projects such as integration of ice core, marine, and terrestrial records refining the record of the last glacial-interglacial transition; studying uncertainty in paleo-environmental reconstruction; response of humans to abrupt environmental transitions (Lowe 2011).

The determination of erupted volume is typically based on the information retained within the isopach maps (Biass and Bonadonna 2011), further, the isopach maps on research areas at this study (Fig. 2.1) was observed by Furukawa and Nakagawa (2010), Koyama and Hayakawa (1996), and Miyabuchi et al. (2003 and 2004). The use of isomass maps, whereby thickness units are replaced by mass per unit area (g/cm^2 or kg/m^2), may provide a way around this sort of uncertainty because the detail of compaction on the deposits and of variation on deposit density with distance from the vent (Bonadonna 2006). As a result, in addition to the classic field parameters including thickness, observations should ideally also include deposit density, particle density, and tephra (or cryptotephra) accumulation per unit area (Bonadonna 2006; Mason et al. 2004).

2.2 Landslides on tephra materials

Tephra deposits, encompassing all pyroclastic materials of any grain size (Lowe

2011), are highly susceptible to slop failure and have been responsible for catastrophic landslides (Kluger et al. 2020). Landslide occurred on tephra materials characterized by soft ground of weathered volcanic cohesive soil (Song et al. 2017). One of the case was occurred at Chaiten volcano which erupted in 2008 and most rapidly some eight years after being covered by tephra (Korup et al. 2017). In 2016, more than 75% of the volume of all slope failures since the eruption (more than 2 million cubic meters) occurred in an

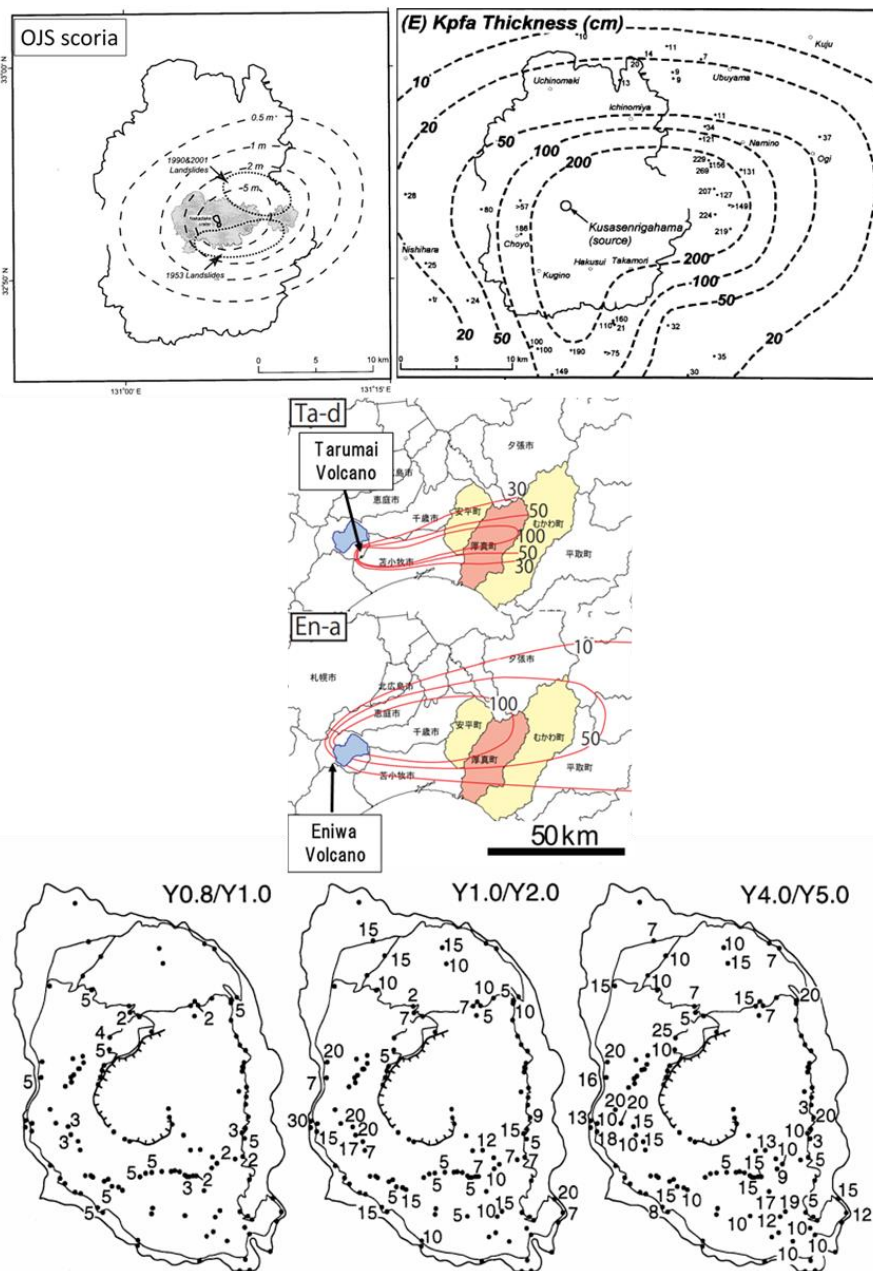


Figure 2.1 Isopach maps on tephra materials at research areas (OJS scoria (Miyabuchi et al. 2004); Kpfa (Miyabuchi et al. 2003; Ta-d and En-a (Furukawa and Nakagawa 2010; Y0.8-Y5.0 (Koyama and Hayakawa 1996)

area of 250 km² around the volcano (Korup et al. 2017). The characteristics features of pyroclastic fall deposits are mantle-bedding, which are slope-parallel bedding, and interlayering of weathered, weak beds and relatively intact beds (Chigira and Suzuki 2016). Unconsolidated superficial tephra deposits that cover the volcanic edifices have great potential for generating serious landslides (Miyabuchi et al. 2015). Moreover, properties of tephra that make them more susceptible to landslides, such as low-density particles, high porosity, low strength or crushable particles, and the particles resist consolidation (Arthurs 2010).

Low density particles, start moving in a landslide more easily and will tend to create longer runout distances compared to similar landslides in denser soils (Arthurs 2010). High porosity and low consolidation increase the available pore volume to store water. More water in tephra will tend to increase the consequences and destructive capacity of a landslide (Arthurs 2010). Moreover, crushable particles tend to add a degree of sensitivity to a soil by significantly changing residual friction angle and can release additional pore water into the soil mass (Arthurs 2010; Del Prete et al. 1998; Fiorillo et al. 2001).

In addition, tephra materials are erupted irregularly, giving some time for weathering and soil formation to begin before burial by the products of another eruption. This creates layers of usually lower-permeability clay-rich soils, which may restrict the movement of ground water and act as slide planes (Del Prete et al. 1998; Fiorillo et al. 2001). Weathered tephra probably also has special characteristics, because particle of tephra has many open voids within a single grain, so when they are sheared, those voids are closed first with the fracturing of void walls, then grain fragments would be floated in squeezed water (Chigira and Suzuki 2016).

Mechanical properties of tephra in the uppermost layers of the ground could have also played a role in the high mobility of landslides recorded (Wang et al. 2019). The crushed and liquefied tephra layers resulted in the high mobility and long run-out distance of the coseismic landslide (Zhang et al. 2019).

2.2.1 Heavy rainfall-induced landslides on tephra materials

The most landslides caused by heavy rainfall on tephra materials were shallow landslide (Miyabuchi et al. 2015). Different physical characteristics on tephra such as particle size and soil hardness cause the difference in permeability (Miyabuchi et al. 2015; Shimizu and Ono 2016). The difference in permeability represents an important barrier

to meteoric water infiltration and, thus, facilitated rupturing near the boundary between the upper tephra and lower soil layers, acting respectively as an overlying permeable layer and an underlying aquiclude (Miyabuchi et al. 2015). The tephra-covered slopes voluminous rainwater infiltrated from the ground surface remains in the upper tephra layers because the lower impermeable soil layers present a barrier. The upper tephra layers become progressively saturated in water and failure occurs (Miyabuchi et al. 2015).

Furthermore, Kluger et al. (2020) reported that the low-permeability tephra (including the highly sensitive layer in the lower tephra) acted as a water infiltration barrier, creating an overlying unconfined aquifer and an underlying confined aquifer in the slope. Water infiltration into the slope will be reduced caused by the low-permeability tephra, therefore the overlying aquifer has increased of pore water pressure (Kluger et al. 2020). Following the effective stress principle and the Mohr-Coulomb failure criterion, an increase in pore water pressure causes a reduction in effective stress, and consequently a reduction in shear strength (Labuz and Zang 2012). Where pore water pressure reduces the shear strength of the slope material to the critical level, landslides are triggered (Kluger et al. 2020).

In addition, the metastable condition of the tephra would fail readily in a wet state or if short term confined water conditions were created as a result of unusually heavy or prolonged rainfall (Del Prete et al. 1998). Particles of tephra have interconnected internal voids whose dimensions' cause suction, as a consequence of which there is a complex diffusion in the water accumulation (Fiorillo et al. 2001).

2.2.2 Earthquake-induced landslides on tephra materials

Earthquakes have induced numerous numbers of landslides, of which a special type is soil slide-avalanche of tephra materials (Chigira and Suzuki 2016). Earthquake shaking necessary to induce a landslide on tephra materials were 5 or more on the scale of Japan Meteorological Agency, which may correspond to 8 or more on MM scale (Chigira and Suzuki 2016).

The main body of the landslide caused by earthquake is composed of cohesive soil with lapilli and blocks (Chiaro et al. 2018). Tephra materials are porous and loose, has low cohesion and lead to slope slide under the earthquake shock. Moreover, the flow type slope failure caused by build-up on water pressure in volcanic soil before and after the earthquake as well as the sensitivity ratio of shear strength (Chiaro et al. 2018). A

halloysite-rich beds also have become a zone that accommodates a sliding layer of earthquake-induced landslides strongly suggests that halloysite is particularly weak to earthquake shaking (Chigira and Suzuki 2016).

2.3 Occurrence of clay minerals in soils

2.3.1 Kaolinite in soils

Kaolinite formation is favoured when alumina is abundant and silica is scarce because of the 1:1 silica:alumina structure, as opposed to the 2:1 silica to alumina structure of the three-layer mineral (Mitchell and Soga 2005). The basic layer has a thickness of 0.72 nm, and the bonding (hydrogen bonds) between successive layers is of sufficient strength to prevent hydration (Fig. 2.2). Therefore, there is no interlayer swelling and layers can be stacked up to make large crystals (Lancellota 2009).

Kaolinite are most abundant in highly weathered soils, which are formed in warm humid climates, although a high rainfall can result in their formation within soils in temperate climates (Weaver 1989). Generally, kaolinites in soils are highly disordered and many of the peaks in their XRD patterns are poorly resolved (Churchman and Lowe 2012). Interstratification between kaolinite (and also halloysite) and smectite quite often occur (Churchman and Lowe 2012). Kaolinite can also form interstratifications with other types of layers besides smectites, for example, vermiculite (Jaynes et al. 1989), and can also participate in interstratified phases involving several different types of layers (Churchman and Lowe 2012).

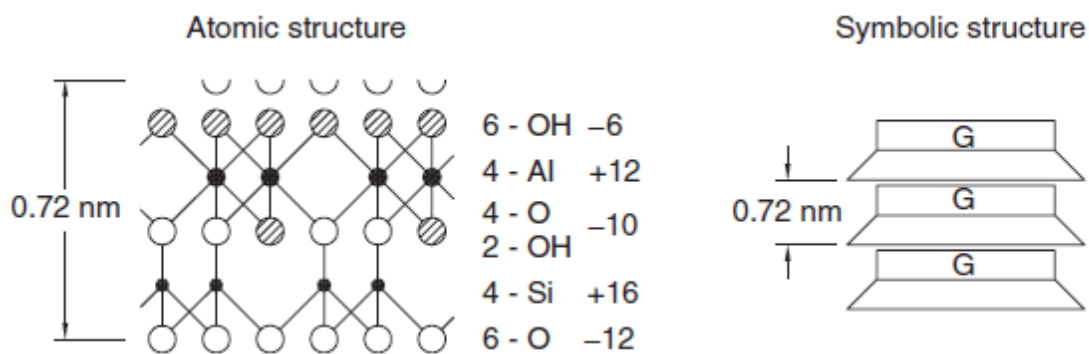


Figure 2.2 Structure of kaolinite (Lancellota 2009)

2.3.2 Halloysite in soils

Halloysite is a 1:1 kaolin-group clay mineral with a similar composition to kaolinite with a repeating structure of one tetrahedral (silica) sheet and one octahedral (alumina) sheet bound with an interlayer space occupied (in hydrated form) by water molecules

(Moon et al. 2015a). Two types of halloysite are commonly found in such soils are hydrated halloysite (1.0 nm) and dehydrated halloysite (0.7-nm) (Kautz and Ryan 2003; Moon et al. 2015a).

Halloysite is a common component of soils formed from volcanic parent materials, particularly tephra including finer components referred to as volcanic ash (Lowe 1986). Halloysite in the soils results from *in situ* alterations of primary minerals, from volcanic

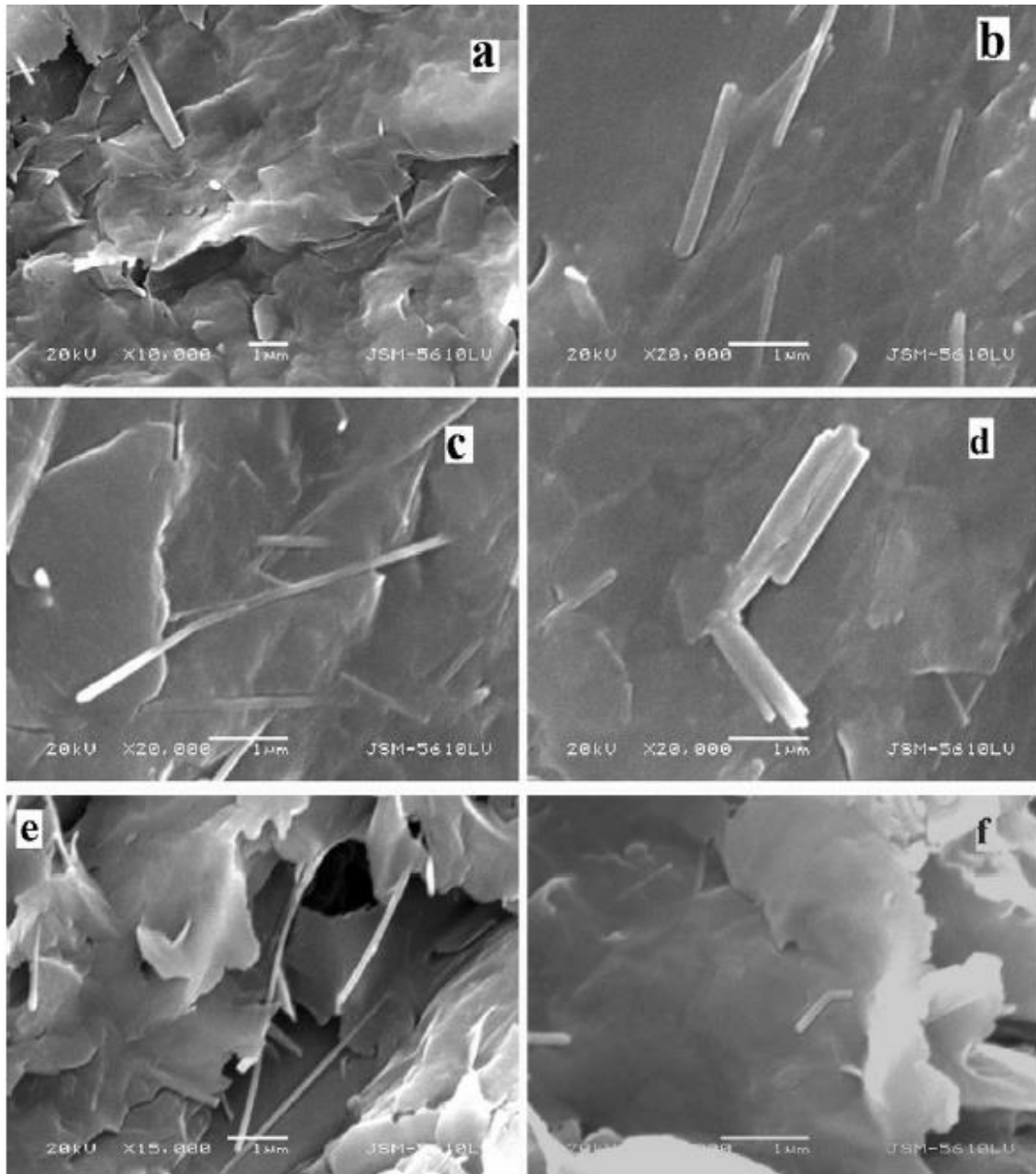


Photo 2.1 SEM images showing various morphologies of halloysite: (a) lamellar particles; (b) tubular or club-like particles; (c) needle-like or fibrous particles; (d) parallel clusters of single tubular halloysite crystals; (e) growth of fibrous halloysite on the edge of platy rectorite; (f) contact twins of halloysite (Hong and Mi 2006)

glasses, from silicification of allophones or finally, from percolating solutions in the soils horizons (Joussein et al. 2005). Halloysite is rare in tephra materials that are of recent age and at the land surface (Lowe 1986), however, halloysite is a common weathering product of rhyolitic (silica-rich) tephra (Churchman and Lowe 2012).

Halloysite can occur in a variety of particle morphologies (Photo 2.1) including tubes and microtubules, spheroids and microspheres, crumpled lamellae, crinkly films, needle-like or fibre-like forms, and prismatic forms (Hong and Mi 2006; Etame et al. 2009). Generally, halloysite formed by process of alteration in volcanic glass and pumice which have the shape of balls or scrolls and sometimes associated with short-tubes (Nagasawa 1978 in Adamo et al. 2001), and to reflect a particular mode of formation for halloysite, the particularly spheroidal appears (Churchman 2000). Spheroidal forms of halloysite appear often in weathering products of volcanic glass, which has a fast dissolution rate, and recrystallization from the resulting supersaturated solution appears to favour this particular shape (Adamo et al. 2001; Singer et al. 2004), possibly when physically constrained, for example, within pumice cavities (Adamo et al. 2001).

Churchman and Lowe (2012) reported that peculiar shape was once regarded as the distinguishing feature of halloysite in comparison with kaolinite, it is rather the occurrence, or else evidence for prior occurrence, of interlayer water that demarcates halloysites from kaolinites. Interlayer water is lost irreversibly from halloysite on drying (Churchman and Lowe 2012). Moreover, halloysite has no indication of swelling, but shrinkage cracks occurred in the halloysite-dominated soils in the dry season (Moon et al. 2015a).

Same with kaolinites, interstratified form has been found between halloysites and smectites. They form in similar conditions (usually alkaline) which give rise to smectites but where the drainage is less restricted (more leaching occurs) than for smectite formation (Smith et al. 1987). However, unlike kaolinite, halloysite represents a potentially weak, sensitive material due to its high water content and unique micro-texture (Joussein et al. 2005; Moon et al. 2015a).

2.3.3 Illite in soils

Illite has undergone considerable transformation to include expansible 2:1 layers of vermiculite and/or smectite is more likely to occur in the fine clay (<0.2 μm) size fraction (Laird et al. 1991; Robert et al. 1991). Illite is similar to montmorillonite, but in this case

the layers are strongly bonded by a potassium atom, which fills the hexagonal hole in the tetrahedral sheet, and crystals have a thickness of about 10 to 30 nm (Fig. 2.3) (Lancellota 2009). The high stability of illite is responsible for its abundance and persistence in soils and sediments (Mitchell and Soga 2005).

Illite is the most commonly found clay mineral in soils encountered in engineering practice (Mitchell and Soga 2005). Illite can form in soils by weathering as a result of transformation, in the solid phase, from micas, and like most of the other secondary minerals, they can also precipitate by neogenesis out of solution. Illite contains some expanded layers; hence some degree of interstratification of the K-rich illite layers with vermiculite or smectite layers that have become depleted in K through its displacement by hydrated cations (Churchman and Lowe 2012). Illite usually occurs as very small, flaky particles mixed with other clay and nonclay materials. High-purity deposits of illite are uncommon (Mitchell and Soga 2005).

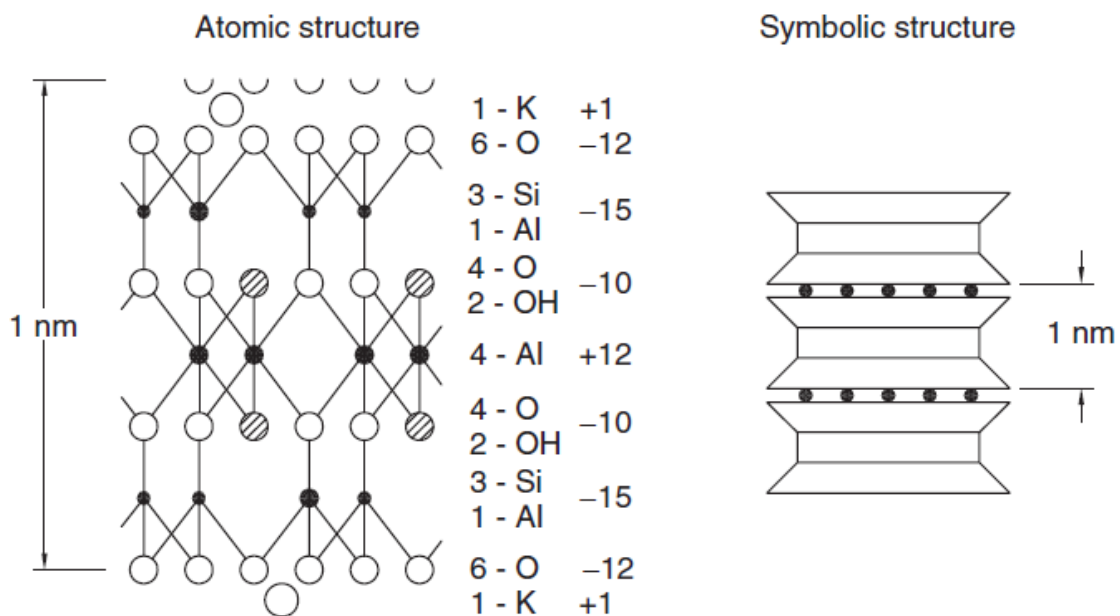


Figure 2.3 Structure of illite (Lancellota 2009)

2.3.4 Vermiculite in soils

Vermiculite is also often found as a clay phase constituent of soils (Mitchell and Soga 2005). Most vermiculites in soils have formed by the transformation of micas by weathering (Wilson 1999 cited in Churman and Lowe 2012), and some form by the analogous transformation of chlorites (Wilson 1999 cited in Churman and Lowe 2012). Although vermiculite is an expansive mineral, the greater interlayer ordering in

vermiculite results in less variability in basal spacing than occurs in the smectite minerals (Mitchell and Soga 2005).

2.3.5 Smectite in soils

Smectite has 2:1 silica:alumina structure, form where silica is abundant, as is the case where both silica and alumina are flocculated (Mitchell and Soga 2005). Smectites appear in soils either because they are inherited from parent materials, have been formed by neogenesis in crystallization from solutions of the constituents of rocks, or else they are the products of transformation from micas and chlorites in the strong, or long-term condition. They share the possibility of an inherited origin with most other types of clay minerals (Churchman and Lowe 2012).

The origin of smectites occurring in soils is not always well-defined. Smectites may appear in relatively large particles since smectites formed by transformation, moreover, smectites most often are especially fine-grained materials (Churchman and Lowe 2012). Generally, smectites in soils are dioctahedral, including the products from alteration process of Mg-rich serpentinite, where saponite might be expected to form (Wildman et al. 1968). Product from weathering process often form the saponite – for example, within the crystals of altered rocks containing ferromagnesian minerals – but it gives way to dioctahedral smectites in the upper parts of soil profiles. Even so, nontronite is thought to be particularly susceptible to attack by complexing agents from roots (Farmer 1997). In addition, there is a montmorillonite which presents a more complicated structure (Fig. 2.4). The bonding between the silica sheets is represented by van der Waals' forces, therefore, it is a weak bond (Lancellota 2009). Molecular water may also appear between

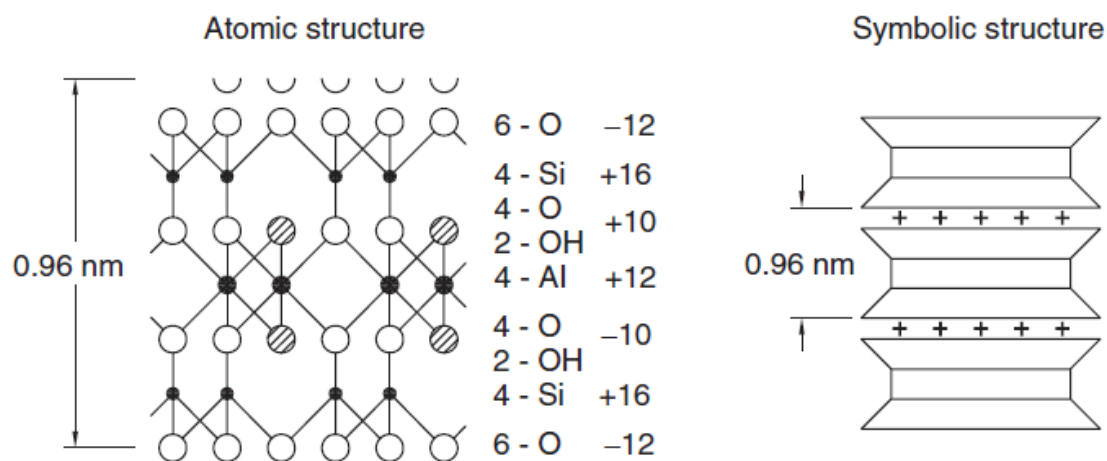


Figure 2.4 Structure of montmorillonite (Lancellota 2009)

layers on montmorillonite, and caused the crystals can be rather small and clay soils with content of montmorillonite are susceptible to swelling, with important engineering implications (Lancellota 2009).

Smectites can be the subject to alteration and change within soils. Interstratified kaolinite-smectites most probably following the prior adsorption of hydroxyl-Al species into their interlayers (Ryan and Huertas 2009).

2.3.6 Palygorskite and sepiolite in soils

The fibrous 2:1 clay minerals, palygorskite and sepiolite undoubtedly occur in the sedimentary parent materials of many soils containing these minerals; until relatively recently, their inheritance from these parent materials was considered to be their source in soils (Singer 2002 cited in Churman and Lowe 2012). Palygorskite is much more common than sepiolite in soils (Singer 2002 cited in Churman and Lowe 2012).

2.4 Clay minerals influence landslides on tephra materials

Studies on formations of volcanic ash, pumice deposits, and tephra aimed at characterizing their clay mineralogy and weathering sequences have been extensively carried out all over the world (Sudo and Shimoda 1978; Wada 1989). The small clay content often contains halloysite, a clay mineral typically associated with unstable soils (Chigira and Yokoyama 2005) and all of the layers accommodating sliding layers were confirmed that they had a halloysite (Fig. 2.5) (Chigira and Suzuki 2016). Furthermore, halloysite has been found to dominate sliding layer in rainfall-induced landslides at Hong Kong, Japan, New Zealand, Hawaii, and the conterminous USA (Chigira and Yokoyama 2005; Irfan 1998; Kluger et al. 2017, 2020; Parry et al. 2000, 2014; Shaller et al. 2016; Taskey 1977; Wen and Aydin 2003; Yamao et al. 2016).

Clay bands which are rich in halloysite and capillary barrier effect lead to a new concept for the mechanism underlying landslides (Chigira and Yokoyama 2005). Downward infiltration of water is first inhibited by a series of clay bands; some perched water might be made on the clay bands, leading to the weight increase of the weathered zone. After breaching the clay band, water goes down to the weathering front, where it is blocked again, this time by the capillary barrier effect (Wen and Aydin 2003). The increase in weight and the decrease in suction are assumed to be the main causes of landslides. Dense structure and low porosity, abundant platy clay particles and particle alignment within the slip zone are three significant indicators reflecting its mechanical behaviour,

involving processes of compaction, comminution and particle rearrangement (Wen and Aydin 2003).

Halloysite is also known to form low-permeability soils with high sensitivity (Kluger et al. 2017, 2020; Moon et al. 2015b; Smalley et al. 1980). High sensitivity of the halloysitic tephra layers within the lower tephra is one of the most important preconditioning factors for the landslides (Kluger et al. 2017, 2019, 2020; Moon et al. 2015b). Low-permeability clay layers interbedded in soil slopes can occur in all types of deposits and environments worldwide, and these situations probably represent the most intensely studied preconditioning factor for pore water pressure-induced landslides (Zaruba and Mencl 1982 cited in Kluger et al. 2020). In addition, the variety of morphologies of the halloysite showed the clay sizes are mainly small and the high porosity occurs almost entirely within very small, interconnected pore spaces. The materials can hold very large amounts of water, but that water cannot move readily within the soils (low permeability) (Moon et al. 2015a).

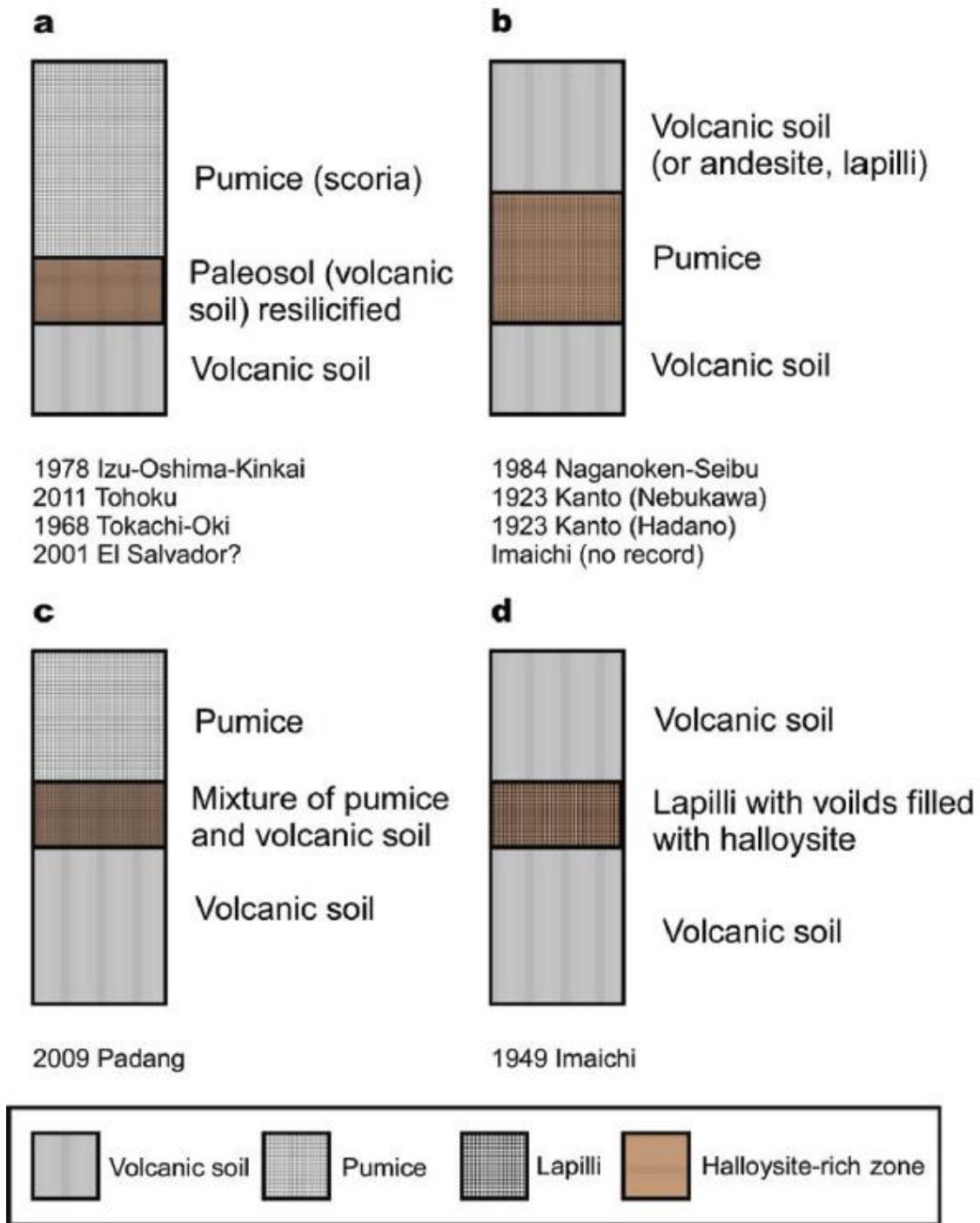


Figure 2.5 Schematic sketch showing the successions including halloysite-rich zone, in which a sliding layer was made (Chigira and Suzuki 2016)

Chapter 3

Research Methods

3.1 Field measurements

Tephra stratigraphic analysis and soil hardness measurements were performed in the field measurements. The stratigraphy analyses of each landslide were performed by scraping the surface using shovels to expose the tephra layers. Tephra layers was separated using colored toothpicks and the depth was measured using the scale (Photo 3.1).

Moreover, soil hardness was measured using a Yamanaka-type soil hardness meter (Photo 3.2), which measures the soil hardness by inserting the device into the exposed

tephra layer at the site. Tokunaga and Goto (2017) found a discontinuity in the strength of pyroclastic materials in Aso volcanic mountains using a soil hardness tester. Sasahara et al. (1995) also examined the slope stability of unconsolidated pyroclastic materials, and they



Photo 3.1 Separating tephra layers using colored toothpicks and measuring depth of tephra layers using scale in field measurements



Photo 3.2 Measuring soil hardness using a Yamanaka-type soil hardness meter

reported that there is a strong positive correlation between the soil hardness measured with a Yamanaka-type soil hardness tester and the shear strength parameters of soil in the Mohr-Coulomb failure criterion.

3.2 Physical properties tests

3.2.1 Liquid limit and plastic limit

Liquid limit and plastic limit tests were performed according to the JIS A1205 from the laboratory testing standards of Geomaterials Vol. 1. Japanese Geotechnical Society Standards (JGS 2015). The water content of a soil in a transition from the plastic state to the liquid state is the liquid limit which can be obtained by means of the liquid limit test. Moreover, the water content of a soil in a transition from the plastic state to the semi-solid state is the plasticity limit which can be obtained by means of a plastic limit test. From the liquid limit and plastic limit value, the plastic index value is known.

Equipment:

- a. Set of the dropper device (Liquid limit test) (Photo 3.3)
- b. Grooving tool (Liquid limit test) (Photo 3.3)
- c. Frosted glass plate (Plastic limit test)
- d. Distilled water

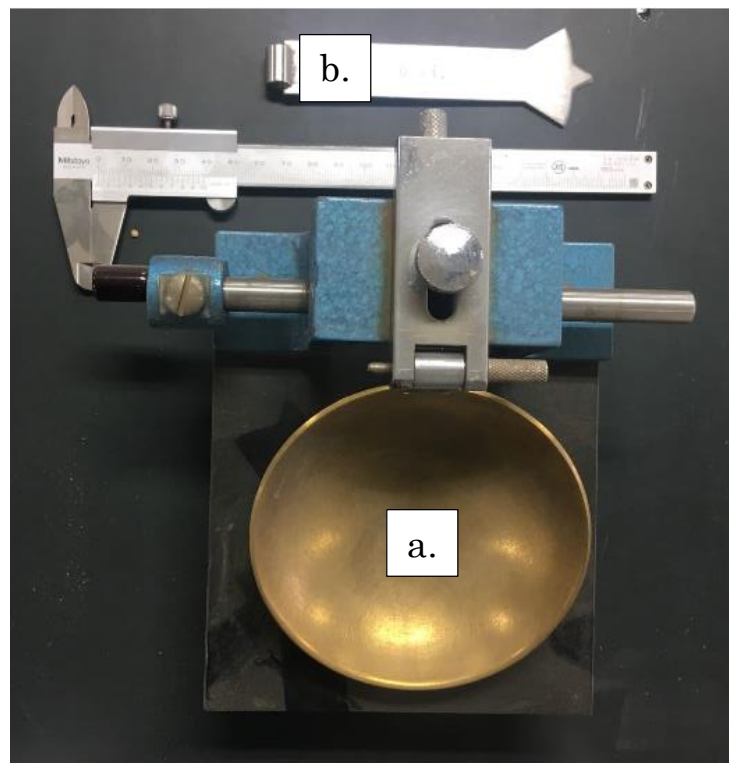


Photo 3.3 Equipment for liquid limit test

Preparation of samples:

- a. The analysis used the material which has passed a sieve with 425 μm mesh and which the original of soil with a natural water content. Sample of air-dried may be used if air drying has no effect on the analysis results for liquid or plastic limit values.
- b. Minimum mass of samples shall be; for the liquid limit test is 200 g and for the plastic limit test is about 30 g.
- c. Place a sample on a glass plate and mix it fully.
 - 1) The moisture content in soil samples shall be the putty-like for the liquid limit test and dumpling-like for the plastic limit test. Distilled water shall be added if the water content in a sample is too low. The sample shall be suitably dehydrated through natural drying if the water content in a sample is too high.
 - 2) For the case if used the air-dried material for the samples, add distilled water and mix thoroughly before allowing the material to sit for ten hours. Responsibility shall be taken to avoid evaporation and assure that the soil and water are fully combined.

Liquid limit test:

- a. Place a gauge between the hard rubber pad and the brass dish, and adjust the dropper such that the drop of the brass dish is 10 ± 0.1 mm.
- b. To place a sample in the brass dish, use the spatula until the maximum thickness of about 1 cm and shape it. Cut a groove in the sample along the diameter of the brass dish while holding the grooving tool perpendicular to the bottom of the brass dish. Dividing the sample into two with the center line of the cam's bearing surface.
- c. Place the brass dish in the dropper device. Lift and drop the dish frequently at a rate of twice per second, the process continuing until the soil at the bottom which divided by the groove has combined together again for a length of about 1.5 cm.
- d. Record the number of drops at the time when the groove combined and collect the water content of the sample near the combined point.

- e. Either add distilled water to the sample or allow some moisture to evaporate, then combine the sample fully and repeat the steps b until d. This process shall be repeated until obtained the two samples of 10 to 25 drops and two samples of 25 to 35 drops.

Liquid limit results:

- a. Plot the number of drops on the logarithmic axis and the soil water content on the arithmetic axis using the semi logarithmic graph paper.
- b. Obtain a best-fit straight line, known as a flow curve.
- c. The liquid limit w_L (%) is determined by the flow curve, using the soil water content corresponding to 25 drops.
- d. The sample is NP (non-plastic) if unable to complete the procedure in the liquid limit test.

Plastic limit test:

- a. Under the palm of the hand, rolling the mixed sample on the glass plate. Form the sample into a string until it matches the 3 mm round rod in diameter. Collect the sample which formed the string of 3 mm diameter and repeats the above process.
- b. Repeat the above process until the string breaks apart as it reaches a diameter of 3 mm. Collect the broken part and obtain the water content of the soil promptly.

Plastic limit results:

- a. In the plastic limit test, the water content of the sample obtained shall be the plastic limit, w_P (%).
- b. The sample is the NP (non-plastic) if unable to obtain the plastic limit in the step of the plastic limit test.

Plastic Index

$$I_P = w_L - w_P \quad (3.1)$$

Where I_P is plastic index

w_L is liquid limit

w_P is plastic limit

If the value is no significant difference between the two, or if it is impossible to obtain

either the liquid or plastic limit, give the sample the index as N_p .

Plastic index and liquid limit value from this test plot on the Atterberg limits, which is used for description, identification, moreover, classification of the cohesive soils and as a basis for mechanical properties preliminary assessment. In addition, Atterberg limits are a basis for the formation of a soil classification system, in the identification of cohesive soils (Casagrande 1948). The system was adopted by the minor modification as a part of the Unified Classification System. The essential part of the Unified Soil Classification System known as *Plasticity chart* which plot of a plasticity index as a function of liquid limit that is divided into different zones (Fig. 3.1).

Plasticity chart separates the soil into various groups based on liquid limit and plasticity index, and also using the vertical line L_w equal to 30% and 50%. Furthermore, line A of plasticity index as a function of liquid limit that is divided into different zones, and it is also expressed as $I_w = 0.73(L_w - 20)$ (Mitchell and Soga 2005). The equation of plasticity index determines the range of water content for a soil and is related to the maximum volume change (compressibility) of the soil. These limits depend on the

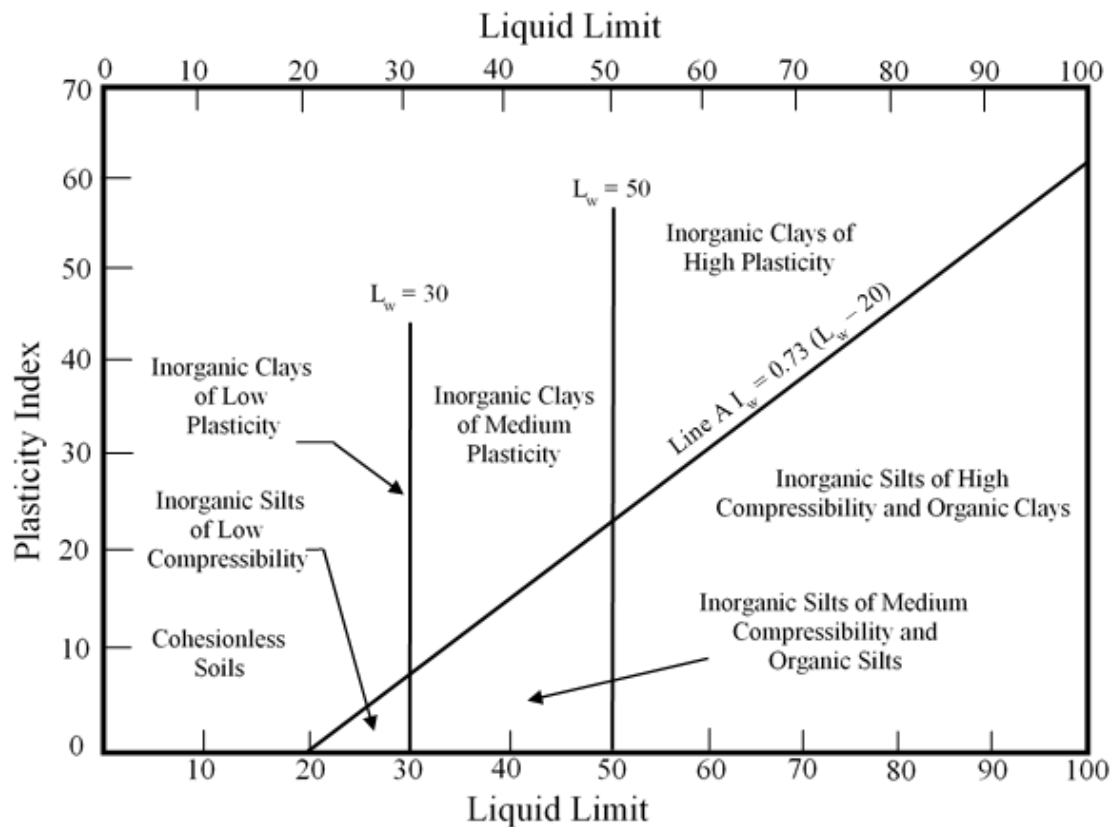


Figure 3.1 Plasticity chart (Casagrande 1948)

grading and on the mineralogy, shape, and also surface texture of the grains. Atterberg limits measure the fraction of a soil sample which smaller than 425 μm , in order this analysis described only the part of a well-graded soil (Atkinson 2007).

In addition, the ratio of the plasticity index to the clay size fraction (percentage by weight of particles finer than 2 μm), termed the *activity*, is very useful (Skempton 1953). Skempton (1953) also suggested three classes of activity: active, normal, and inactive, and subdivided them into five groups (Tab. 3.1). The greater the activity, the more important the influence of the clay fraction on properties and the more susceptible their values to changes in such factors as type of exchangeable cations and pore fluid composition (Mitchell and Soga 2005).

$$Activity = \frac{Plasticity\ Index}{\% < 2\mu m} \quad (3.2)$$

Table 3.1 Classes of activity value (Skempton 1953)

Classes of activity	Activity value
Inactive	<0.5
Inactive	0.5 – 0.75
Normal	0.75 – 1.25
Active	1.25 – 2
Active	>2

3.2.2 Particle size distribution

Particle size distribution analysis was performed according to the JIS A1204 from the laboratory testing standards of Geomaterials Vol. 1. Japanese Geotechnical Society Standards (JGS 2015). The distribution of particle sizes in soils expressed by mass percentage is particle size distribution.

Particle size distribution test method (Photo 3.4):

- a. Sieve analysis is a particle size test by using metal wire cloth sieves and shall apply to soil particles remaining on the metal wire cloth sieve with an aperture width of 75 μm .
- b. Sedimentation analysis is particle size test by calculating the suspension of density soil and shall apply to soil particles passing a metal wire cloth sieve with an aperture width of 75 μm .

The first step, separate the soil sample using a sieve with an aperture width of 2 mm.

Sedimentation analysis of the section passing a sieve with an aperture width of 2 mm. The sedimentation analysis may be omitted if the distribution of particle sizes below 0.075 mm is not required. Sieve analysis of the section passing a sieve with an aperture width of 2 mm and the section remaining on a sieve with an aperture width of 75 μm .

Equipment:

1. Test apparatuses
 - a. Sieves (75 μm , 106 μm , 250 μm , 425 μm , 850 μm , 2 mm, 4.75 mm, 9.5 mm, 19 mm, 26.5 mm, 37.5 mm, 53 mm, and 75 mm)
 - b. Density hydrometer, which graduated in a 0.001 g/cm^3 division scale between 0.995 g/cm^3 and 1.050 g/cm^3
 - c. Dispersion devise, which capable of sufficiently dispersing soil particles by mechanical means.
 - d. Measuring cylinders (250 mL and 1,000 mL)
 - e. Thermometer, readable to 0.5° C or 1° C
 - f. Constant-temperature water bath, which capable of maintaining the temperature of a soil suspension in a measuring cylinder nearly constant. If the sedimentation analysis is carried out in a constant-temperature room, the bath is not required.

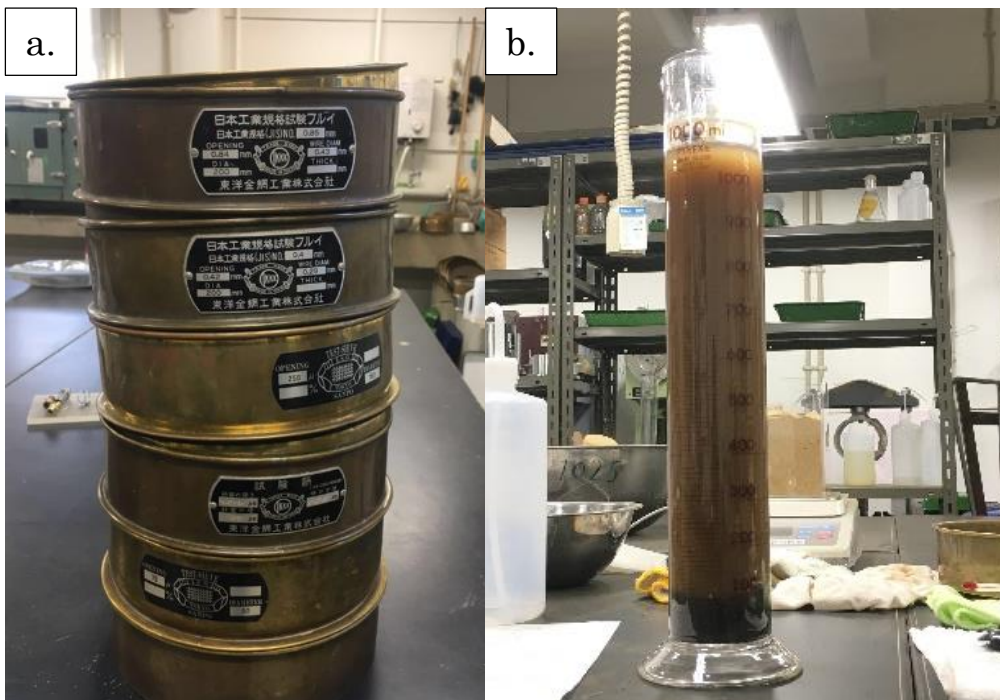


Photo 3.4 Particle size distribution test method: (a) Sieve analysis; (b) Sedimentation analysis

- g. Beaker of 500 mL or more in nominal capacity
- h. Balances, sensitive to 0.01 g for weighing a sample 100 g and below, 0.1 g for weighing 100 g to 1 kg, and 1 g for weighing over 1 kg.
- i. Vernier calliper with a minimum reading of 0.05 mm or less
- j. Water content measuring apparatus
- k. Loosening apparatus
- l. Rubber spatula
- 2. Reagents
 - a. Hydrogen peroxide of 6% solution
 - b. The dispersing agent shall be the saturated solution of sodium hexametaphosphate

Sample preparation and sieving of soil sample using a sieve with an aperture width of 2 mm:

- a. The sample of analysis may use a wet or air-dried sample. When the sedimentation analysis is carried out, the minimum oven-dried mass of a sample passing a sieve with an aperture width of 2 mm shall be around 115 g for sandy soil and 65 g for silty or clayey soil.
- b. Take the sample around one-fourth of the sample and obtain the water content of the sample w (%).
- c. Take the total amount of remaining sample (hereinafter referred to as the total sample) as the sample for particle size test and weigh the mass of the sample as m (g).
- d. Sieve the total sample through a sieve with an aperture width of 2 mm. Separate the soil particles passing the sieve as the portion passing the sieve with an aperture width of 2 mm and the particles remaining on the sieve as the portion retained on the sieve with an aperture width of 2 mm. Pass as many fine fractions as possible adhering to the surface of coarse particles retained on the sieve through the sieve during the sieving operation.

Sieve analysis of the portion remaining on the sieve with an aperture width of 2 mm:

1. Sample preparation
 - a. Wash the portion remaining on the sieve with an aperture width of 2 mm. Wash away the soil particles passing the sieve with an aperture width of 2 mm with water on the sieve.
 - b. Dry the total amount of sample remaining on the sieve in an oven at $(110 \pm 5)^\circ$ C to a constant mass, and weigh the mass of the sample as m_{0s} (g).
2. Sieving of soil sample
 - a. Sieve the oven-dried sample through the sieves with an aperture width of 75 mm, 53 mm, 37.5 mm, 26.5 mm, 19 mm, 9.5 mm, and 4.75 mm. Until the portion passing the sieve becomes approximately 1% or less of the portion remaining on the sieve, sieve the sample continuously for one minute. Move the sieve laterally and vertically while vibrating the sieve so as to keep the sample moving continuously over the surface of the sieve during the sieving operation.
 - b. Obtain the mass of the sample remaining on each sieve, and take the mass of the sample remaining on the sieve with an aperture width of d_i as $m(d_i)$ (g). Further, obtain the mass of the sample passing the sieve with an aperture width of 4.75 mm, and take the mass of the sample remaining on the sieve with an aperture width of 2 mm as $m(2 \text{ mm})$ (g).

Sedimentation analysis of the portion passing the sieve with an aperture width of 2 mm:

1. Test of hydrometer
 - a. Float the hydrometer in distilled water, obtain the top of the meniscus r_U and the bottom r_L in the decimal part of the hydrometer. Wash in advance the stem of the hydrometer with alcohol or a detergent.
 - b. Using a measuring cylinder of 250 mL in nominal capacity, measure the length of the bulb of the hydrometer L_B (mm) to the nearest 0.1 mm, and the volume V_B (cm^3) to the nearest 1 cm^3 .
 - c. Measure the length l_1 (mm) from the top of the hydrometer bulb to the 1.000 mark and the length l_2 (mm) to the 1.050 mark to the nearest 0.1 mm.

- d. With a nominal capacity of 1,000 mL to the nearest 0.01 cm², determine the cross-sectional area A (cm²) of the measuring cylinder.
2. Sample preparation
 - a. Take the oven-dried mass around 115 g of sandy soil and around 65 g for silty or clayey soil as the sample from the portion passing the sieve with an aperture width of 2 mm.
 - b. Take around one-fourth of the sample and obtain the water content of the sample as w_1 (%).
 - c. Take the total amount of the remaining sample as the sample for sedimentation analysis, and obtain the mass of the sample as m_1 (g).
3. Dispersion of soil sample
 - a. For soil sample less than 20 in plasticity index
 - 1) Add distilled water to the sample contained in a beaker, stir to combine the soil-water mixture uniformly and separate the soil particles in the water.
 - 2) Let the combined sample stand for 15 hours or more. After that, transfer the total amount of the combined sample in the beaker into a container of the dispersion device and add distilled water until the total volume is around 700 mL.
 - 3) Add 10 mL of a dispersing agent, and stir the combined sample by using the dispersion device for around 1 minute.
 - b. For soil sample not less than 20 in plasticity index
 - 1) Gently add 100 mL of hydrogen peroxide 6% solution to the sample contained in a beaker, and stir to mix the soil mixture uniformly and separate the soil particles in the solution.
 - 2) Put it in a constant-temperature drying oven at (110±5)° C with the glass plate cover or the like on the beaker. If the sample in the beaker boils over the beaker, repeat the procedure from sample preparation.
 - 3) Take the beaker out of the constant-temperature drying oven after around 1 hour and add approximately 100 mL of distilled water to separate the soil particles in the water.

- 4) Let the combined sample stand for 15 hours or more. After that, transfer the total amount of the combined sample in the beaker into a container of the dispersion device and add distilled water until the total volume is around 700 mL.
- 5) Add 10 mL of a dispersing agent, and stir the combined sample by using the dispersion device for around 1 minute.
4. Sedimentation measurement
 - a. Transfer the total amount of dispersed sample to a measuring cylinder and fill to the 1 L mark with distilled water.
 - b. Place the measuring cylinder in a constant-temperature water bath or constant-temperature room, and let it stand until the temperature of the sample in the measuring cylinder is almost the same as the temperature of the water in the constant-temperature water bath or the room temperature in the constant-temperature room. Stir the soil sample with a rod from time to time during this procedure.
 - c. Place a cover on the measuring cylinder, turn the cylinder upside down and back to upright for around 1 min after the sample in the measuring cylinder is uniformly suspended, and let it stand. At that time do not lose any soil sample even if it is a small amount.
 - d. After letting the measuring cylinder stand, float the hydrometer in the cylinder, obtain the reading (r) of decimal part of the scale at the top of the meniscus to the nearest 0.0005, and at the same time also take the temperature T ($^{\circ}$ C) of the suspension at specific intervals of time. The intervals of time t (min) for taking the reading after letting the cylinder stand are 1 min, 2 min, 5 min, 15 min, 30 min, 60 min, 240 min, and 1440 min.

Sieve analysis of the portion passing the sieve with an aperture width of 2 mm and the portion remaining on the sieve with an aperture width of 75 μ m:

- a. Sample preparation, obtain the total amount of the sample used for sedimentation analysis as the sample.

- b. Washing the soil sample with water on the sieve with an aperture width of 75 μm with water, and after sufficiently washing away fine particles, dry the total amount of residue in an oven at $(110\pm 5)^\circ\text{C}$ to a constant mass.
- c. Sieving the oven-dried soil sample through sieves with an aperture width of 850 μm , 425 μm , 250 μm , 106 μm , and 75 μm . After that, measure the mass $m(d_i)$ (g) of the sample retained on each sieve.

Test results:

1. Calculation of particle size based on sieve analysis results
 - a. Calculate the mass percentage passing of soil samples remaining on the sieves with an aperture width of 2 mm or more using the following equations

$$P(d_i) = \left(1 - \frac{\Sigma m(d_i)}{m_s}\right) \times 100$$

$$m_s = \frac{m}{1 + \frac{w}{100}} \quad (3.3)$$

Where d_i is aperture width of a sieve (mm)

$P(d_i)$ is mass percentage passing the sieve with an aperture width of d_i (%)

m_s is oven-dried mass of total sample (g)

m is mass of total sample (g)

w is water content of the total sample (%)

$m(d_i)$ is oven-dried mass of the sample that had remained on the sieve with an aperture width of d_i (g)

$\Sigma m(d_i)$ is sum of the oven-dried mass of samples that had remained on the sieves with an aperture width of not less than d_i (g)

- b. Calculate the mass percentage passing the sieve with an aperture width of 2 mm and those that had remained on the sieve with an aperture width of 75 μm using the following equation

$$P(d_i) = \frac{m_s - m_{0s}}{m_s} \left\{1 - \frac{\Sigma m(d_i)}{m_{1s}}\right\} \times 100$$

$$m_{1s} = \frac{m_1}{1 + \frac{w_1}{100}} \quad (3.4)$$

Where m_{0s} is oven-dried mass of the sample that had remained on the sieve with an aperture width of 2 mm (g)

m_{1s} is oven-dried mass of the sample for sedimentation analysis (g)

m_1 is mass of the sample for sedimentation analysis (g)

w_1 is water content of the sample for sedimentation analysis (%)

2. Calculation of particle size based on sedimentation analysis results

a. Calculate the meniscus correction value using the following equation

$$C_m = r_L - r_U \quad (3.5)$$

Where C_m is meniscus correction value

r_L is reading of decimal part of hydrometer at the bottom of the meniscus

r_U is reading of decimal part of hydrometer at the top of the meniscus

b. Calculate the effective depth of hydrometer based on the reading r of decimal part of hydrometer using the following equation

$$L = L_1 + \frac{1}{2} \left(L_B - \frac{V_B}{A} \times 10 \right)$$
$$L_1 = l_1 - 20(r + C_m)(l_1 - l_2) \quad (3.6)$$

Where L is effective depth of hydrometer bulb center (mm)

L_1 is length from the top of hydrometer bulb to the reading r (mm)

l_1 is length from the top of hydrometer bulb to the mark 1.000 (mm)

l_2 is length from the top of hydrometer bulb to the mark 1.050 (mm)

r is reading of decimal part of the hydrometer

L_B is overall length of the hydrometer bulb (mm)

V_B is volume of hydrometer bulb (cm³)

A is cross-sectional area of measuring cylinder (cm²)

c. Calculate the diameter of particle based on respective hydrometer readings using the following equation

$$d = \sqrt{\frac{30\eta}{g_n(\rho_s - \rho_w) t} L} \quad (3.7)$$

Where d is diameter of particle based on the reading r of decimal part of hydrometer (mm)

t is interval of time from the beginning of sedimentation to the taking of the reading (min)

η is coefficient of viscosity of water at the temperature T (° C) of the suspending medium when taking the reading of the hydrometer

ρ_s is density of soil particles determined according to JIS A 1202 (g/cm³)

ρ_w is density of water at the temperature T (° C) of the suspending medium when taking the reading of the hydrometer (g/cm³)

g_n is acceleration of gravity (980 cm/s²)

- d. Calculate the mass percentage passing $P(d)$ (%) the sieve with an aperture width of 75 μm using the following equation

$$P(d) = \frac{m_s - m_{0s}}{m_s} \cdot \frac{V}{m_{1s}} \cdot \frac{\rho_s}{\rho_s - \rho_w} \times (r + C_m + F) \rho_w \times 100 \quad (3.8)$$

Where V is volume of suspension (1,000 cm³)

F is the correction factor at the temperature of the suspension when taking the reading of hydrometer

3. Particle size accumulation curve

- a. Based on the hydrometer reading on a logarithmic scale, take the aperture width d_1 (mm) and particle size d (mm) on a logarithmic scale as the abscissa and the mass percentage passing $[P(d_1)]$ and $P(d)$ to an arithmetic scale as the ordinate of a semi-logarithmic graph paper. Plot the relation between d_1 and $P(d_1)$ and d and $P(d)$, obtain the smooth curve representing the relation, and take it as the particle size accumulation curve.
- b. Read the particle size D (mm) when the mass percentages passing are 10%, 30%, 50%, and 60% from the particle size accumulation curve and take them as the particle size at 10% passing by mass D_{10} (mm), the particle size at 30% passing by mass D_{30} (mm), the particle size at 50% passing by mass D_{50} (mm), and the particle size at 60% passing by mass D_{60} (mm), respectively.
- c. Read the percentages passing at particle sizes 2 mm, 0.425 mm, and 0.075 mm from the particle size accumulation curve.
- d. Read the mass percentages passing of the following samples from the particle size accumulation curve.
- 1) Coarse gravel of 19 to 75 mm in the soil particle size range
 - 2) Medium gravel of 4.75 to 19 mm in the soil particle size range

- 3) Fine gravel of 2 to 4.75 mm in the soil particle size range
 - 4) Coarse sand of 0.850 to 2 mm in the soil particle size range
 - 5) Medium sand of 0.250 to 0.850 mm in the soil particle size range
 - 6) Fine sand of 0.075 to 0.250 mm in the soil particle size range
 - 7) Silt of 0.005 to 0.075 mm in the soil particle size range
 - 8) Clay of not more than 0.005 mm in the soil particle size range
4. Calculations of coefficient of uniformity and coefficient of curvature.

The coefficient of uniformity and coefficient of curvature shall be calculated using the following equations

$$U_c = \frac{D_{60}}{D_{10}}$$

$$U_c' = \frac{(D_{30})^2}{D_{10} \times D_{60}} \quad (3.9)$$

Where U_c is coefficient of uniformity

U_c' is coefficient of curvature

D_{10} is particle size at 10% passing by mass

D_{30} is particle size at 30% passing by mass

D_{60} is particle size at 60% passing by mass

3.2.3 Density of soil particles

Density of soil particles test was performed according to the JIS A1202 from the laboratory testing standards of Geomaterials Vol. 1. Japanese Geotechnical Society Standards (JGS 2015). The density of soil particles is mass per unit volume of the solid part of the soil.

Equipment:

- a. Pycnometer with the capacity of 50 mL (Photo 3.5)
- b. Balance with the sensitivity of 0.001 g (Photo 3.5)
- c. Thermometer which sensitivity of 0.5° C or 0.1° C
- d. Constant-temperature drying oven (110±5)° C
- e. Desiccator
- f. Apparatus for separating soil particles and for crushing soil
- g. Boiling water bath
- h. Distilled water

Samples:

- a. The sample shall consist of soil which has passed through a sieve with a 9.5 mm mesh.
- b. Use the apparatus for separating soil particles or for crushing soil, soil particles shall be fully separated.
- c. The sample may be oven-dried, air dried, or wet. For pycnometer with the nominal capacity of up to 100 mL, the sample shall be 10 g or more in oven-dried. Moreover, for pycnometer with the nominal capacity of greater than 100 mL, the sample shall be 25 g or more in oven-dried.

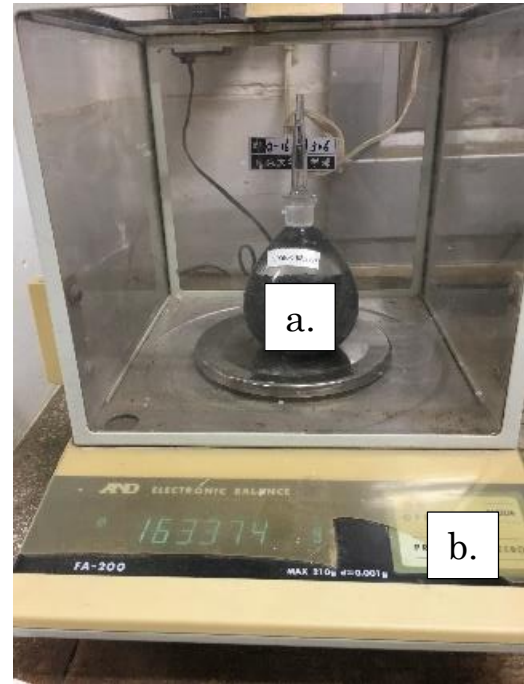


Photo 3.5 Equipment for density of soil particles test

Density of soil particles test methods:

- a. Obtain the mass of a pycnometer, m_f (g).
- b. Filling the pycnometer with the distilled water, obtain the total mass, m_a' (g), and the temperature of distilled water in the pycnometer, $T'(^{\circ}\text{C})$.
- c. After that, throw the distilled water from pycnometer and put in the soil sample to the pycnometer and add further distilled water until the total volume reaches two-thirds of the pycnometer capacity.
- d. Boil the pycnometer using the boiling water bath. To prompt air bubbles to escape, shake pycnometer from time to time. Allow the sample to stand until it reaches room temperature after all the air has escaped (40 minutes for highly organic soil, and not less than 2 hours for volcanic ash soil).
- e. Add distilled water to fill the pycnometer and obtain the total mass as m_b (g), and temperature, $T(^{\circ}\text{C})$, of the contents.
- f. Remove all of the contents from the pycnometer and until a constant mass is reached, dry them in the oven at $(110\pm 5)^{\circ}\text{C}$. Obtain the mass of the oven-

dried sample as m_s (g), after cool down the sample in a desiccator until the temperature around the room temperature.

Density of soil particles test results:

- a. Calculate the mass of the pycnometer filled with distilled water at $T^\circ \text{C}$ using the following equation

$$m_a = \frac{\rho_w(T)}{\rho_w(T')} (m_a' - m_f) + m_f \quad (3.10)$$

Where m_a is mass of the pycnometer filled with distilled water at $T^\circ \text{C}$ (g)

m_a' is mass of the pycnometer filled with distilled water at $T'^\circ \text{C}$ (g)

T' is temperature of the pycnometer contents when m_a' is obtained ($^\circ \text{C}$)

m_f is mass of pycnometer (g)

$\rho_w(T)$ is density of distilled water at $T^\circ \text{C}$

$\rho_w(T')$ is density of distilled water at $T'^\circ \text{C}$

- b. Calculate the density of soil particles using the following equation

$$\rho_s = \frac{m_s}{m_s + (m_a - m_b)} \rho_w(T) \quad (3.11)$$

Where ρ_s is density of soil particles (g/cm^3)

m_s is mass of the oven-dried sample (g)

m_b is mass of the pycnometer filled with distilled water and the sample at $T^\circ \text{C}$ (g)

T is temperature of the pycnometer contents when m_b is obtained ($^\circ \text{C}$)

3.2.4 Saturated permeability of soils

The test for saturated permeability properties was performed according to the methods for the saturated permeability of soils by Daiki (DIK-4012). The purpose of saturated hydraulic conductivity test is to determine the hydraulic conductivity in a saturated condition using an undisturbed sample that collected in a soil sampling cylinder. Furthermore, wet density, dry density, and water content also were measured on this test.

Equipment:

- a. Soil permeability measuring instrument (Fig. 3.2)
- b. Circular filter paper
- c. Deep bat

- d. Degassed water
- e. Stopwatch

Saturated permeability of soils test methods:

a. Preparation

It is necessary to saturate the undisturbed sample which collected in the stainless steel sample cylinder for 24 hours before the test. The procedure is shown below

1. Remove one lid of the stainless steel sample cylinder and cover with the filter paper. After that, the stainless steel sample cylinder is installed in the deep vat so that the filter paper is on the lower part. Remove the top lid and place the sample holding lid.
2. Pour distilled water into a deep vat so that the center of the stainless steel sample cylinder and the water surface coincide with each other. Saturate the sample for around 24 hours.

b. Set up the sample and measuring instrument

1. Cover one side of the stainless steel sample cylinder containing the saturated sample with a rubber ring with an ami board attached.
2. Cover another side of the stainless steel sample cylinder with an ami plate.
3. Install the water tank horizontally, attach a silicon tube for constant water level, and extend it to any drainage site.

構成

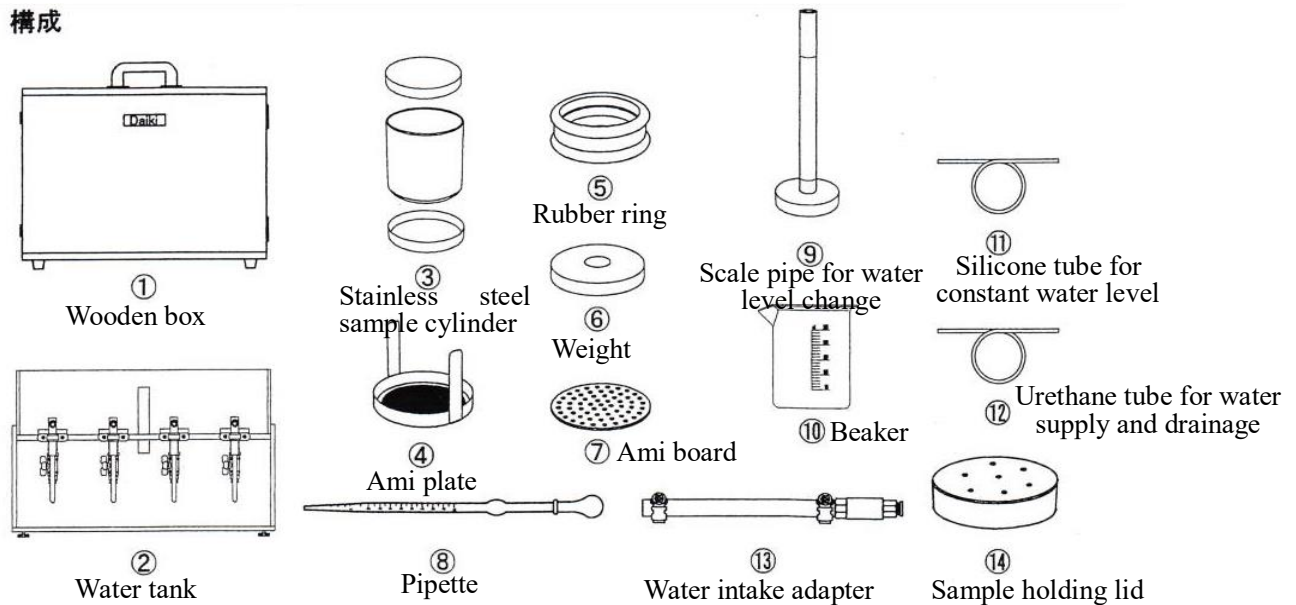


Figure 3.2 Soil permeability measuring instrument (DIK-4012)

4. Close all valves in the water tank and store degassed water until it flows out from the water level control pipe to the constant water level silicon tube.
 5. Put the sample in the water tank, remove the air bubbles in the rubber ring, and then install it (Photo 3.6).
- c. Measurement
1. Weigh the beaker mass m_b (g) and place it at the water tank.
 2. Measuring the time using a stopwatch and open the measurement valve and titrate in the same time.
 3. With 100 to 150 mL of water in the beaker, close all measurement valves and record the time t (s) and weigh the beaker mass m_b (g).
 4. Repeat the steps until three times.

Saturated permeability of soils test results:

- a. From the weight of the beaker before and after the measurement, calculate the flow rate Q (mL) from the following equation

$$Q = m'_b - m_b \quad (3.12)$$

- b. The saturated hydraulic conductivity K (mm/s) can be calculated by the following equation

$$K = \frac{Q \times L}{A \times t \times \Delta H \times 100} \quad (3.13)$$

Where L is thickness of sample (mm)

A is cross-section sample area (mm²)

ΔH is difference of position (mm)



Photo 3.6 Saturated hydraulic conductivity test (Constant water level test)

- c. For those where settlement occurred after measurement, the following equation if correcting the L value on equation 3.13

$$L = L - \Delta h_f \quad (3.14)$$

- d. The hydraulic conductivity K_{15} (mm/s) at the temperature of 15° C can be calculated by the following equation

$$K_{15} = K_T \times \frac{\eta_T}{\eta_{15}} \quad (3.15)$$

Where K_T is coefficient of water permeability at temperature T (° C) (mm/s)

η_T is coefficient of water permeability at temperature T (° C) (Pa·s)

η_{15} is coefficient of water permeability at temperature 15° C (Pa·s)

3.2.5 X-Ray Powder Diffraction

The test for x-ray powder diffraction was performed according to the methods for randomly oriented aggregate mounts, ethylene glycol treatment, and heat treatment from U. S. Geological Survey (USGS 2020). XRD was very successful in determining that much of the clay-sized inorganic material in soils was composed of regular crystals like those that had been identified in minerals in rocks or other geological deposits. Although many other instrumental techniques have been applied to their identification and characterization over the intervening years, the search for and refinement of crystal structures has remained a major pursuit of clay mineralogist and XRD has continued to be their major work-horse. Its use, whether for structural determination or as the major instrument for the identification of clay-sized minerals in soils, has defined classical clay mineralogy (Churchman and Lowe 2012). A laboratory manual for XRD by the USGS divided the clay minerals into seven groups: chlorite, illite, kaolinite, mixed-layer clays, smectite, sepiolite and palygorskite, and vermiculite.

1. Randomly oriented powder mounts for x-ray powder diffraction

Bulk mineralogy of a sediment sample can be determined by X-ray diffraction with a randomly oriented powder mount. The random orientation insures that the incident X-rays have an equal chance of diffracting off any given crystal lattice face of the minerals in the sample. The use of a powder press to make randomly oriented powder mounts is undesirable because excessive force could cause preferred orientation of the crystallites. Although some orientation is inevitable (platy minerals tend toward some preferred orientation), the method described

below is sufficient for most applications.

Sample splits are commonly dried at 60° C prior to the preparation of randomly oriented powder mounts. The mounts are typically X-rayed between the angles of 5 and 50 degrees two theta using copper K alpha radiation at a scanning rate of 2 degrees per minute.



Photo 3.7 Oriented powder in sample holder

a. Materials required:

- 1) Mortar and pestle
- 2) ASTM number 230 (0.062 mm mesh) sieve stiff brush
- 3) Spatulas
- 4) Sample holder

b. Preparation of randomly oriented powder mounts

- 1) Grind the dried sample thoroughly so that it is easily brushed through the sieve. The particles should be much finer than 0.062 mm to avoid fractionation of the minerals. The sieve is used only to achieve even distribution and to ensure that the grinding is complete.
 - 2) Place the sieve over the sample holder and brush the sample from the mortar. (Note: the sample may become contaminated from the sieve and utensils. These contaminants will not affect the x-ray diffraction analysis, but do not plan to reuse this cut of the sample for sensitive chemical analyses.)
 - 3) Use the spatula to loosen any sample that has stuck to the mortar and brush the material into the sieve.
 - 4) Brush the sample through the sieve into the cavity of the sample holder (Photo 3.7). The purpose of the brushing is to obtain an even distribution and to minimize preferred orientation of the particles.
 - 5) Remove the sieve and mask.
2. Ethylene Glycol Treatment

Organic liquids, primarily ethylene glycol and glycerol, are extensively used as an auxiliary treatment to expand swelling clays. Whether or not a mineral expands

and the amount of expansion can provide essential supplementary information aiding clay-mineral identification. Swelling clays include smectites (such as montmorillonite, nontronite, and beidellite), some mixed-layer clays, and vermiculite.

Two methods are presented here: a vapour treatment and a rapid method. The advantage of the vapour treatment is less disturbance of the sample and less amorphous scattering of X-rays by excess liquid than in the case of the rapid method. This study using the vapour treatment for the ethylene glycol treatment on XRD test.

a. Ethylene glycol vapour treatment

1) Materials required:

- Ethylene glycol
- Oven
- Desiccator
- Desiccator shelf

2) Method on ethylene glycol vapor treatment

- Pour ethylene glycol to about 1 cm depth in base of desiccator (Photo 3.8).
- Place oriented aggregate mounts on the shelf of desiccator (Photo 3.8). Additional shelves may be stacked if necessary.
- Place desiccator in oven at 60 to 70° C for about 4 hours or overnight. Longer times will not hurt samples. Do not remove mounts until they are to be run on the X-ray diffractometer.

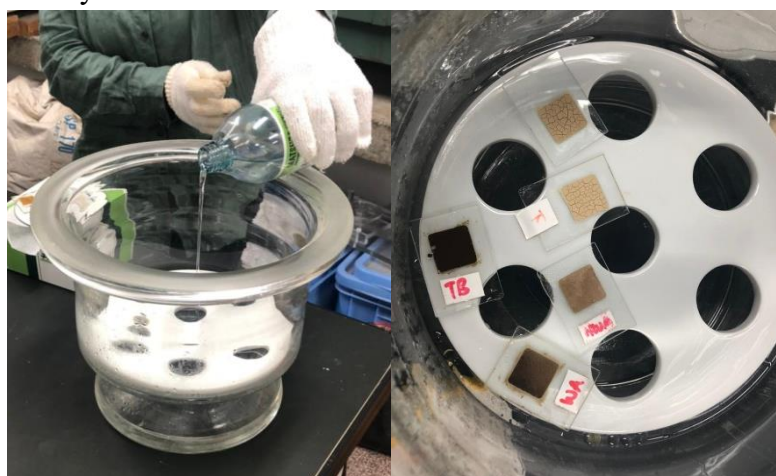


Photo 3.8 Method on ethylene glycol vapour treatment

b. Ethylene glycol rapid method

1) Materials required:

- Ethylene glycol
- Glass rod
- Lab tissue

2) Method on ethylene glycol rapid method

- Apply a drop of ethylene glycol directly to the surface of the oriented aggregate mount with the glass rod. Spread the ethylene glycol if necessary.
- Mounts are ready to be X-rayed as soon as liquid is uniformly absorbed. Excess ethylene glycol may be gently mopped up with lab tissue.

3. Heat treatments for x-ray powder diffraction

Heat treatments at various temperature are commonly used to help identify clay minerals by revealing changes in crystal structure spacings or loss of the structure. Depending on the temperature and the mineral species, these treatments can collapse the structure by dehydration, or in the case of other minerals destroy the crystal structures. However, it is important for the analyst to remember that some of the changes caused by the heat treatments may be temporary, and that partial or complete rehydration may during cooling.

a. Materials required:

- 1) Furnace
- 2) Tongs
- 3) Wire hook

b. Method on heat treatment

- 1) Preheat the oven to 400° C.
- 2) Place the oriented aggregate mount in the furnace using the tongs. Leave sample in the furnace not less than one half hour at 400° C.
- 3) Remove mount by pulling it forward with the wire hook until the edge of the mount can be grasped with the tongs. Do not remove mounts until they are ready to be run on the diffractometer.
- 4) X-ray the sample and repeat the above procedure at 550° C.

4. Theory of XRD analysis (Centre for Instrumental Analysis 2016):
- a. X-ray beam focused centered on these planes of atoms and transmitted the part of the beam. Part will diffraction after the part refracted and scattered. Part is involved in the sample. Analogous to diffraction of light by droplets of water and producing the familiar rainbow same with the diffraction of an x-ray beam by a crystalline solid. Depend on what atoms make up the crystal lattice and how these atoms are arranged, x-rays are diffracted by each mineral differently.
 - b. X-ray are generated within a sealed tube that is located in under vacuum. The heats a filament is applied from the current within the tube. The filament transmits the greater number of electrons. The production of electrons in a television picture tube is analogous to this electrons generation. A high voltage, typically 15-60 kilovolts, is applied within the tube. The target commonly made from copper which hit by the high voltage accelerates the electrons. X-rays are produced when these electrons hit the target. The characteristics of that target are the wavelength of these x-rays. The sample has been ground to a fine powder (typically to produce particle sizes of less than 10 microns) and x-rays are collimated and directed onto the sample. The signal is then processed either by a microprocessor or electronically, converting the signal to a count rate after the detector detects the X-ray signal. X-ray scan is changing the angle between the X-ray source, the sample, and the detector at a controlled rate between pre-set limits (Fig. 3.3).
 - c. We can measure the distances between the planes of the atoms mat constitute the sample by applying Bragg's Law when an X-ray beam hits a sample and is diffracted. Bragg's Law is

$$2d\sin\theta = n\lambda \quad (3.16)$$

Where n is order of the diffracted beam

λ is wavelength of the incident X-ray beam

d is distance between adjacent planes of atoms (the d-spacings)

θ is angle of incidence of the X-ray beam

In a typical X-ray scan provides a unique "fingerprint" of the mineral or

minerals present in the sample generated as the character set of *d-spacings*. The “fingerprint” allows for identification of the material when properly interpreted, by comparison with standard reference patterns and measurements.

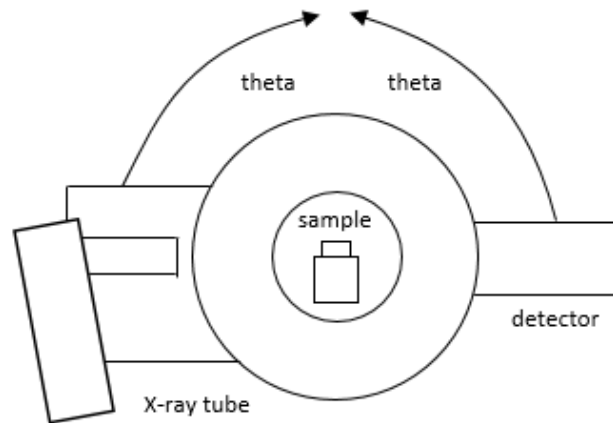


Figure 3.3 Simplified sketch of one possible configuration of the X-ray source (X-ray tube), the X-ray detector, and the sample during an X-ray scan. In this configuration, the X-ray tube and the detector both move through the angle theta (θ) and the samples remains stationary

Chapter 4

Research Areas

4.1 Research area consisting of tephra materials

4.1.1 Aso volcanic mountains in Kumamoto

Takadake area is east mountain from the caldera and also the highest mountain which has a 1,592 m high from five peak mountains surrounding Aso volcanic mountains. Aso volcanic mountains is located at Kumamoto, Kyushu island, southwestern Japan. Aso volcanic mountain has a big caldera with a 25 km north-south and 18 km east-west in diameter. Four gigantic pyroclastic-flow eruptions were formed the Aso caldera from approximately 270,000 to 90,000 years ago. Moreover, after the last-caldera forming eruption, post-caldera also initiated and produced not only local lava flows but also voluminous tephra layers which fell far beyond the caldera (JMA 2020).

Shallow landslides occur frequently on the Aso volcanic mountains. Sediment disasters caused by the landslides repeatedly occurred in June 1953, July 1990, and June 2001, with the last one occurring on July 12th, 2012 (Goto and Kimura 2019; Higaki et al. 2019; Kimura et al. 2019; Miyabuchi et al. 2004) when a cumulative rainfall of 508 mm triggered numerous landslides throughout the month. The soil materials in shallow landslides at Aso volcanic mountains consist of tephra layers formed by volcanic

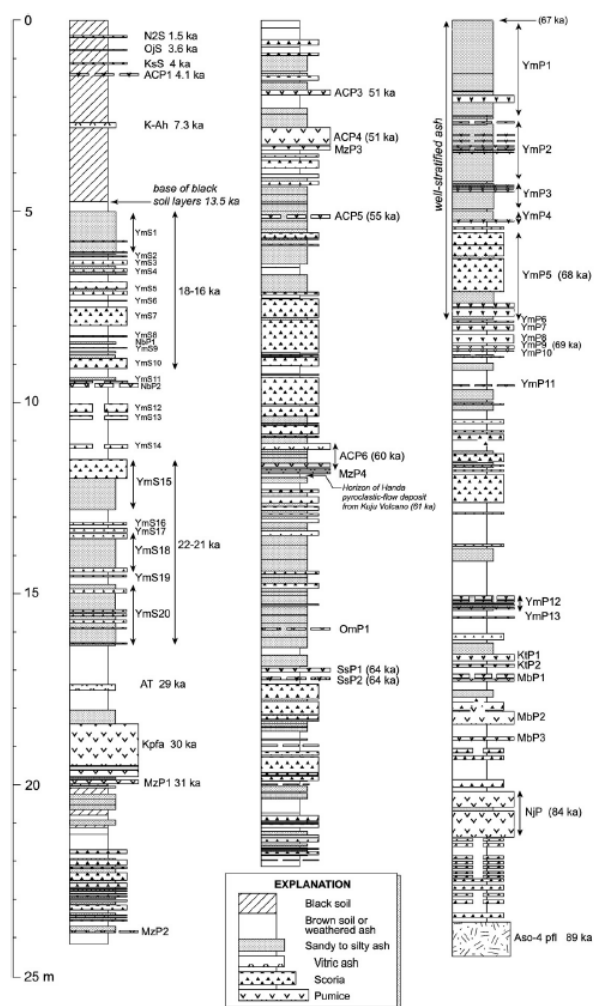


Figure 4.1 Schematic stratigraphy of fallout tephra deposits from post-caldera central cones of Aso volcano (Miyabuchi 2009)

activities. Most tephra layers distributed in and around Aso caldera are consequently mafic scoria-fall and ash-fall deposits (Miyabuchi 2011). Miyabuchi et al. (2003) identified 36 pumice beds in the thick tephra sequence (Fig. 4.1), and Miyabuchi (2009) constructed a 90,000-year tephrostratigraphic framework based on the marker pumice beds.

Three areas were selected as the research area in Aso volcanic mountains, two areas were located at Takadake area and another area was located at Takanodai area (Fig. 4.2). The distance between Takadake 1 and Takadake 2 is around 600 m, and the distance between Takadake landslides and Takanodai is around 11 km. Takadake 1 and Takadake 2 were shallow landslides caused by heavy rainfall on July 12th, 2012 with a cumulative rainfall of 508 mm triggered numerous landslides throughout the month (JMA 2020). Dimension of shallow landslide in Takadake 1 has 34 in length and 10 m in width (Photo 4.1), and in Takadake 2 has 18 m in length and 39 m in width (Photo 4.2). Takadake 1 and Takadake 2 landslides consist of OJS scoria and N2S scoria; the main tephra layers in Takadake 1 was divided into 6 sub-layers from the surface down to a depth of 1.39 m (Photo 4.1) and the main tephra layers in Takadake 2 was divided into 7 sub-layers from the surface down to a depth of 1.37 m (Photo 4.2). The oldest of tephra layer in Takadake areas was OJS scoria. OJS scoria is the scoria bed which erupted from Ojodake volcanoes located in the north-western part of the central cones which composed in around 3.6 ka and N2S scoria is a very poorly-sorted tephra deposit occurring above OJS from

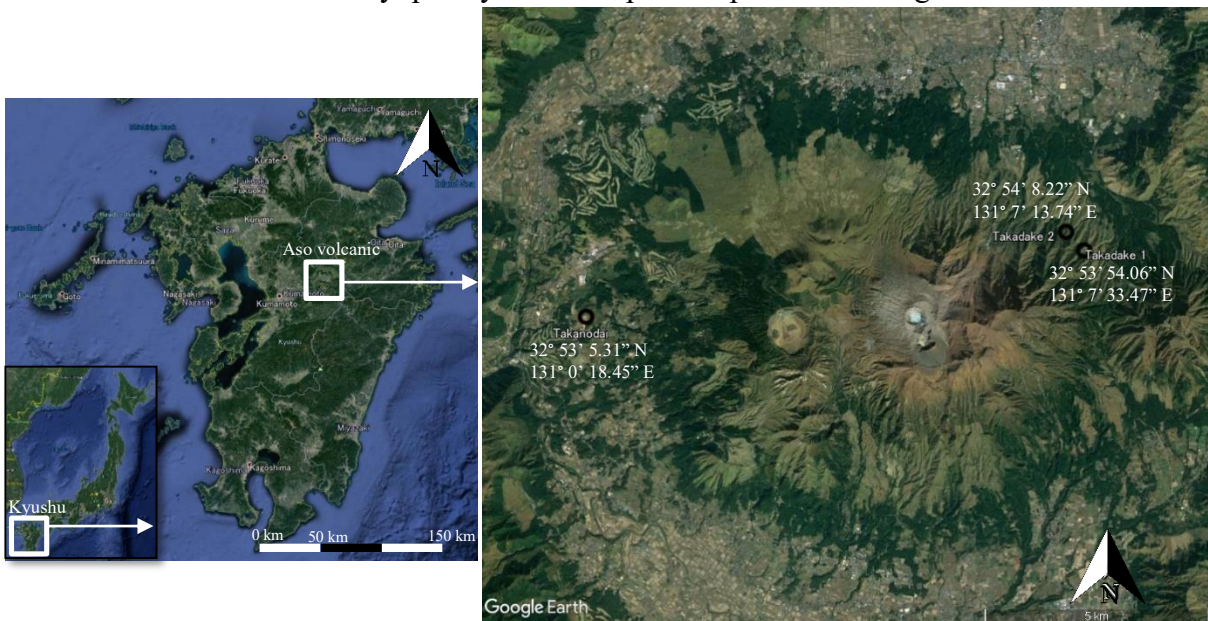


Figure 4.2 Landslides in Aso volcanic mountains (Google Earth)

Nakadake volcano which composed in around 1.5 ka (Miyabuchi and Watanabe 1997; Miyabuchi et al. 2004; Ono and Watanabe 1985). N2S scoria is characterized by a brown scoria bed with an abundance of altered white lithic fragments, believed to be a product of a large phreatomagmatic eruption at Nakadake volcano (Miyabuchi 2009).

The volcano activity in Aso volcanic mountain showed by the deposits of tephra. Active period in research areas showed the deposits of scoria and the rest period showed the deposits of kuroboku. Miyabuchi et al. (2004), Ono and Watanabe (1985) reported 13 active periods from N1 to N13 which erupted from Nakadake volcano. The tephra

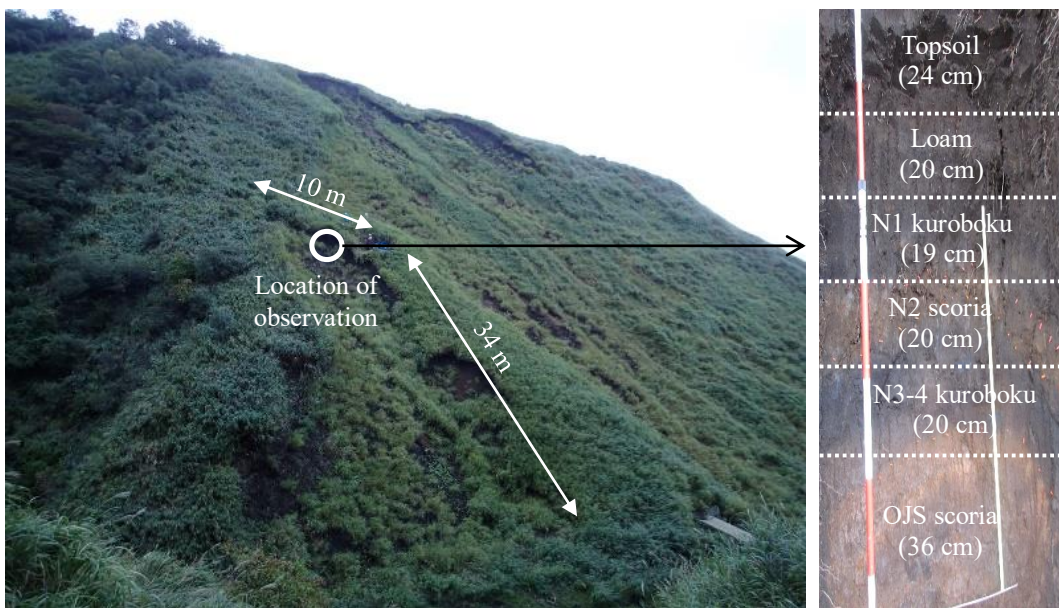


Photo 4.1 Takadake 1 and tephra stratigraphy in the landslide (Taken on October 2016)

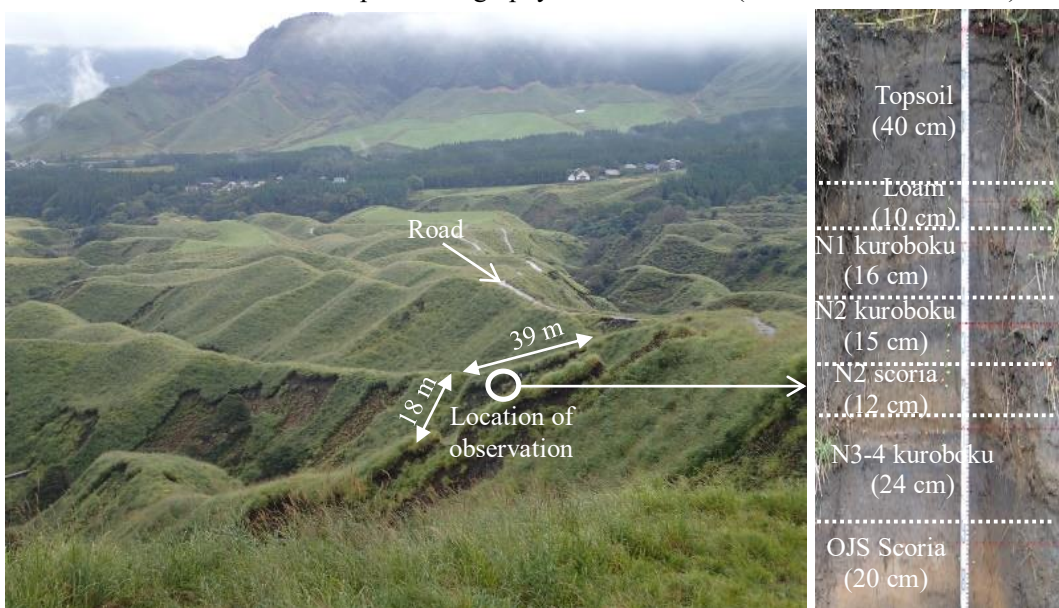


Photo 4.2 Takadake 2 and tephra stratigraphy in the landslide (Taken on October 2016)

deposits in research areas showed the active periods from N1 to N4 periods, which showed by N1 kuroboku, N2 kuroboku, N2 scoria, and N3-4 kuroboku. N3-4 kuroboku are divided into two sub-layers, upper part (U) and lower part (L) because the different characteristics were observed in the field.

Furthermore, Takanodai area was the landslide caused by earthquake with $6.5 M_j$ (Japan Meteorological Agency magnitude) at 21:26 JST on April 14th, 2016 included the M_j 7.3 as the mainshock at 01:26 on April 16th, 2016 (Shirahama et al. 2016). Dimension of Takanodai landslide was 206 m in length and 101 m in average width approximately (Photo 4.3) (Song et al. 2017). The landslide main body is composed of Kusasenrigahama volcanic pumice (Kpfa) tephra beds. Kpfa is the largest fallout tephra deposit during the post-caldera stage (Miyabuchi 2011). The source is Kusasenrigahama crater (ca. 1 km in diameter), which is located at the western part of the post-caldera central cones (Miyabuchi 2011). The crater rim and western and southern slopes adjacent to the crater are covered by thickly welded Kusasenrigahama pumice (Ono and Watanabe 1985).

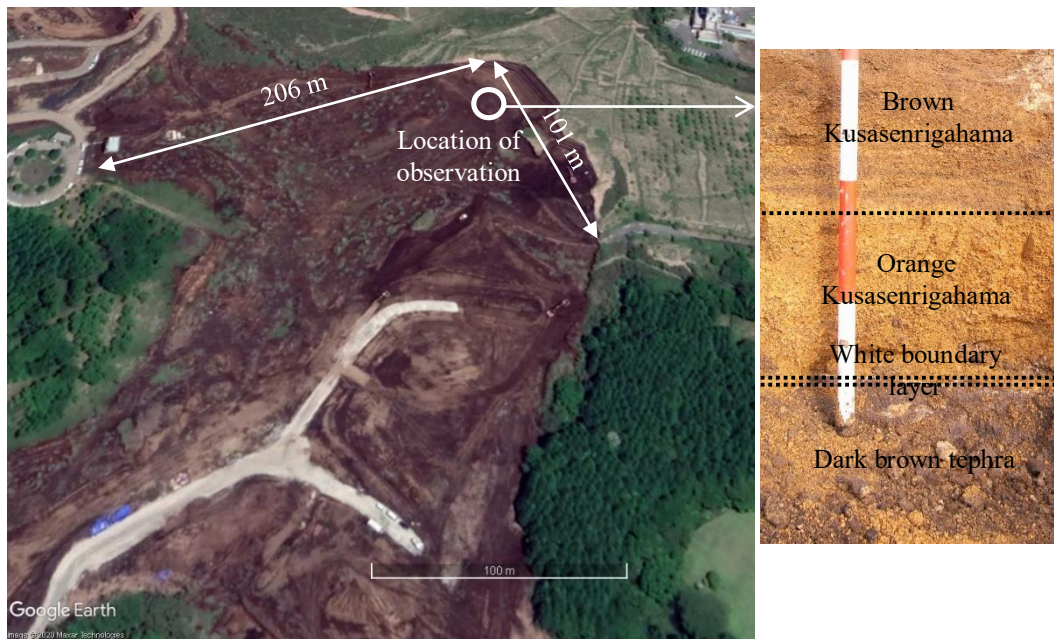


Photo 4.3 Takanodai and tephra stratigraphy in the landslide (Taken on December 2016)

4.1.2 Izu Oshima in Tokyo

Izu Oshima is the island with elliptical volcanic shape, located about 100 km from Tokyo and it is a basaltic stratovolcano belonging to the Izu Mariana volcanic arc (Miyabuchi et al. 2015). Izu Oshima volcano began its activity about 30,000-40,000 years ago, covering the older dissected volcanoes (Isshiki 1984; Kawanabe 1998). The volcano has produced not only mafic lava flows but also voluminous tephra fallout deposits, constructing the main edifice and NW-SE queuing flank volcanoes (fissures, scoria cones, tuff cones, and maars), which are thought to be arranged parallel to the maximum horizontal stress axis (Nakamura 1977 cited in Miyabuchi et al. 2015).

The Older Oshima Group occupies the greater part of the main volcanic edifice and comprises alternations of basaltic lava flows and tephra fall deposits. However, the exposure of the Older Oshima Group is limited because the main edifice is almost entirely covered by the Younger Oshima Group (Miyabuchi et al. 2015). Nakamura (1964) (cited in Miyabuchi et al. 2015) subdivided the Younger Oshima Group into 12 tephra members: S2-S1 (Sashikiji Formation; 4th century), N4-N1 (Nomashi Formation; 8-12th centuries) and Y6-Y1 (Yuba Formation; 13-18th centuries) (Tsukui et al. 2013 cited in Miyabuchi et al. 2015) in ascending order by the existence of paleosols or weathered ash.

The latest large-scale historical eruption (Y1 eruption) occurred in 1777-1778 (Miyabuchi et al. 2015). Historical eruptions usually began with scoria fall and were followed by effusion of lava flows and continuous emission of ash. Some historical activities accompanied flank eruptions and formed scoria cones and maars (Nakamura



Figure 4.3 Main landslide on the western part of Izu Oshima island (Google Earth 2020)

1964 cited in Miyabuchi et al. 2015). After the Y1 eruption, medium to small eruptions have been recognized at multi-decadal interval (Isshiki 1984; Kawanabe 1988).

Heavy rainfall associated with the typhoon T1326 (Wipha) caused the landslides in Izu Oshima on October 16th, 2013 with the cumulative rainfall increased up to 824 mm (JMA 2020). Heavy rainfall triggered numerous landslides of the tephra-rich slopes, particularly in the western area of the island (Miyabuchi et al. 2015). The most landslide in Izu Oshima is debris rapidly transformed into lahars and floods to downwards inhabited

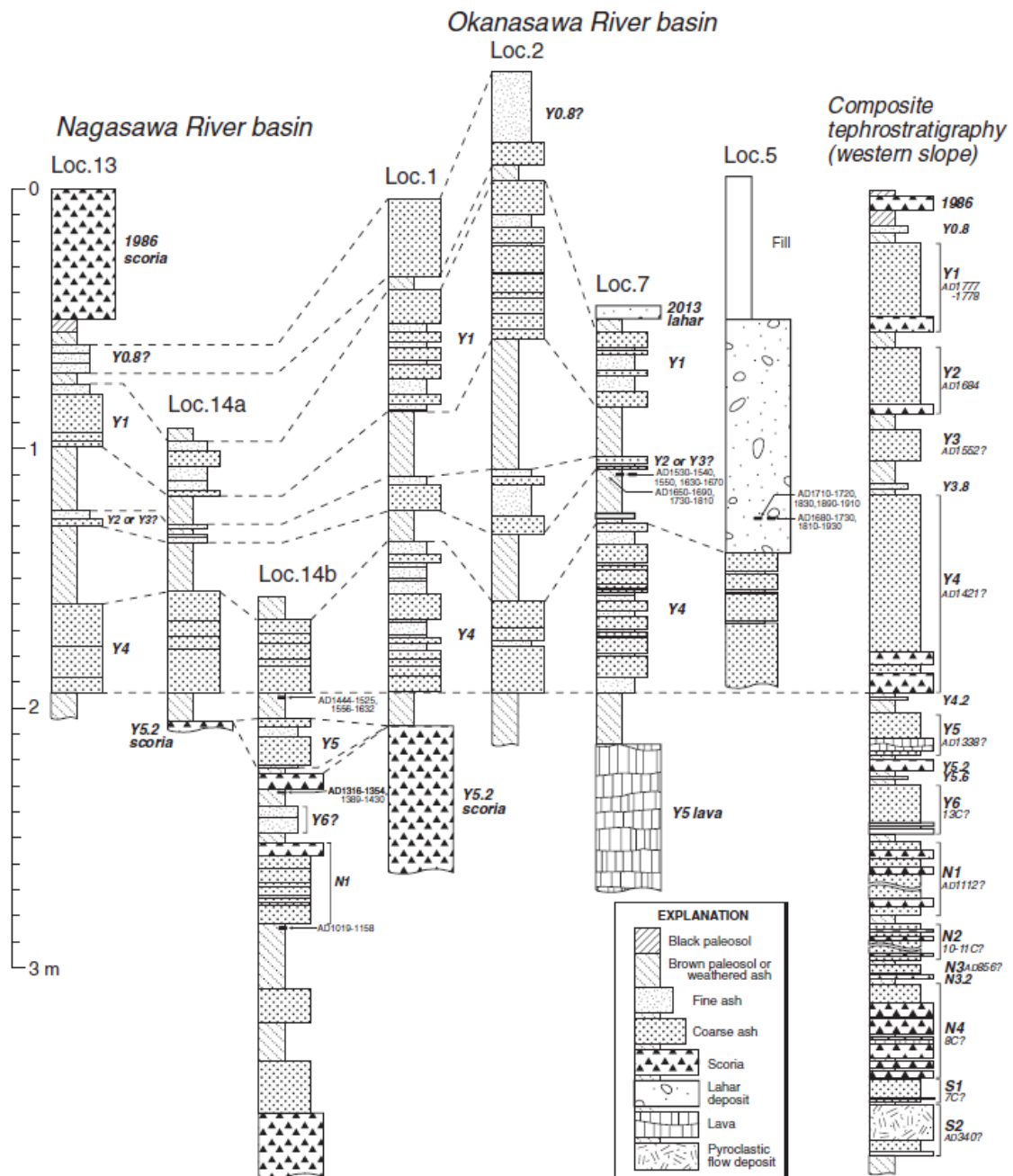


Figure 4.4 Stratigraphic relations of tephra fallout layers and lava on the western slope of Izu Oshima volcano (Miyabuchi et al. 2015)

the area. Research area on this study is located in the main landslide at the western part of the island (Fig. 4.3). Miyabuchi et al. (2015) reported that the scarps of the October 2013 landslides and the slopes eroded by the associated lahars in the western part of Izu Oshima volcano, the Y5 member and the overlying tephra members were exposed (Fig. 4.4). Moreover, tephra layers which exposed on this study were younger than Y5.2 tephra (Photo 4.4).

Nakamura (1964) (cited in Miyabuchi 2015) described that Y5 member was composed of a basal scoria-fall deposit and the overlying stratified ash-fall deposits. However, Koyama and Hayakawa (1996) distinguished the basal scoria as Y5.2 from the overlying and underlying ash deposits (Y5.0 and Y5.6 respectively) because the scoria and stratified ash were separated by a thin paleosol. Miyabuchi et al. (2015) also recognized a brown paleosol (2 cm thick) between the Y5.2 scoria and the upper stratified ash (Y5.0) at locality. The Y5 member is believed to be the 1338 eruption deposits (Nakamura 1964 cited in Miyabuchi 2015). The 1338 eruption accompanied two fissure eruptions producing scoria and lava flows, and the lavas are distributed on the western slope of Izu Oshima volcano including Motomachi town (Kawanabe 1998). Miyabuchi et al. (2015) calibrated ^{14}C date was obtained as AD 1316-1354 or 1389-1430 from charcoal just below the Y5.2 scoria.

Y4 tephra is an alternating bed of coarse and fine ash-fall deposits which characterized by the existence of several thin purple or pink fine ash layers although most are dark gray or black coarse ash beds (Miyabuchi et al. 2015). Miyabuchi et al. (2015) also obtained calibrated ^{14}C age of charcoal just below the Y4 member is AD 1444-1525 or 1556-1632. Furthermore, there is a tephra unit composed of two or three ash fall layers in the paleosol between Y4 and Y1 units (Miyabuchi et al. 2015). Miyabuchi et al. (2015) suggest a possibility that the tephra unit is Y3 (AD 1552) or Y2 (AD 1684) member.

Y1 tephra comprises alternating beds of dark gray to black coarse ash and pink fine ash with a black scoriaceous coarse ash layer (3-6 cm thick), which is thought to

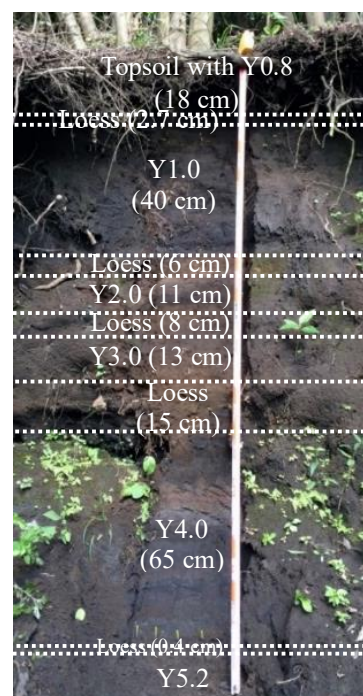


Photo 4.4 Tephra stratigraphy in Izu Oshima (Taken on November 2016)

correspond to the basal scoria layer of Y1 eruption, exist near the base of the Y1 member (Miyabuchi et al. 2015). The Y1 tephra is regarded as products of the largest historical eruption occurred in 1777-1778 (Nakamura 1964 cited in Miyabuchi et al. 2015).

4.1.3 Iburi Region in Hokkaido

Hokkaido, the northernmost main island of Japan, includes three Holocene volcanic belts (chains) (Minato et al. 1972). The study areas are located at the Iburi Region in Hokkaido and the Pleistocene pumiceous deposits of Iburi Region in Hokkaido may be classified into ash and pumice flows, either welded or non-welded, ash and pumice falls, and pumiceous gravel (Minato et al. 1972). The ash or pumice fall in this area generally occupy the lower horizon of any given volcanic sequence such as the Noboribetsu, Ponayoro I and II, Shadai, Morino, and Shikotsu Formations (Minato et al. 1972).

Tephra layers which exposed on this study were younger than Shikotsu Formation and the schematic stratigraphy of fallout tephra deposits was figured in Fig. 4.5. Lake Shikotsu is a cocoon-shaped caldera lake with a major axis of 12 km and a minor axis of 6 km (GSJ 2020). GSJ (2020) also reported that the first activity of the Shikotsu caldera was about 60 ka or older, and ejected pyroclastic fall (Ssfa) and pyroclastic flow (Ssfl).

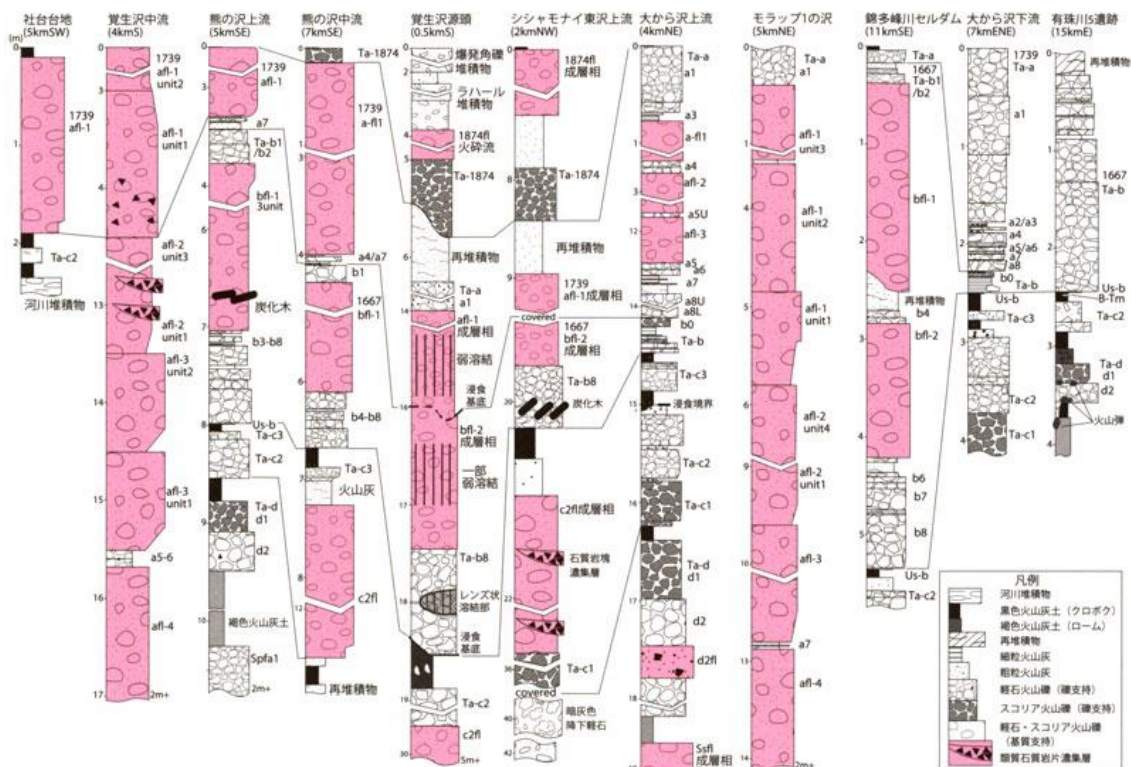


Figure 4.5 Schematic stratigraphy of fallout tephra deposits in Iburi Region at Hokkaido (GSJ 2020)

The Shikotsu pumice fall was dated as 32,000 ys. B.P. by Carbon¹⁴ (Minato et al. 1972). Furthermore, Minato et al. (1972) reported the volcanoes Fuppushi, Eniwa, and Tarumai were born along the caldera wall, after the caldera sinking had occurred.

Eniwa (En-a) is a breccia layer or a pumice falls deposits which was ejected at about 19 to 21 ka (cal.) (Osanaï et al. 2019). However, since En-a contains fresh andesite lava homogenous rock fragments, it is highly possible that the activity had started before that (GSJ 2020). Furthermore, Tarumai volcano started its activity about 9,000 years ago. Activity of eruption is divided into three active periods with a rest period of 1,000 years or more. The first activity is about 9,000 years ago, the second activity is about 2,500 to 2,000 years ago, and the third activity is from 1,667 to the present (GSJ 2020).

The first activity was deposited from the Plinian eruption and it deposited the Tarumai-d (Ta-d), which consists of the lower lithological unit Ta-d2 and the upper Ta-d1 (GSJ 2020). There is no evidence of a time gap between the two, however, Ta-d2 is mainly composed of red-orange pumice with a specific gravity of 0.4 to 0.6 and the layer thickness is about 30 cm to 1 m (GSJ 2020). It consists of red-orange pumice lapilli, which is the same quality as pumice fall. The upper Ta-d1 consists of gray scoria lapilli with a specific gravity of 1.6 to 1.8 (GSJ 2020). Ta-d was dated as 8.7 to 9.2 ka from the carbonized plant pieces and black volcanic ash soil directly under Ta-d2 (Furukawa et al. 2006).

In the second active period, which had a rest period of about 6,500 years, Tarumai-c (Ta-c) was deposited (GSJ 2020). The earliest Ta-c1 fall pyroclastic deposits (Soya and

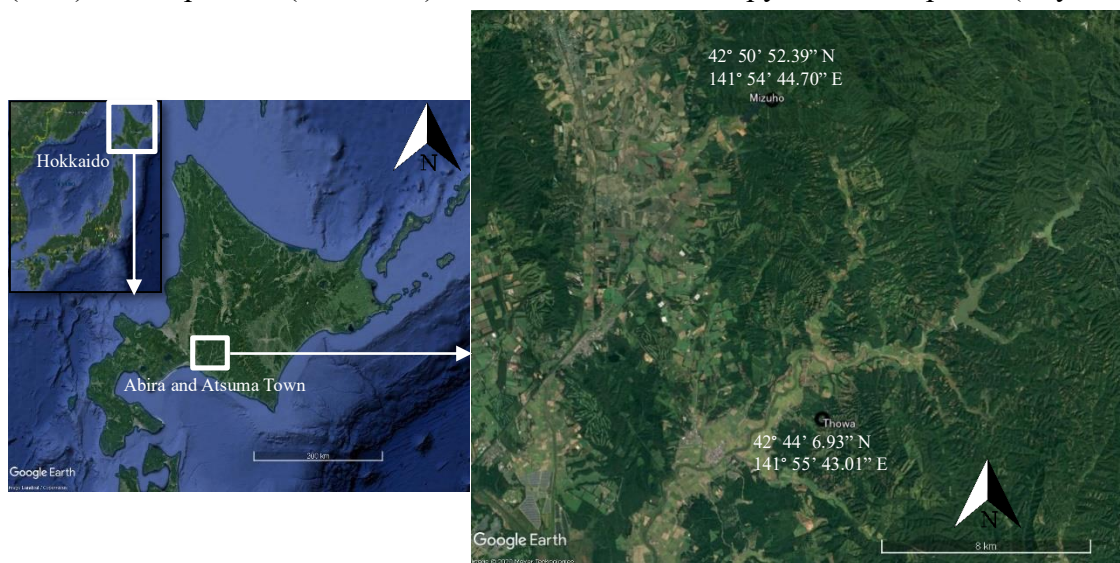


Figure 4.6 Landslides in Iburi Region at Hokkaido (Google Earth 2020)

Sato 1980) consist of dark gray scoria lapilli, with a specific gravity of 1.6 to 1.8 (GSJ 2020). The upper Ta-c2 (Soya and Sato 1980) is mainly composed of brownish white pumice lapilli (GSJ 2020). The gap between the Ta-c1 and Ta-c2 is geologically short, and it is within several tens to 100 years. The eruption age of Ta-c2 is about 2.5 ka from the black volcanic ash soil and peat layer directly below (Suzuki 1994). Furthermore, Ta-c3 is mainly composed of fined brown pumice lapilli and it is found within 15 km from the crater and becomes coarser and thicker toward the current summit of Tarumai (GSJ 2020).

The last active period is occurred after 1667 and the large-scale plinian eruptions occurred in 1667 and 1739 with more than 70 eruptions have been recorded (GSJ 2020). Due to the eruption on 1667, Tarumai-b (Ta-b) were widely deposited in the east, and pyroclastic flows were deposited at the foot of the mountain (GSJ 2020). Moreover, Tarumai-a (Ta-a) was widely deposited in the northeast caused by the eruption on 1739, and the pyroclastic flow flowed down to the foot of the mountain (GSJ 2020).

Earthquake 6.7 M_j struck the Iburi Region, Hokkaido, Japan at 03.08 local time (JST) on September 18th, 2018 and triggered many shallow landslides. The maximum intensity of 7 was occurred at Atsuma Town. Earthquake triggered landslides over about 20 km² area behind Atsuma Town (Yamagishi and Yamazaki 2018). Since the Meiji Era (1868-

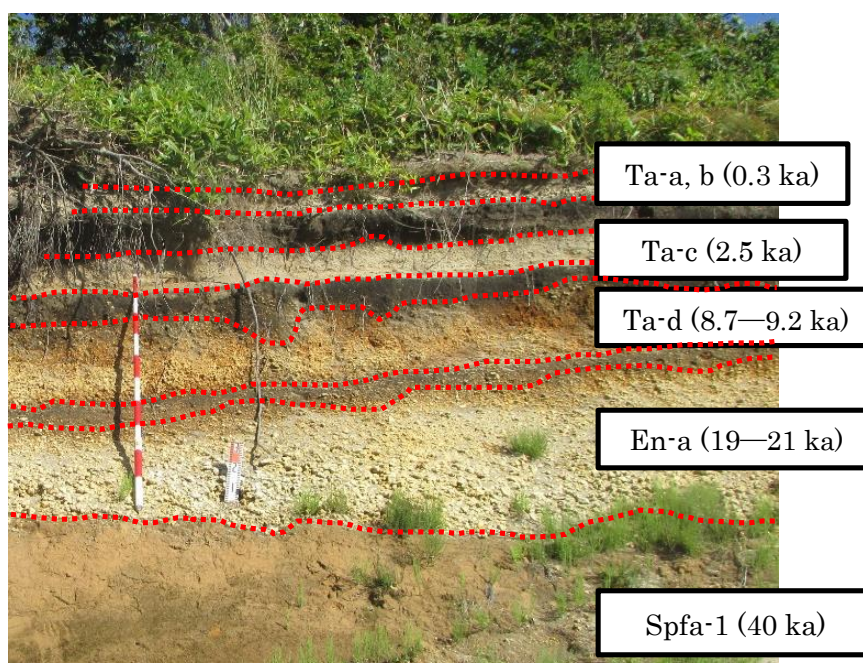


Photo 4.5 Tephra layers from Ta-a until Spfa-1 which located nearby the research area (Taken on September 2019)

1912), the number of landslides and the total area of the landslides caused by Hokkaido Eastern Iburi Earthquake 2018 were the largest in Japan (Osanai et al. 2019). Most landslides were shallow landslides and are mostly classified as planar and spoon types, and some deep-seated landslides of dip-slipping type were also found in the southeast part of the mountains (Osanai et al. 2019; Yamagishi and Yamazaki 2018).

Two areas were selected as the research area in Iburi Region at Hokkaido (Fig. 4.6),

(a) Towa landslide



(b) Mizuho landslide



Photo 4.6 (a) Towa landslide and (b) Mizuho landslide, and tephra stratigraphy in the landslides (Taken on September 2019)

one area was located at Atsuma Town which called Towa landslide and another landslide in Abira Town which called Mizuho landslide. The distance between these landslides is around 12.5 km. Stratigraphy of tephra deposits in research areas was found in Atsuma Town (Photo 4.5). It showed the tephra layers derived from Tarumai volcano, including Ta-a, b (0.3 ka), Ta-c (2.5 ka), and Ta-d (8.7-9.2 ka). Other tephra layers were erupted from Eniwa volcano (En-a (19-21 ka)) and Shikotsu caldera (Spfa-1 (40 ka)).

Dimension of shallow landslide in Towa has 34 m in length and 54 m in width, and tephra deposits in this area derived from the Tarumai volcano, including Ta-c and Ta-d tephra layers (Photo 4.6 (a)). Furthermore, dimension of shallow landslide in Mizuho has 80 m in length and 50 m in width, and tephra deposits in this area derived from the Tarumai and Eniwa volcano, Ta-d and En-a tephra layers were found in Mizuho landslide (Photo 4.6 (b)). Soya and Sato (1980); Furukawa and Nakagawa (2010) reported that the buried humus (kuroboku soil) layers are sandwiched between Ta-b and Ta-c, and between Ta-c and Ta-d. The topsoil layer is generally composed of alternate layers of pyroclastic fall deposits and buried humus, with its thickness about 2.5 to 3.5 m on the middle of the slope. In this study, thin kuroboku layer (6 cm) was found as a topsoil in Towa landslide. The tephra layers from Tarumai and Eniwa in research areas are divided into two sub-layers, upper part (U) and lower part (L) because the different characteristics which found in the field.

4.2 Research area consisting of tuff breccia and andesite

Heavy rainfall frequently occurred in Northern Kyushu and triggers the landslides every year. This study observed the landslides which occurred in Oita Prefecture, Kyushu, Japan. The landslides in Ohtsuru and Ono were influenced by heavy rainfall on 5th July, 2017. On that day, a wide area in Hita City was affected by heavy rainfall and the precipitation data was shown on Fig. 4.7. The total rainfall on 5th July was 336 mm (JMA 2020) and it induced a landslide at Ohtsuru. On the next day after heavy rainfall, 6th July, the landslide occurred at Ono with total rainfall of 66.5 mm (JMA 2020). Furthermore, on 11th April 2018, a large-scale landslide occurred in Yabakei, Nakatsu City. The landslide in Yabakei was not influenced by earthquakes or rainfall. The lower part of the landslide was the collapsed soil, which contained sedimentary rock formations (1.17 million years ago; Cenozoic to Quaternary) (Yabakei landslide investigation committee

2018).

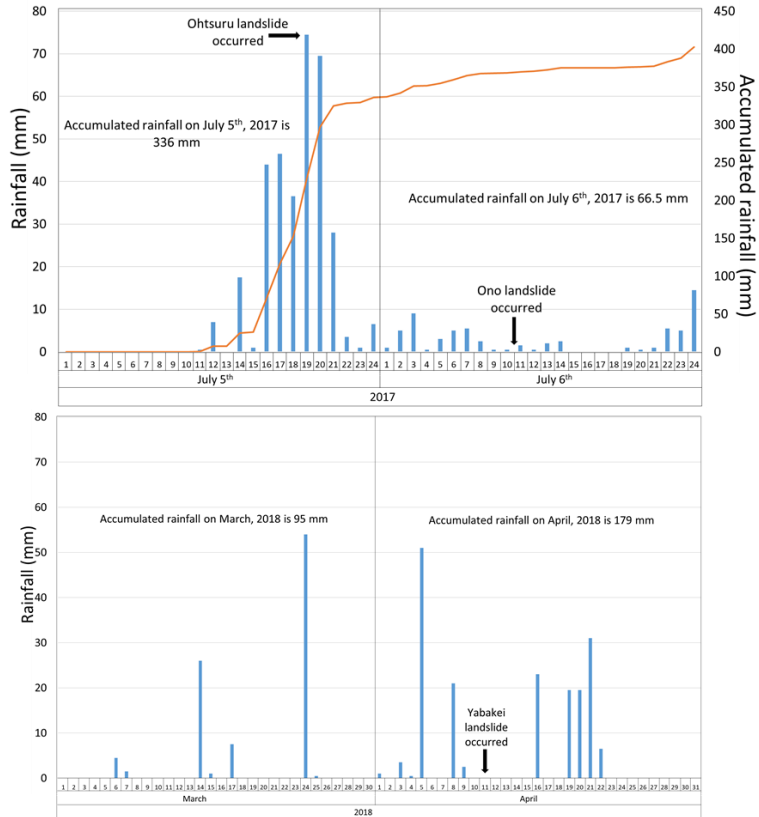


Figure 4.7 Precipitation data in Hita City and Nakatsu City, Oita Prefecture (JMA 2020)

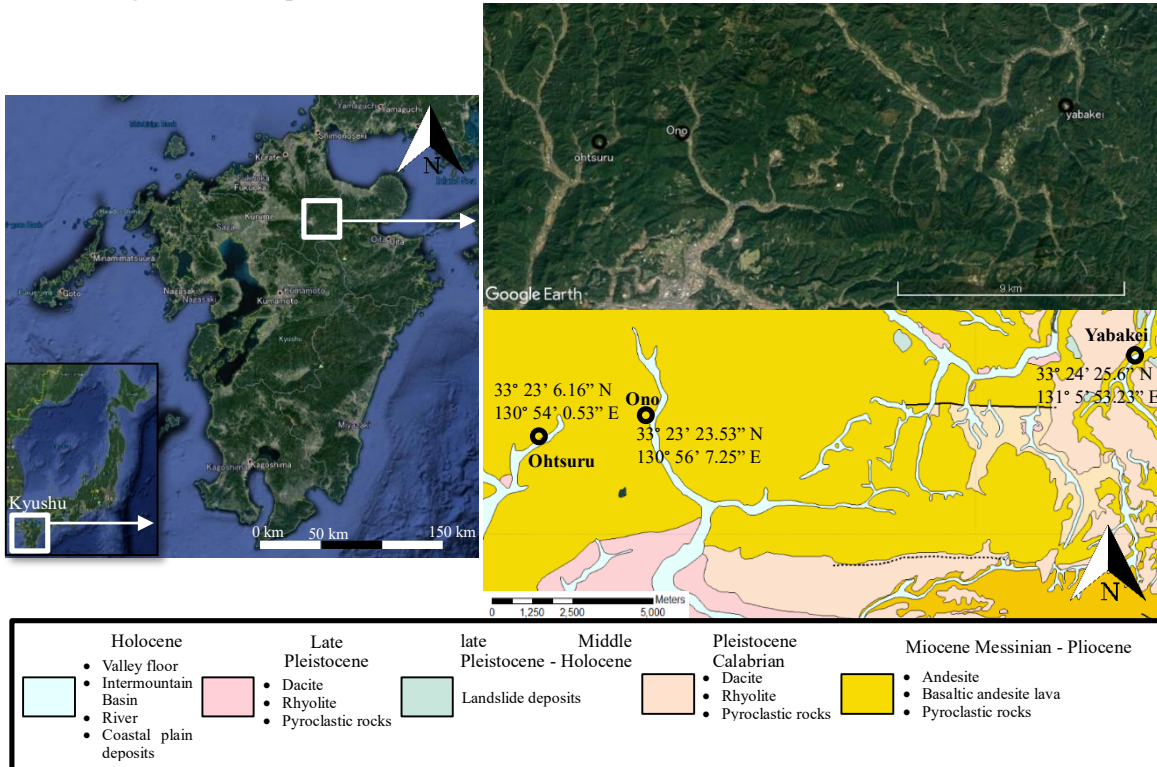


Figure 4.8 Geological map of landslides consisting of tuff breccia and andesite in Hita Prefecture (Google Earth and GSJ 2020)

Three landslides that occurred in Oita Prefecture, two landslides in Hita City, and another landslide in Nakatsu City were selected as the research area consisting of tuff breccia and andesite. The landslides in Hita City are named Ohtsuru and Ono landslides, and the distance between these landslides was around 3.3 km. Ohtsuru landslide occurred near Yanase, Hita City, and the Ono landslide occurred near the Ono River, Hita City in Joguyama Mountain (645 m). Another landslide, called the Yabakei, occurred in the Yabakei area, Nakatsu City.

The areas in this study consisting of the same geological formations, igneous rock formation: andesite, basaltic andesite lava, and pyroclastic rocks from the Neogene period (Fig. 4.8) (GSJ 2020). The Yabakei landslide also consists of river deposits from the Holocene, Quaternary period (GSJ 2020). The areas in this study consisted of the same materials; however, the landslide mechanisms in this study are different. Ohtsuru landslide occurred during the peak rainfall and it was a shallow landslide with a narrow slope (Photo 4.7). Dimension of shallow landslide in Ohtsuru has 185 m in length and 35 m in width. The main soil layer in Ohtsuru landslide was divided into 3 sub-layers from the surface to a depth of 6 m; consists of topsoil, highly weathered andesite, weathered andesite, and tuff breccia.

Large-scale landslides in Ono occurred the next day after heavy rainfall and it has a depth around 20 to 30 m (Ochiai et al. 2017). Dimension of landslide in Ono has 300 m



Photo 4.7 Ohtsuru landslide and soil materials in the landslide (Taken on July 2017)



Photo 4.8 Ono landslide and soil materials in the landslide (Taken on July 2017) in length and 200 m in width, furthermore, two collapses occurred in the Ono landslide; andesite was exposed in the lower collapse and weathered tuff breccia was exposed in the upper collapse (Photo 4.8). Similar to the Ohtsuru landslide, Ono landslide was divided into 3 sub-layers; consists of weathered andesite, weathered tuff breccia, and tuff breccia. Unfortunately, because of the condition of the field which difficult to exposed the soil layers, the depth of the soil layers in the Ono landslide could not be identified.

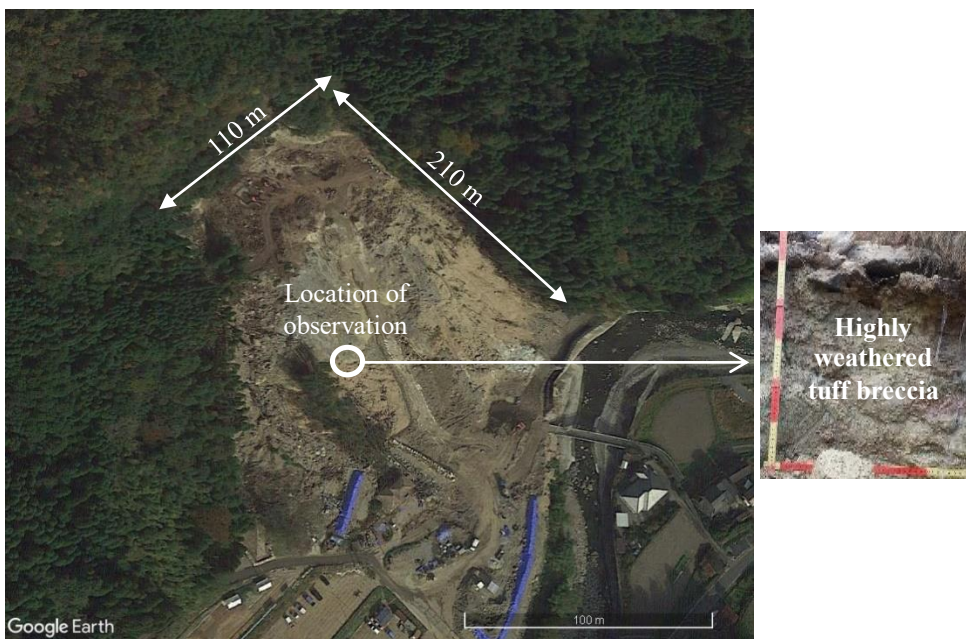


Photo 4.9 Yabakei landslide and soil material in the landslide (Taken on July 2018)

The last landslide which consisting of tuff breccia and andesite is Yabakei landslide, and it was a large-scale landslide in this study. Dimension of landslide in Yabakei has 210 m in length and 110 m in width (Photo 4.9). Layering of soil in Yabakei landslide also could not be exposed due to unfavourable conditions. Moreover, a depth of 1 m on the highly weathered tuff breccia was observed (Istiyanti and Goto 2020b).

Chapter 5

Case Studies of Landslides at Volcanic Area

5.1 Takadake landslides caused by heavy rainfall 2012

The sliding layer of the shallow landslides on the Aso volcanic mountains has been observed based on the difference in the value of hydraulic conductivity (Shimizu and Ono 2016). The layer below the sliding layer has lower hydraulic conductivity and the difference in the hydraulic conductivity was the control on the tephra layer (Shimizu and Ono 2016). Furthermore, Sato et al. (2017, 2019) reported that the gravitational deformation of the slope deposits on the Aso volcanic mountains which resulted from the “flow” of the highly permeable kuroboku layer over the less permeable tephra layer was observed.

Kuroboku layers are located on the scoria layers in each area (Fig. 5.1). Takadake 1 has two kuroboku layers with two scoria layers, both of which are located on scoria layers (N1 kuroboku is located on the N2 scoria and N3-4 kuroboku is located on OJS scoria). Furthermore, Takadake 2 has three kuroboku layers with two scoria layers: N1 kuroboku and N2 kuroboku are located on the N2 scoria layers and N3-4 kuroboku is located on the OJS scoria layer. N3-4 kuroboku layer is divided into 2 sub-layers in each area, N3-4 kuroboku U and N3-4 kuroboku L, which aimed at simplifying on the estimation of sliding layer in this study. Dissimilarity in soil hardness is observed between the kuroboku and scoria layers, and the low average soil hardness indicates the location of the sliding layer.

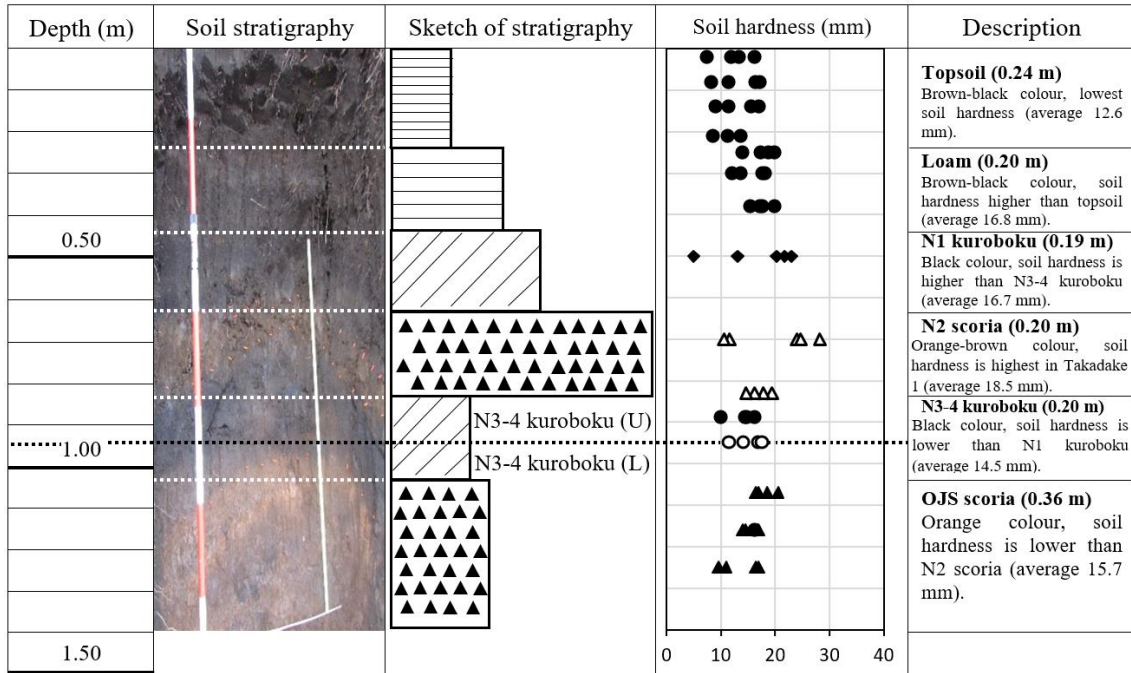
Miyabuchi and Daimaru (2004) reported that the sliding layers were formed near the boundary between the kuroboku and scoria layers. In this study, the low average soil hardness value in each area is located at the N3-4 kuroboku layer; furthermore, according to the stratigraphic analysis results of the field observations, the N3-4 kuroboku layer is a sliding layer in the studied area. Therefore, low average soil hardness indicates the location of the sliding layer in Takadake area.

Particle size distribution curve shows no dissimilarities in tephra layers at Takadake landslides and all the tephra layers indicate poorly-graded soil material (Fig. 5.2). However, the fine fraction content (less than 0.075 mm) on tephra layers (Fig. 5.3) show

the difference between kuroboku and scoria layers. For this reason, this study suggest that the particle size distribution curve is difficult to use for estimating the sliding layer, but the fine fraction content can be used as a factor for estimating the sliding layer.

Fig. 5.4 shows the physical properties of the tephra layer, which generally shows that the scoria and kuroboku layers are different. Scoria layers have a low fine fraction content

(a) Takadake 1



(b) Takadake 2

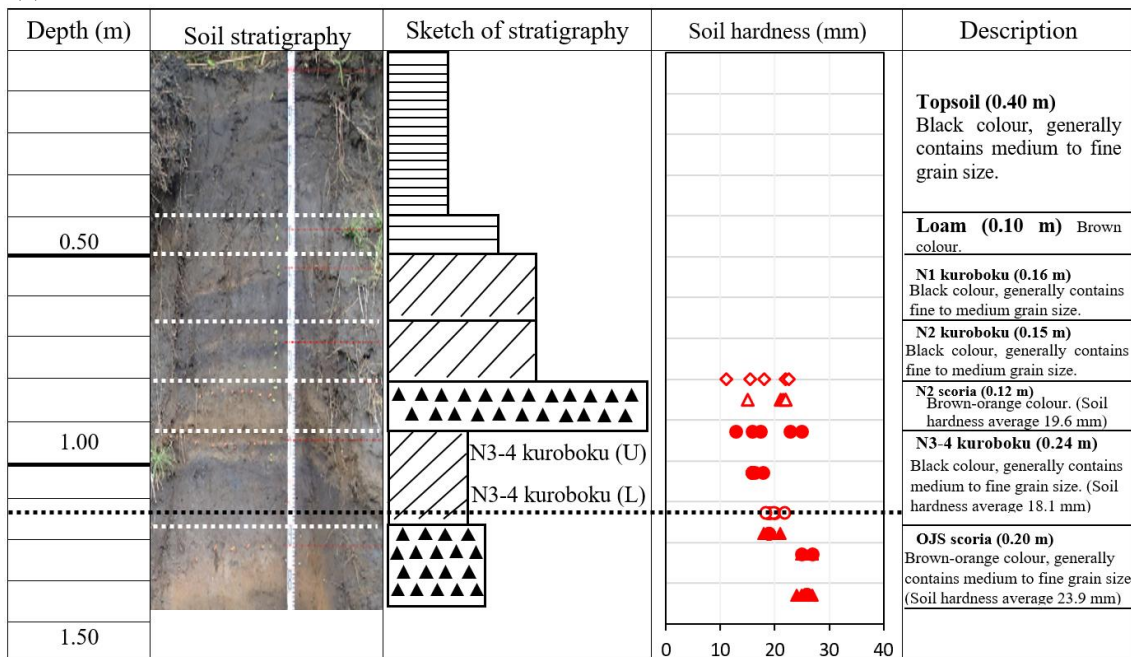


Figure 5.1 Soil stratigraphy in Takadake 1 (a) and in Takadake 2 (b); black dotted lines indicate sliding layer by field observation

and plasticity index, and a high density of soil particles. Meanwhile, kuroboku layers have high fine fraction content and plasticity index, and low density of soil particles. Dissimilarity on coefficient of saturated permeability, on void ratio, and on dry density between kuroboku and scoria layers are observed. Dissimilarity on void ratio and dry

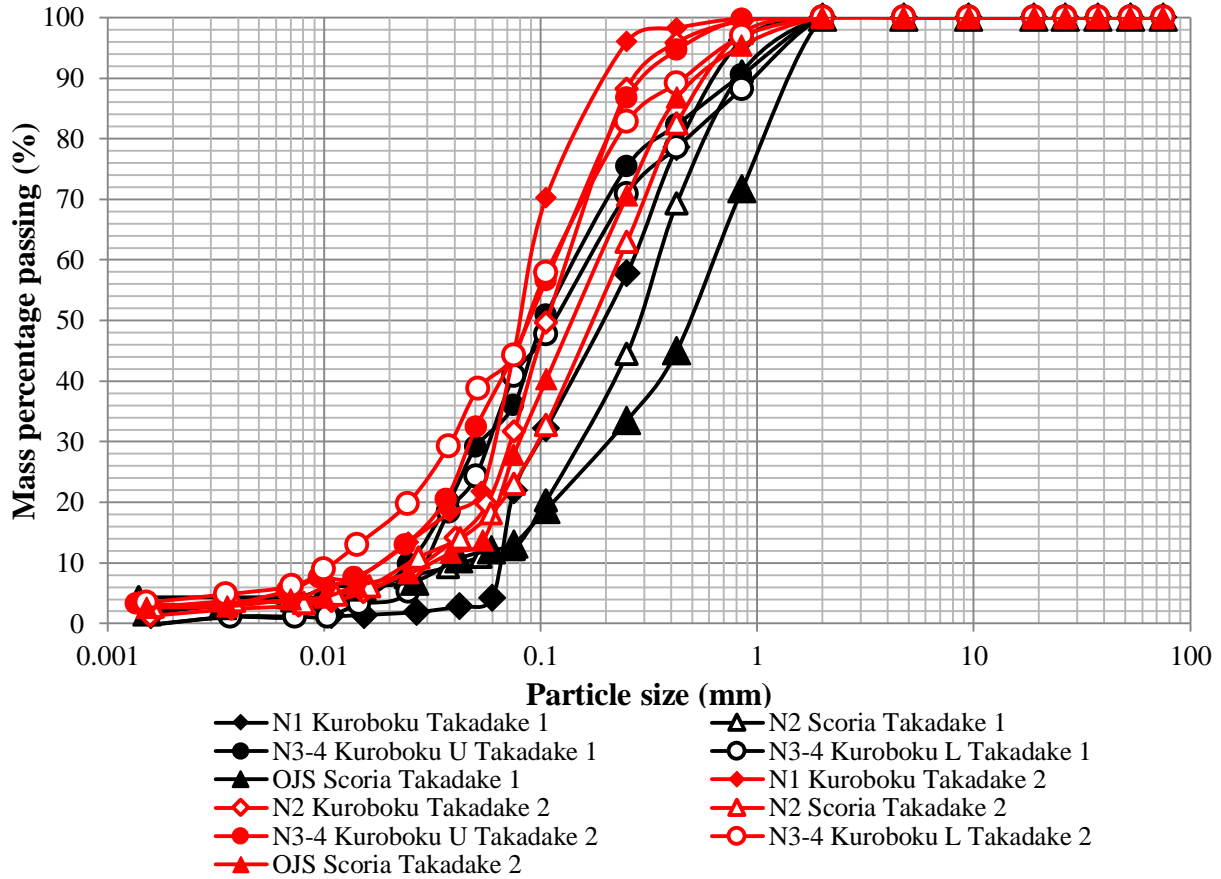


Figure 5.2 Particle size distribution curves of Takadake materials

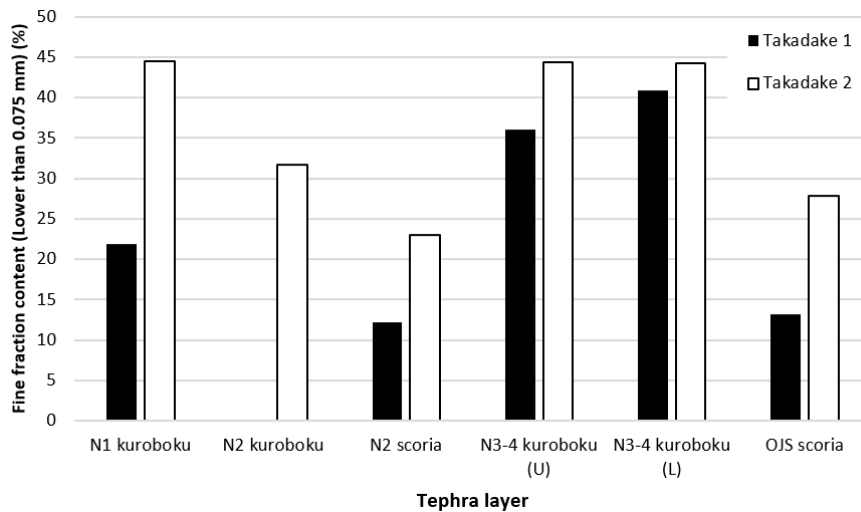


Figure 5.3 Fine fraction content (% 0.075 mm) on Takadake landslides shows the dissimilarity between kuroboku and scoria layers

density value between kuroboku and scoria showed that kuroboku has loose structure, and during heavy rainfall, low coefficient of saturate permeability in OJS scoria layer was the reason which increased the pore water pressure on N3-4 kuroboku layer.

Fig. 5.4 also shows that the plasticity index is different between the kuroboku and scoria layers. The liquid limit and plastic limit test results are plotted on a plasticity chart (Fig. 5.5) to classify the tephra layers, which are separated between the sampling location (Takadake 1 and Takadake 2) and the type of tephra materials (kuroboku and scoria). Takadake 1 and Takadake 2 tephra layer data are denoted by filled and un-filled symbols, respectively, and sliding layers on each area are denoted by white circles with different colored outlines. Furthermore, the kuroboku and scoria groups are denoted by the line

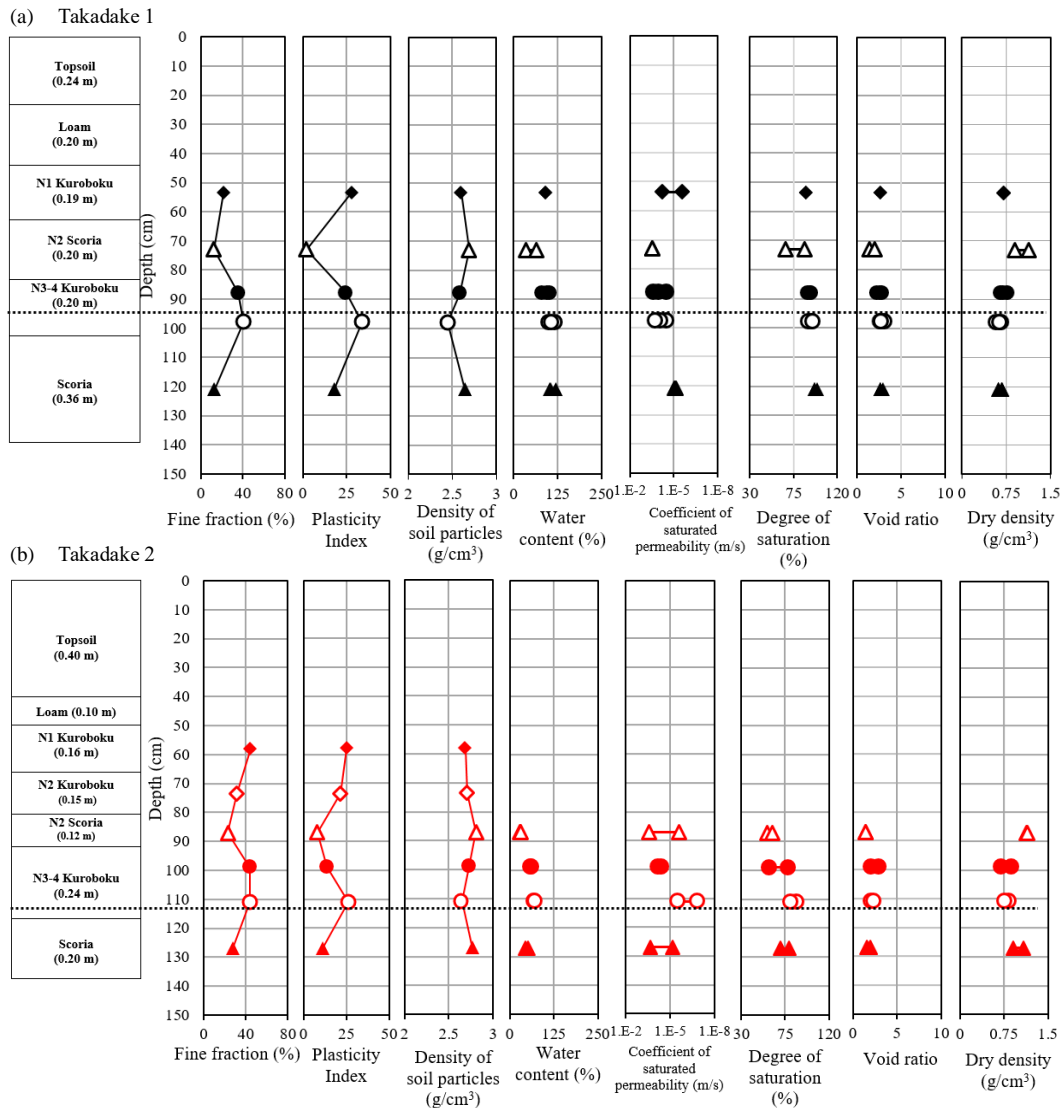


Figure 5.4 Physical properties and saturated permeability properties of soil in Takadake 1 (a) and in Takadake 2 (b); black dotted lines indicated location of sliding layer by field observation

and dotted of ellipse symbols, respectively.

The plotted data in Fig. 5.5 show a similar classification of the tephra layer for Takadake 1 and Takadake 2. That shows all of the plotted data on kuroboku layers are inorganic silts of high compressibility and organic clays and the OJS scoria layers plotted at the same location as the kuroboku layers. The N2 scoria layers, however, are inorganic silts of medium compressibility and organic silts. The plasticity index and liquid limit values of the kuroboku layers are different, but higher than the scoria layers. The plotted data from Takadake 1 and Takadake 2 both show that the N3-4 kuroboku L layer has the highest plasticity index and liquid limit values, while the N2 scoria layer has the lowest plasticity index and liquid limit values. Therefore, the N3-4 kuroboku L layers (sliding layers) have the highest values and are plotted in the kuroboku group on the plasticity chart. The plasticity index and liquid limit can be used as factors for estimating the sliding

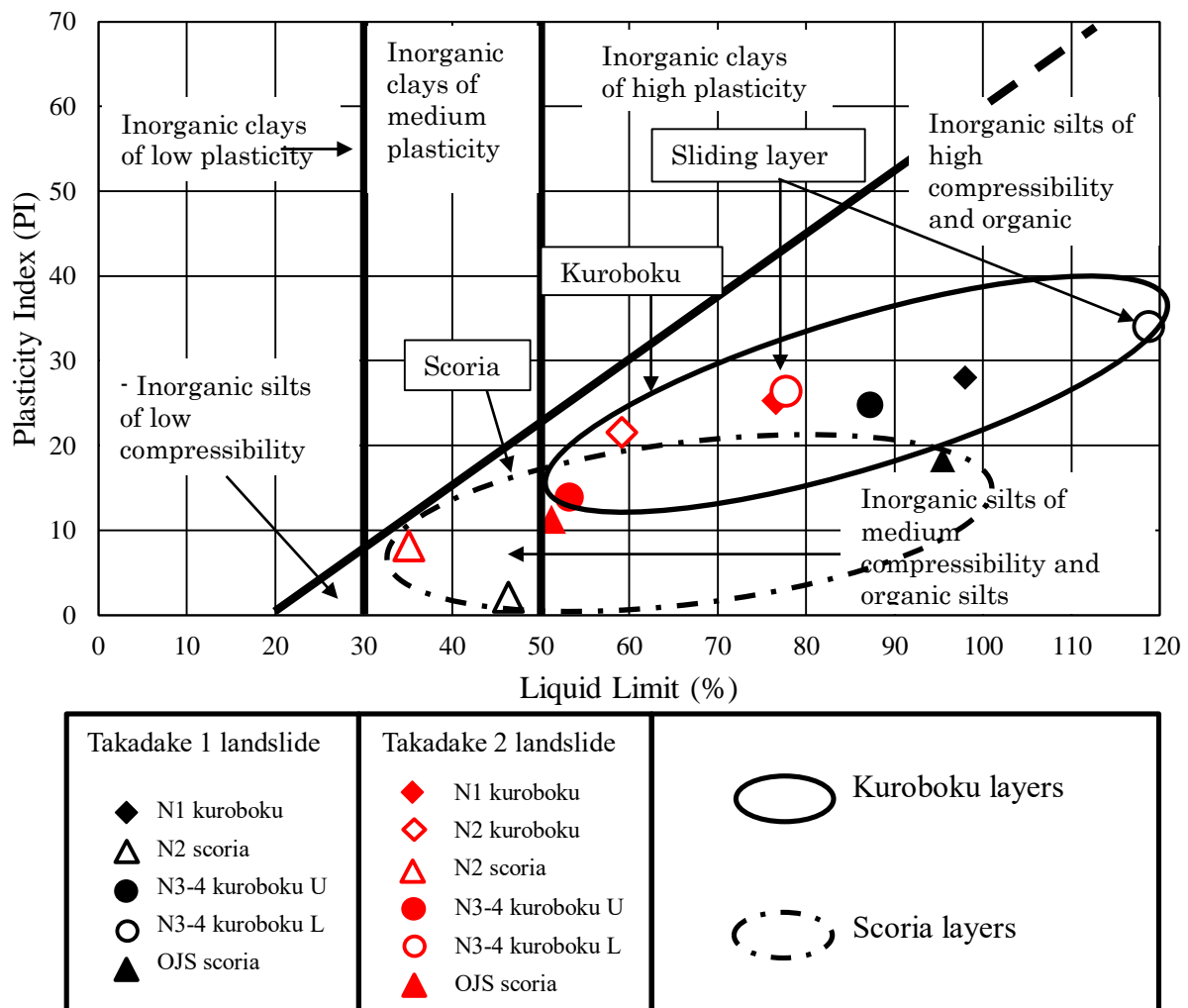


Figure 5.5 Plasticity chart shows the dissimilarity between kuroboku and scoria layers

layer.

According to the factors for estimating the sliding layer, a correlation between the plasticity index and fine fraction content is observed in Fig. 5.6, showing nearly the same results as the plasticity chart. The correlation shows the plotted data are separated between the sampling location (Takadake 1 and Takadake 2) and the type of tephra materials (kuroboku and scoria). Takadake 1 and Takadake 2 tephra layer data are denoted by filled and un-filled symbols, respectively, and sliding layers on each area are denoted by white circles with different colored outlines. The data from Takadake 1 fitted to the Takadake 1 trend line, and the data from Takadake 2 also fitted to the Takadake 2 trend line. The trend lines show that the plasticity index is directly proportional to the fine fraction content. Furthermore, the kuroboku and scoria layers are denoted using the line and dotted of ellipse symbols, respectively.

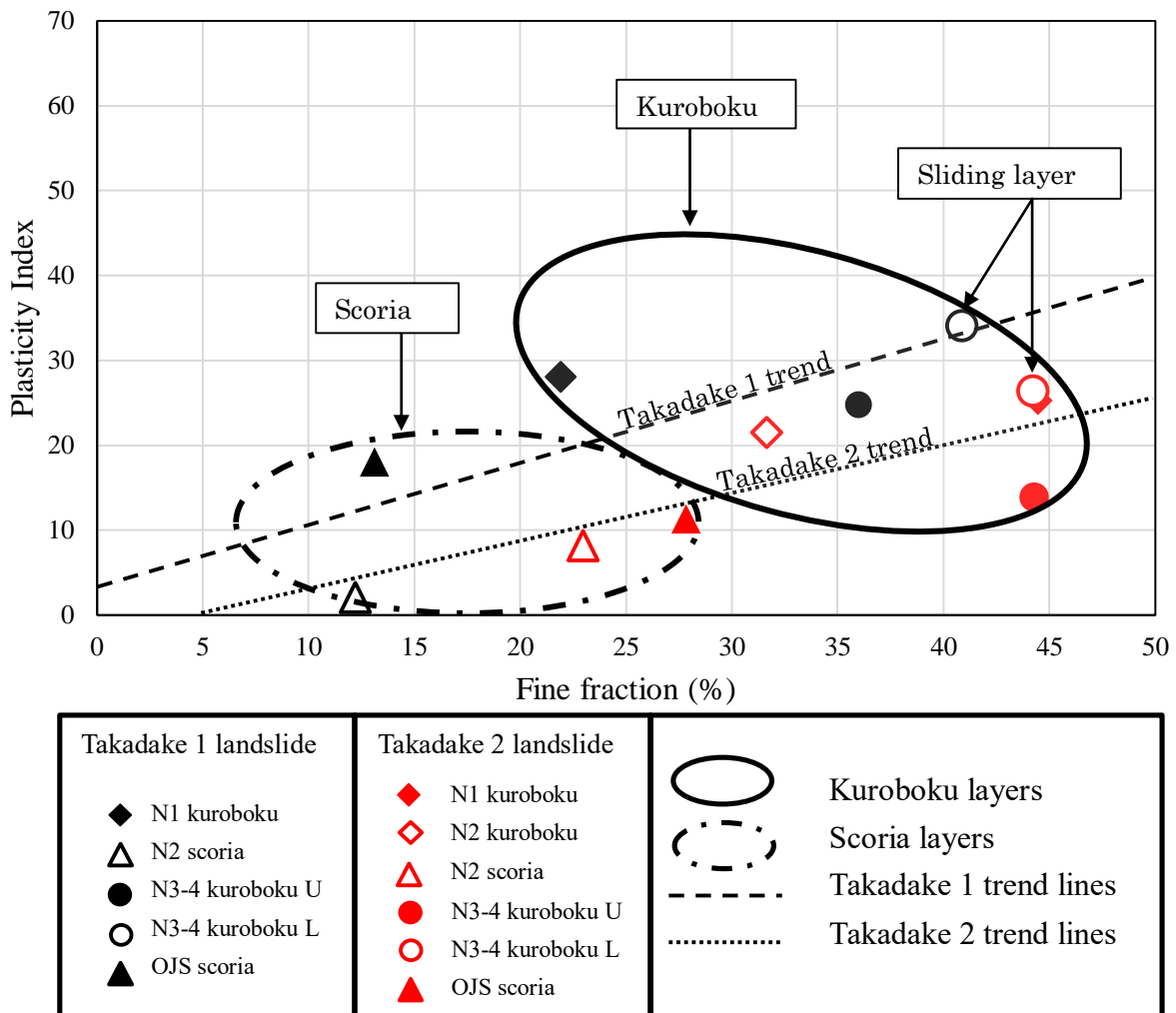


Figure 5.6 Correlation between fine fraction content (% 0.075 mm)-plasticity index shows dissimilarity between kuroboku and scoria

The correlation shows dissimilarity between the kuroboku and the scoria layers. Scoria layers show low fine fraction content and plasticity index values and kuroboku layers show high fine fraction content and plasticity index values. The data from Takadake 1 and Takadake 2 both show that the N3-4 kuroboku L layer has the highest plasticity index and fine fraction content values, while the N2 scoria layer has the lowest plasticity index and fine fraction content values. Therefore, the sliding layers (N3-4 kuroboku L) are plotted in the kuroboku group on the correlation and has the highest values of plasticity index and fine fraction content. However, the plots of this correlation have a wide scattering, which could be caused by the difference in soil materials at the different volcanic activity periods and the historical landslides in the Aso volcanic mountains.

The content of clay minerals on tephra layers from Takadake 1 and Takadake 2 does

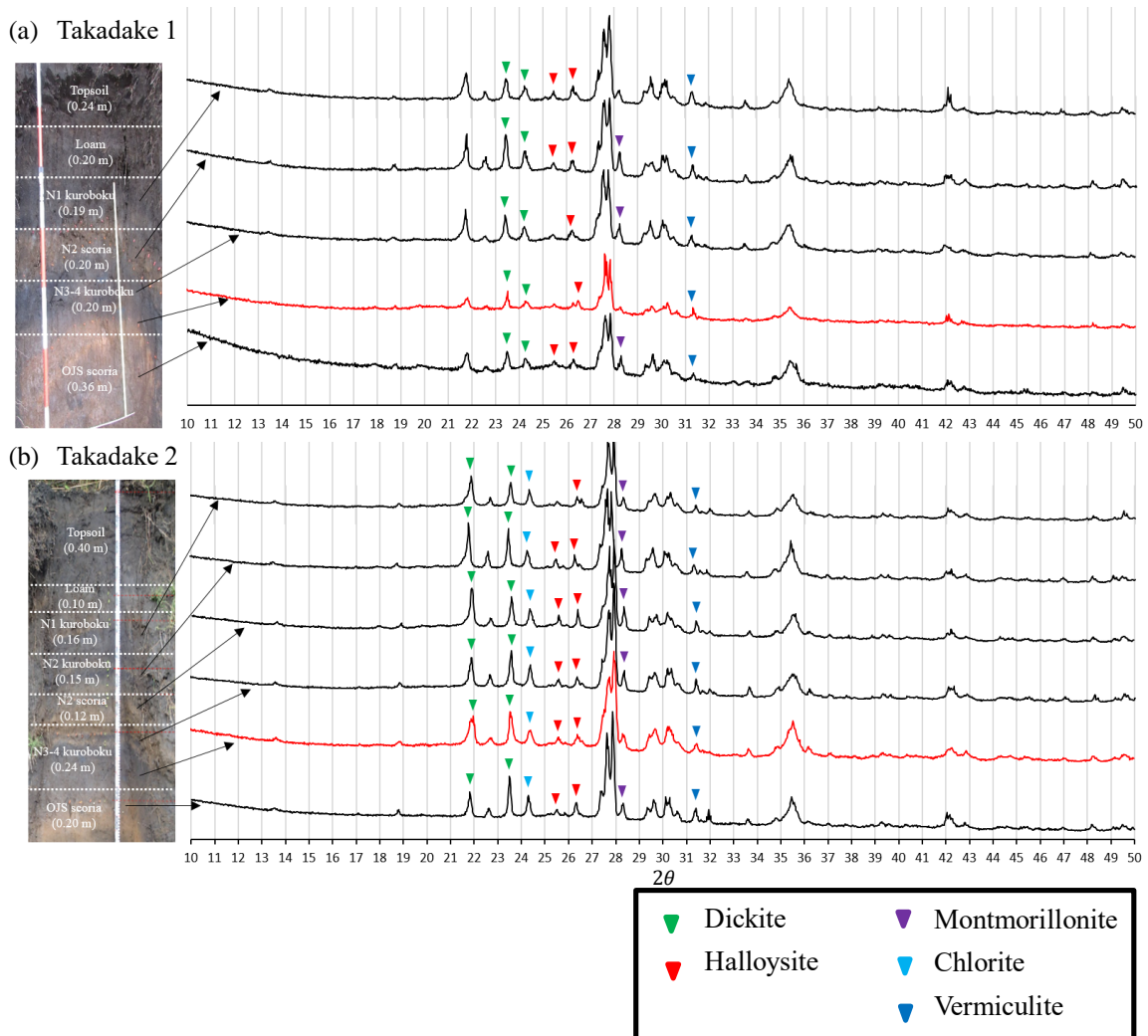


Figure 5.7 Clay minerals on tephra materials from Takadake 1 (a) and Takadake 2 (b) (Red lines indicated sliding layers)

not shows the dissimilarity, however, tephra layers from Takadake 2 consist of chlorite mineral (Fig. 5.7). Tephra layers from Takadake landslides are generally contain kaolinite clay minerals group (dickite and halloysite), smectite clay minerals group (montmorillonite), and vermiculite. Furthermore, characteristic of sliding layer from content of clay minerals in Takadake landslides is not observed.

5.2 Izu Oshima landslide caused by heavy rainfall 2013

Landslides occurred in unconsolidated superficial tephra deposits, and were shallow soil slips; the thickness of the slides usually ranged from 1 to 2 m (Miyabuchi et al. 2015). The head scarps on the thick tephra-covered slopes are blackish in color, whereas the sliding layers are brownish. This indicates that the rupture surfaces of most slides were located near the boundary between the upper blackish and lower brownish tephra layers (Miyabuchi et al. 2015).

Miyabuchi et al. (2015) also recognized differences in physical properties of tephra deposits between above and below the rupture surfaces. The deposits in the upper tephra layers above the rupture surface are coarser-grained and poorly consolidated, whereas the

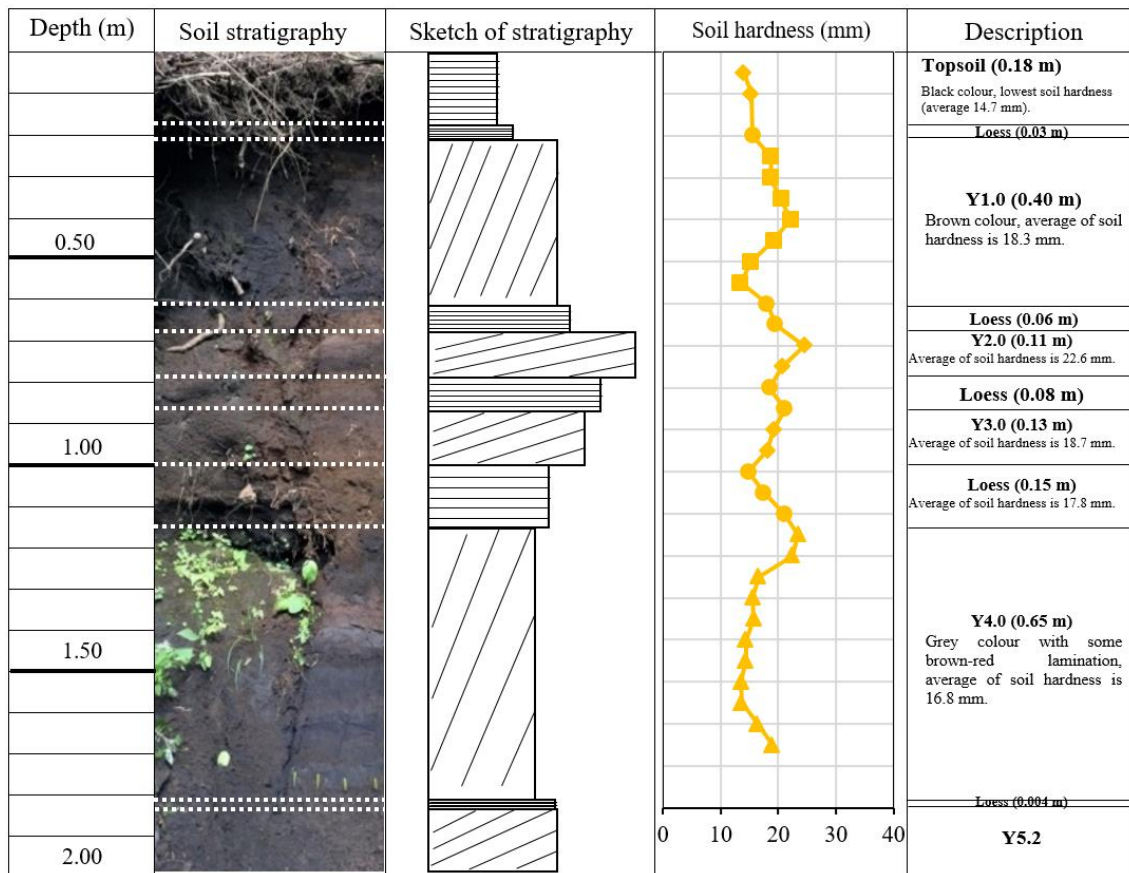


Figure 5.8 Soil stratigraphy by field observation in Izu Oshima

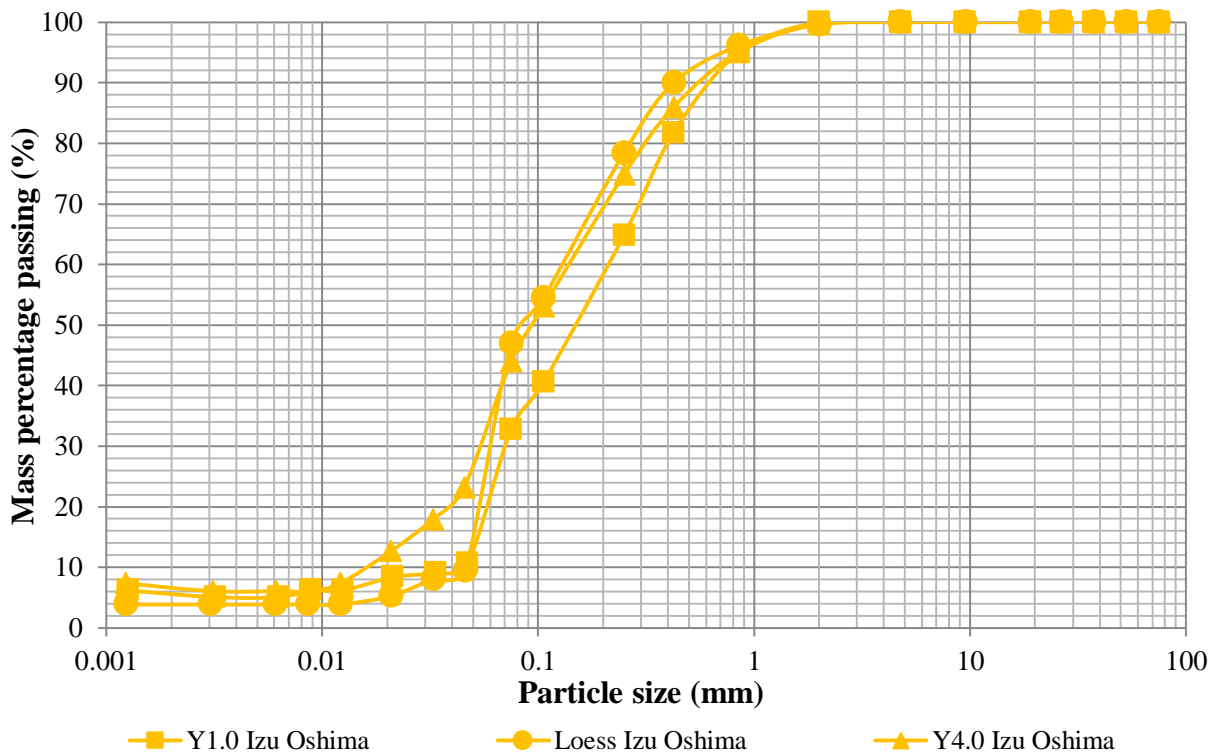


Figure 5.9 Particle size distribution curves of Izu Oshima materials

lower loess are finer-grained and moderately consolidated. The grain-size and soil hardness data also suggest that these differences in physical characteristics cause the difference in permeability (Miyabuchi et al. 2015). The saturated hydraulic conductivities of the lower

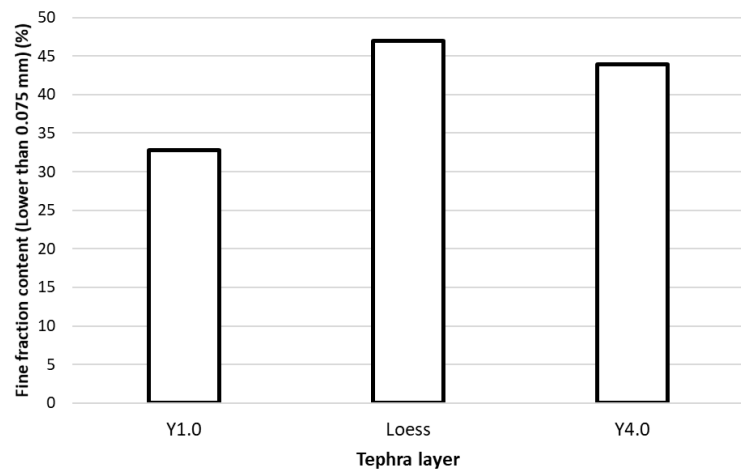


Figure 5.10 Fine fraction content (% 0.075 mm) on Izu Oshima

soils below the rupture surface are approximately one to two orders lower than those of the upper tephra. The difference in permeability represents an important barrier to meteoric water infiltration and, thus, facilitated rupturing near the boundary between the upper tephra and lower soil layers, acting respectively as an overlying permeable layer and an underlying aquiclude. Thus, on the tephra-covered slopes voluminous rainwater infiltrated from the ground surface remains in the upper tephra layers because the lower impermeable soil layers present a barrier. The upper tephra layers become progressively

saturated in water and failure occurs (Miyabuchi et al. 2015).

Loess and Y tephra layers were layering in Izu Oshima landslide (Fig. 5.8). Y tephra layers from Izu Oshima landslide in this study consist of Y1.0 to Y5.2 tephra, and this study observed Y1.0, loess, and Y4.0 layers. Dissimilarity between loess and Y tephra layers in soil hardness is not observed, however, Y1.0 and Y2.0 layers have lower soil hardness rather than the under loess layers.

Particle size distribution curve shows no dissimilarities in tephra layers, and all the tephra layers indicate poorly-graded soil material (Fig. 5.9). Fine fraction content (less than 0.075 mm) on tephra layers (Fig. 5.10) show the difference between Y1.0 and Y4.0 layers, and it show that the lower layers could have higher fine fraction content rather than upper layers.

Characteristics of physical properties on tephra layers from Izu Oshima landslide is not observed (Fig. 5.11). Miyabuchi et al. (2015) reported dissimilarity of permeability in tephra layers, however, the dissimilarity is not observed in this study. Dissimilarity of tephra layer in the liquid limit and plastic limit test results which plotted on a plasticity chart (Fig. 5.12) is also not observed. All tephra layers are inorganic silts of low compressibility and cohesion less soils with low plasticity index and liquid limit values.

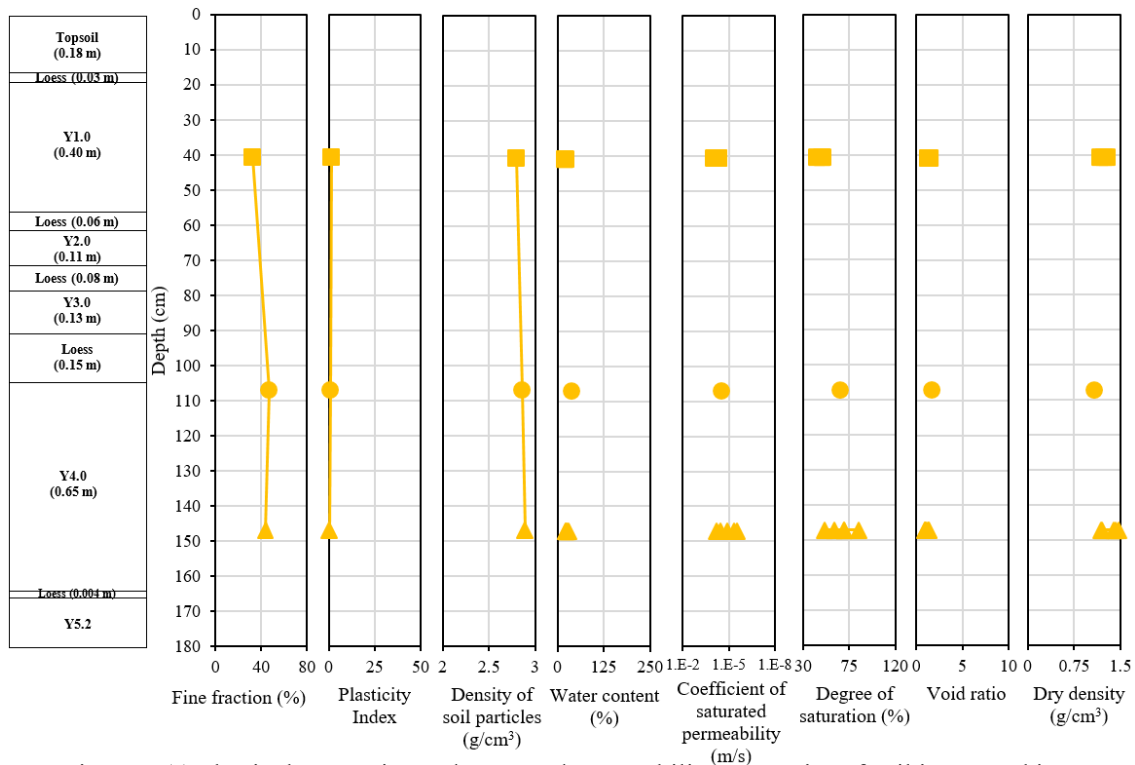


Figure 5.11 Physical properties and saturated permeability properties of soil in Izu Oshima

The content of clay minerals on tephra layers from Izu Oshima shows the dissimilarity between Y1.0 and Y4.0 tephra (Fig. 5.13). Y1.0 and loess layers has a similar content of clay minerals; kaolinite clay minerals group (dickite) and smectite clay

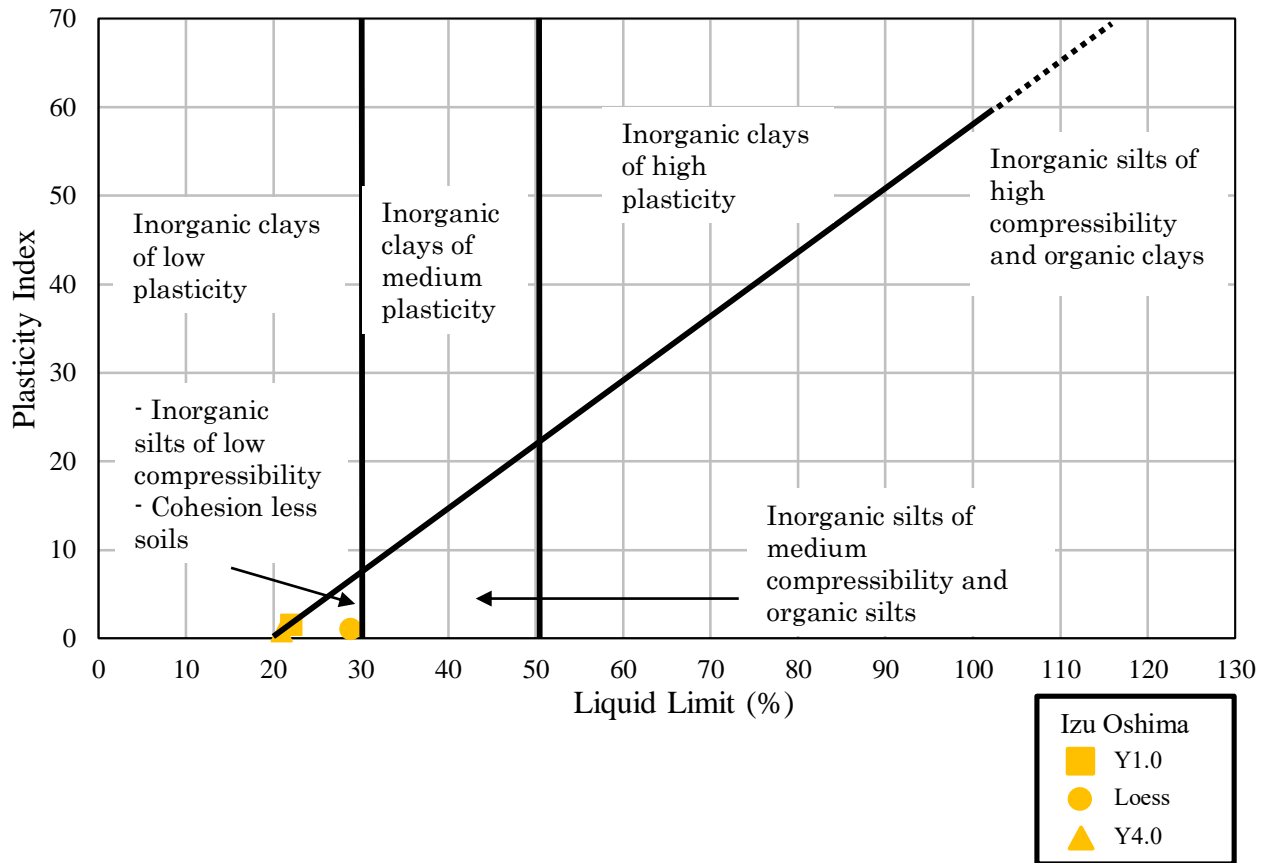


Figure 5.12 Plasticity chart on tephra layers from Izu Oshima

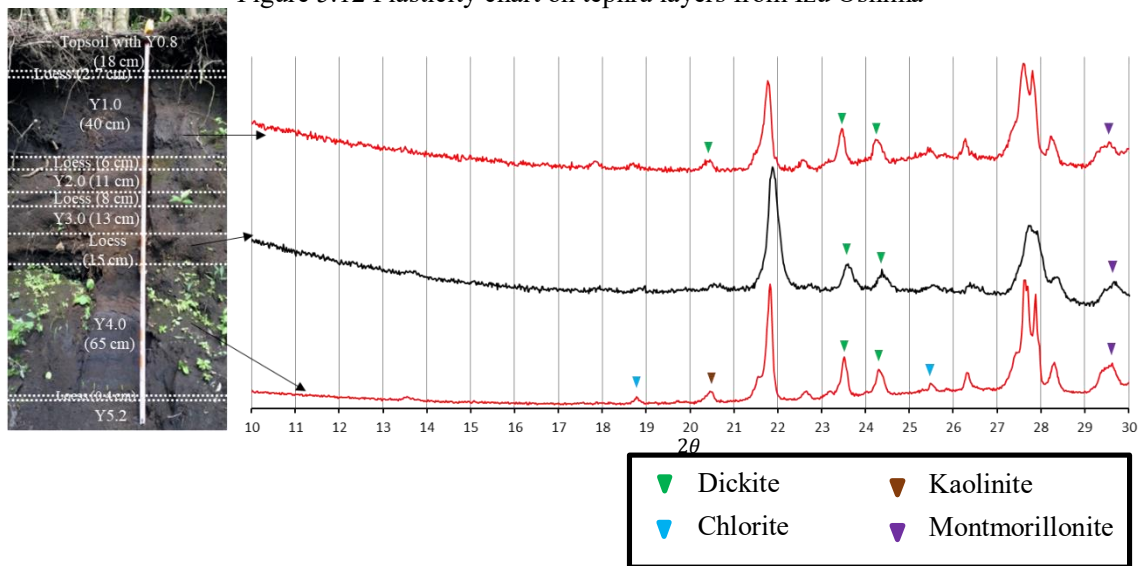


Figure 5.13 Clay minerals on tephra materials from Izu Oshima (Red lines indicated sliding layers) minerals group (montmorillonite), on the other hand, Y4.0 has kaolinite clay minerals

group (dickite and kaolinite), smectite clay minerals group (montmorillonite), and chlorite. Therefore, influence of clay minerals on sliding layer is not observed in Izu Oshima landslide.

5.3 Takanodai landslide caused by earthquake 2016

The key soil to cause the slope failure could be the orange-colored pumice soil deposit (Mukunoki et al. 2016; Chiaro et al. 2017). Moreover, the sensitivity ratio of shear strength of this volcanic soil before and after the earthquake as well as the water pressure build-up could be the cause for the flow type slope failure (Chiaro et al. 2018), and Chiaro et al. (2018) evaluated the liquefaction potential of the Aso pumice. Dynamic soil response and seismic slope stability analyses confirmed that orange-colored pumice layer was responsible of the activation of the landslide (Chiaro et al. 2018). Furthermore, Song et al. (2017) characterized landslide soil composition by soft ground of weathered volcanic cohesive soil. The soil, which is porous and loose, has low cohesion and lead to slope slide under the earthquake shock.

Tephra layers from Takanodai landslide were located in the deep layer, and tephra layers which observed on this study was located at around 8 m depth from the surface. Different colors on tephra layers is observed on this landslide, and thin white boundary layer was found between orange Kusasenrigahama and dark brown tephra layers (Fig. 5.14). Dissimilarity in soil hardness is observed, orange Kusasenrigahama layer has the highest value and dark brown tephra layer has the lowest value.

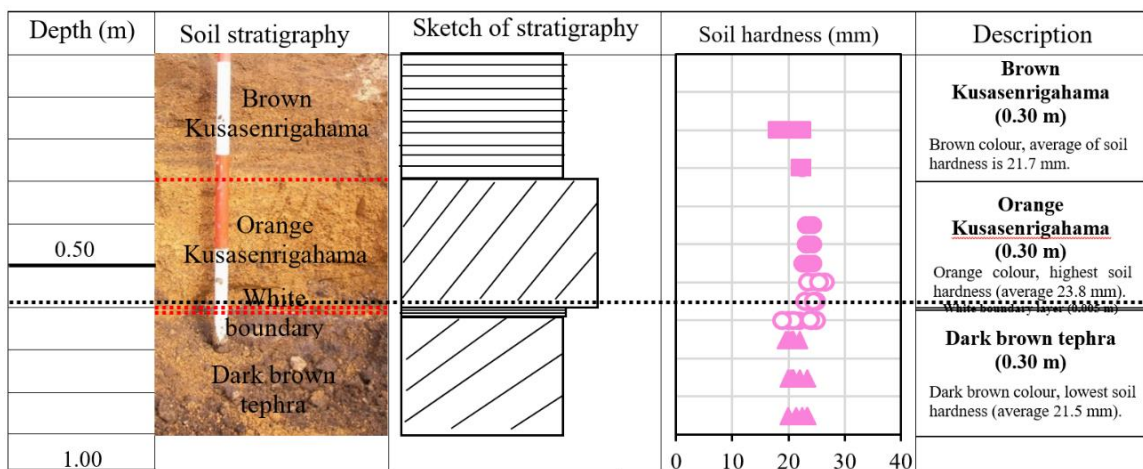


Figure 5.14 Soil stratigraphy by field observation in Takanodai; black dotted lines indicated location of sliding layer by field observation

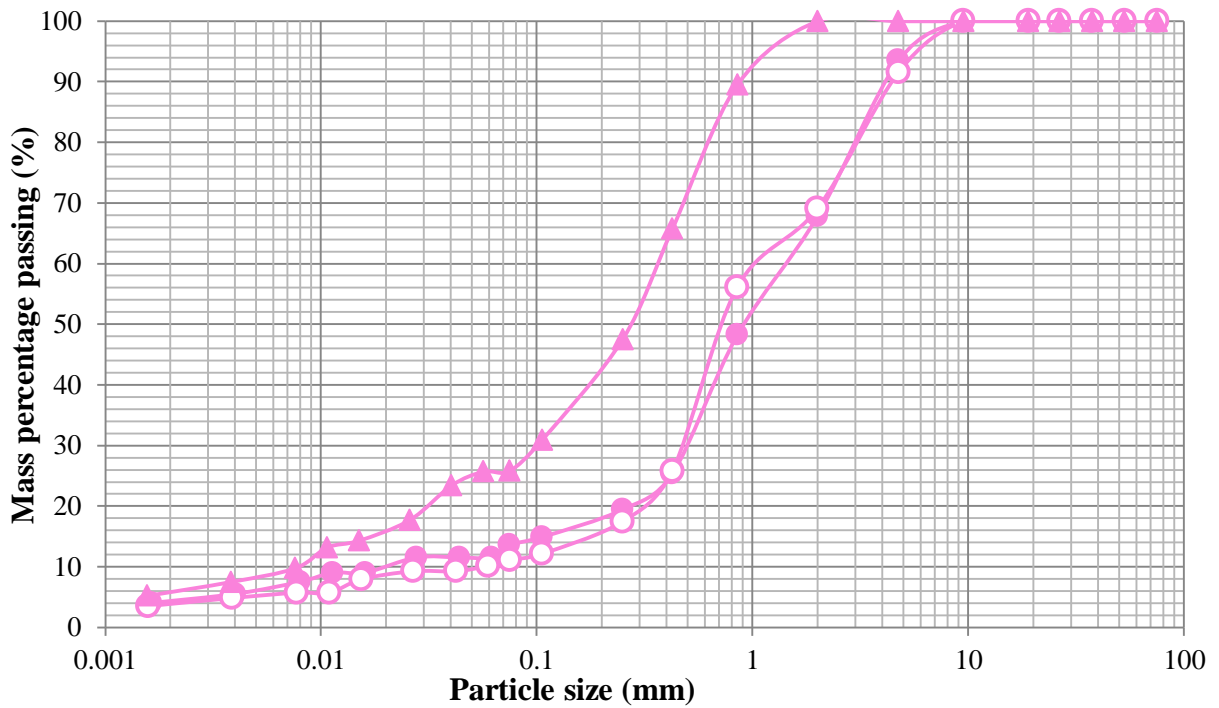


Figure 5.15 Particle size distribution curves of Takanodai materials

Particle size distribution curve shows no dissimilarities in tephra layers at Takanodai landslide and all the tephra layers indicate well-graded soil material (Fig. 5.15). However, dissimilarity of fine fraction content (less than 0.075 mm) on tephra layers (Fig. 5.16) is observed, dark brown tephra has the highest fine fraction content and orange Kusasenrigahama has the lowest fine fraction content. Tephra layers from Takanodai landslide show that soil hardness is not directly proportional with fine fraction content (less than 0.075 mm). Orange Kusasenrigahama has highest value of soil hardness and lowest fine fraction content, on the other hand, dark brown tephra has lowest value of soil hardness and highest fine fraction content, respectively.

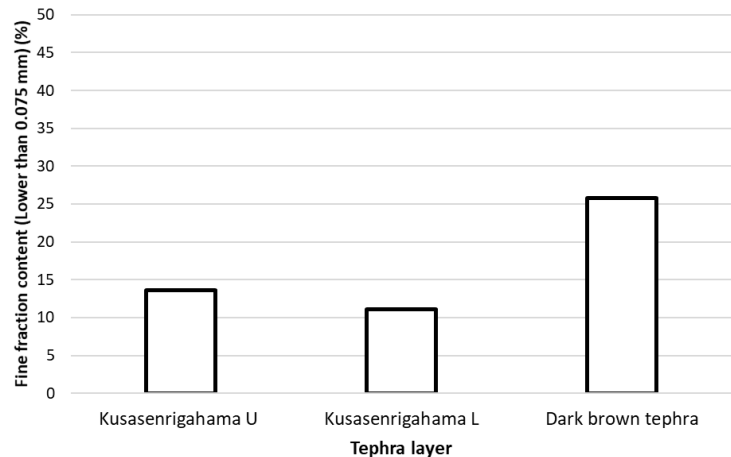


Figure 5.16 Fine fraction content (% 0.075 mm) on Takanodai landslides

Figure 5.17 shows the physical properties of tephra layer, and the dissimilarity on dark brown tephra layer is observed. Dark brown tephra layer has plasticity index, and has

highest fine fraction content, density of soil particles, water content, and degree of saturation. Furthermore, thin white boundary layer which located between orange Kusasenrigahama and dark brown tephra layers, could have caused the low saturated permeability in dark brown tephra. Although an influence of rainfall was not observed on Takanodai landslide, different characteristics between orange Kusasenrigahama and dark brown tephra could be trigger the landslide in Takanodai. Plasticity index on tephra layers from Takanodai landslide also observed the dissimilarity between orange Kusasenrigahama and dark brown tephra layers. Orange Kusasenrigahama layer is non-plastic soil, and dark brown tephra layer is inorganic silts of high compressibility and organic clays with liquid limit and plastic limit are 66.80% and 48.36%, respectively.

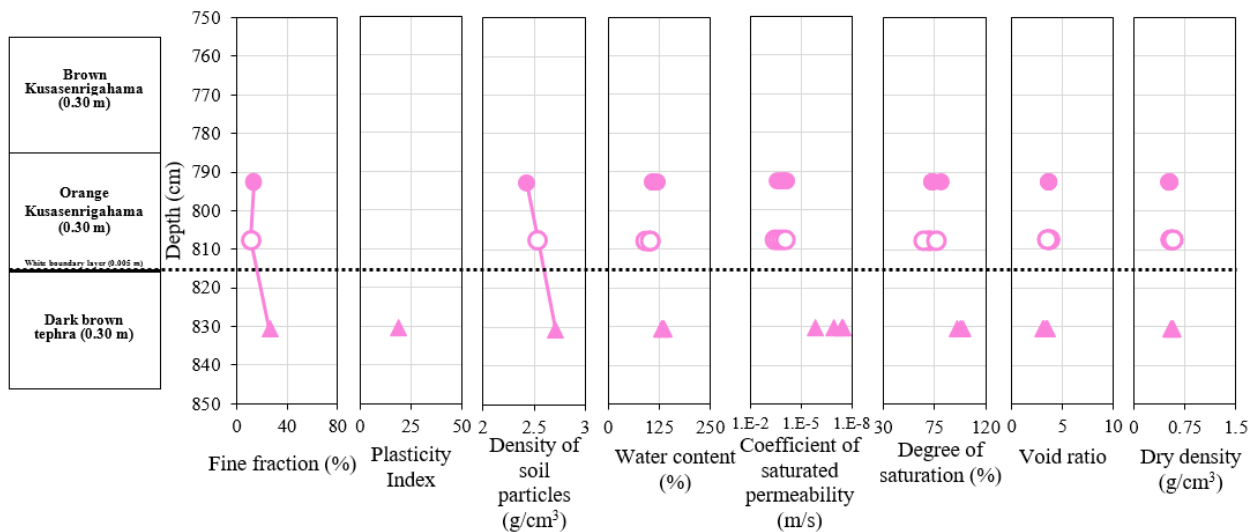


Figure 5.17 Physical properties and saturated permeability properties of soil in Takanodai landslide; black dotted lines indicated location of sliding layer by field observation

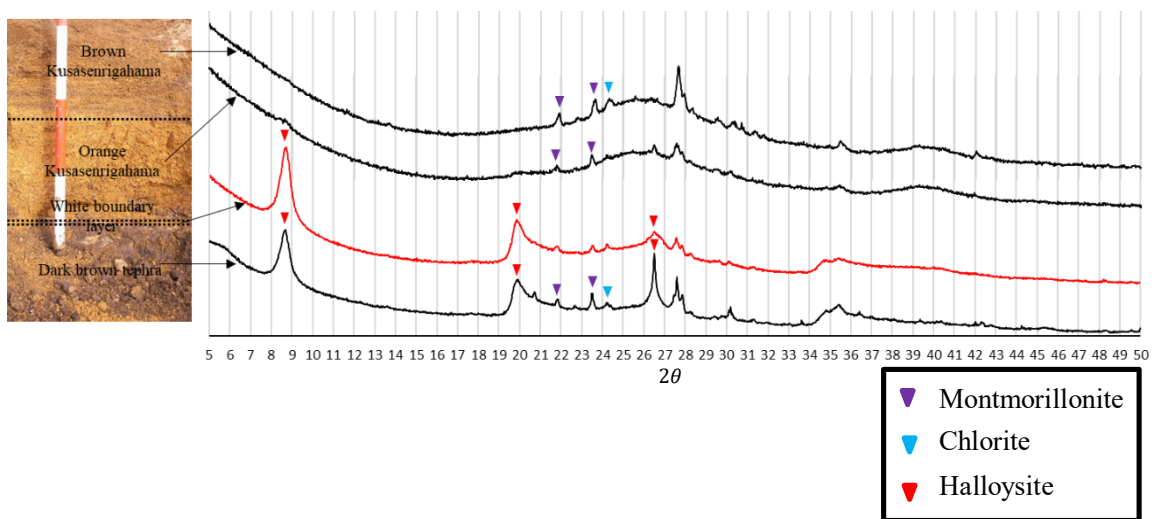


Figure 5.18 Clay minerals on tephra materials from Takanodai landslide (Red lines indicated sliding layers)

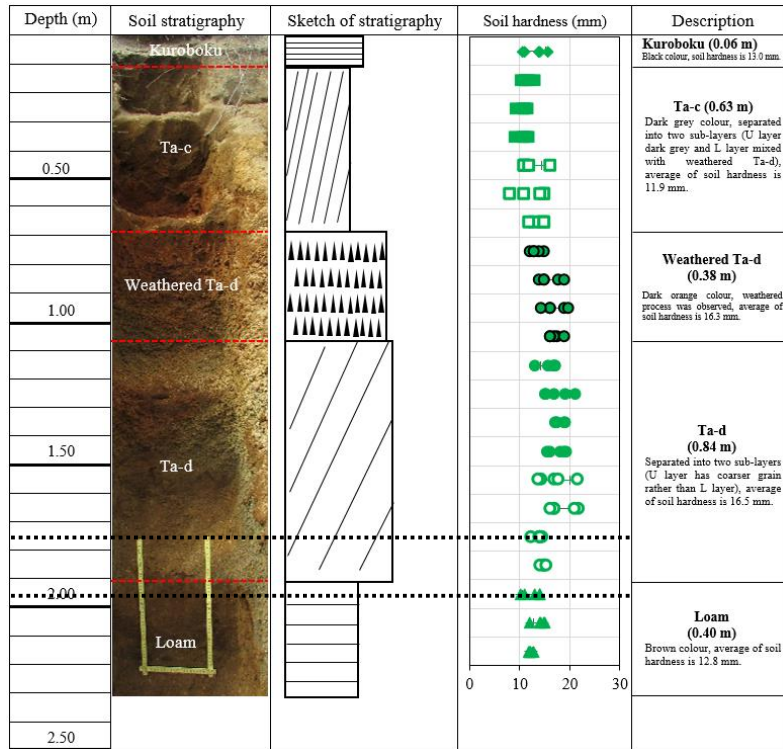
The dissimilarity on content of clay minerals in tephra layers from Takanodai is observed (Fig. 5.18). Kusasenrigahama layers, brown and orange Kusasenrigahama, contain smectite clay minerals group (montmorillonite), in addition, brown Kusasenrigahama also has chlorite mineral. Different with Kusasenrigahama layers, white boundary and dark brown tephra layers contain kaolinite clay minerals group (halloysite), furthermore, dark brown tephra layer also has montmorillonite and chlorite. Influence of clay minerals on sliding layer in Takanodai landslide is observed. White boundary layer which located between orange Kusasenrigahama and dark brown tephra is halloysite-rich layer. Halloysite represent a potential weak (Moon et al. 2015a) of the layer, and orange Kusasenrigahama could be easily to collapse during earthquake since it is located on the white boundary layer.

5.4 Towa and Mizuho landslides caused by Hokkaido Eastern Iburi Earthquake 2018

The hypothesis has been proposed to explain the numerous landslides observed in Hokkaido Eastern Iburi Earthquake. Hypothesis suggested that owing to the typhoon in the previous day could have led to the saturation of pumice strata, which is known to absorb large quantities of water. Hence, it might have caused a rapid pore-pressure increase in the surficial soils during ground shaking and led to liquefaction and slope failure (Wang et al. 2019). Soil wetness could be play an important role in the observed large failures, as the seismically induced liquefaction of loose soils leads to flow-like slope failure (Kokusho and Fujita 2001). However, hourly intensity rainfall before the earthquake were lower and not enough to trigger landslide.

Wang et al. (2019) reported the assessments conducted by the Geological Survey of Japan (GSJ) as well as Yamagishi and Yamazaki (2018) showed that the area is blanketed by tephra layers with depths of 4-12 m with standard penetration test values less than 10 N-value indicating they are unconsolidated, highly compressible, and crushable (Miura 2012). The sliding layer of landslides caused by Hokkaido Eastern Iburi Earthquake predominantly formed near the bottoms of layers consisting of volcanic ash and pumice from the Tarumai volcano (Ta-d) and it also formed in other tephra layers, such as En-a (Nakagawa et al. 2018, Kasai and Yamada 2019, Osanai et al. 2019). Furthermore, Ta-d were presumed to be vulnerable to ground shaking, and thus reduced cohesion (Kasai and Yamada 2019).

(a) Towa



(b) Mizuho

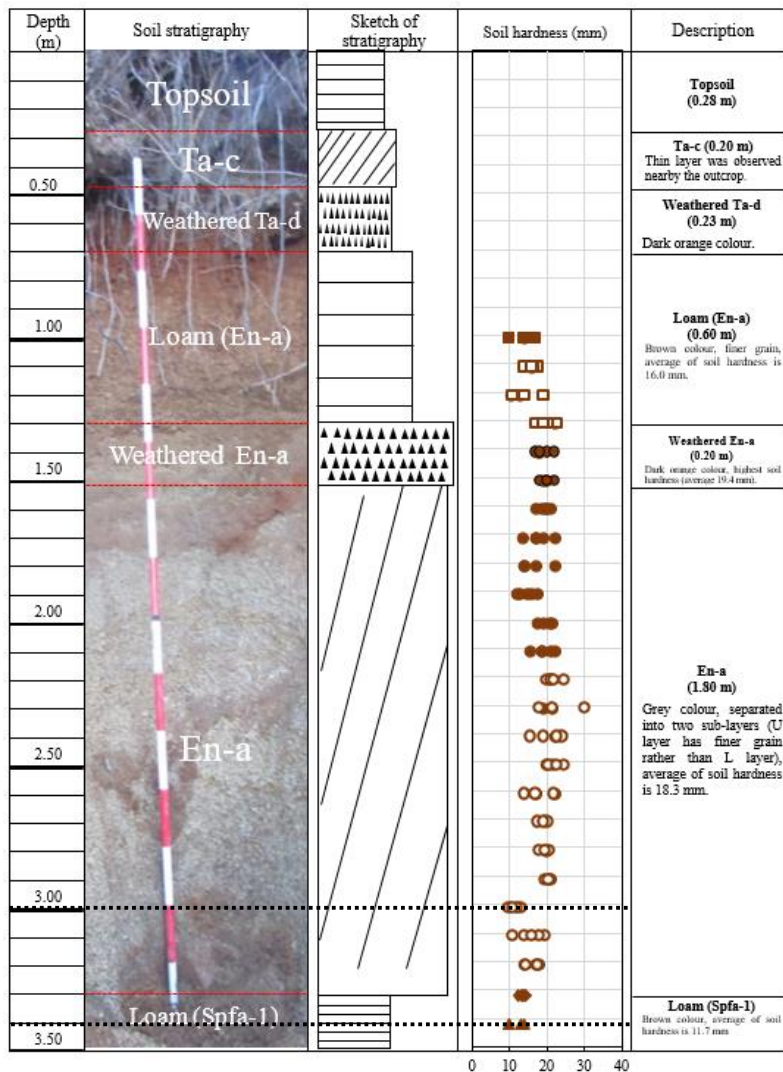


Figure 5.19 Soil stratigraphy in Towa (a) and Mizuho (b) landslides; black dotted lines indicate sliding layer by field observation

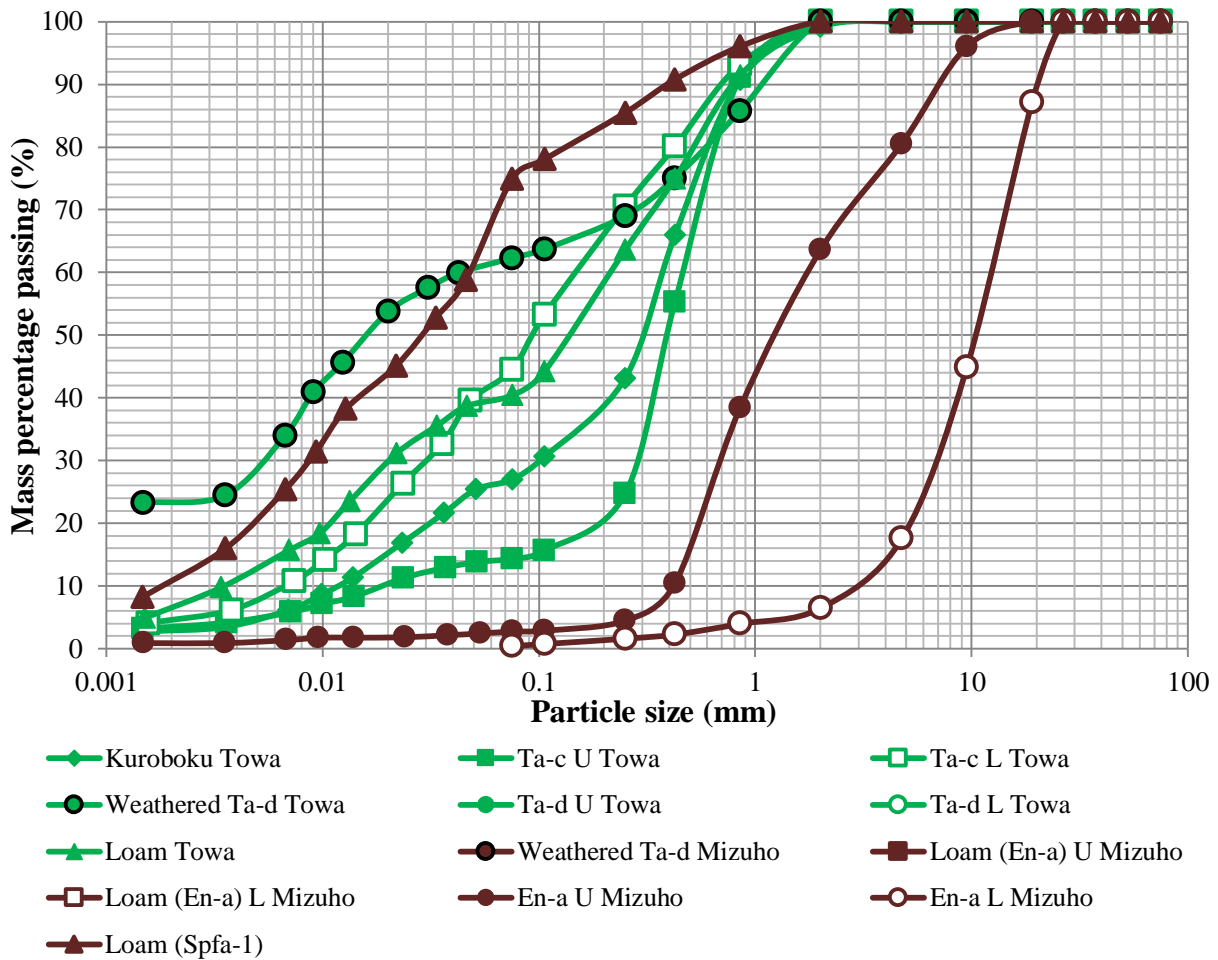


Figure 5.20 Particle size distribution curves of Towa and Mizuho materials

The sliding layer from field observation were located in the Ta-d and En-a layers at the Towa and Mizuho landslides (Fig. 5.19), respectively. The soil hardness in Towa landslide indicates that the Ta-c U layer has the lowest average value of soil hardness, whereas the Ta-d U layer has the highest average value of soil hardness. Additionally, the soil hardness in Mizuho landslide shows that the Loam (Spfa-1) has

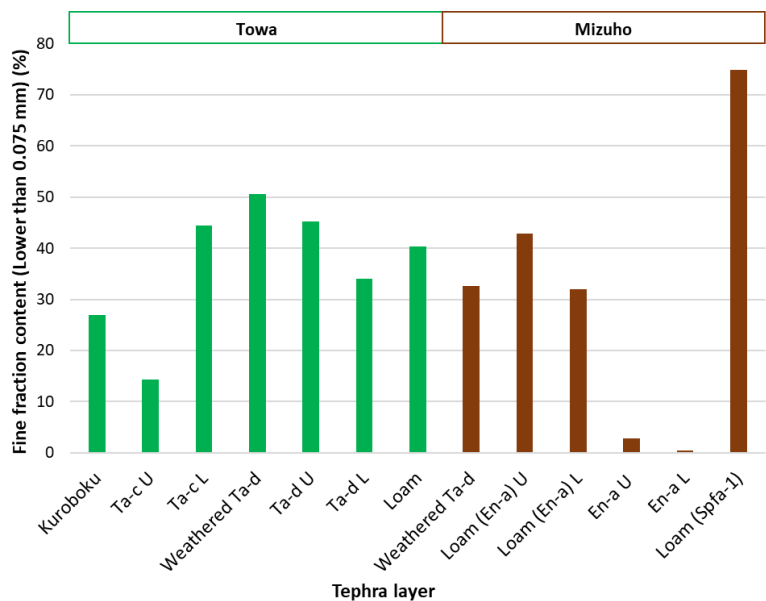


Figure 5.21 Fine fraction content (% 0.075 mm) on Towa and Mizuho landslides

the lowest average value of soil hardness, whereas weathered En-a layer has the highest average value of soil hardness. Unfortunately, the characteristics of sliding layer on soil hardness is not observed in both landslides.

Particle size distribution curve (Fig. 5.20) shows two types of tephra materials; tephra materials which indicated a well-graded soil material and tephra materials which indicated a poor-graded soil material. Tephra materials which have a well-graded soil material are kuroboku, Ta-c L, and Loam layers from Towa landslides; and Loam (En-a) U, Loam (En-a) L, and Loam (Spfa-1) layers from Mizuho landslide. Furthermore, tephra materials which have a poor-graded soil material are Ta-c U, weathered Ta-d, Ta-d U, and Ta-d L layers from Towa landslide; and weathered Ta-d, En-a U, and En-a L layers from Mizuho landslide. Dissimilarity on fine fraction content (less than 0.075 mm) was observed in Towa and Mizuho landslides (Fig. 5.21). Sliding layer in Towa and Mizuho landslides have lower fine fraction content (less than 0.075 mm) rather than the under layer. Furthermore, this study observed the similarity on characteristics of particle size distribution in Ta-d layers from Towa landslide and En-a layer from Mizuho landslide.

Fig. 5.22 shows physical properties of tephra layers in Towa and Mizuho landslides, which observed the dissimilarity between sliding layer and the under layer. Dissimilarity on void ratio and on dry density showed that sliding layers have loose structure. Although pore water pressure was not influence the earthquake-induced landslides, however, loose structure on sliding layers could have been influenced. During the earthquake, sliding layers which have loose structure could be easily to collapse.

Furthermore, Fig. 5.23 shows the plasticity chart for classifying the soil materials using the liquid limit and plastic limit results, which are denoted by different colors, and sliding layers on each area are denoted by white circles with different colored outlines. Tephra materials from Towa and Mizuho landslides are divided into three types; inorganic silts of medium compressibility and organic silts, inorganic silts of high compressibility and organic clays, and non-plastic (NP). Kuroboku and Ta-c L layers from Towa landslide, and Loam (En-a) U and Loam (En-a) L layers from Mizuho landslide are inorganic silts of medium compressibility and organic silts which have lower liquid limit and plasticity index values. Furthermore, weathered Ta-d, Ta-d U, and Loam layers from Towa landslide, and weathered Ta-d layer from Mizuho landslide are inorganic silts of high compressibility and organic clays which have higher liquid limit and plasticity index

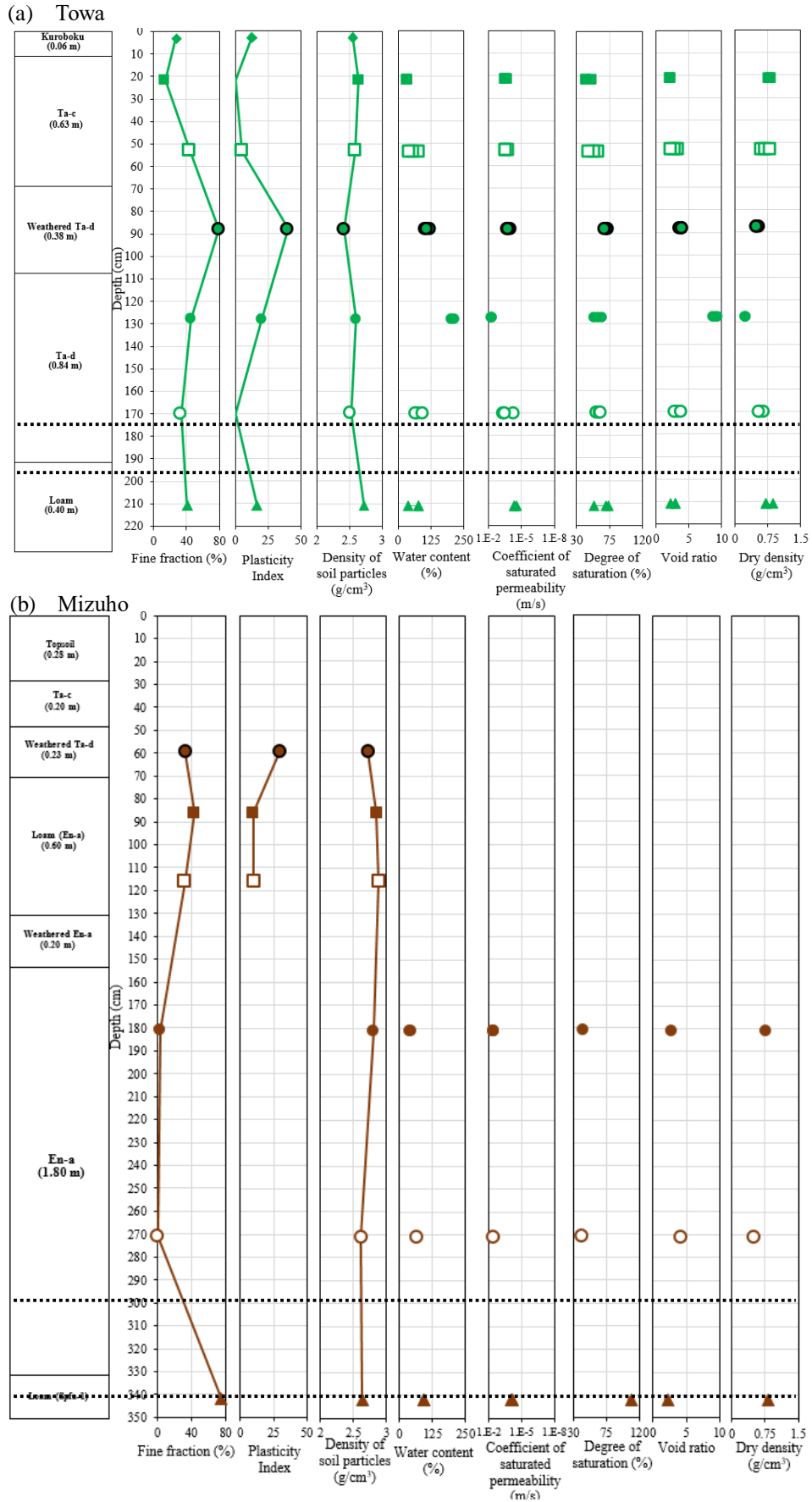


Figure 5.22 Physical properties and saturated permeability properties of soil in Towa (a) and Mizuho (b) landslides; black dotted lines indicated location of sliding layer by field observation

values. Non-plastic group consists of Ta-c U and Ta-d L layers from Towa landslide, and En-a and Loam (Spfa-1) layers from Mizuho landslide.

The content of clay minerals of tephra layers from Towa landslide are generally contain smectite clay minerals group (Fig. 5.24 (a)). Kuroboku layers contain chlorite, illite-smectite, and montmorillonite (smectite group). Moreover, Ta-c U, Ta-c L, and Loam layers contain montmorillonite (smectite group). Weathered Ta-d layer contains chlorite and montmorillonite (smectite group), and Ta-d L layer contains halloysite (kaolinite group) and montmorillonite (smectite group). Unfortunately, the peak was not shown on Ta-d U layer. Influence of clay minerals on sliding layer in Towa landslide is observed. Ta-d L layer contains halloysite while other tephra layers do not contain halloysite. Koyasu et al. (2020) and Chigira et al. (2018a) confirmed that sliding layer was located at Ta-d layer which has halloysite and a lot of water content was contained inside the formation of halloysite.

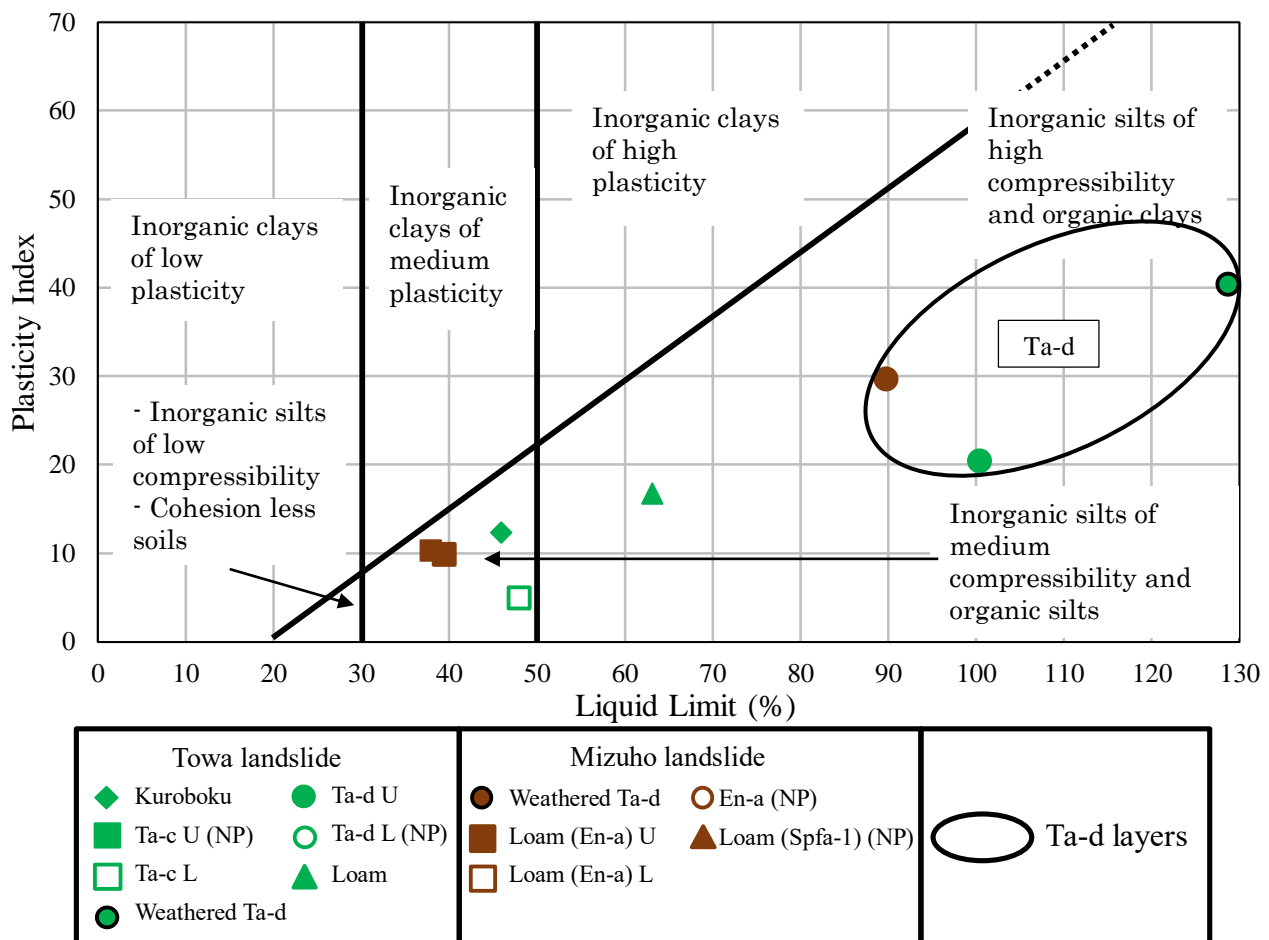


Figure 5.23 Plasticity chart on tephra layers at Towa and Mizuho landslides shows the group of Ta-d layers

Furthermore, the content of clay minerals on tephra layers from Mizuho landslide are generally contain smectite and kaolinite clay mineral group (Fig. 5.24 (b)). Weathered Ta-d layer contains illite, chlorite, smectite group (montmorillonite and smectite), and kaolinite group (dickite and halloysite). Unfortunately, characteristic of sliding layer on

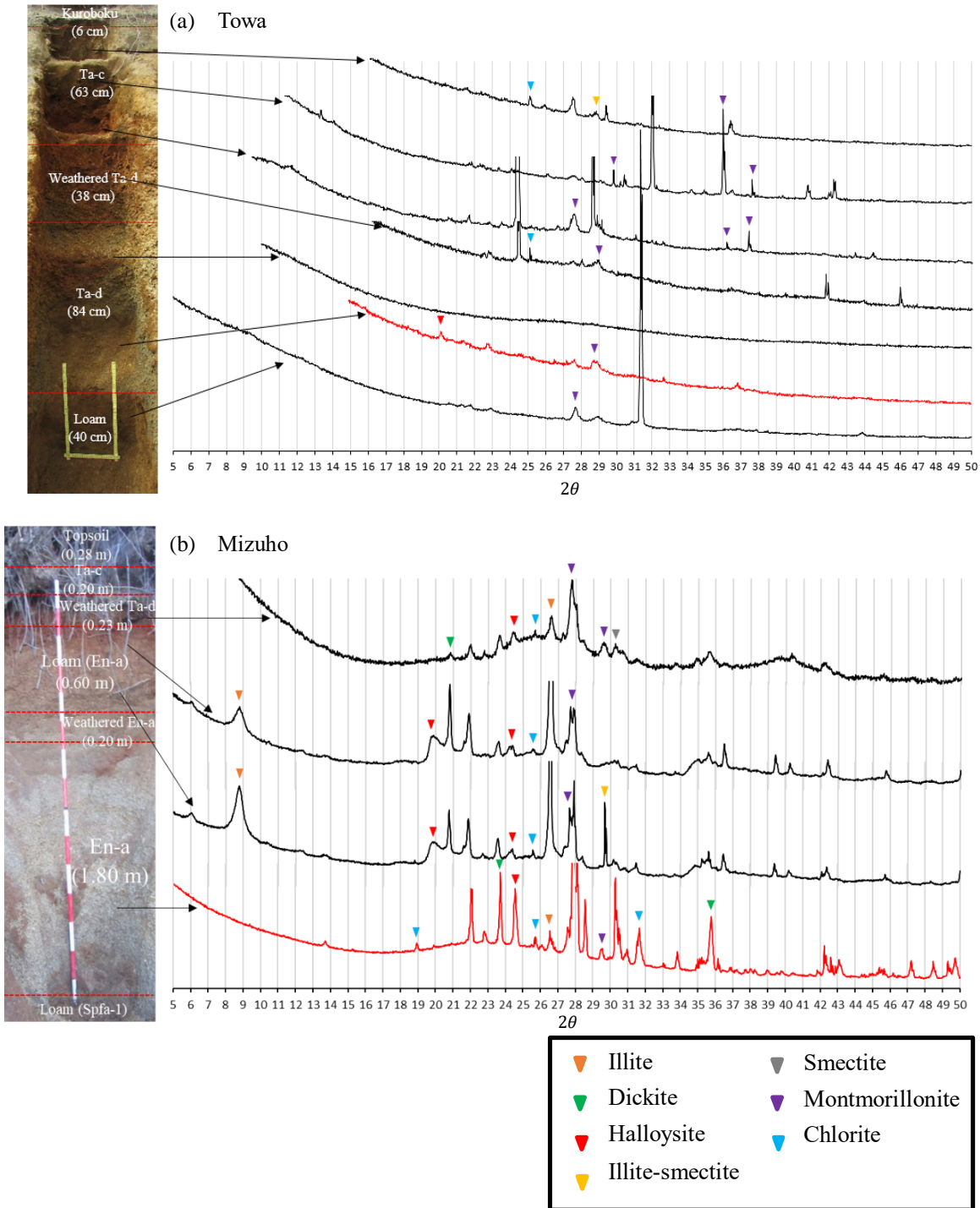


Figure 5.24 Clay minerals on tephra materials from Towa (a) and Mizuho (b) landslides (Red lines indicated sliding layers)

the content of clay minerals is not observed in Mizuho landslide.

5.5 Diverse mechanisms of landslides in Oita Prefecture, Kyushu, Japan

Landslides in Ohtsuru and Ono were influenced by heavy rainfall on July 2017. Ohtsuru landslide occurred during the peak of rainfall and large-scale landslides in Ono occurred the day after the peak of rainfall. Ono landslide occurred probably because the permeability behaviour in thick collapsed of soil layer which has a depth around 20 to 30 m (Ochiai et al. 2017). Two collapses occurred in the Ono landslide; andesite was exposed in the lower collapse and weathered tuff breccia was exposed in the upper collapse (Photo 5.1). Observation is performed in the upper collapse, and the soil sample was taken from this location.

Chigira et al. (2018b) reported that the right bank of the Ono River collapsed and blocked the river channel, forming a small lake. Reddish-brown layer was exposed, suggesting that a sliding layer was formed in this layer. This reddish-brown layer is clayey tuff breccia and the clay probably forms on this layer and make the impermeable zone in this layer; the upper layer (andesite lava) is saturated and the water pressure increases near the boundary (Chigira et al. 2018b). Additionally, many cracks have occurred in the upper part of the landslide (Ochiai et al. 2017). Some of them are considered to be old cracks and cliffs. Ochiai et al. (2017) reported that the cliffs around the landslide suggested that the landslide occurred repeatedly. Furthermore, Chigira et al. (2018b) reported that evidence of landslide activity in the past was observed in the Ono landslide.

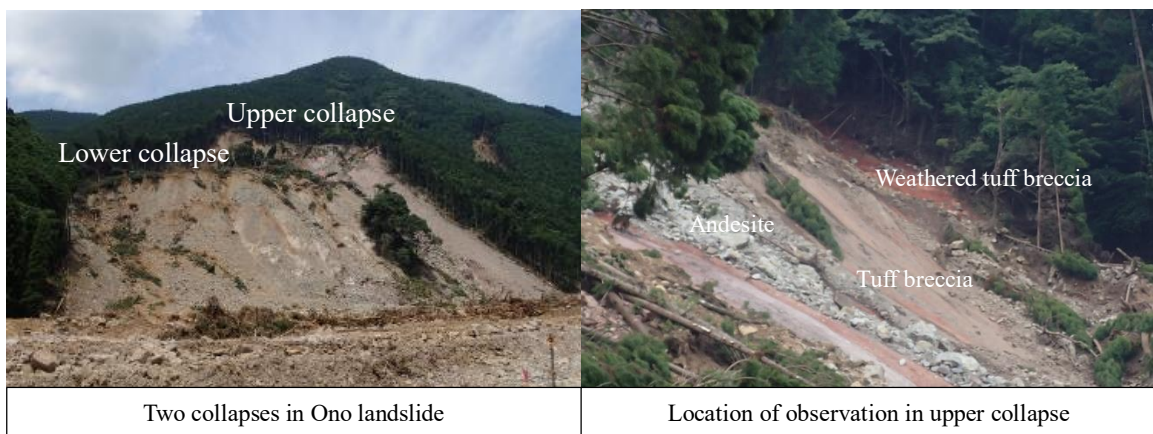
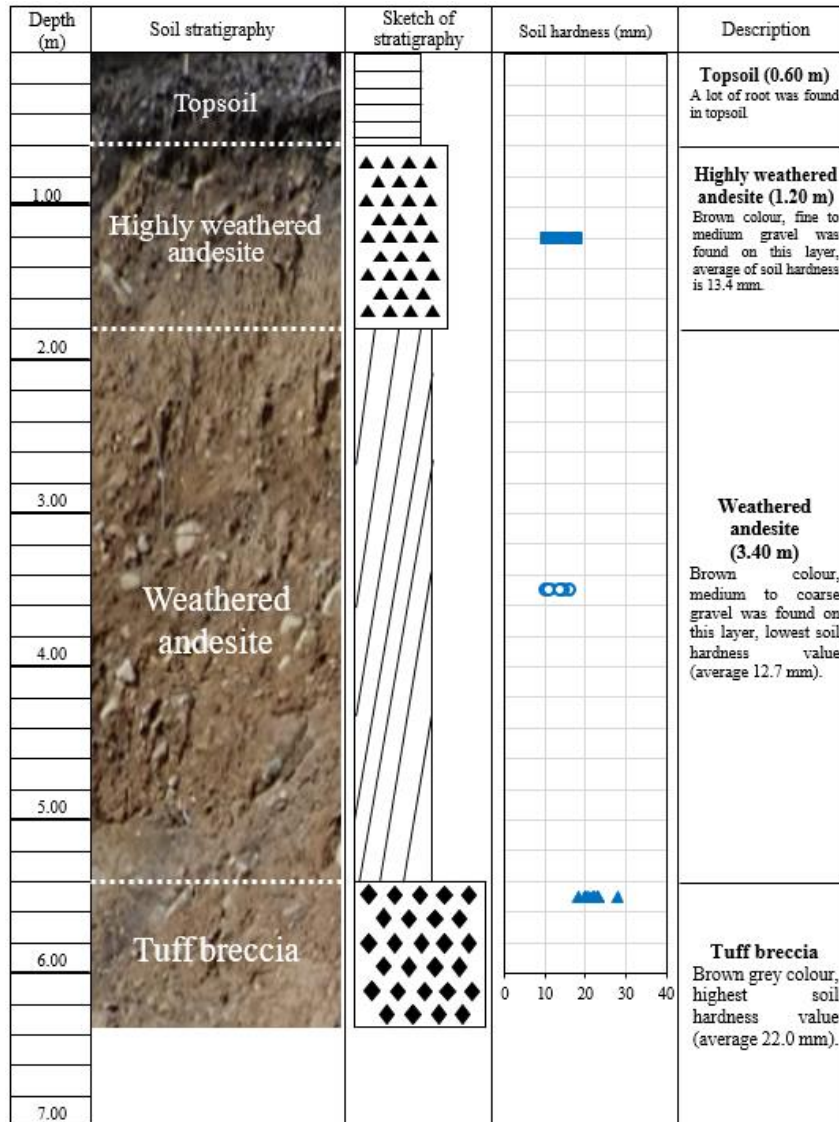


Photo 5.1 Two collapses in Ono landslide (Photo taken on July 2018)

(a) Ohtsuru



(b) Ono

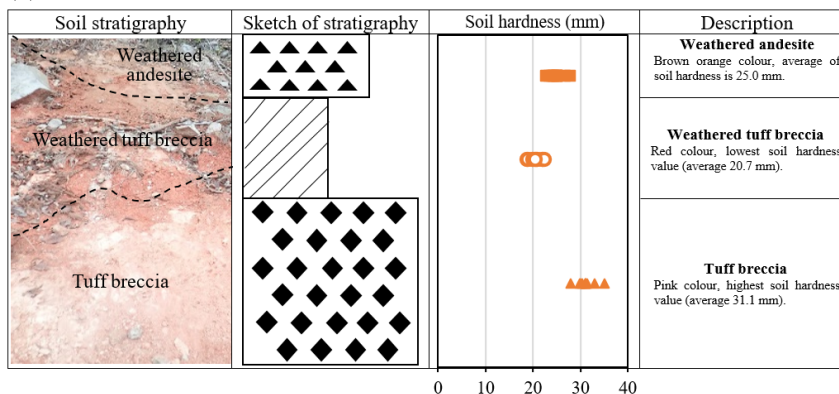


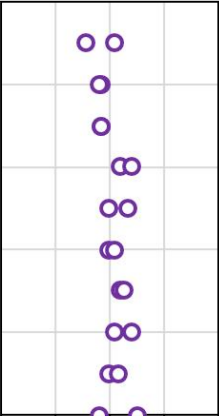
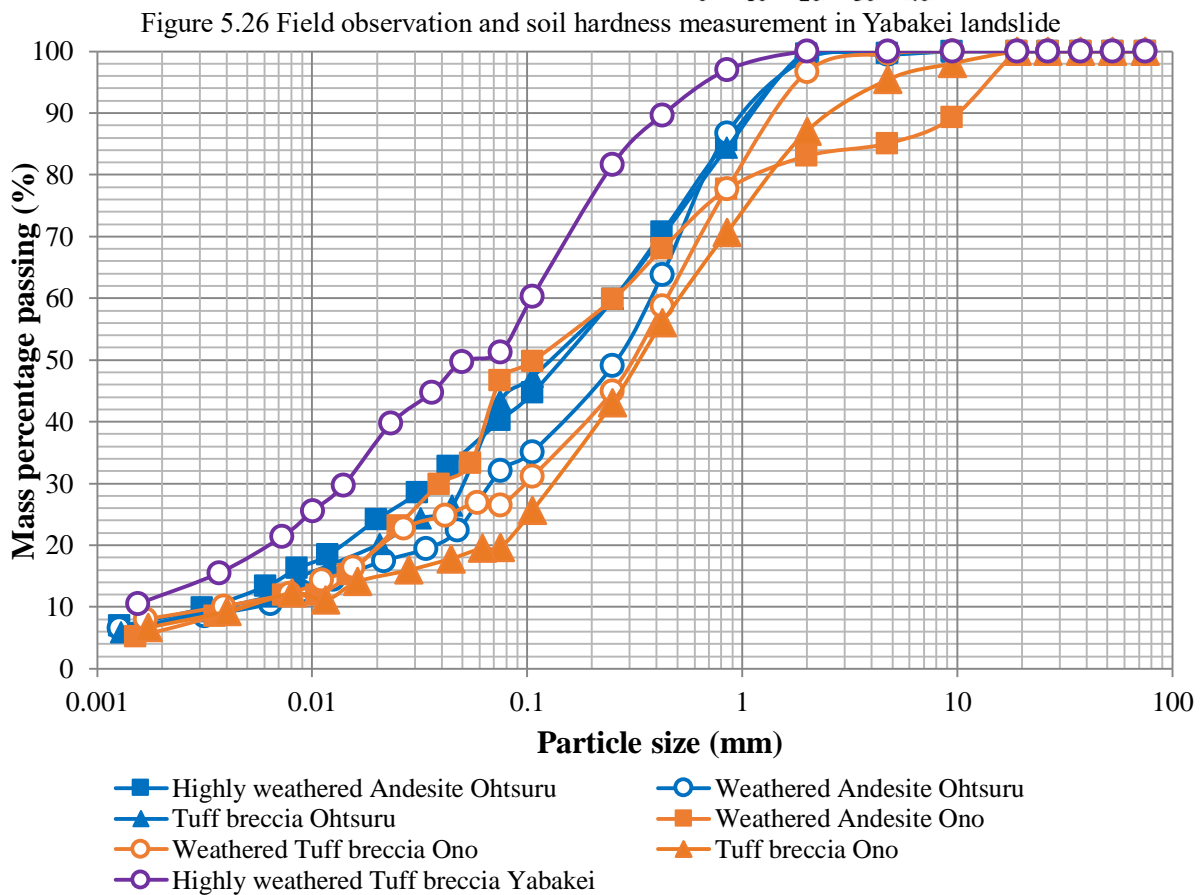


Figure 5.25 Soil stratigraphy in Ohtsuru (a) and Ono (b) landslides

Depth (m)	Soil stratigraphy	Sketch of stratigraphy	Soil hardness (mm)	Description
0.50	 <p>Highly weathered tuff breccia</p>			<p>Highly weathered tuff breccia Grey pink colour, highly weathered process was observed, average of soil hardness is 20.7 mm.</p>
1.00				



Different with other landslides, Yabakei landslide was a large-scale landslide that occurred without the occurrence of heavy rainfall or an earthquake. The smectification process was observed on the sliding layer in Yabakei landslide (Yabakei landslide investigation committee 2018). Kubota et al. (2018) reported that the major cause of the Yabakei was the weathered clay layer formed from the tuff breccia by a mineral-

groundwater reaction.

Groundwater was gushed out from approximately 20 m above sea level in the landslide, and the surrounding bedrock was significantly altered and clayey (Kubota et al. 2018). It was presumed that there is a discontinuous layer of permeability in tuff breccia layer (Kubota et al. 2018). Highly weathered tuff

breccia is observed in this study, which is the sliding layer in Yabakei landslide. Yabakei area repeatedly suffered from landslides, and the landslides always occurred in the same location at Yabakei area (Yabakei landslide investigation committee 2018).

Soil materials in Ohtsuru and Ono landslides are divided into andesite and tuff breccia materials (Fig. 5.25). An obvious difference in the soil hardness is observed between tuff breccia and the upper layer in Ohtsuru and Ono landslides. Soil hardness in Ohtsuru landslide shows that tuff breccia has the highest soil hardness value, and weathered andesite has the lowest soil hardness value. Furthermore, soil hardness in Ono landslide also shows that tuff breccia has the highest soil hardness value, and weathered tuff breccia has the lowest soil hardness value (Istiyanti and Goto 2020b). Different with Ohtsuru and Ono landslides, soil materials in Yabakei landslide is observed on highly weathered tuff breccia (Fig. 5.26) and it has a lower soil hardness value rather than tuff breccia from Ohtsuru and Ono landslides.

Characteristic of particle size distribution curve in sliding layers is not observed at the landslides and all the soil materials indicate well-graded soil material (Fig. 5.27). However, the dissimilarity of fine fraction content (less than 0.075 mm) on soil materials (Fig. 5.28) is observed. Tuff breccia from Yabakei landslide has the highest fine fraction content, however, tuff breccia from Ono landslide has the low fine fraction content.

Characteristics of soil materials on physical properties from Ohtsuru and Ono landslides are not observed (Fig. 5.29), however, highly weathered tuff breccia from

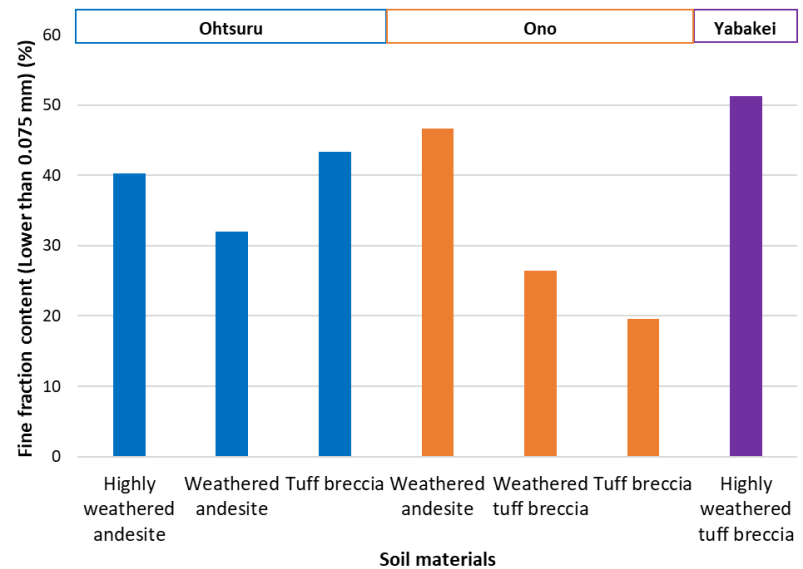


Figure 5.28 Fine fraction content (% 0.075 mm) on soil materials

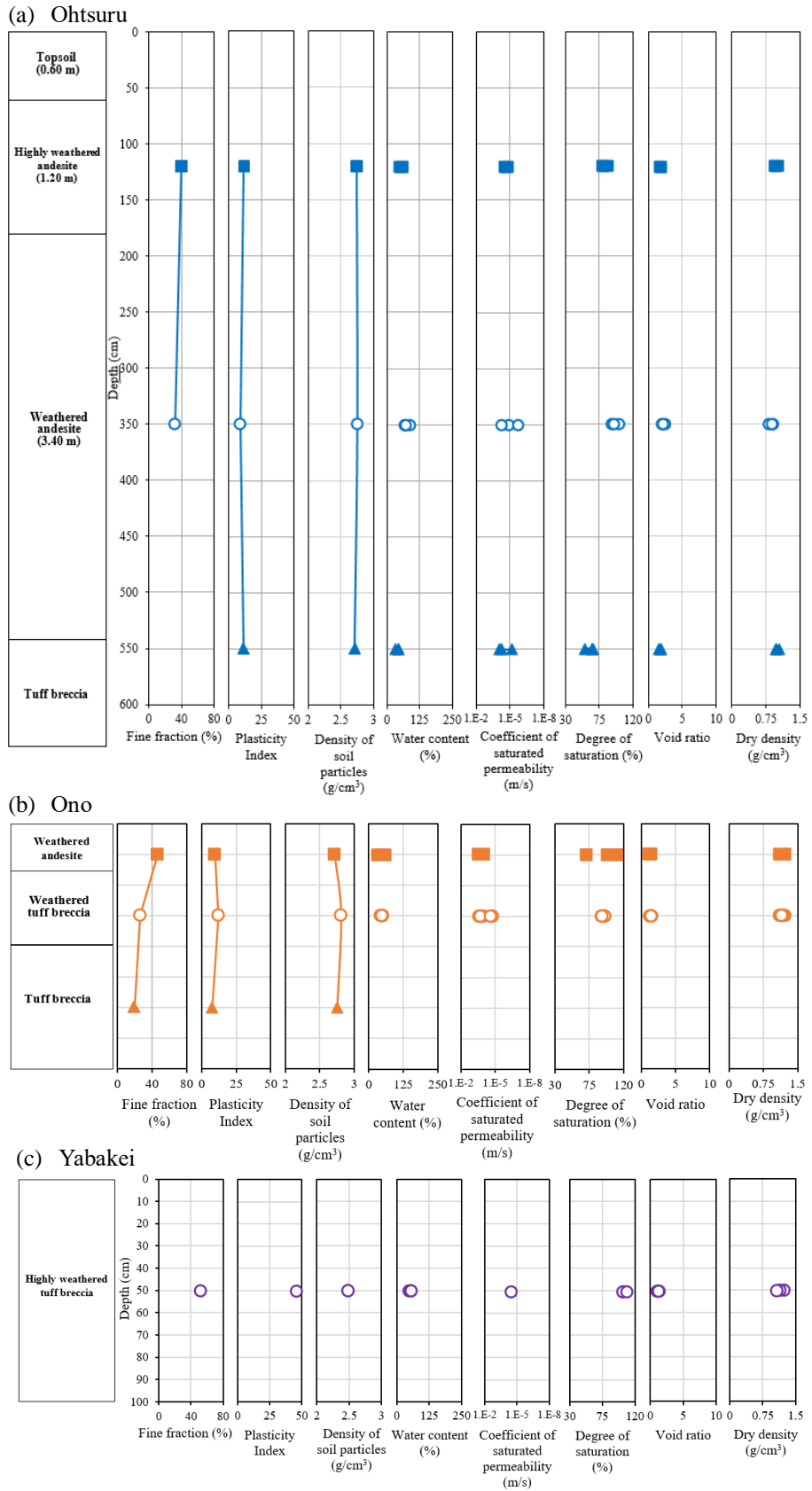


Figure 5.29 Physical properties and saturated permeability properties of soil in Ohtsuru (a), Ono (b), and Yabakei (c) landslides

Yabakei landslide has lower density of soil particles rather than other soil materials. Plotted data on plasticity chart showed that soil materials from Ohtsuru landslide are inorganic silts of medium compressibility and organic silts (Fig. 5.30). Furthermore, plotted data of Ono and Yabakei landslides are inorganic silts of high compressibility and organic clays. Generally, soil materials from Ohtsuru and Ono landslides have similar characteristics of plasticity index with different liquid limit. Highly weathered tuff breccia from Yabakei landslide has highest plasticity index and liquid limit values.

Characteristic on content of clay minerals in soil materials from Ohtsuru landslide is not observed (Fig. 5.31 (a)). Furthermore, content of clay minerals on soil materials from Ono landslide shows that weathered tuff breccia and tuff breccia layers contain halloysite minerals (Fig. 5.31 (b)), and highly weathered tuff breccia from Yabakei landslide contains of illite, chlorite, and montmorillonite (Fig. 5.32 (c)). Characteristics of sliding layer from content of clay minerals are observed on tuff breccia and andesite materials.

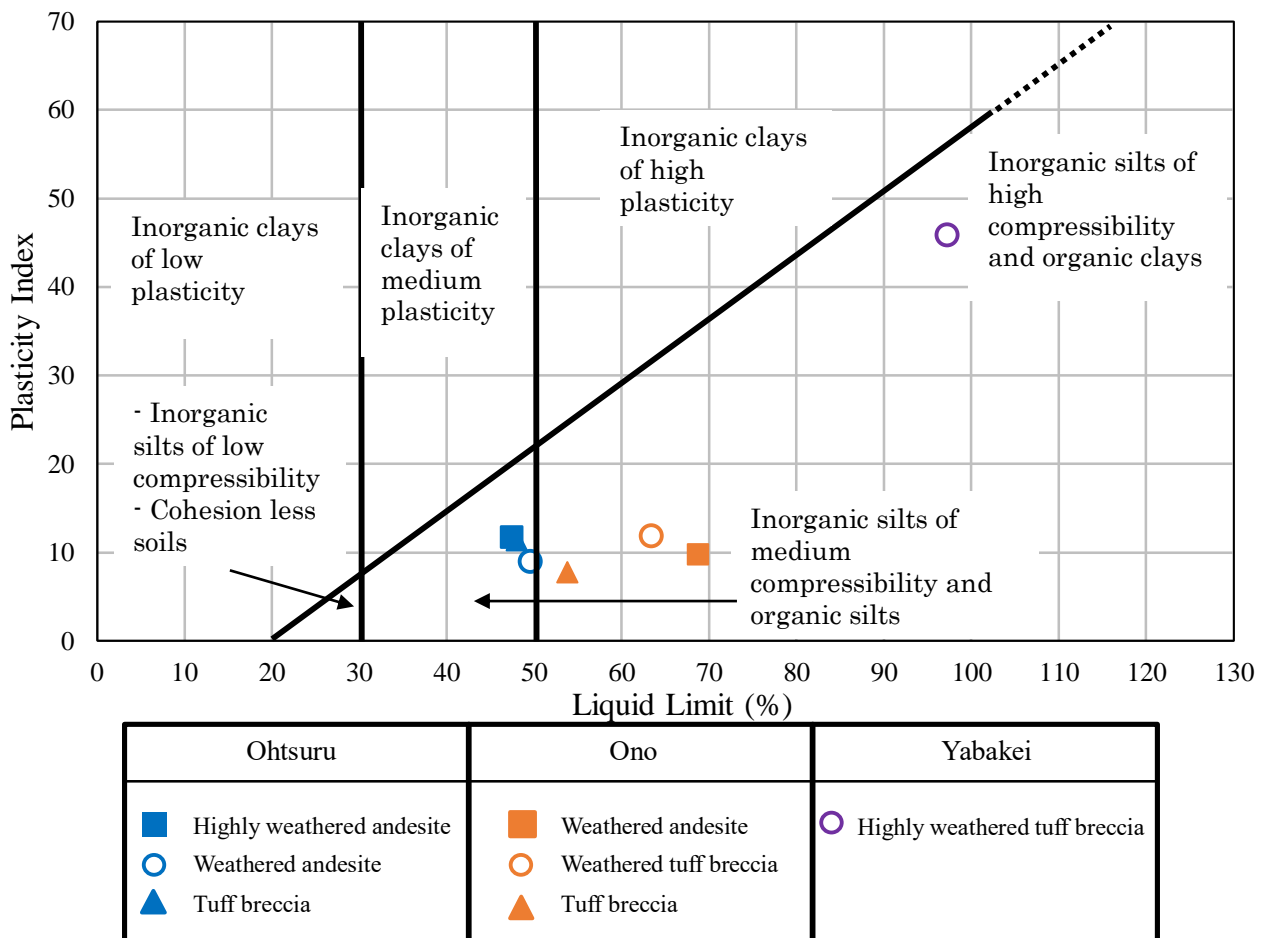
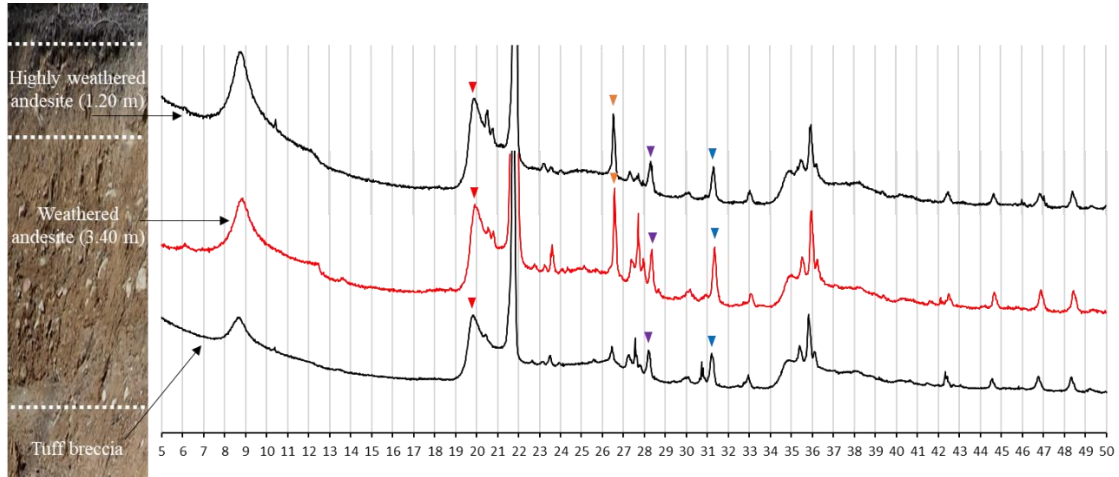


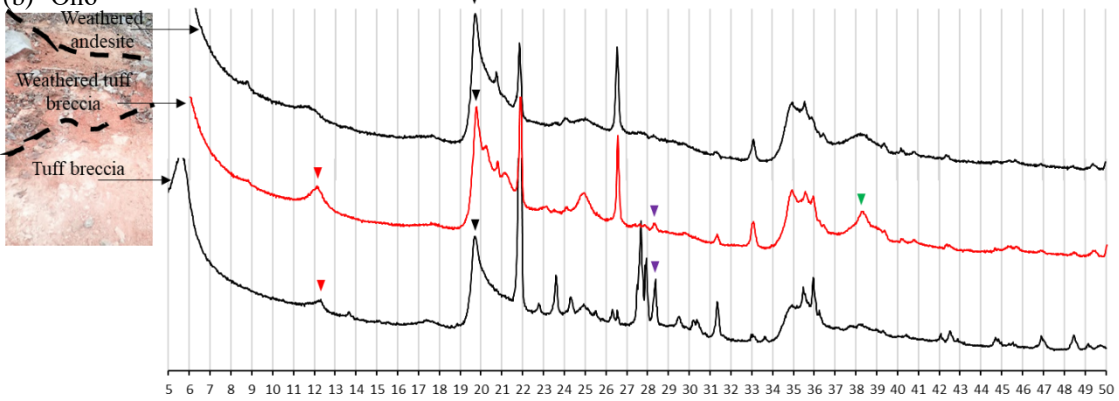
Figure 5.30 Plasticity chart shows the dissimilarity characteristics on highly weathered tuff breccia

Sliding layer from all of landslides consist of montmorillonite.

(a) Ohtsuru



(b) Ono



(c) Yabakei

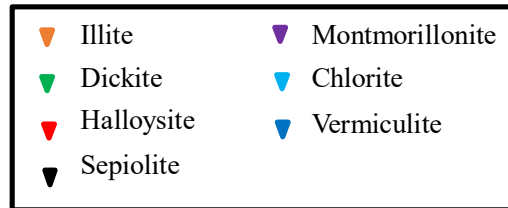
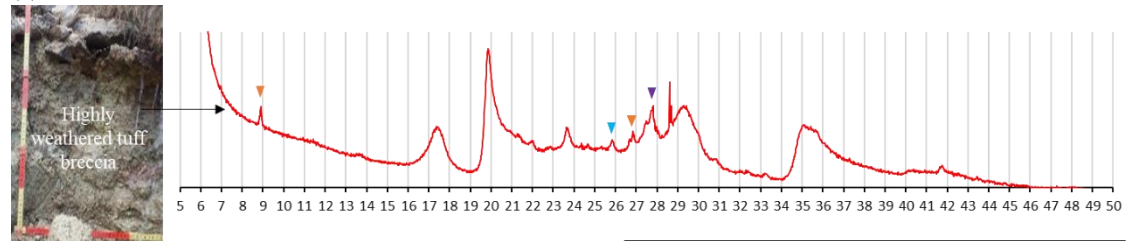


Figure 5.31 Clay minerals on tuff breccia and andesite materials in Ohtsuru (a), Ono (b), and Yabakei (c) landslides (Red lines indicated sliding layers)

Chapter 6

Soil Physical Properties in Landslides at Volcanic Area

6.1 Soil hardness measurements

6.1.1 Soil hardness measurements on tephra materials

On this study, mechanical properties were performed by soil hardness measurements on each tephra layers. Unfortunately, soil hardness was not measured on all tephra layers at some areas, such as Takadake 2 and Mizuho landslides. Shimizu and Ono (2016) reported dissimilarity in soil hardness between tephra layers at Aso volcanic mountain area, which showed an indication of sliding layer. Furthermore, this study performed the soil hardness measurements in two cases of landslide on tephra materials; heavy rainfall-induced landslides and earthquake-induced landslides. The results of soil hardness measurements showed the sliding layer on heavy rainfall-induced landslides has the low value of soil hardness, and characteristic of soil hardness on earthquake-induced landslides is not observed (Fig. 6.1).

In Takadake landslides which are heavy rainfall-induced landslides, dissimilarity in soil hardness is observed between the kuroboku and scoria layers. The soil hardness of tephra layers in Takadake 1 shows N2 scoria has the highest soil hardness value (average = 18.5 mm) and N3-4 kuroboku L has the lowest soil hardness value (average 14.5 mm). The soil hardness value in Takadake 2 also shows the OJS scoria has the highest soil hardness value (average 23.9 mm) and N3-4 kuroboku L has the lowest soil hardness value (average 18.1 mm). Soil hardness value in Takadake landslides showed the dissimilarity between scoria and kuroboku layers, and the dissimilarity between OJS scoria and N3-4 kuroboku L was observed in both areas. Moreover, N3-4 kuroboku L has the lowest soil hardness value in both areas (Istiyanti et al. 2020a).

Izu Oshima landslide is also heavy rainfall-induced landslide, however, soil hardness measurement at Izu Oshima landslide was not measured exactly on the landslide area but was measured at the location nearby the landslide. Miyabuchi et al. (2015) reported the sliding layer in Izu Oshima landslides occur at two horizons: the boundary between the Y1 tephra and the underlying loess and between Y4 tephra and the underlying loess, and Y1.0 and Y4.0 on this study have a low soil hardness value. The soil hardness

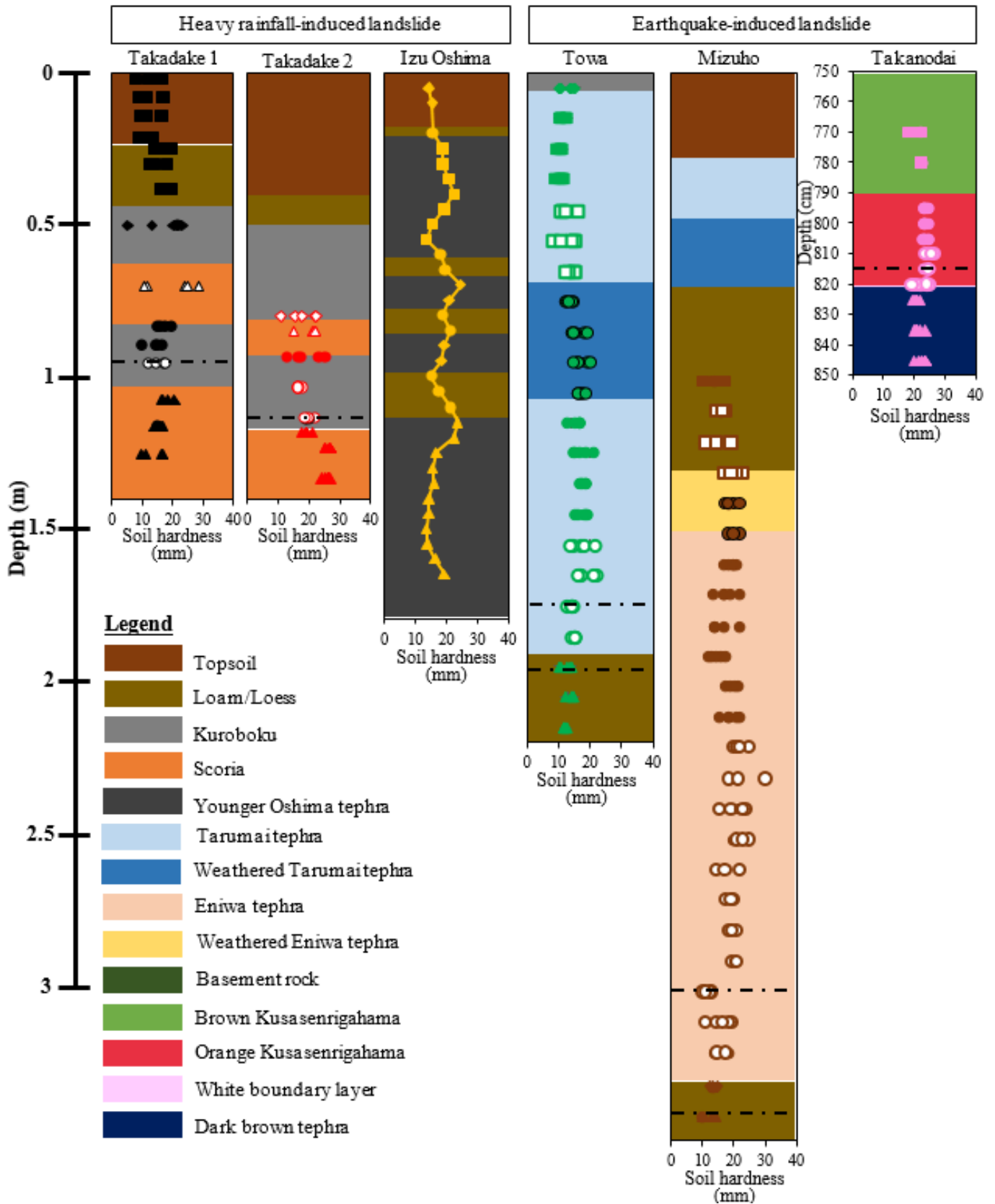


Figure 6.1 Stratigraphic and soil hardness profiles at landslide areas which consisting of tephra materials; black dotted lines indicated location of sliding layer by field observation

of tephra layers in Izu Oshima shows Y2.0 has the highest soil hardness value (average = 22.63) and Y4.0 has the lowest soil hardness value (average = 16.84 mm). Furthermore, the dissimilarity between Y1.0 tephra and the under loess layer was observed on this study, Y1.0 tephra has the lower soil hardness value rather than the underlying loess layer.

Different with soil hardness results on heavy rainfall-induced landslides, characteristic on soil hardness at sliding layer in earthquake-induced landslides is not observed. The soil hardness of tephra layers in Towa landslide at Iburi Region shows Ta-d L has the highest soil hardness value (average = 17.9 mm) and Ta-c has the lowest soil hardness value (average = 11.4 mm). Soil hardness value in Mizuho landslide shows weathered En-a has the highest soil hardness value (average = 19.4 mm) and Loam (Spfa-1) has the lowest soil hardness value (average = 11.75 mm). Furthermore, an obvious dissimilarity is not observed in Takanodai landslide at Aso volcanic mountain area. The difference of average soil hardness value on each tephra layer is not more than 2 mm; orange Kusasenrigahama has the highest soil hardness value (average = 23.8 mm) and dark brown tephra has the lowest soil hardness value (average = 21.5 mm). However, sliding layer on earthquake-induced landslides has the highest value of soil hardness.

Therefore, the results of soil hardness measurements showed the sliding layer on heavy rainfall-induced landslides has the dissimilarity between the under layer, it has the lower soil hardness value rather than the under layer. Furthermore, characteristic of sliding layer on earthquake-induced landslides is not observed.

6.1.2 Soil hardness measurements on tuff breccia and andesite materials

Fig. 6.2 and 6.3 show the soil hardness measurements on tuff breccia and andesite materials. An obvious dissimilarity in the soil hardness is observed between tuff breccia and the upper layer in the Ohtsuru and Ono landslides. The soil hardness in the Ohtsuru landslide shows that the tuff breccia has the highest soil hardness value, and the weathered andesite has the lowest soil hardness value. Furthermore, the soil hardness in Ono landslide also shows that tuff breccia has the highest soil hardness value, and the weathered tuff breccia has the lowest soil hardness value (Istiyanti and Goto 2020b).

The soil hardness value in the Yabakei landslide was measured 1 m from the surface on the highly weathered tuff breccia layer. We could not observe layering of soil in Yabakei landslide. Moreover, highly weathered tuff breccia from Yabakei landslide has a

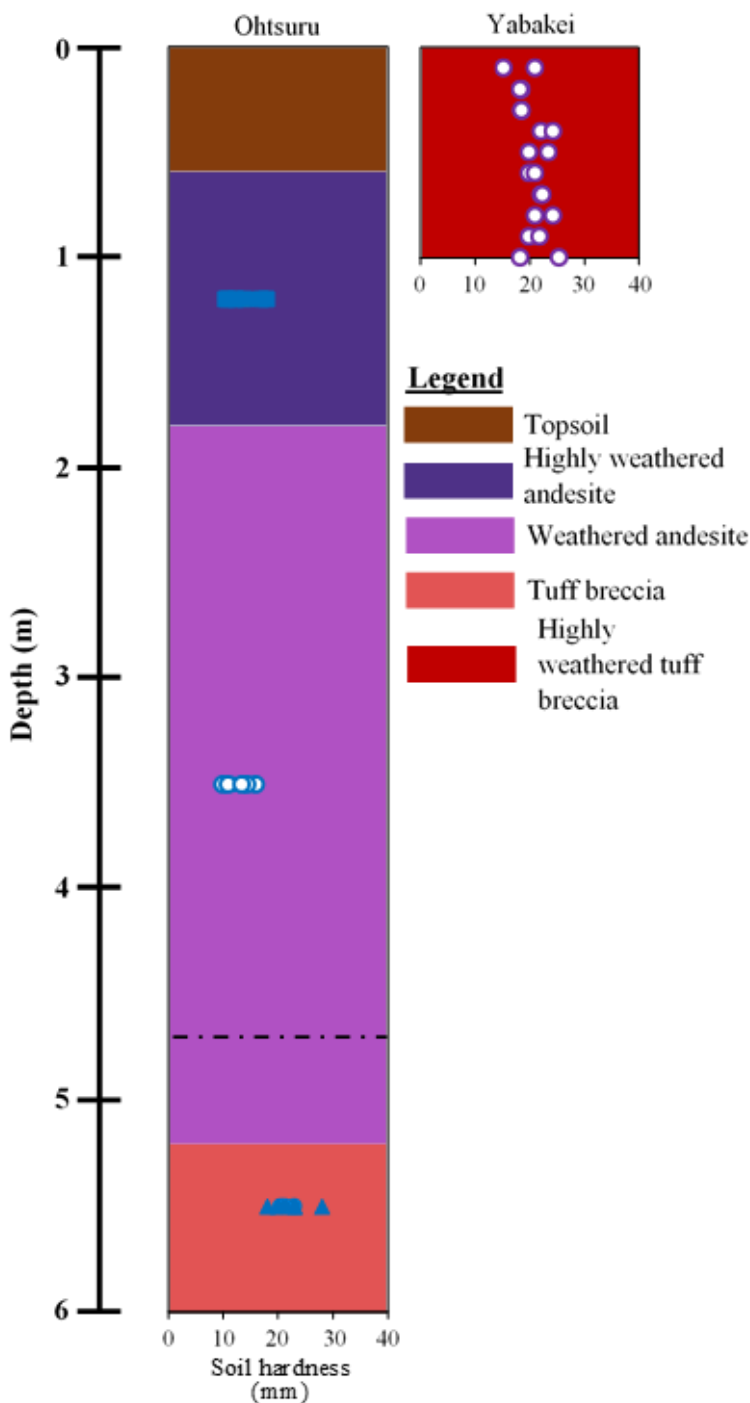


Figure 6.2 Stratigraphic and soil hardness profiles at Ohtsuru and Yabakei landslides which consisting of tuff breccia and andesite; black dotted lines indicated location of sliding layer by field observation

lower soil hardness value rather than tuff breccia from Ohtsuru and Ono landslides because the highly weathering process.

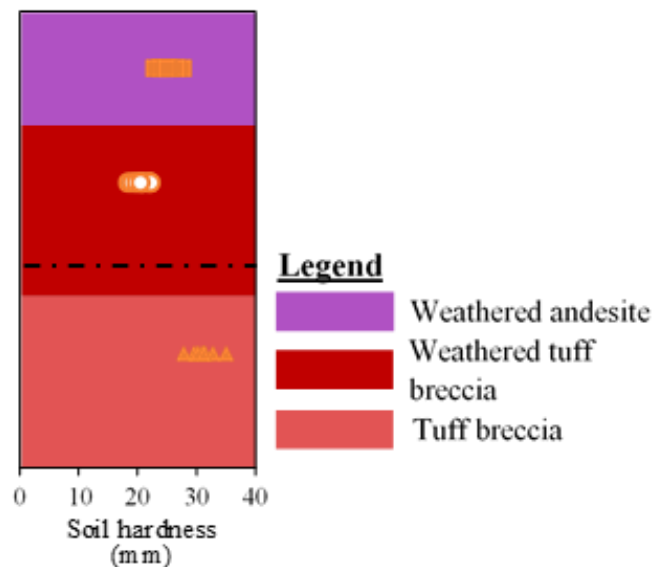


Figure 6.3 Stratigraphic and soil hardness profiles at Ono landslide which consisting of tuff breccia and andesite; black dotted lines indicated location of sliding layer by field observation

6.2 Plasticity index

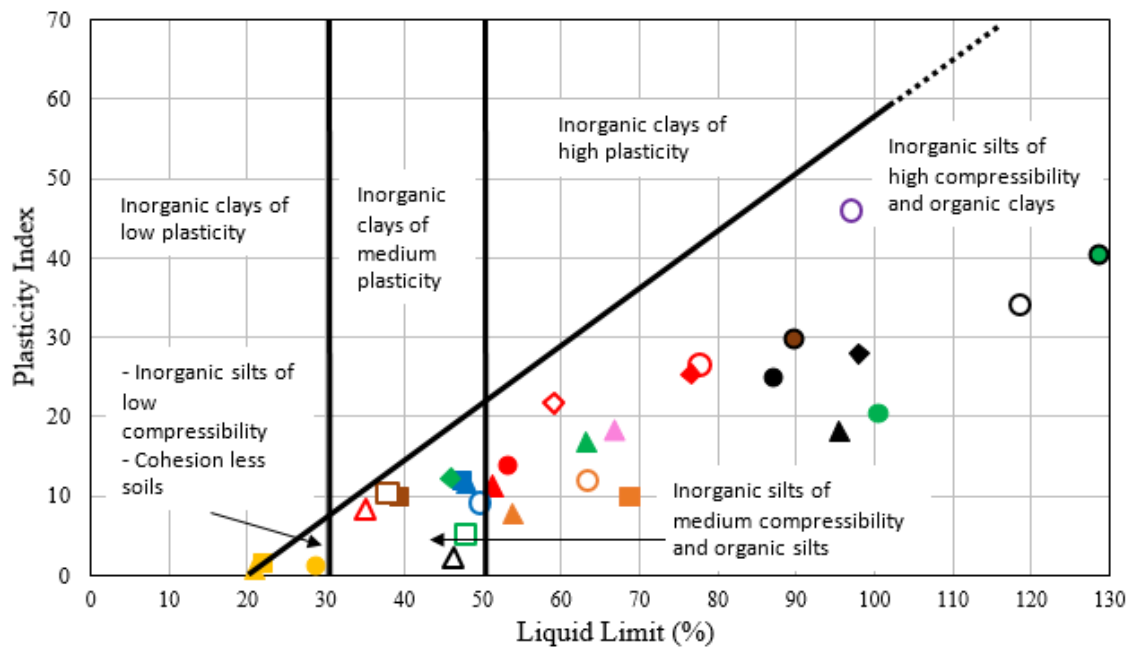
Fig. 6.4 shows the plasticity chart for classifying the soil materials using the liquid limit and plastic limit test results, which are denoted by different colors, and sliding layers on each area are denoted by white circles with different colored outlines.

Soil materials on this study are

divided into four types; inorganic silts of low compressibility and cohesion less soils, inorganic silts of medium compressibility and organic silts, inorganic silts of high compressibility and organic clays, and non-plastic soils.

6.2.1 Plasticity index on tephra materials

The plotted data on plasticity chart in tephra materials shows that tephra materials are divided into four groups and it were related to the period of tephra materials (Fig. 6.5). Younger group Oshima (AD 1400-1800) with the age younger than 0.5 ka years ago has lowest plasticity index and liquid limit values. Tephra materials with the age between 1.5 to 3 ka years ago, such as N2 scoria from Takadake landslides and Ta-c from Towa landslide, have the higher plasticity index and liquid limit values. Tephra materials with



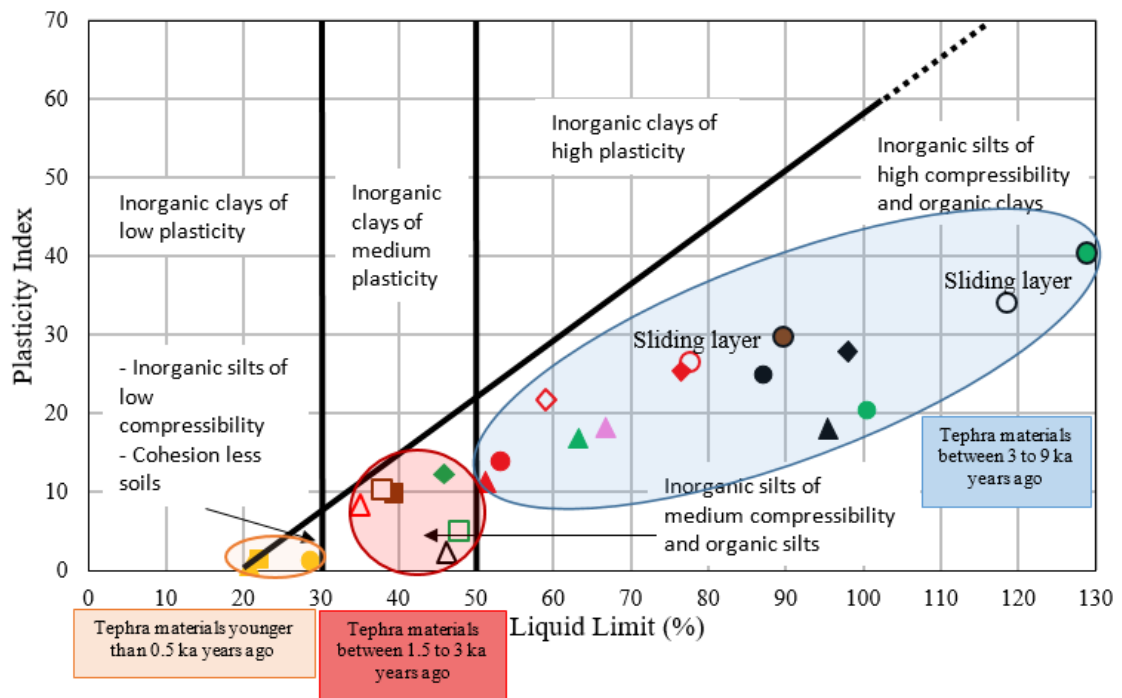
Legend

Tephra materials						
Heavy rainfall-induced landslides			Earthquake-induced landslides			
Takadake 1	Takadake 2	Izu Oshima	Takanodai	Towa	Mizuho	
◆ N1 kuroboku △ N2 scoria ● N3-4 kuroboku U ○ N3-4 kuroboku L ▲ OJS scoria	◆ N1 kuroboku ◇ N2 kuroboku △ N2 scoria ● N3-4 kuroboku U ○ N3-4 kuroboku L ▲ OJS scoria	■ Y1.0 ● Loess ▲ Y4.0	Orange ● Kusanenrigahama (NP) ▲ Dark brown tephra	◆ Kuroboku ■ Ta-c U (NP) □ Ta-c L ● Weathered Ta-d	● Ta-d U ○ Ta-d L (NP) ▲ Loam ● Weathered Ta-d	● Weathered Ta-d ■ Loam (En-a) U □ Loam (En-a) L ○ En-a (NP) ▲ Loam (Spfa-1) (NP)
Tuff breccia and andesite materials						
Ohtsuru		Ono		Yabakei		
■ Highly weathered andesite ○ Weathered andesite ▲ Tuff breccia	■ Weathered andesite ○ Weathered tuff breccia ▲ Tuff breccia	○ Highly weathered tuff breccia				

Figure 6.4 Plotted data of soil materials on plasticity chart

the age between 3 to 9 ka years ago, such as OJS scoria from Takadake landslides and Ta-d from Towa and Mizuho landslides, have the highest plasticity index and liquid limit values on this study. Furthermore, the oldest tephra materials, such as Kusasenrigahama (30 ka) from Takanodai landslide and En-a (20 ka) from Mizuho landslide, are non-plastic soil. This study also found the different results on dark brown tephra (30 ka) from Takanodai landslide which belongs to the highest plasticity index and liquid limit group.

Furthermore, each tephra group based on the eruption period also represent characteristics of soil. Fig. 6.5 also shows that tephra materials younger than 0.5 ka years ago are inorganic silts of low compressibility and have less cohesion, tephra materials between 1.5 to 3 ka years ago are inorganic silts of medium compressibility and organic silts, and tephra materials between 3 to 9 ka years ago are inorganic silts of high compressibility and organic clays.



Legend

Heavy rainfall-induced landslides			Earthquake-induced landslides		
Takadake 1	Takadake 2	Izu Oshima	Takanodai	Towa	Mizuho
◆ N1 kuroboku	◆ N1 kuroboku	■ Y1.0	Orange	◆ Kuroboku	● Weathered Ta-d
△ N2 scoria	◇ N2 kuroboku	● Loess	● Kusasenrigahama (NP)	■ Ta-c U (NP)	■ Loam (En-a) U
● N3-4 kuroboku U	△ N2 scoria	● Y4.0	● Dark brown tephra	□ Ta-c L	□ Loam (En-a) L
○ N3-4 kuroboku L	● N3-4 kuroboku U			● Ta-d U	○ En-a (NP)
▲ OJS scoria	○ N3-4 kuroboku L			▲ Loam	▲ Loam (Spfa-1) (NP)
	▲ OJS scoria			● Weathered Ta-d	

Figure 6.5 Plotted data of tephra materials on plasticity chart

This study observed the different characteristics of plasticity index on sliding layers in tephra materials at heavy rainfall-induced landslides and at earthquake-induced landslides. Characteristics of plasticity index on sliding layers in tephra materials at heavy rainfall-induced landslides have a high plasticity index and liquid limit values. Sliding layers in Takadake landslides which are heavy rainfall-induced landslides, have the highest values of plasticity index and liquid limit. However, characteristics of plasticity index on sliding layers in tephra materials at earthquake-induced landslides are non-plastic soils; sliding layers in Takanodai, Towa, and Mizuho landslides are non-plastic soils.

6.2.2 Plasticity index on tuff breccia and andesite materials

The plotted data on plasticity chart in tuff breccia and andesite materials shows that the materials are divided into two groups (Fig. 6.6). The soil materials from Ohtsuru

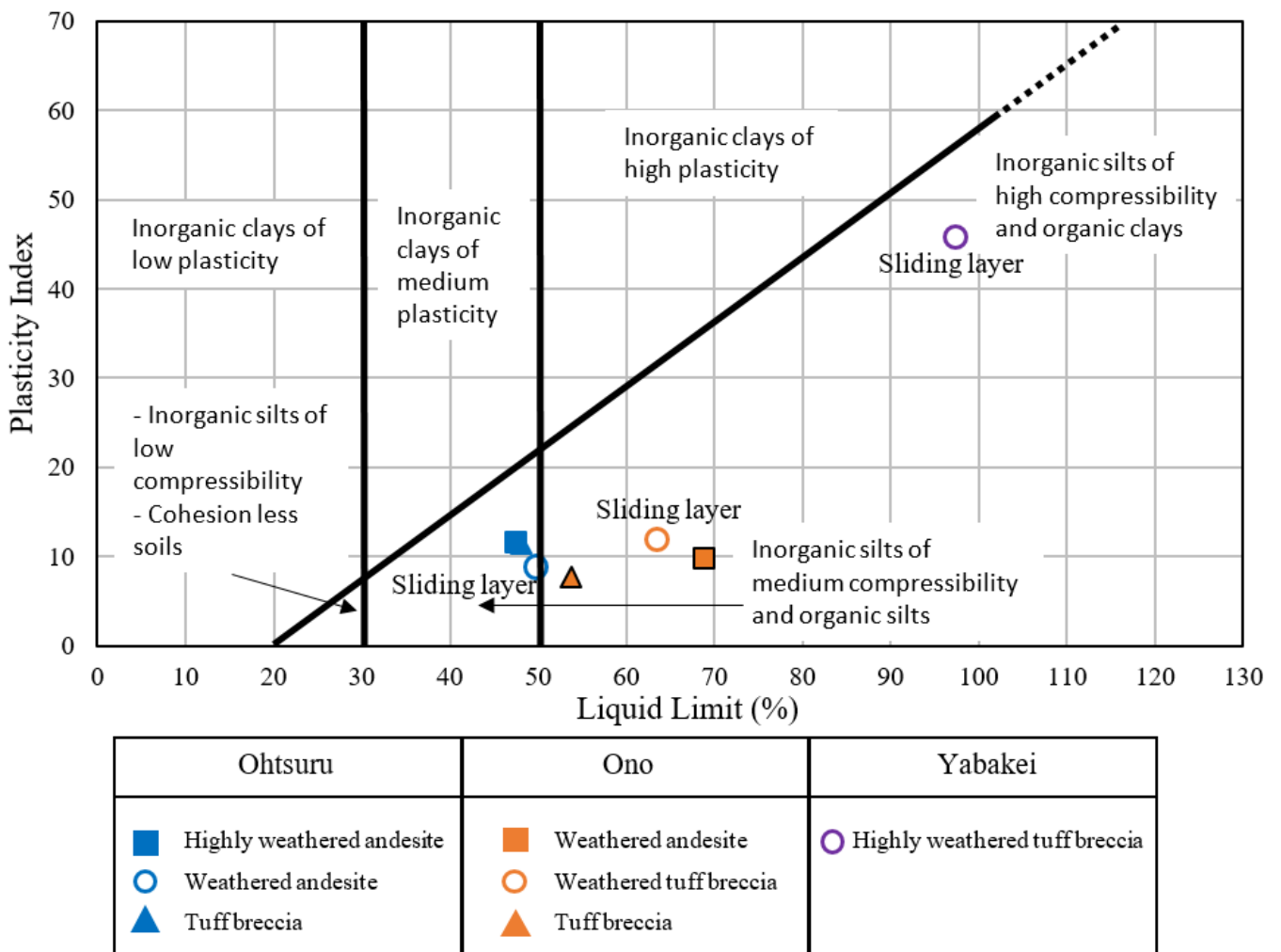


Figure 6.6 Plotted data of tuff breccia and andesite materials on plasticity chart

landslide are inorganic silts of medium compressibility and organic silts, and the plotted data of the Ono and Yabakei landslides are inorganic silts of high compressibility and organic clays. The soil materials from Ohtsuru and Ono landslides have lower plasticity index, however, highly weathered from Yabakei landslide has higher plasticity index. Highly weathered in tuff breccia at Yabakei landslide could be had the relation with the weathering process. Plasticity index on tuff breccia and andesite materials in this study observed that weathering process has a relation with plasticity index, and weathering process could make the plasticity index value increased.

Different with characteristics of plasticity index on sliding layers in tephra materials, characteristics of plasticity index on sliding layers in tuff breccia and andesite materials are not observed. Characteristics of plasticity index on sliding layers are different in each area. Sliding layer in Ohtsuru landslide has higher liquid limit but lower plasticity index values rather than other soil layers, and sliding layer in Ono landslide also has higher plasticity index but lower liquid limit values rather than other soil layers. Furthermore, layering of soil materials were not found in Yabakei landslide although highly weathered tuff breccia from Yabakei landslide has highest plasticity index and liquid limit values rather than soil materials from Ohtsuru and Ono landslides.

6.3 Particle size distribution

The particle size distribution curve (Fig. 6.7) shows two types of soil materials; soil materials which indicated a well-graded soil materials and soil materials which indicated a poor-graded soil material. Type of soil on particle size distribution was observed by coefficient of uniformity (U_c) and coefficient of curvature (U_c'); soil materials which have a value of $U_c \geq 10$ and U_c' between 1~3 are included into well-graded soil materials (JGS, 2015).

6.3.1 Particle size distribution on tephra materials

Particle size distribution on tephra materials were different on each area. In Takadake landslides and Izu Oshima landslide, all tephra materials are poor-graded soil materials, furthermore, all tephra materials in Takanodai landslide are well-graded soil materials. Different with those areas, tephra materials in Towa and Mizuho landslides consist of two types of tephra materials; tephra materials which indicated well-graded soil materials and tephra materials which indicated poor-graded soil materials. Tephra materials which have a well-graded soil material are kuroboku, Ta-c L, and Loam layers from Towa landslide;

and Loam (En-a) U, Loam (En-a) L, and Loam (Spfa-1) layers from Mizuho landslide. Furthermore, tephra materials which have a poor-graded soil material are Ta-c U, weathered Ta-d, Ta-d U, and Ta-d L layers from Towa landslide; and weathered Ta-d, En-a U, and En-a L layers from Mizuho landslide.

This study observed characteristics of particle size distribution on sliding layers in tephra materials at heavy rainfall-induced landslides and at earthquake-induced landslides are poor-graded soil materials. However, the sliding layer from Takanodai landslide is well-graded soil material. Holtz and Kovacs (1981) reported that poor-graded soils are more susceptible to soil liquefaction than well graded soils. Therefore, poor-graded on tephra materials could be considered as one of the reason on sliding layer which easily to

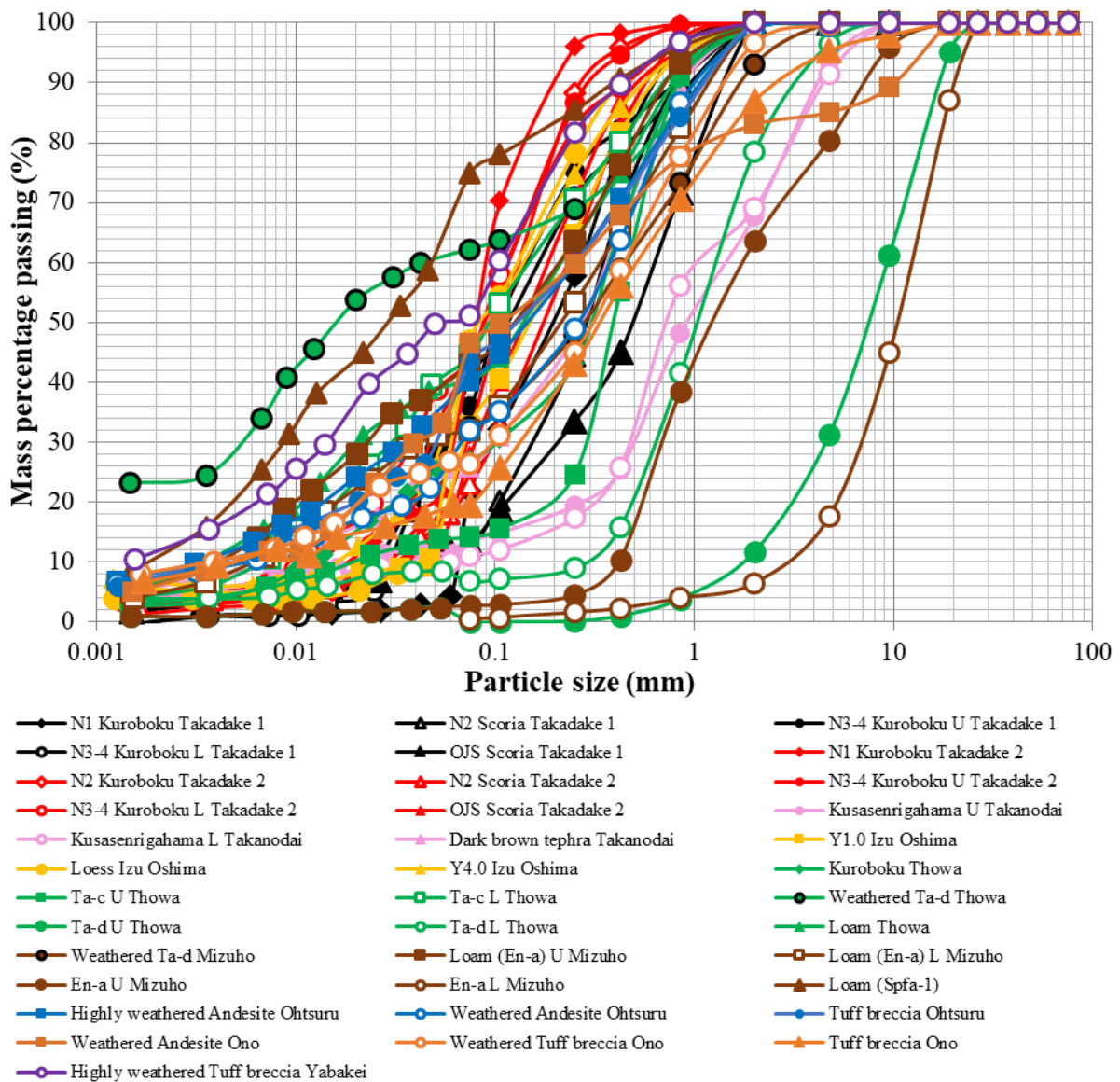


Figure 6.7 Particle size distribution curves of soil materials

collapse.

6.3.2 Particle size distribution on tuff breccia and andesite materials

Particle size distribution on tuff breccia and andesite materials in all areas shows no dissimilarities among the soil materials, and all the soil materials indicated well-graded soil materials. Furthermore, the particle size distribution curve on tuff breccia from Yabakei landslide has a high fine fraction content caused by the highly weathering process on that soil material. Different with characteristics of particle size distribution on sliding layers in tephra materials, characteristics of particle size distribution on sliding layers in tuff breccia and andesite materials are well-graded soil materials.

6.4 Activity of soil materials

Bell and Maud (1995) observed the relation between plasticity index and clay content ($\% > 0.002 \text{ mm}$) to estimate of the degree of expansiveness of some clay soils from Natal, South Africa (Fig. 6.8). This study also observed the relation between plasticity index and clay content ($\% > 0.002 \text{ mm}$) in soil materials to show the activity in soil materials. The range of activity value in Bell and Maud (1995) was from 0.5 to 2.0; however, because

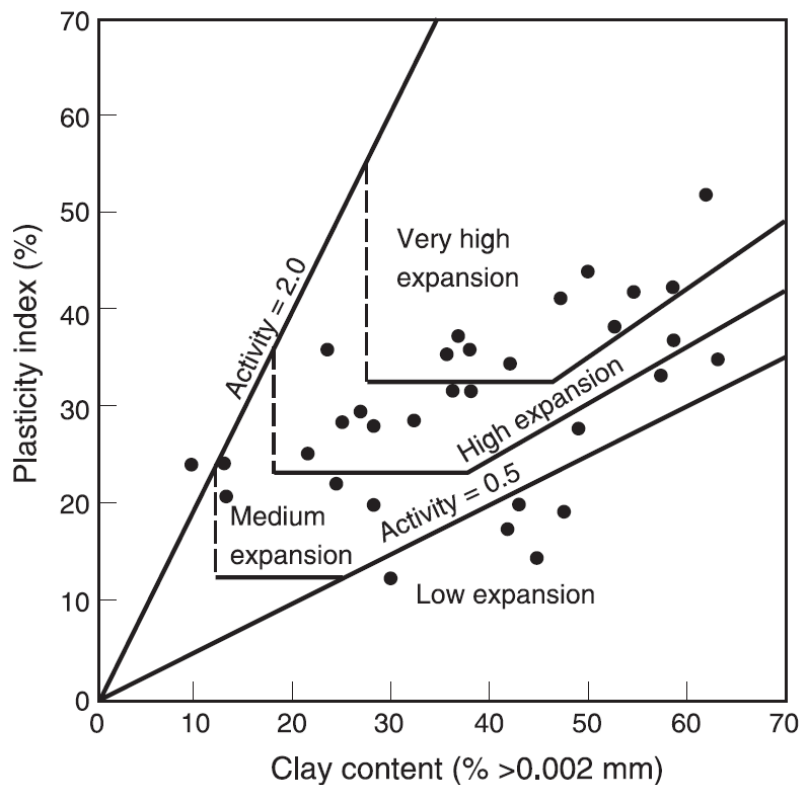
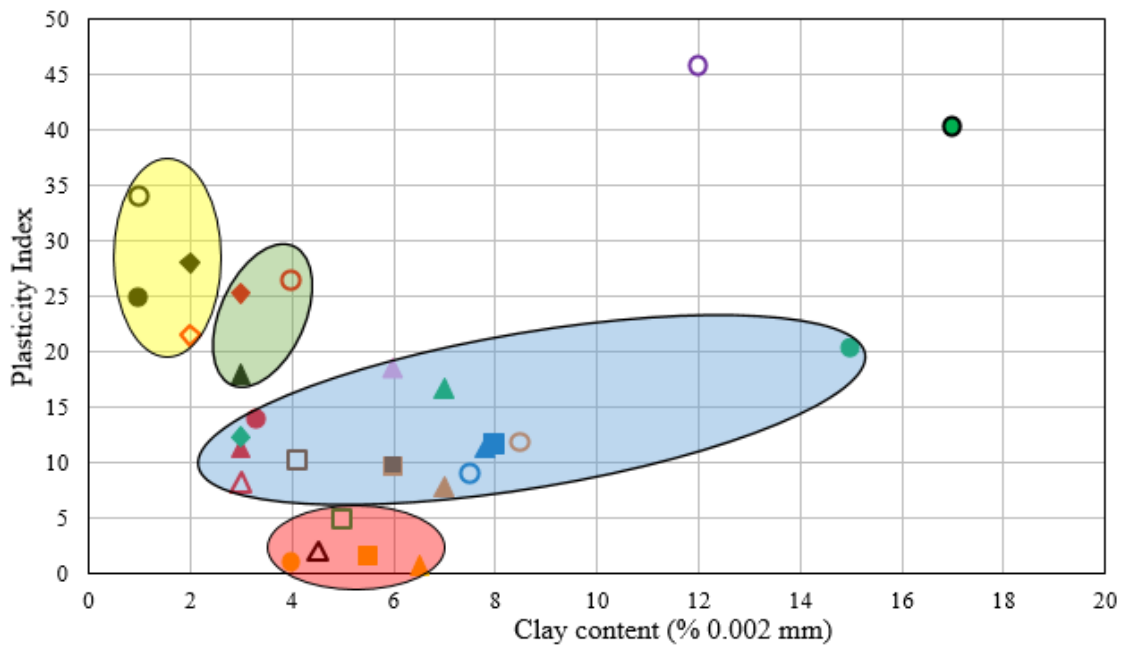


Figure 6.8 Estimate the degree of expansiveness of some clay soils from Natal, South Africa using the activity chart (Bell and Maud 1995)

the content of 0.002 mm in soil materials is not as high as clay soils, the range of activity value in soil materials at this study is 0 to 35.

The content of 0.002 mm in soil materials on this study is not high, furthermore, the content of 0.075 mm is high. This study observed the relation between plasticity index and clay content (% 0.002 mm) (Fig. 6.9), and the relation between plasticity index and fine fraction content (% 0.075 mm) (Fig. 6.10) to show the active value on soil materials. The active value was divided into four groups; 0-1 is *inactive*, 1-5 is *normal activity*, 6-

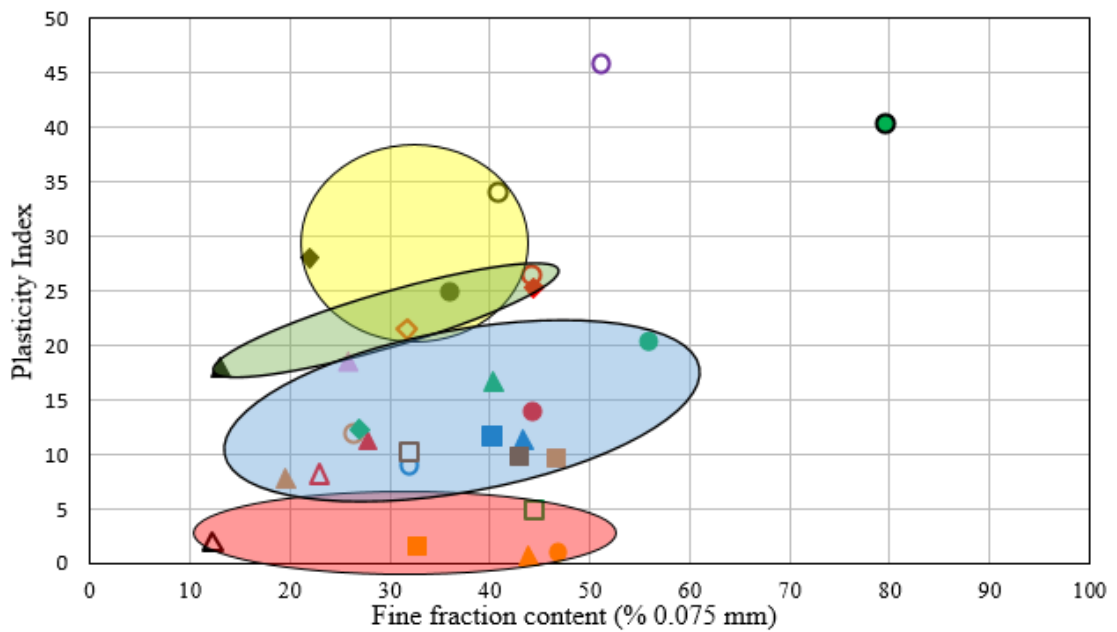


Legend

Tephra materials						
Heavy rainfall-induced landslides			Earthquake-induced landslides			
Takadake 1	Takadake 2	Izu Oshima	Takanodai	Towa	Mizuho	
◆ N1 kuroboku △ N2 scoria ● N3-4 kuroboku U ○ N3-4 kuroboku L ▲ OJS scoria	◆ N1 kuroboku ◇ N2 kuroboku △ N2 scoria ● N3-4 kuroboku U ○ N3-4 kuroboku L ▲ OJS scoria	■ Y1.0 ● Loess ▲ Y4.0	Orange ● Kusanenrigahama (NP) ▲ Dark brown tephra	◆ Kuroboku ■ Ta-c U (NP) □ Ta-c L ● Weathered Ta-d	● Ta-d U ○ Ta-d L (NP) ▲ Loam ● Weathered Ta-d	● Weathered Ta-d ■ Loam (En-a) U □ Loam (En-a) L ○ En-a (NP) ▲ Loam (Spfa-1) (NP)
Tuff breccia and andesite materials				<ul style="list-style-type: none"> ● Very active ● Active ● Normal activity ● Inactive 		
Ohtsuru	Ono	Yabakei				
■ Highly weathered andesite ○ Weathered andesite ▲ Tuff breccia	■ Weathered andesite ○ Weathered tuff breccia ▲ Tuff breccia	○ Highly weathered tuff breccia				

Figure 6.9 Relation between plasticity index and clay content (% 0.002 mm) show the active value on soil materials

10 is *active*, and > 10 is *very active*. The sliding layers on this study have different type of activity soil; Sliding layer which located at Takadake 1 landslide is *very active* soil, at Takadake 2 landslide is *active* soil, and at other landslides are *normal activity*. Furthermore, highly weathered tuff breccia from Yabakei landslide and weathered Ta-d from Towa landslide are plotted in the outside of grouping area although those are *normal activity* soils. Weathering process on highly weathered tuff breccia from Yabakei landslide and weathered Ta-d from Towa landslide caused the clay content (0.002 mm) on that



Legend

Tephra materials						
Heavy rainfall-induced landslides			Earthquake-induced landslides			
Takadake 1	Takadake 2	Izu Oshima	Takanodai	Towa	Mizuho	
◆ N1 kuroboku ▲ N2 scoria ● N3-4 kuroboku U ○ N3-4 kuroboku L ▲ OJS scoria	◆ N1 kuroboku ◇ N2 kuroboku ▲ N2 scoria ● N3-4 kuroboku U ○ N3-4 kuroboku L ▲ OJS scoria	■ Y1.0 ● Loess ▲ Y4.0	Orange ● Kusasenrigahama (NP) ▲ Dark brown tephra	◆ Kuroboku ■ Ta-c U (NP) □ Ta-c L ● Weathered Ta-d	● Ta-d U ○ Ta-d L (NP) ▲ Loam ● Weathered Ta-d	● Weathered Ta-d ■ Loam (En-a) U □ Loam (En-a) L ○ En-a (NP) ▲ Loam (Spfa-1) (NP)
Tuff breccia and andesite materials					● Very active ● Active ● Normal activity ● Inactive	
Ohtsuru	Ono	Yabakei				
■ Highly weathered andesite ○ Weathered andesite ▲ Tuff breccia	■ Weathered andesite ○ Weathered tuff breccia ▲ Tuff breccia	○ Highly weathered tuff breccia				

Figure 6.10 Relation between plasticity index and fine fraction content (% 0.075 mm) show the active value on soil materials

layers are higher rather than other soil materials, and it caused the layers are not plotted in the group of *normal activity* soils.

Activity values showed that tephra from Takadake 1 generally consist of *very active* and *active* tephra materials, however, OJS scoria is inactive tephra material. Tephra from Takadake 2 consist of *normal* to *active* tephra materials, and tephra from Izu Oshima consist of *inactive* tephra materials. Furthermore, activity values showed the sliding layer on heavy rainfall-induced landslides has *active* tephra materials.

Activity values on tephra materials from earthquake-induced landslides showed that tephra from Towa consist of *inactive* to *normal activity* tephra materials, and tephra from Mizuho consist of *normal activity* tephra materials. Tephra from Takanodai consist of *normal activity* tephra materials. Since the sliding layers on earthquake-induced landslides are non-plastic materials, activity values are not observed. Moreover, tuff breccia and andesite materials are *normal activity* soil.

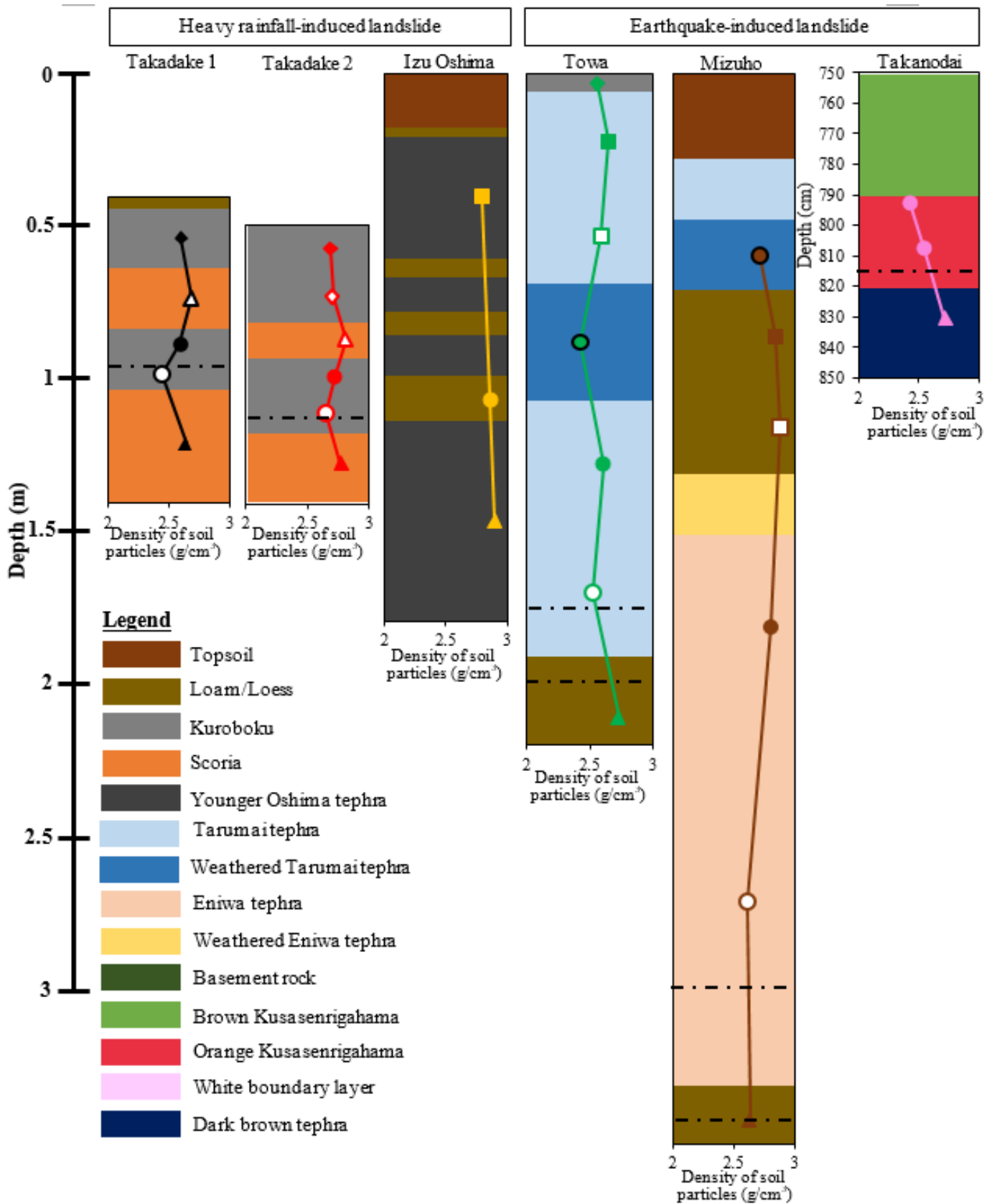
6.5 Density of soil particles

6.5.1 Density of soil particles on tephra materials

Density of soil particles was measured on each tephra layers in the landslides, unfortunately, density of soil particles in Mizuho and Takanodai landslides were not measured in the upper layers. This study observed the dissimilarity on density of soil particles between sliding layer and the under layer in heavy rainfall-induced landslides and in earthquake-induced landslides (Fig. 6.11). Density of soil particles on sliding layer is lower rather than the density of soil particles on the under layer.

6.5.2 Density of soil particles on tuff breccia and andesite materials

The density of soil particles (Fig. 6.12 and Fig. 6.13) show that the soil materials from the Ohtsuru and Ono landslides have no dissimilarities; however, highly weathered tuff breccia from Yabakei landslide has a low density of soil particles. Therefore, density of soil particles could be related with weathering process in tuff breccia and andesite materials.



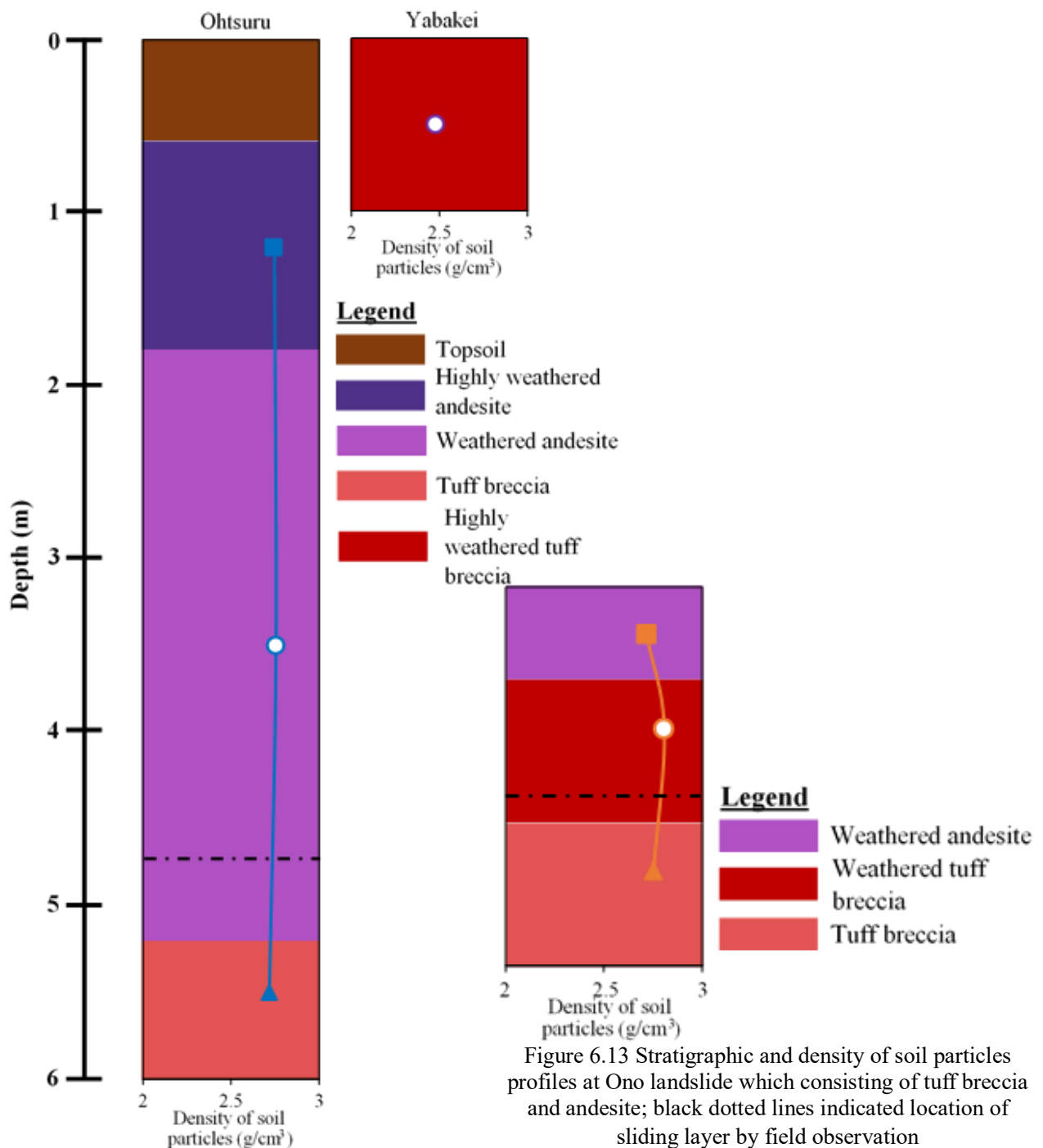


Figure 6.12 Stratigraphic and density of soil particles profiles at Ohtsuru and Yabakei landslides which consisting of tuff breccia and andesite; black dotted lines indicated location of sliding layer by field observation

Figure 6.13 Stratigraphic and density of soil particles profiles at Ono landslide which consisting of tuff breccia and andesite; black dotted lines indicated location of sliding layer by field observation

6.6 Saturated permeability of soils

JGS (2015) reported the relation between coefficient of permeability and type of soil (6.14). Type of soil materials on this study have medium permeability to very low

permeability. Permeability properties on this study observed water content, coefficient of saturated permeability, degree of saturation, void ratio, and dry density values.

	10^{-11}	10^{-10}	10^{-9}	10^{-8}	10^{-7}	10^{-6}	10^{-5}	10^{-4}	10^{-3}	10^{-2}	10^{-1}	10^0
	Impermeable		Very low		Low		Medium		High			
	Cohesive soil		Fine sand, silt, sand-silt clay mixed soil				Sand and gravel			Clean gravel		

Figure 6.14 Relation between coefficient of permeability and type of soil

6.6.1 Characteristics on saturated permeability in tephra materials

Fig. 6.15 shows water content on each tephra layers on the landslides. This study observed the water content had influence on sliding layer at the landslides caused by heavy rainfall. The sliding layer at Takadake 1 and Takadake 2 landslides has the highest water content, and the dissimilarity between the under layer is observed. N3-4 kuroboku L layer from Takadake 1 and Takadake 2 landslides has the higher water content rather than OJS scoria layer. On the other hand, characteristics on sliding layer at earthquake-induced landslides are not observed on this study.

Different with water content, dissimilarity on coefficient of saturated permeability (Fig. 6.16), on void ratio (Fig. 6.17), and on dry density (Fig. 6.18) at sliding layer in heavy rainfall-induced landslides and in earthquake-induced landslides are observed. Generally, tephra materials have medium permeability, however, N3-4 kuroboku L from Takadake 2 and dark brown tephra from Takanodai have low permeability.

Dissimilarity on coefficient of saturated permeability, on void ratio, and on dry density in sliding layer at the heavy rainfall-induced landslides are observed. However, an unconformity is observed in the characteristics of coefficient of saturated permeability in sliding layer at Takadake 1 and Takadake 2. N3-4 kuroboku L layer has higher coefficient of saturated permeability rather than OJS scoria layer in Takadake 1, whereas, N3-4 kuroboku L layer has lower coefficient of saturated permeability rather than OJS scoria layer in Takadake 2. Shimizu and Ono (2016) also reported the dissimilarity on coefficient of saturated permeability between N3-4 kuroboku layer and OJS scoria layer; coefficient of saturated permeability of OJS scoria layer were 1 to 2 orders of magnitude lower than N3-4 kuroboku layer. Shimizu and Ono (2016) suggested that OJS scoria layer act as a hydraulic aquiclude, and during heavy rainfall, the pore water pressure locally increases near the boundary between N3-4 kuroboku and OJS scoria.

Therefore, this study observed characteristics of saturated permeability had influence

on sliding layer at the heavy rainfall-induced landslides. Dissimilarity on void ratio and dry density value between sliding layer and the under layer showed that the sliding layer has loose structure. During heavy rainfall, pore water pressure was increase on sliding layer which has loose structure, and it was easily to collapse.

Furthermore, although heavy rainfall was not influence on the earthquake-induced landslides, dissimilarity on coefficient of saturated permeability, on void ratio, and on dry density are observed. Loose structure on sliding layer could have been influenced on the landslides. Same with sliding layer on heavy rainfall-induced landslides, sliding layer on the earthquake-induced landslides also has high void ratio and dry density. Chigira and Suzuki (2016) also suggested that many open voids within single grain on tephra are closed first with the fracturing of void wall when they are sheared, and grain fragments would be floated. Therefore, this study also suggests that loose structure on sliding layer could have caused the sliding layer easily to collapse during the earthquake.

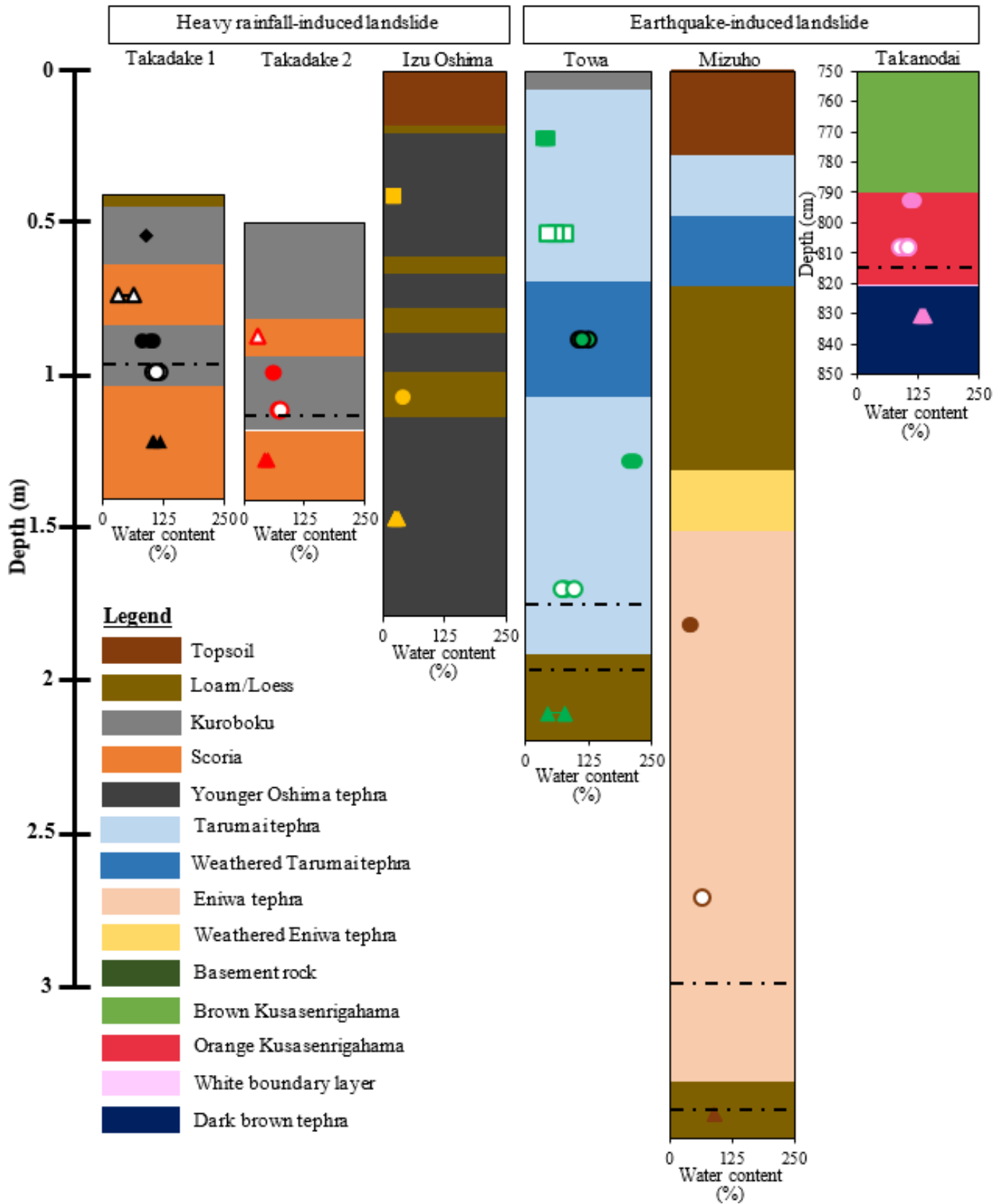


Figure 6.15 Stratigraphic and water content profiles at landslide areas which consisting of tephra materials; black dotted lines indicated location of sliding layer by field observation

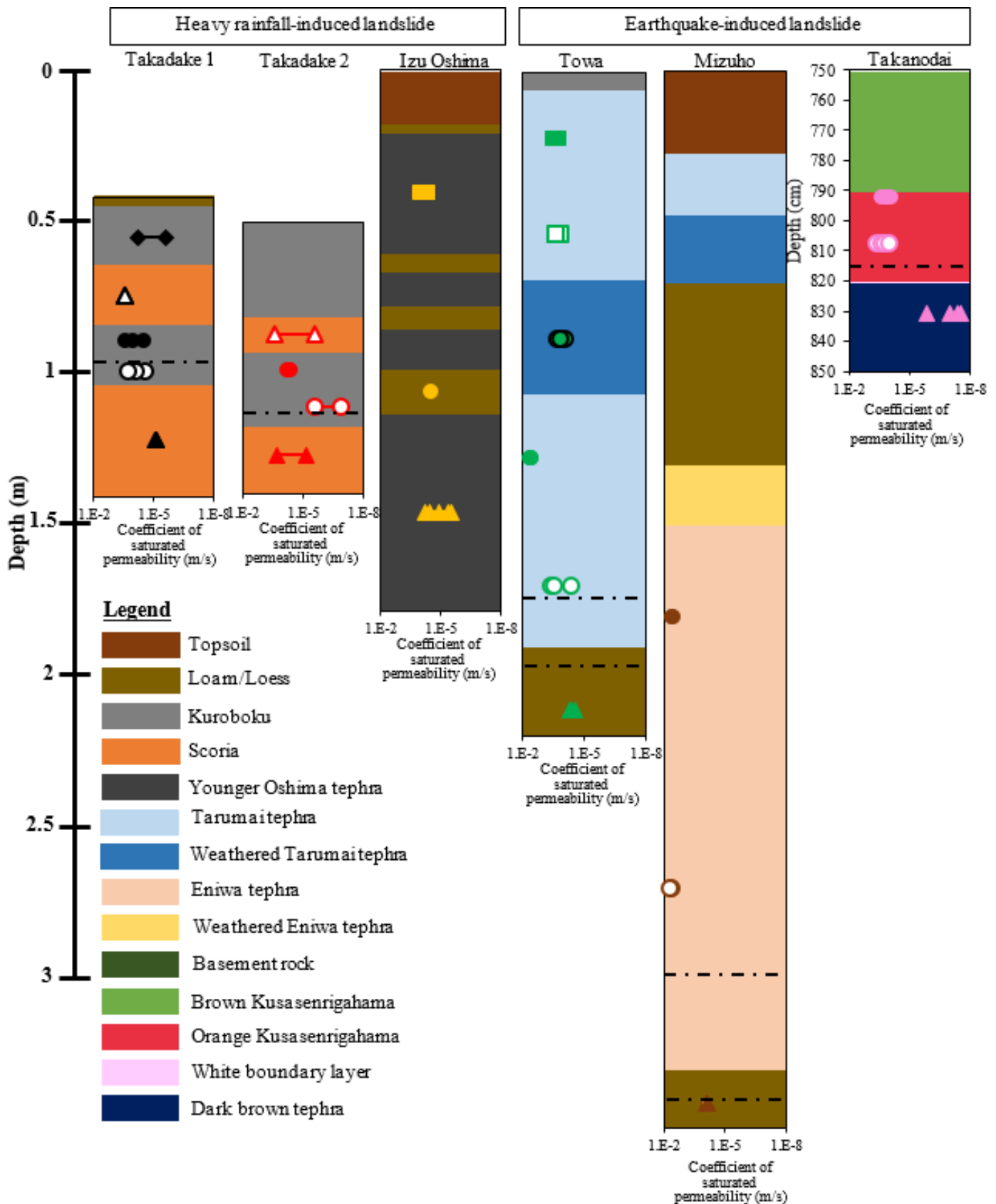


Figure 6.16 Stratigraphic and coefficient of saturated permeability profiles at landslide areas which consisting of tephra materials; black dotted lines indicated location of sliding layer by field observation

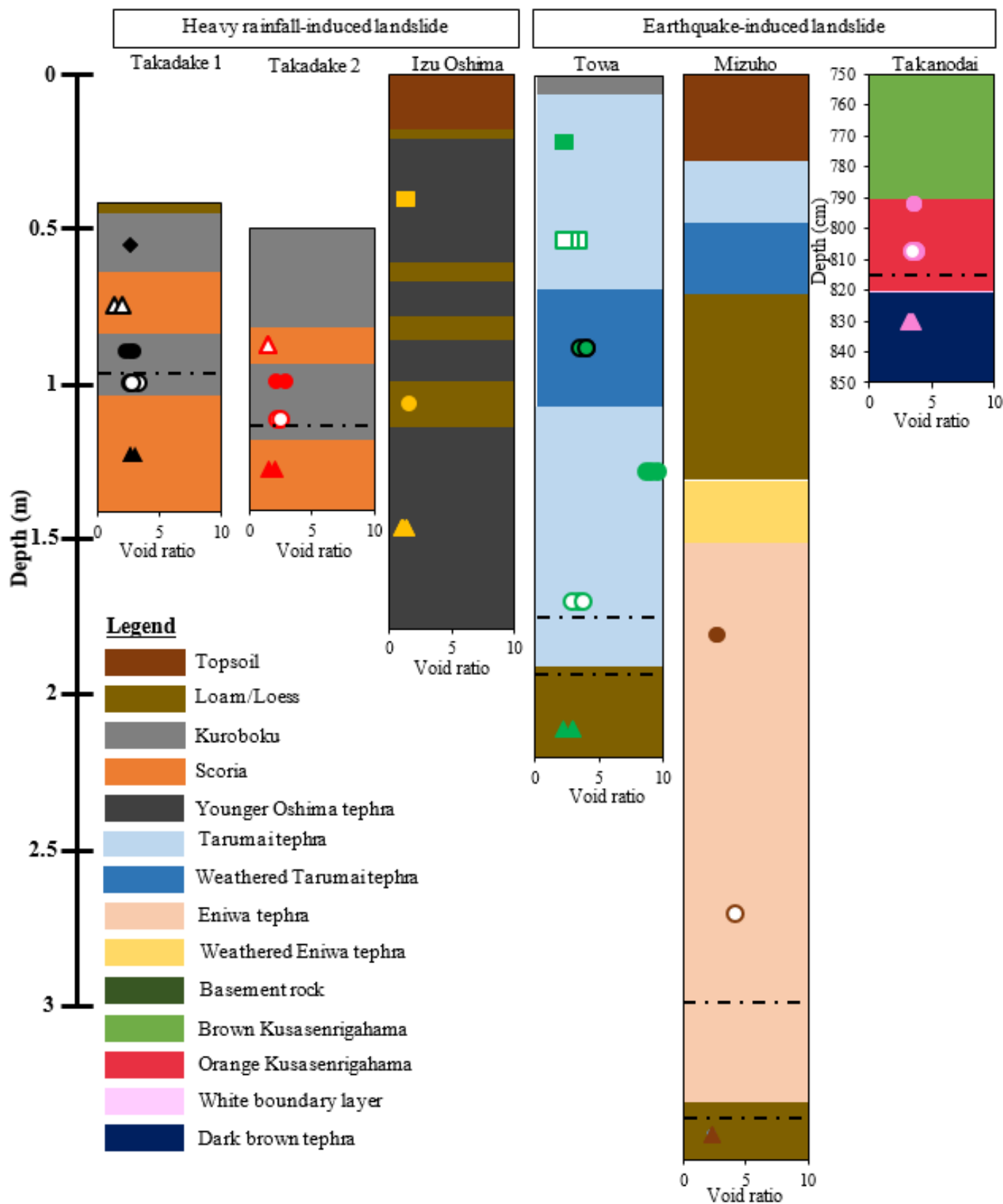


Figure 6.17 Stratigraphic and void ratio profiles at landslide areas which consisting of tephra materials; black dotted lines indicated location of sliding layer by field observation

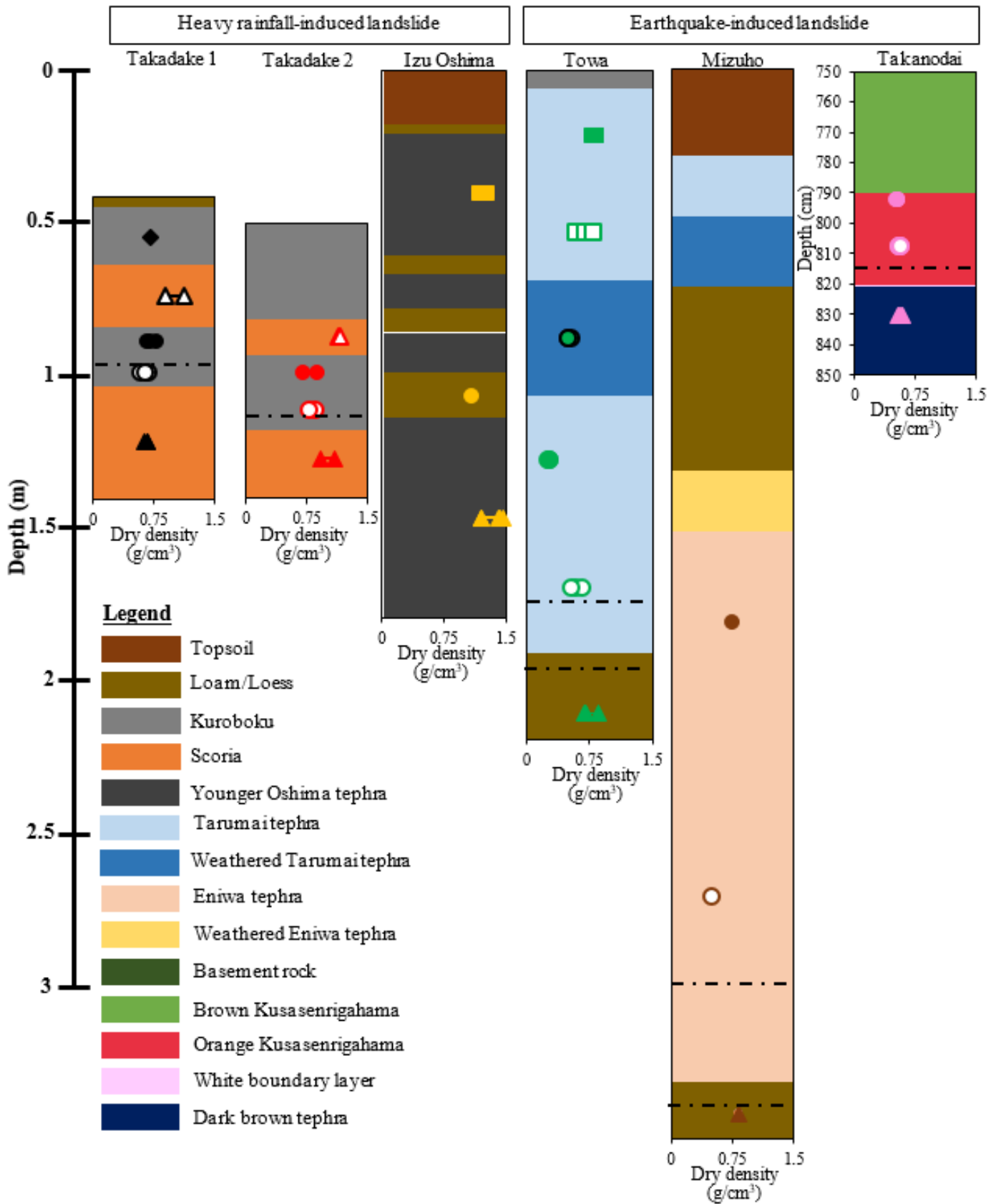


Figure 6.18 Stratigraphic and dry density profiles at landslide areas which consisting of tephra materials; black dotted lines indicated location of sliding layer by field observation

6.6.2 Characteristics on saturated permeability in tuff breccia and andesite materials

Characteristics on saturated permeability was observed on each layer at Ohtsuru

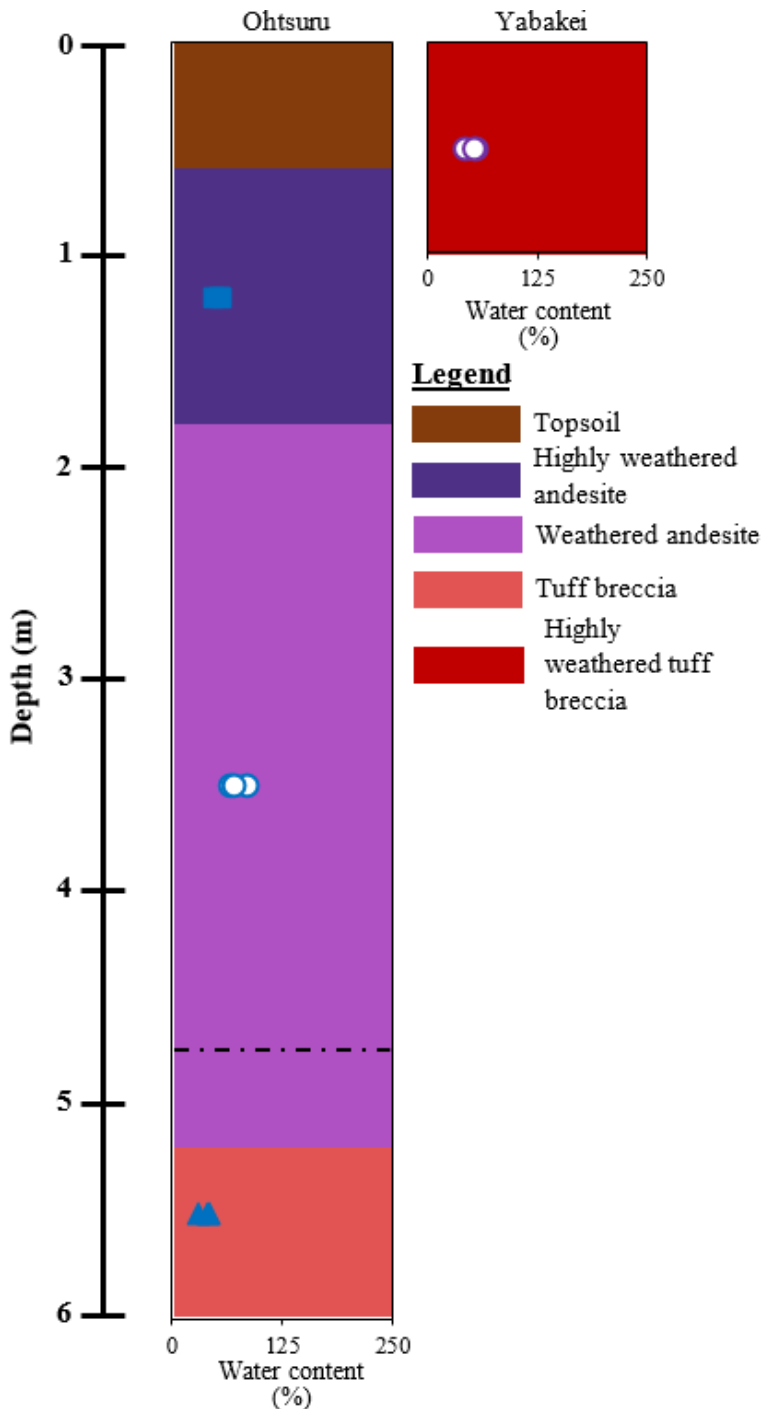


Figure 6.19 Stratigraphic and water content profiles at Ohtsuru and Yabakei landslides which consisting of tuff breccia and andesite; black dotted lines indicated location of sliding layer by field observation

landslide, on weathered andesite and weathered tuff breccia at Ono landslide, and on highly weathered tuff breccia on Yabakei landslide. Dissimilarity between sliding layer and under layer on the landslides could not observed in all landslides, however, dissimilarity between sliding layer and under layer in Ohtsuru landslides could be represented characteristics of saturated permeability in tuff breccia and andesite materials at landslide

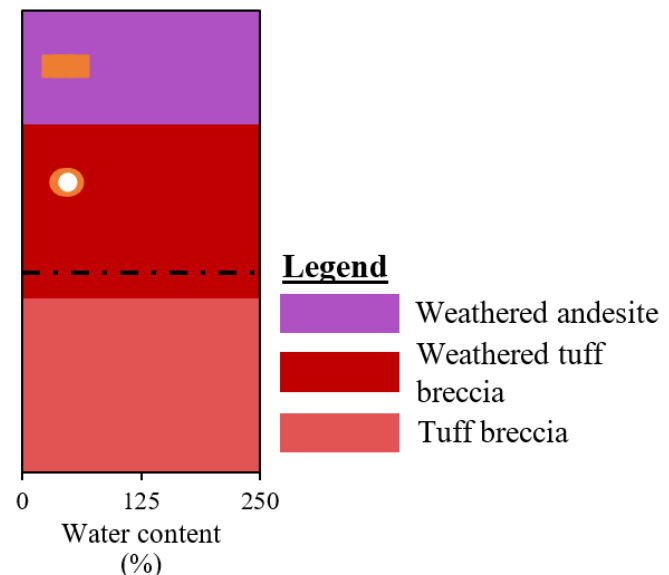


Figure 6.20 Stratigraphic and water content profiles at Ono landslide which consisting of tuff breccia and andesite; black dotted lines indicated location of sliding layer by field observation

caused by heavy rainfall.

Fig. 6.19 and Fig. 6.20 show water content on soil materials on the landslides, and dissimilarity on water content between sliding layer and under layer is observed at

Ohtsuru landslide. Weathered andesite is a sliding layer in Ohtsuru landslide and it has higher water content rather than tuff breccia layer which located under the weathered andesite.

Dissimilarity on coefficient of saturated permeability (Fig. 6.21 and Fig. 6.22), on degree of saturation (Fig. 6.23 and Fig. 6.24), on void ratio (Fig. 6.25 and Fig. 6.26), and on dry density (Fig. 6.27 and Fig. 6.28) are observed at landslides in tuff breccia and andesite materials. All of tuff

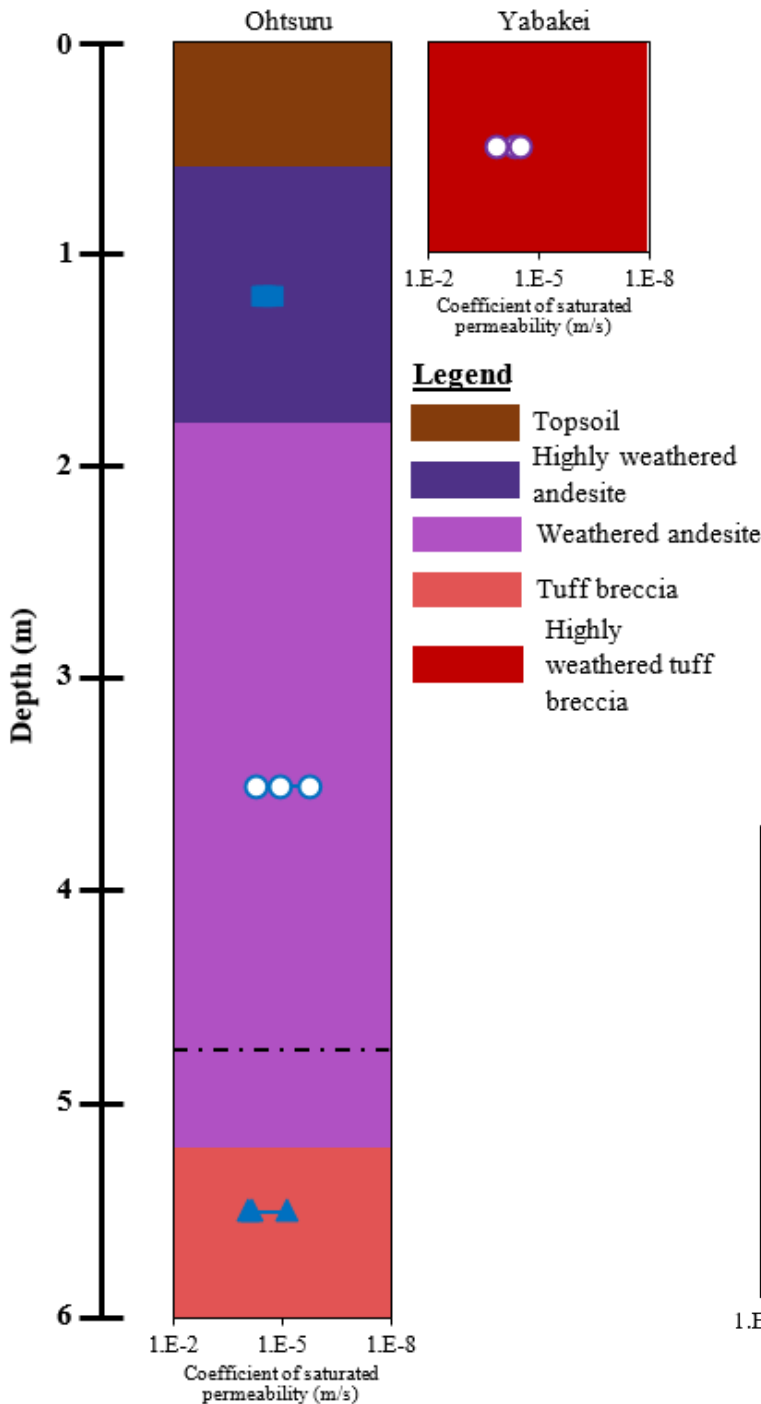


Figure 6.21 Stratigraphic and coefficient of saturated permeability profiles at Ohtsuru and Yabakei landslides which consisting of tuff breccia and andesite; black dotted lines indicated location of sliding layer by field observation

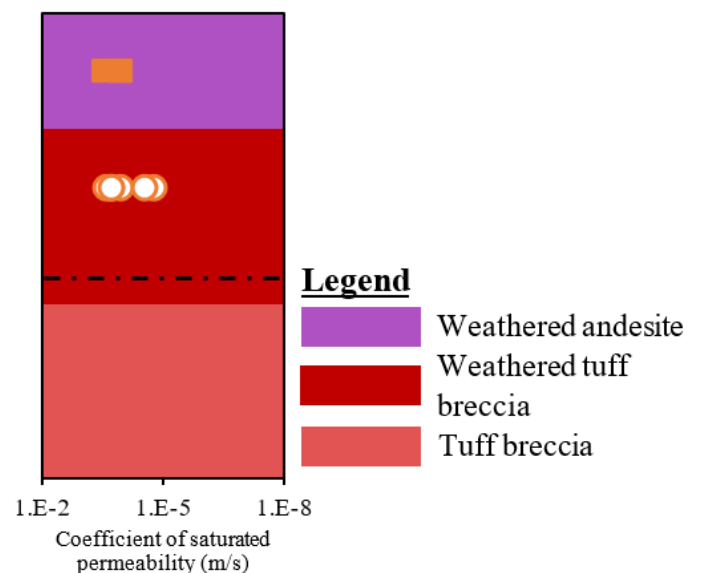


Figure 6.22 Stratigraphic and coefficient of saturated permeability profiles at Ono landslide which consisting of tuff breccia and andesite; black dotted lines indicated location of sliding layer by field observation

breccia and andesite materials on this study have medium permeability. Ohtsuru and Ono landslides are the heavy rainfall-induced landslides, and dissimilarity on coefficient of saturated permeability and on degree of saturation at sliding layer and the under layer are observed in Ohtsuru landslide. Sliding layer in Ohtsuru landslide has lower coefficient of

saturated permeability and it has higher degree of saturation rather than the under layer.

Sliding layer has higher void ratio rather than the under layer and the sliding layer has lower permeability rather than the under layer. Characteristics on saturated permeability showed that sliding layer has many open void, however, water pressure on sliding layer

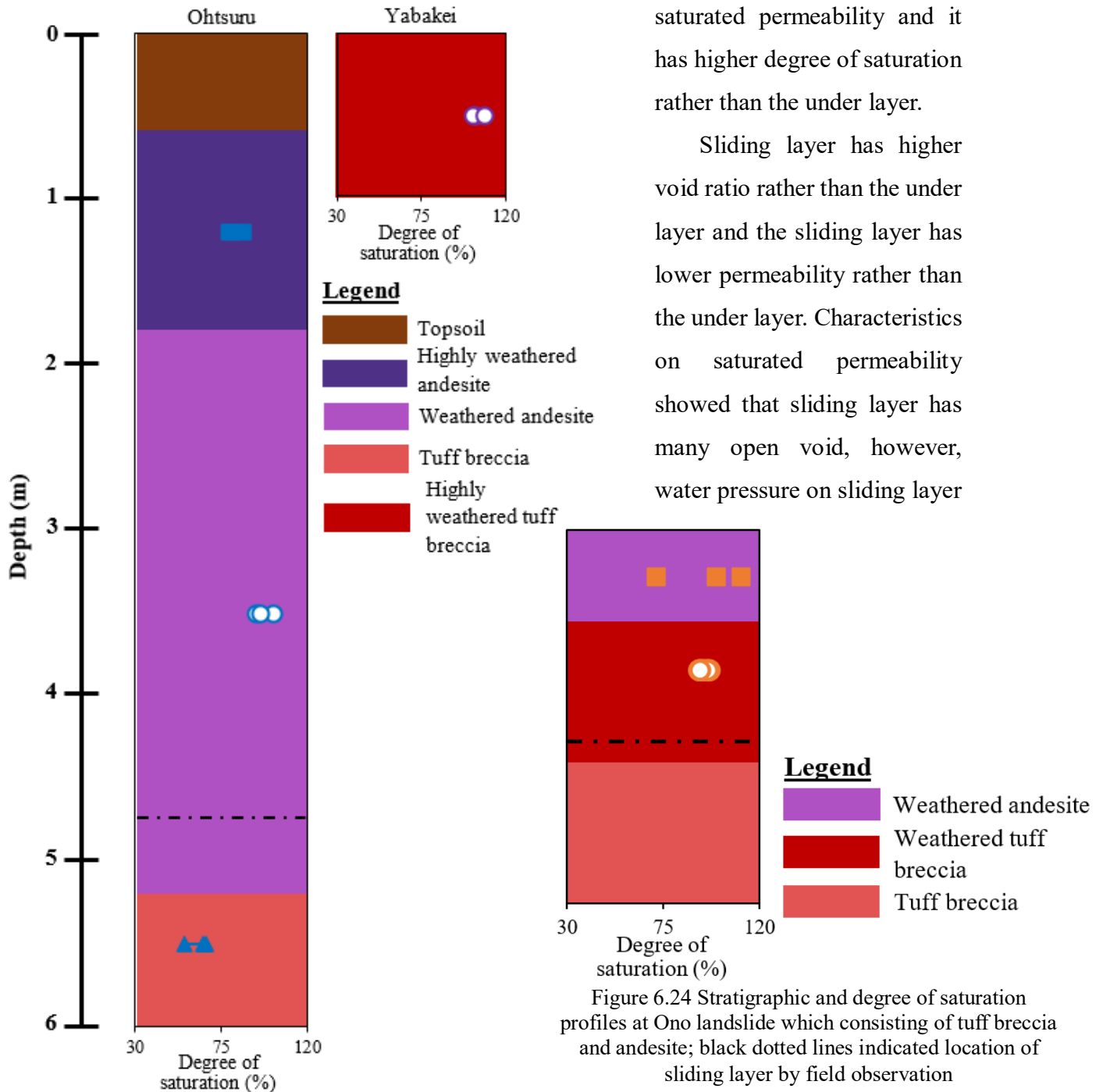


Figure 6.23 Stratigraphic and degree of saturation profiles at Ohtsuru and Yabakei landslides which consisting of tuff breccia and andesite; black dotted lines indicated location of sliding layer by field observation

Figure 6.24 Stratigraphic and degree of saturation profiles at Ono landslide which consisting of tuff breccia and andesite; black dotted lines indicated location of sliding layer by field observation

at Ohtsuru landslide was increased during heavy rainfall caused by low coefficient of saturated permeability and high degree of saturation on sliding layer, and it could be caused the landslide occurred in Ohtsuru and Ono landslide.

Furthermore, tuff breccia from three of landslides has the same range of coefficient

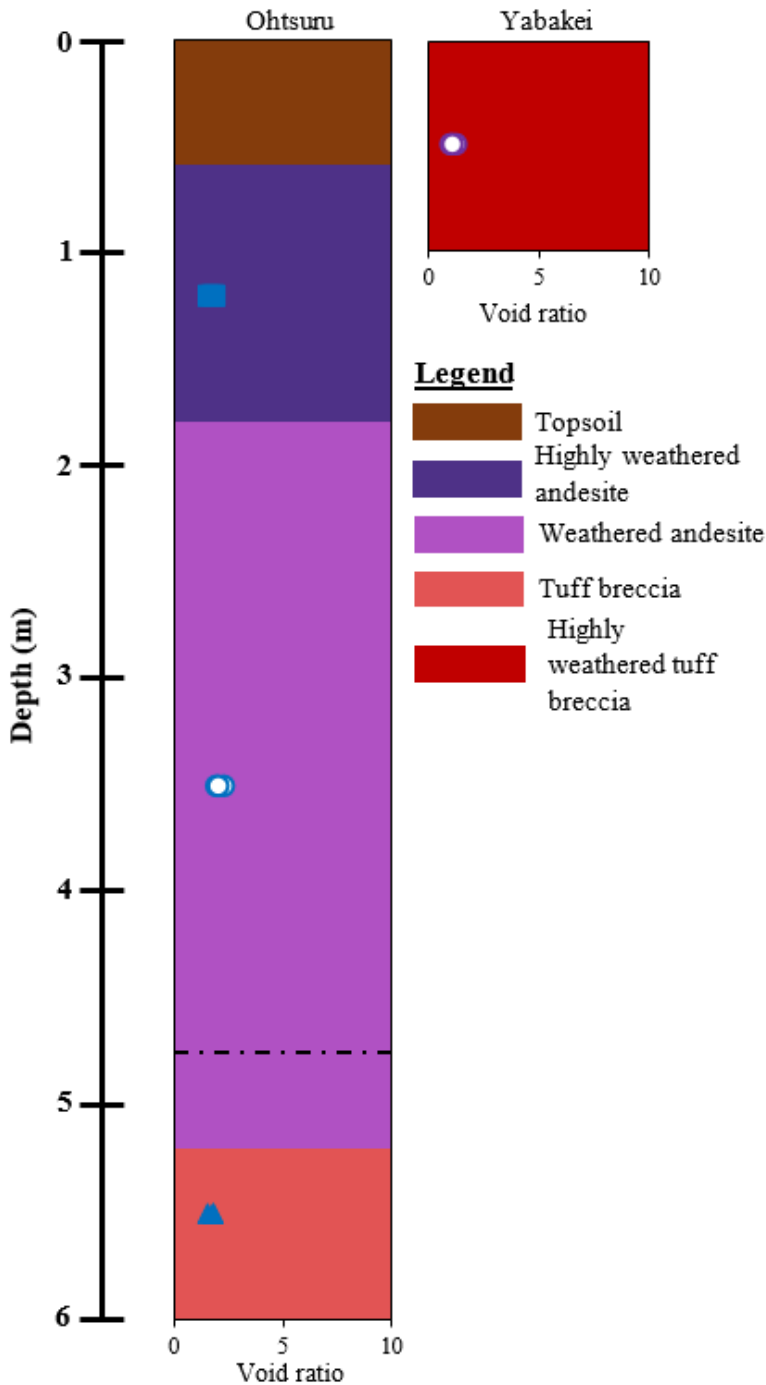


Figure 6.25 Stratigraphic and void ratio profiles at Ohtsuru and Yabakei landslides which consisting of tuff breccia and andesite; black dotted lines indicated location of sliding layer by field observation

of saturated permeability. This study observed that void ratio has a relation with weathering process (Fig. 6.27); highly weathered tuff breccia has a lower void ratio rather than tuff breccia from Ohtsuru and Ono landslides, and highly weathered andesite also has lower void ratio rather than weathered andesite in Ohtsuru landslide. Andesite materials from Ohtsuru and Ono landslides also showed different of coefficient of saturated permeability and void ratio values. Andesite materials from Ohtsuru landslide have

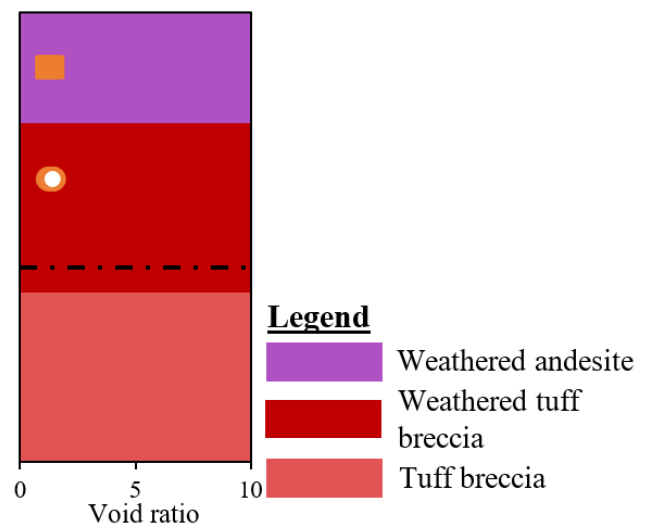
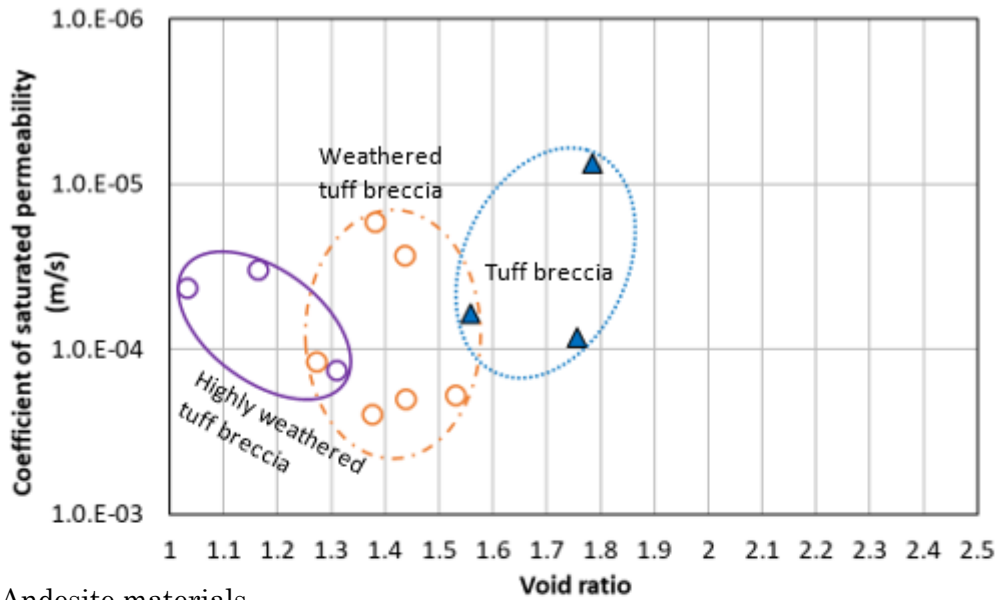


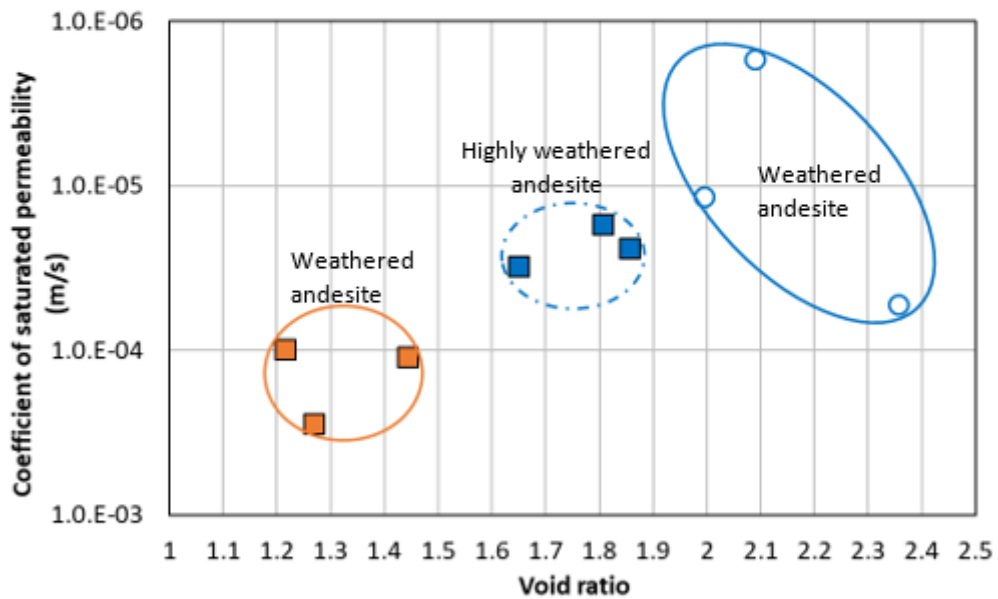
Figure 6.26 Stratigraphic and void ratio profiles at Ono landslide which consisting of tuff breccia and andesite; black dotted lines indicated location of sliding layer by field observation

lower coefficient of saturated permeability and higher void ratio rather than those from Ono landslide.

(a) Tuff breccia materials



(b) Andesite materials



Tuff breccia and andesite materials		
Ohtsuru	Ono	Yabakei
■ Highly weathered andesite	■ Weathered andesite	○ Highly weathered tuff breccia
○ Weathered andesite	○ Weathered tuff breccia	
▲ Tuff breccia	▲ Tuff breccia	

Figure 6.27 Correlation between coefficient of saturated permeability (m/s) and void ratio on (a) tuff breccia materials and (b) andesite materials

6.7 Content of clay minerals

A quantitative of clay minerals is not observed on this study, and more than one clay mineral are contained on each tephra layers. The dissimilarity between characteristics of clay minerals in sliding layers at heavy rainfall-induced landslides and at earthquake-induced landslides is observed (Fig. 6.28). On heavy rainfall-induced landslides, characteristic of clay minerals on sliding layer is not observed. Clay mineral which contained into sliding layer in Takadake landslides and Izu Oshima is dickite, however, further studies are required to observe the quantitative of dickite on sliding layer and influence of dickite on heavy rainfall-induced landslides on tephra materials.

On earthquake-induced landslides, dissimilarity of clay minerals on sliding layer is observed. In Takanodai landslide, this study observed that white boundary layer which located between orange Kusasenrigahama and dark brown tephra layers is halloysite-rich layer. Sliding layer in Towa landslide also contains halloysite; the other layers in Towa landslide do not contain halloysite, and Ta-d L layer contains halloysite. Based on the halloysite-rich which observed in Takanodai landslide, halloysite on sliding layer in tephra materials could be influenced the earthquake-induced landslides.

Same with heavy rainfall-induced landslides, characteristic of clay minerals is also not observed in tuff breccia and andesite materials (Fig. 6.29). Clay mineral which contained into sliding layer in Ohtsuru, Ono, Yabakei landslides is montmorillonite, however, further studies are required to observe the quantitative of montmorillonite on sliding layer and influence of montmorillonite on heavy rainfall-induced landslides on tuff breccia and andesite materials.

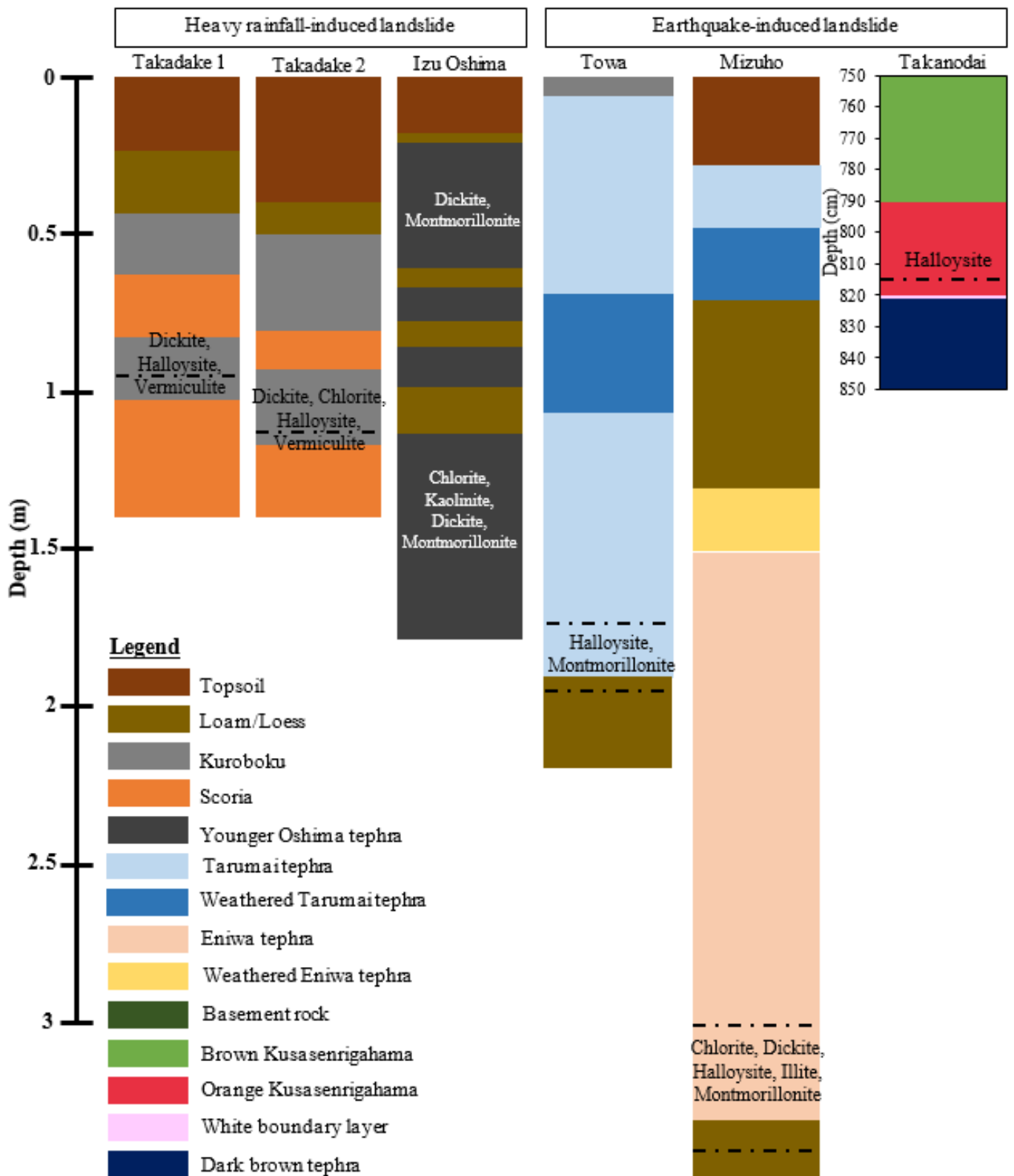


Figure 6.28 Stratigraphic and content of clay minerals on sliding layers at landslide areas which consisting of tephra materials; black dotted lines indicated location of sliding layer by field observation

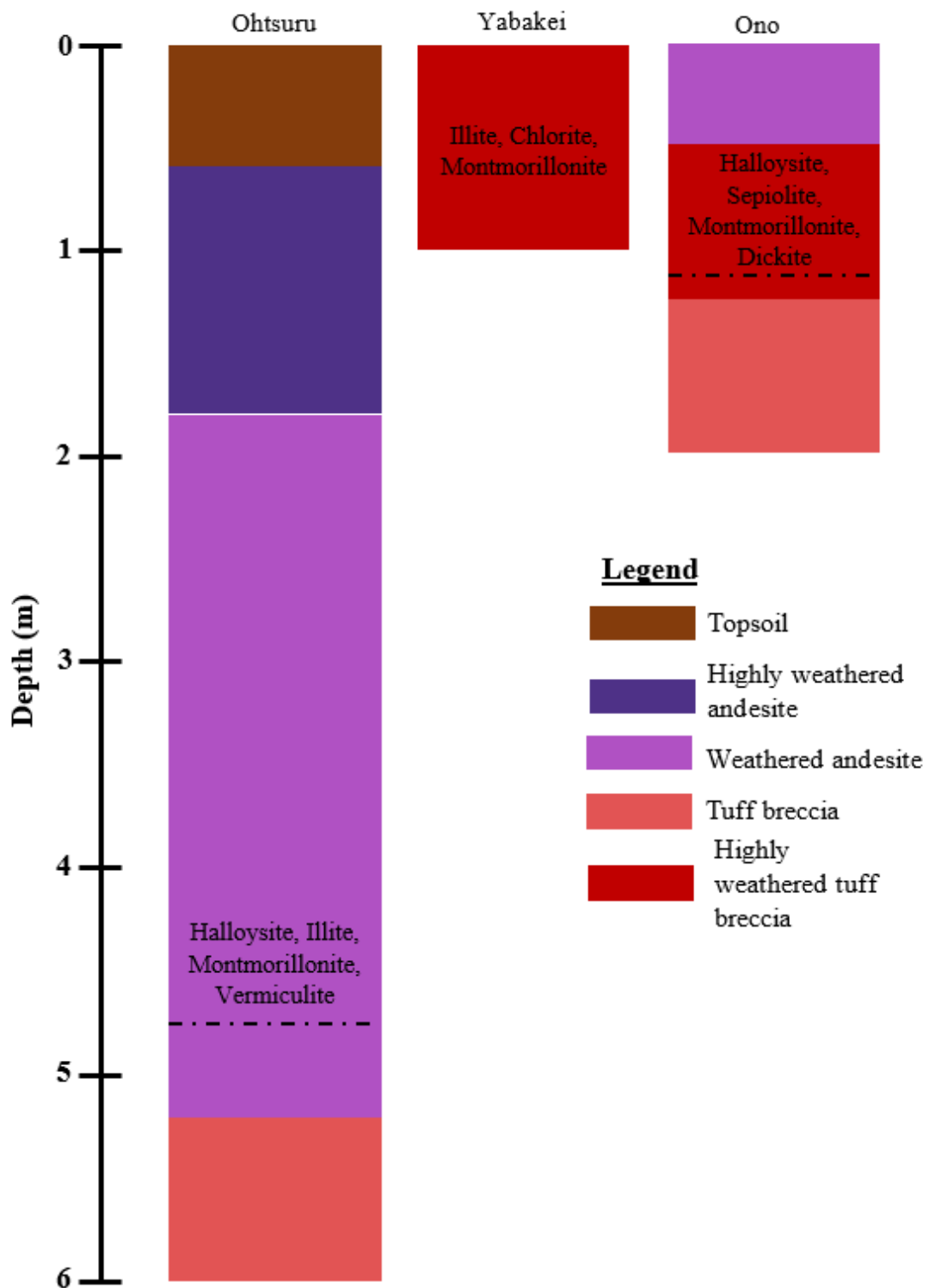


Figure 6.28 Stratigraphic and content of clay minerals on sliding layers at landslide areas which consisting of tuff breccia and andesite materials; black dotted lines indicated location of sliding layer by field observation

Chapter 7

Characteristics of Soil Physical Properties on Sliding Layer in Heavy Rainfall-induced Landslides and in Earthquake-induced Landslides at Volcanic Area

7.1 Heavy rainfall-induced landslides on tephra materials

This study observed the dissimilarity between sliding layer and the under layer on tephra materials in heavy rainfall-induced landslides. Sliding layer on heavy rainfall-induced landslides has low soil hardness, high plasticity index, high fine fraction content (less than 0.075 mm), active soil, low density of soil particles, high water content, high coefficient of saturated permeability, high void ratio, and low dry density. Physical properties on sliding layer showed that sliding layer has loose structure with low strength and active soil.

High plasticity soil and active soil on sliding layer showed that sliding layer could be easily to swell, and high water content on sliding layer also showed that sliding layer could be able to absorb the large amount of water. Furthermore, high void ratio and low dry density showed that sliding layer has a loose structure which could also influence characteristics of saturated permeability, and this study showed that sliding layer has higher coefficient of saturated permeability rather than the under layer. Therefore, during heavy rainfall, pore water pressure increases near the boundary between sliding layer and the under layer, and the landslide was occurred.

7.2 Earthquake-induced landslides on tephra materials

Dissimilarity between sliding layer and the under layer on tephra materials in earthquake-induced landslides is also observed on this study. Sliding layer on earthquake-induced landslides is non-plastic soil, low density of soil particles, high coefficient of saturated permeability, high void ratio, and low dry density. High void ratio and low dry density on sliding layer showed that sliding layer has loose structure which could also influence characteristics of saturated permeability. Although the influence of rainfall condition is not observed on earthquake-induced landslides on tephra materials, this study showed that sliding layer has higher coefficient of saturated permeability rather than the under layer. Furthermore, sliding layer on earthquake-induced landslide has halloysite

which also could have been influenced the layer during an earthquake since halloysite represents a potential weak and occurred the shrinkage cracks (Moon et al. 2015a).

7.3 Characteristics of tuff breccia-andesite in diverse mechanisms of landslides

Three landslides that occurred in Oita Prefecture are observed in this study. Ohtsuru and Ono landslides caused by heavy rainfall on 5th July 2017 in a wide area at Hita City. Ohtsuru landslide occurred during the peak rainfall, and Ono landslide occurred in the next day, on 6th July 2017. Furthermore, different landslide mechanisms triggered the large-scale landslides in Yabakei, which occurred on 11th April 2018.

The dissimilarity on characteristics of tuff breccia and andesite; physical properties, saturated permeability properties, and the content of clay minerals in diverse mechanisms of landslides on this study are not observed. On the other hand, weathering process in Yabakei landslides formed the highly weathered tuff breccia which has high plasticity index, fine fraction content, activity value, and low soil strength and density of soil particles.

According to the results, this study found that landslides in the andesite and tuff breccia areas could be divided into three types based on the timing of the landslide occurrence, scale of the landslide, and landslide mechanisms.

- 1) The landslide which occurred during the peak rainfall and it has the narrow slope (Photo 7.1). Generally, this type of landslide was found in the one area. This study also found the other three landslides in Ohtsuru area which have the same type with Ohtsuru landslide.
- 2) The large-scale landslide that occurred the day after the peak of heavy rainfall, such as the Ono landslide (Photo 7.2). The landslide activity in the past formed the low permeability zone and the infiltration of rainfall to the large-scale of slope was taking a several time. Therefore, the scale of the landslide and landslide activity in the past delayed the timing of the landslide occurrence.
- 3) The large-scale landslide that occurred without the occurrence of heavy rainfall or an earthquake, such as Yabakei landslide (Photo 7.3). The landslide activity in the past, which repeatedly occurred in Yabakei, made the groundwater gushed out. Furthermore, the weathering process in the soil high and the strength of the soil decreased.

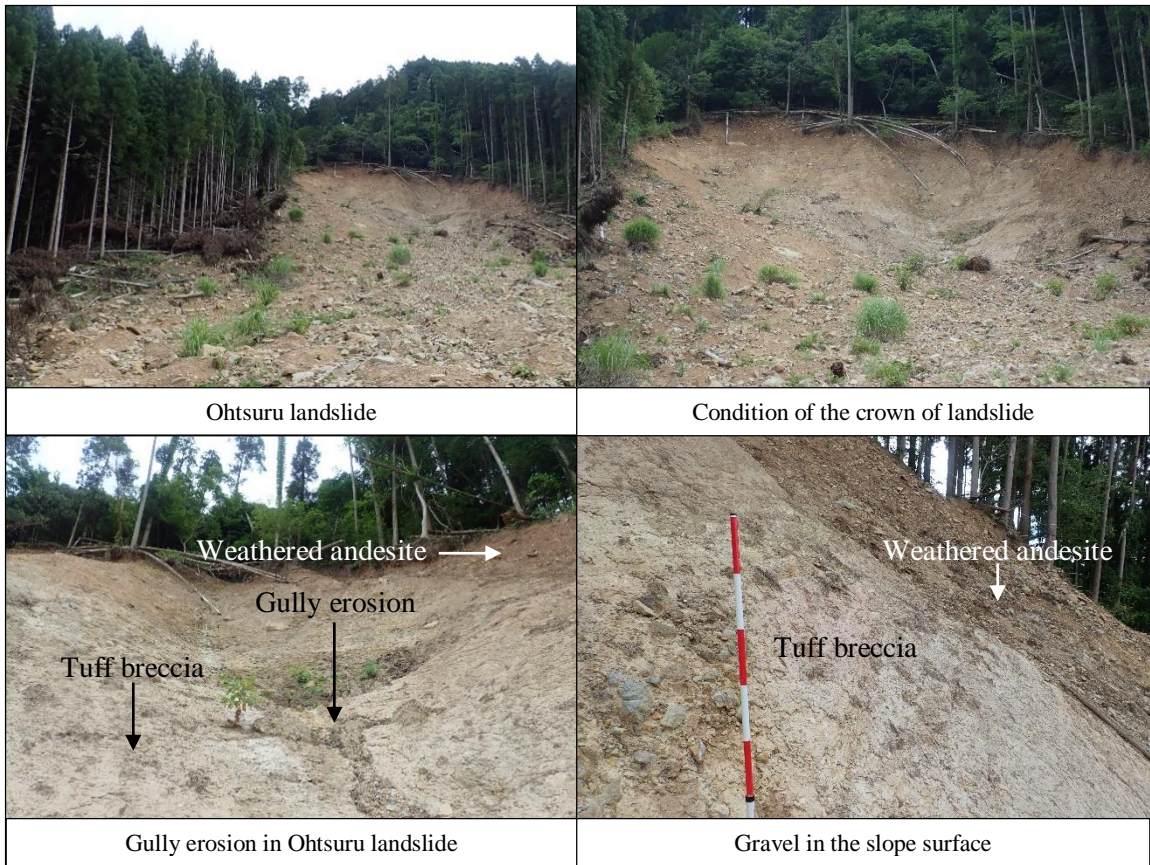


Photo 7.1 Condition of Ohtsuru landslide (Photos taken on July 2018)

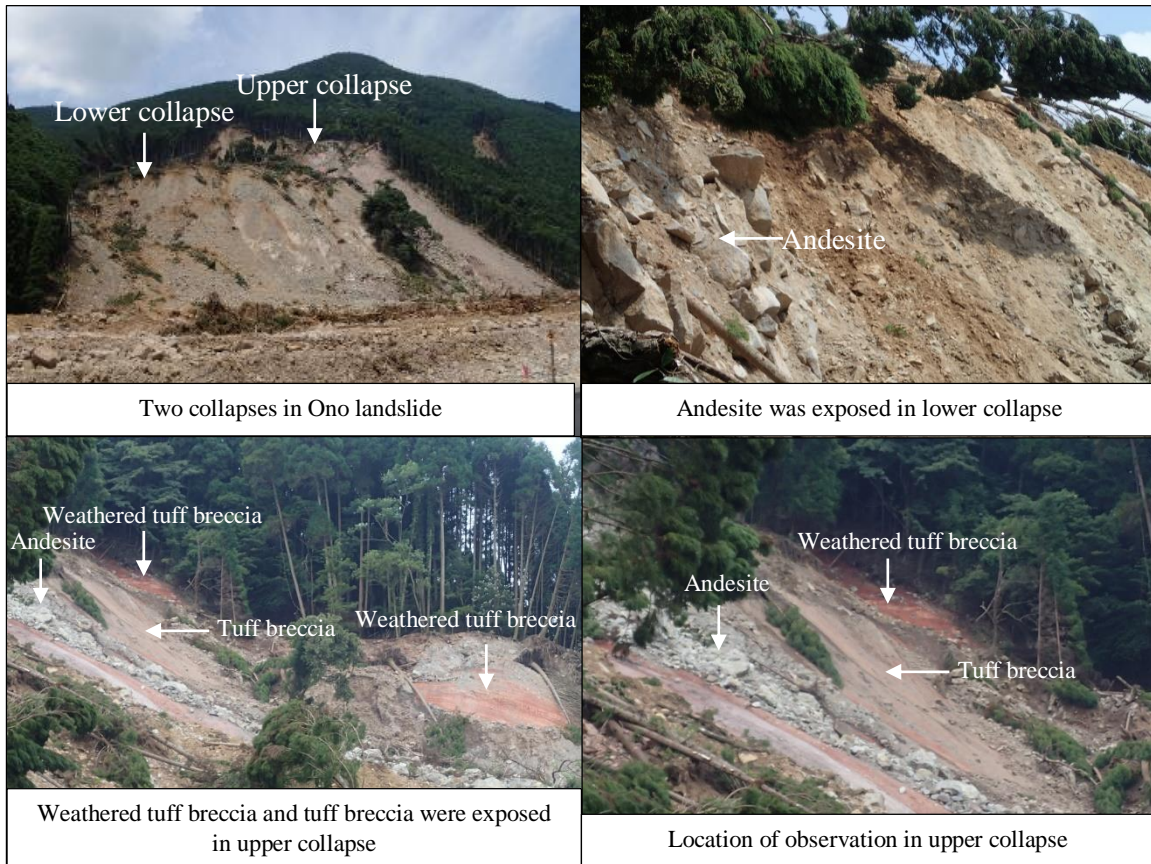


Photo 7.2 Condition of Ono landslide (Photos taken on July 2017)

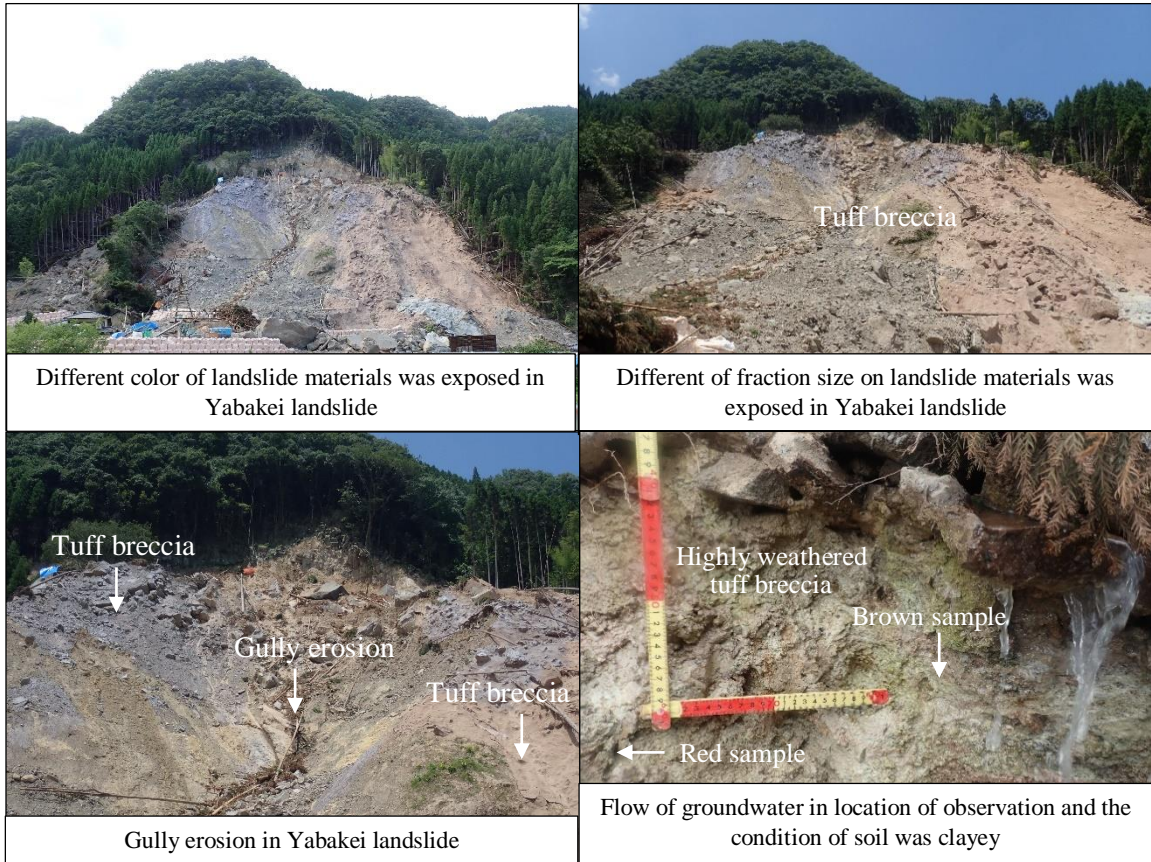


Photo 7.3 Condition of Yabakei landslide (Photos taken on July 2018)

Chapter 8

Conclusions

Occurrence of the landslides in the mountain area of tephra materials are recorded higher either during heavy rainfall or earthquake. Frequency of landslides in mountain area and the number of volcanoes in Japan, are one of the background of this study. This study observed heavy rainfall-induced landslides on tephra materials which were occurred at Takadake area in Aso mountain and at Izu Oshima in Tokyo, and earthquake-induced landslides on tephra materials which were occurred at Takanodai area in Aso mountain and Eastern Iburi Region in Hokkaido. Furthermore, this study also observed the landslides on tuff breccia and andesite materials in Oita Prefecture for comparison.

Generally, research on landslides in tephra materials were conducted by mechanical properties and less research has been conducted by physical properties. Therefore, this study is aiming to investigate the characteristics of physical properties on sliding layer in tephra materials at heavy rainfall-induced landslides and at earthquake-induced landslides; which observe by mechanical properties using soil hardness testing, by physical properties using liquid limit and plastic limit tests, particle size distribution test, and density of soil particles test, by saturated permeability properties using saturated permeability of soil testing, and content of clay minerals using X-ray diffraction test. This study has implication for geotechnical engineering, especially on field of landslides, and the methods of this study are basic methods on geotechnical engineering which applicable around the world.

Investigation of physical properties showed that sliding layer in tephra materials at heavy rainfall-induced landslides and at earthquake-induced landslides has the low density of soil particles, high void ratio and low dry density. High void ratio and low dry density showed that sliding layer on tephra materials has the loose structure. Furthermore, dissimilarity of permeability characteristics on sliding layer and the under layer was observed. Sliding layer has higher coefficient of saturated permeability rather than the under layer.

Characteristics of sliding layer in heavy rainfall-induced landslides are observed in Takadake landslides. Sliding layer in heavy rainfall-induced landslides has low soil

hardness, high plasticity index, high fine fraction content (less than 0.075 mm), low density of soil particles, high water content, high void ratio, and low dry density. Physical properties on sliding layer in heavy rainfall-induced landslides showed that sliding layer has loose structure with low strength and active soil.

Moreover, characteristics of sliding layer in earthquake-induced landslide are observed in Takanodai, Towa, and Mizuho landslides. Sliding layer in earthquake-induced landslides is non-plastic soil with low density of soil particles, high void ratio, and low dry density. Sliding layer on earthquake-induced landslide also has halloysite which influenced the layer during an earthquake.

This study also investigates the landslides on tuff breccia and andesite materials. Characteristic of sliding layer in tuff breccia and andesite materials is observed in soil hardness value which showed an obvious dissimilarity between sliding layer and the under layer. Relation between physical properties and weathering process is also observed in tuff breccia and andesite materials. Highly weathered tuff breccia from Yabakei landslide has higher plasticity index, fine fraction content, activity value, and lower density of soil particles rather than other tuff breccia from Ohtsuru and Ono landslides.

Classifications on tephra materials are also observe on this study. Relation between plasticity index and clay content (% 0.002 mm) and the relation between plasticity index and fine fraction content (% 0.075 mm) showed the estimation of activity value in tephra materials. This study observed both relations because the content of 0.002 mm in soil materials on this study is not high and the content of 0.075 mm in soil materials is high. Also because of that reason, the range of activity value on this study is 0 to 35. Activity value on tephra materials is divided into four groups; 0-1 is *inactive*, 1-5 is *normal activity*, 6-10 is *active*, and > 10 is *very active*. The sliding layers on this study are *normal* to *very active* soil; sliding layer in Takadake 1 landslide is *very active* soil, in Takadake 2 and Yabakei landslides are *active* soil, and in Ohtsuru and Ono landslides are *normal activity* soil. Activity value is related with soil plasticity and sliding layers in earthquake-induced landslides are non-plastic soil, because of that, activity values on sliding layer in earthquake-induced landslides are not observed.

Each research areas on this study consist of tephra materials deposits which produced from the eruption activity in the difference of period. The oldest tephra material on this study is Kusasenrigahama from Takanodai area which erupted from 30 ka years ago, and

the youngest tephra material on this study is Younger group Oshima from Izu Oshima area which erupted at AD 1400-1800. This study also observe classification of tephra materials based on the age of tephra materials using the plasticity chart. Younger group Oshima with the age younger than 0.5 ka years ago have lowest plasticity index and liquid limit values, and that are inorganic silts of low compressibility and have less cohesion. Tephra materials with the age between 1.5 to 3 ka years ago, such as N2 scoria from Takadake landslides and Ta-c from Towa landslides, have the higher plasticity index and liquid limit values, and that are inorganic silts of medium compressibility and organic silts. Tephra materials with the age between 3 to 9 ka years ago, such as OJS scoria from Takadake landslides and Ta-d from Towa and Mizuho landslides, have the highest plasticity index and liquid limit values, and that are inorganic silts of high compressibility and organic clays. Furthermore, the oldest tephra materials, such as Kusasenrigahama (30 ka) from Takanodai landslide and En-a (20 ka) from Mizuho landslide, are non-plastic soil, although the different results were found on dark brown tephra (30 ka) from Takanodai landslide which belongs to the highest plasticity index and liquid limit group.

Therefore, this study showed that characteristics on sliding layer were observed by physical properties. However, further studies are required to investigate the slope stability using the relation between physical properties and mechanical properties.

REFERENCES

- Adamo P, Violante P, Wilson MJ (2001) Tubular and spheroidal halloysite in pyroclastic deposits in the area of the Roccamonfina volcano (Southern Italy), *Geoderma*, 99(3–4), pp. 295–316. doi: 10.1016/S0016-7061(00)00076-8.
- Alfano F, Bonadonna C, Volentik ACM, Connor CB, Watt SFL, Pyle DM, Connor LJ (2011) Tephra stratigraphy and eruptive volume of the May, 2008, Chaitén eruption, Chile, *Bulletin of Volcanology*, 73(5), pp. 613–630. doi: 10.1007/s00445-010-0428-x.
- Arthurs JM (2010) The nature of sensitivity in rhyolitic pyroclastic soils from New Zealand, *Doctoral dissertation, University of Auckland*.
- Atkinson J (2007) The mechanics of soils and foundations (Second Edition), *Taylor & Francis Group: London and New York*.
- Bell FG, Maud RR (1995) Expansive clays and construction, especially of low-rise structures: a viewpoint from Natal, South Africa, *Environmental and Engineering Geoscience*, 1, pp. 41–59.
- Biass S, Bonadonna C (2011) A quantitative uncertainty assessment of eruptive parameters derived from tephra deposits: The example of two large eruptions of Cotopaxi volcano, Ecuador, *Bulletin of Volcanology*, 73(1), pp. 73–90. doi: 10.1007/s00445-010-0404-5.
- Bonadonna C (2006) Probabilistic modelling of tephra dispersion, *Statistics in Volcanology, Special Publications of IAVCEI*, 1, pp. 243–259, Geological Society, London.
- Casagrande A (1948) Classification and identification of soils, *Transactions of the American Society of Civil Engineers*, pp. 901-902.
- Centre for Instrumental Analysis (2016) X-ray diffractometer SmartLab manual, *University of Yamanashi*.
- Chiaro G, Alexander G, Brabhaharan P, Massey C, Koseki J, Yamada S, Aoyagi Y (2017) Reconnaissance report on geotechnical and geological aspects of the 14-16 April 2016 Kumamoto earthquakes, Japan, *Bulletin of the New Zealand Society for Earthquake Engineering*, 50(3), pp. 365–393. doi: 10.5459/bnzsee.50.3.365-393.
- Chiaro G, Umar M, Kiyota T, Massey C (2018) The Takanodai Landslide, Kumamoto, Japan: Insights from Post-Earthquake Field Observations, Laboratory Tests, and Numerical Analyses, (June), pp. 98–111. doi: 10.1061/9780784481486.011.
- Chigira M, Ling S, Matsushi Y, (2018b) Landslide disaster induced by the 2017 northern Kyushu Raistorm, *Disaster Prevention Research Institute Annuals*, 61, pp. 28–35. (in Japanese with English abstract)
- Chigira M, Suzuki T (2016) Prediction of earthquake-induced landslides of pyroclastic fall deposits, *Landslides and Engineered Slopes. Experience, Theory and Practice*, 1, pp. 93–100. doi: 10.1201/b21520-10.
- Chigira M, Tajika J, Ishimaru S (2018a) Formation beds of sliding surface-weathering and clay minerals, *Hokkaido University Press, Sapporo, Japan*. (in Japanese with

English abstract)

- Chigira M, Yokoyama O (2005) Weathering profile of non-welded ignimbrite and the water infiltration behavior within it in relation to the generation of shallow landslides, *Engineering Geology*, 78(3–4), pp. 187–207. doi: 10.1016/j.enggeo.2004.12.008.
- Churchman GJ, Lowe DJ (2012) Alteration, formation, and occurrence of minerals in soils, In: Huang, P.M.; Li, Y; Sumner, M.E. (editors) “Handbook of Soil Sciences. 2nd edition. Vol. 1: Properties and Processes”, *CRC Press (Taylor & Francis), Boca Raton, FL*, pp.20.1–20.72.
- Cutler NA, Streeter RT, Engwell SL, Bolton MS, Jensen BJJ, Dugmore AJ (2020) How does tephra deposit thickness change over time? A calibration exercise based on the 1980 Mount St Helens tephra deposit, *Journal of Volcanology and Geothermal Research*. Elsevier B.V., 399, p. 106883. doi: 10.1016/j.jvolgeores.2020.106883.
- Daiki (DIK-4012) Manual for soil permeability analysis using an instrument with 4 points. (in Japanese)
- Del Prete M, Guadagno FM, Hawkins AB (1998) Preliminary report on the landslides of 5 May 1998, Campania, southern Italy, *Bulletin of Engineering Geology and the Environment*, 57(2), pp. 113–129. doi: 10.1007/s100640050028.
- Etame J, Gerard M, Suh CE, Bilong P (2009) Halloysite neoformation during the weathering of nephelinitic rocks under humid tropical conditions at Mt Etinde, Cameroon, *Geoderma*. Elsevier B.V., 154(1–2), pp. 59–68. doi: 10.1016/j.geoderma.2009.09.013.
- Farmer VC (1997) Conversion of ferruginous allophanes to ferruginous beidellites at 95 °C under alkaline conditions with alternating oxidation and reduction, *Clays and Clay Minerals*, 45(4), pp. 591–597.
- Fiorillo F, Guadagno FM, Aquino S, de Blasio A (2001) The December 1999 Cervinara landslides: Further debris flows in the pyroclastic deposits of Campania (Southern Italy), *Bulletin of Engineering Geology and the Environment*, 60(3), pp. 171–184. doi: 10.1007/s100640000093.
- Furukawa R, Nakagawa M (2010) Geological map of Tarumae volcano, https://gbank.gsj.jp/volcano/Act_Vol/tarumae/index-e.html. Accessed October 2020.
- Furukawa R, Nakagawa M, Furukata C, Yoshimoto M (2006) Eruptive activity in the prehistoric period of Tarumae volcano, In: https://gbank.gsj.jp/volcano/Act_Vol/tarumae/text/exp15-2.html. Accessed November 2020. (in Japanese)
- Geology Survey of Japan. <https://gbank.gsj.jp/geonavi/geonavi.php>. Accessed October 2020.
- Goto S, Kimura T (2019) Introduction of the special issue on “Toward the prediction of shallow landslides induced by heavy rainfalls on tephra-covered slopes”, *Journal of the Japan Landslides Society*, 56, pp. 211–217. doi: 10.3313/jls.56.218. (in

- Japanese with English abstract)
- Higaki D, Li X, Hayashi I, Tsou C, Kimura T, Hayashi S, Sato G, Goto S (2019) Geomorphological setting of shallow landslides by heavy rainfall on tephra-covered slopes of Aso volcano, southwest Japan, *Journal of the Japan Landslide Society*, 56, pp. 218–226. doi: 10.3313/jls.56.218. (in Japanese with English abstract)
- Holtz RD, Kovacs WD (1981) An introduction to geotechnical engineering, *Prentice Hall, Englewood Cliffs*.
- Hong HL, Mi JX (2006) Characteristics of halloysite associated with rectorite from Hubei, China, *Mineralogical Magazine*, 70(3), pp. 257–264. doi: 10.1180/0026461067030329.
- Hurst T, Smith W (2004) A Monte Carlo methodology for modelling ashfall hazards, *Journal of Volcanology and Geothermal Research*, 138(3–4), pp. 393–403. doi: 10.1016/j.jvolgeores.2004.08.001.
- Irfan TY (1998) Structurally controlled landslides in saprolitic soils in Hong Kong, *Geotechnical and Geological Engineering*, 16(3), pp. 215–238. doi: 10.1023/A:1008805827178.
- Isshiki N (1984) Geology of the Oshima district, with geological sheet map at 1: 50,000, *Geol. Surv. Jpn*, pp. 133. (in Japanese with English abstract)
- Istiyanti ML, Goto S, Kimura T, Sato G, Hayashi S, Wakai A, Higaki D (2020a) Sliding layer estimation of shallow landslides on Aso volcanic mountains in Japan based on tephra layer-physical properties of soil, *Geoenvironmental Disasters*. *Geoenvironmental Disasters*, 7(1). doi: 10.1186/s40677-020-00163-x.
- Istiyanti ML, Goto S (2020b) Differences of physical properties between tephra and tuff breccia-andesite on sliding layers of landslides, *Proceedings of the 10th Symposium on Sediment-related Disasters, Japan*.
- Jaynes WF, Bigham JM, Smeck NE, Shipitalo MJ (1989) Interstratified 1:1-2:1 mineral formation in a polygenetic soil from Southern Ohio, *Soil Science Society of America Journal*, 53(6), pp. 1888–1894. doi: 10.2136/sssaj1989.03615995005300060046x.
- Jenkins SF, Magill CR, McAneney KJ (2007) Multi-stage volcanic events: A statistical investigation, *Journal of Volcanology and Geothermal Research*, 161(4), pp. 275–288. doi: 10.1016/j.jvolgeores.2006.12.005.
- Japan Meteorological Agency (2017 and 2018). www.data.jma.go.jp/obd.stats.etrn/. Accessed August 2020.
- Joussein E, Petit S, Churchman J, Theng B, Righi D, Delvaux B (2005) Halloysite clay minerals — a review, *Clay Minerals*, 40(4), pp. 383–426. doi: 10.1180/0009855054040180.
- Kasai M, Yamada T (2019) Topographic effects on frequency-size distribution of landslides triggered by the Hokkaido Eastern Iwate Earthquake in 2018, *Earth, Planets and Space*. Springer Berlin Heidelberg, 71(1). doi: 10.1186/s40623-019-1069-8.
- Kautz CQ, Ryan PC (2003) The 10 Å to 7 Å halloysite transition in a tropical soil

- sequence, Costa Rica, *Clays and Clay Minerals*, 51(3), pp. 252–263. doi: 10.1346/CCMN.2003.0510302.
- Kawanabe Y (1998) Geological map of Izu-Oshima Volcano, 1: 25,000, Geological map of volcanoes 10, *Geol. Surv. Jpn.* (in Japanese with English abstract)
- Kimura T, Goto S, Sato G, Wakai A, Hayashi S, Higaki D (2019) Evaluation of landslide susceptibility by slope stability analysis using an estimated distribution of tephra deposits—a case study in the Northeastern part of Aso caldera—, *Journal of the Japan Landslide Society*, 56, pp. 240–249. doi: 10.3313/jls.56.240. (in Japanese with English abstract)
- Kluger MO, Jorat ME, Moon VG, Kreiter S, de Lange WP, Morz T, Robertson T, Lowe DJ (2020) Rainfall threshold for initiating effective stress decrease and failure in weathered tephra slopes, *Landslides*, 17(2), pp. 267–281. doi: 10.1007/s10346-019-01289-2.
- Kluger MO, Kreiter S, Moon VG, Orense RP, Mills P, Morz T (2019) Undrained cyclic shear behaviour of weathered tephra, *Geotechnique*, 69(6), pp. 489–500. doi: 10.1680/jgeot.17.P.083.
- Kluger MO, Moon VG, Kreiter S, Lowe DJ, Churchman GJ, Hepp DA, Seibel D, Jorat ME, Morz T (2017) A new attraction-detachment model for explaining flow sliding in clay-rich tephra, *Geology*, 45(2), pp. 131–134. doi: 10.1130/G38560.1.
- Kokusho T, Fujita K (2001) Water films involved in post-liquefaction flow failure in Niigata City during the 1964 Niigata Earthquake, *International conferences on recent advances in geotechnical earthquake engineering and soil dynamics*, 25. <https://scholarsmine.mst.edu/icrageesd/04icrageesd/session05/25>. Accessed October 2020.
- Korup O, Seidemann J, Mohr C (2017) Tephra, trees, and trouble: forest dieback delays landslide response to pyroclastic eruption, 19, pp. 8557.
- Koyama M, Hayakawa Y (1996) Syn- and Post-caldera eruptive history of Izu Oshima Volcano based on tephra and loess stratigraphy, *Journal of Geography*, 105(2), pp. 133–162. (in Japanese with English abstract)
- Koyasu H, Ishimaru S, Wang G, Furuya G, Watanabe N, Cai F, Uchimura T, Kimura T (2020) Geological and geotechnical characteristics of sliding layers of landslides introduced by the 2018 Hokkaido Eastern Iwate earthquake. <http://www.dpri.kyoto-u.ac.jp/hapyo/20/pdf/D32.pdf>. Accessed November 2020.
- Kubota T, Jitousono T, Nagai Y, Shimizu O, Mizuno H, Nomura Y, Suzuki Y, Yamakoshi T, Koi T, Ohishi H, Hirakawa Y (2018) Overview of the Yabakei landslide occurred on April 11th 2018 in Nakatsu city, Oita Prefecture, Japan, *J. Jpn. Soc. Erosion Control Eng*, 71, pp. 34–41. (in Japanese with English abstract)
- Labuz JF, Zang A (2012) Mohr-Coulomb failure criterion, *Rock Mechanics and Rock Engineering*, 45(6), pp. 975–979. doi: 10.1007/s00603-012-0281-7.
- Laird DA, Barak P, Nater EA, Dowdy RH (1991) Chemistry of Smectitic and Illitic Phases in Interstratified Soil Smectite, *Soil Science Society of America Journal*,

- 55(5), pp. 1499–1504. doi: 10.2136/sssaj1991.03615995005500050050x.
- Lancellota R (2009) Geotechnical Engineering (Second edition), *Taylor & Francis, ISBN 0-201-92783-4 Master e-book ISBN.*
- Lowe DJ (1986) Controls on the rates of weathering and clay mineral genesis in airfall tephra: a review and New Zealand case study, *Rates of chemical weathering of rocks and minerals*, pp. 265–330.
- Lowe DJ (2011) Tephrochronology and its application: A review, *Quaternary Geochronology*. Elsevier B.V, 6(2), pp. 107–153. doi: 10.1016/j.quageo.2010.08.003.
- Machida H (2002) Volcanoes and tephra in the Japan area, *Global Environmental Research*, 6, pp. 19–28. Available at: http://www.airies.or.jp/attach.php/6a6f75726e616c5f30362d32656e67/save/0/0/06_2-03.pdf. Accessed on October 2020.
- Mason BG, Pyle DM, Oppenheimer C (2004) The size and frequency of the largest explosive eruptions on Earth, *Bulletin of Volcanology*, 66(8), pp. 735–748. doi: 10.1007/s00445-004-0355-9.
- Minato M, Hashimoto S, Fujiwara Y, Kumano S, Okada S (1972) Stratigraphy of the Quaternary ash and pumiceous products in Southwestern Hokkaido, N. Japan, *Journal of the Faculty of Science, Hokkaido University, Series 4, Geology and Mineralogy*, 15(3-4), pp. 679–736.
- Mitchell JK, Soga K (2005) Fundamentals of soil behaviour. ISBN-13:978-0-471-46302-3.
- Miura S (2012) Mechanical behaviour and earthquake-induced failures of volcanic soils in Japan, *2nd ICTG September 10-12, Sapporo, Japan*. <https://www.eng.hokudai.ac.jp/labo/geomech/tc202conference/paper/Prof.%20Miura.pdf>. Accessed October 2020
- Miyabuchi Y (2009) A 90,000-year tephrostratigraphic framework of Aso Volcano, Japan, *Sedimentary Geology*, Elsevier B.V., 220(3–4), pp. 169–189. doi: 10.1016/j.sedgeo.2009.04.018.
- Miyabuchi Y (2011) Post-caldera explosive activity inferred from improved 67-30ka tephrostratigraphy at Aso Volcano, Japan, *Journal of Volcanology and Geothermal Research*, Elsevier B.V., 205(3–4), pp. 94–113. doi: 10.1016/j.jvolgeores.2011.05.004.
- Miyabuchi Y, Daimaru H (2004) The June 2001 rainfall-induced landslides and associated lahars at Aso volcano, southwestern Japan: implication for hazard assessment, *Acta Vulcanol*, 16(1–2), pp. 21–36.
- Miyabuchi Y, Hoshizumi H, Takada H, Watanabe K, Xu S (2003) Pumice-fall deposits from Aso Volcano during the past 90,000 years, southwestern Japan, *Bulletin of the Volcanological Society of Japan*, 48, pp. 195–214. (in Japanese with English abstract)
- Miyabuchi Y, Hoshizumi H, Watanabe K (2004) Late Pleistocene tephrostratigraphy of

- Aso Volcano, southwestern Japan, after deposition of AT ash, *Bulletin of the Volcanological Society of Japan*, 49, pp. 51–64. (in Japanese with English abstract)
- Miyabuchi Y, Maeno F, Nakada S (2015) The October 16, 2013 rainfall-induced landslides and associated lahars at Izu Oshima Volcano, Japan, *Journal of Volcanology and Geothermal Research*. Elsevier B.V., 302, pp. 242–256. doi: 10.1016/j.jvolgeores.2015.07.012.
- Miyabuchi Y, Watanabe K (1997) Eruption ages of Holocene tephra from Aso Volcano, southwestern Japan, inferred from ¹⁴C ages of buried Andisols, *Bulletin of the Volcanological Society of Japan*, 42, pp. 403–408. (in Japanese with English abstract)
- Moon VG, Lowe DJ, Cunningham MJ, Wyatt JB, de Lange WP (2015a) Sensitive pyroclastic-derived halloysitic soils in northern New Zealand: Interplay of microstructure, minerals, and geomechanics, *Volcanic Rocks and Soils - Proceedings of the International Workshop on Volcanic Rocks and Soils*, pp. 3–21. doi: 10.1201/b18897-1.
- Moon VG, de Lange WP, Garae CP, Morz T, Jorat ME, Kreiter S (2015b) Monitoring the landslide at Bramley Drive, Tauranga, New Zealand, *ANZ 2015 Changing the Face of the Earth, Geomechanics and Human Influence, 12th Australia New Zealand Conference on Geomechanics*, pp. 737–744.
- Mukunoki T, Kasama K, Murakami S, Ikemi H, Ishikura R, Fujikawa T, Yasufuku N, Kitazono Y (2016) Reconnaissance report on geotechnical damage caused by an earthquake with JMA seismic intensity 7 twice in 28 h, Kumamoto, Japan, *Soils and Foundations*, Elsevier, 56(6), pp. 947–964. doi: 10.1016/j.sandf.2016.11.001.
- Nakagawa M, Amma-Miyasaka M, Tomijima C, Matsumoto A, Hase R (2018) Eruption Sequence of the 46 ka Caldera-forming Eruption of Shikotsu Volcano, Inferred from Stratigraphy of Proximal Deposits at South of Lake Shikotsu, Japan, *Journal of Geography*, 127(2), pp. 247–271. doi: 10.5026/jgeography.127.247.
- Ochiai H, Sakurai M, Higaki D, Goto S, Wakai A, Fukuoka H, Nakamura S, Kimura S (2017) Landslide disasters induced by the northern Kyushu heavy rainfall in July 2017, *J Jpn Landslide Soc*, 54, pp. 225–228. (in Japanese)
- Óladóttir BA, Sigmarsson O, Larsen G, Thordarson T (2008) Katla volcano, Iceland: Magma composition, dynamics and eruption frequency as recorded by Holocene tephra layers, *Bulletin of Volcanology*, 70(4), pp. 475–493. doi: 10.1007/s00445-007-0150-5.
- Ono K, Watanabe K (1985) Geological map of Aso volcano (1: 50,000), Geological map of volcanoes 4, In: Geological survey of Japan. Accessed on October 2020. (in Japanese with English abstract)
- Osanai N, Yamada T, Hayashi S, Kastura S, Furuichi T, Yanai S, Murakami Y, Miyazaki T, Tanioka Y, Takiguchi S, Miyazaki M (2019) Characteristics of landslides caused by the 2018 Hokkaido Eastern Iwate Earthquake, *Landslides*, 16, pp. 1517–1528. doi: 10.1007/s10346-019-01206-7.

- Parry S, Campbell SDG, Churchman GJ (2000) Kaolin-rich zones in Hong Kong Saprolites – their interpretation and engineering significance, *ISRM International Symposium*.
- Parry S, Campbell SDG, Churchman GJ (2014) The origin and shear strength of Kaolin-rich Zones in Hong Kong, *Advances in Geotechnical Engineering: The Skempton Conference - Proceedings of a Three Day Conference on Advances in Geotechnical Engineering, organised by the Institution of Civil Engineers*, pp. 1342–1353.
- Ryan PC, Huertas FJ (2009) The temporal evolution of pedogenic Fe-smectite to Fe-kaolin via interstratified kaolin-smectite in a moist tropical soil chronosequence, *Geoderma*, 151(1–2), pp. 1–15. doi: 10.1016/j.geoderma.2009.03.010.
- Sasahara K, Ebihara K, Tsunaki R (1995) Evaluation of the Shirasu slope stability using soil hardness values, *J Jpn Soc Erosion Control Eng*, 48, pp. 20–24. (in Japanese with English abstract)
- Sato G, Goto S, Kimura T, Hayashi S, Istiyanti ML, Komori J (2017) Gravitational deformation as a precursor of shallow landslide within tephra-covered slope deposits in the Aso caldera, Japan, *Journal of the Japan Landslide Society*, 54(5), pp. 199–204. doi: 10.3313/jls.54.199. (in Japanese with English abstract)
- Sato G, Wakai A, Goto S, Kimura T (2019) Strength characteristics of gravitationally deformed slope deposits of tephra and kuroboku soils in the Aso caldera, Japan – Application of revised vane-shear-cone test for estimating shear strength–, *Journal of the Japan Landslide Society*, 56, pp. 250–253. doi: 10.3313/jls.56.250. (in Japanese with English abstract)
- Shaller P, Sykora D, Doroudian M, Churchman G (2016) Rapid in situ conversion of late-stage volcanic materials to halloysite implicated in catastrophic dam failure, Hawaii, *Clay Minerals*, 51(3), pp. 499–515. doi: 10.1180/claymin.2016.051.3.10.
- Shane P (2000) Tephrochronology: A New Zealand case study, *Earth Science Reviews*. doi: 10.1016/S0012-8252(99)00058-6.
- Shimizu O, Ono M (2016) Relationship of tephra stratigraphy and hydraulic conductivity with slide depth in rainfall-induced shallow landslides in Aso Volcano, Japan, *Landslides*, 13(3), pp. 577–582. doi: 10.1007/s10346-015-0666-2.
- Shirahama Y, Yoshimi M, Awata Y, Maruyama T, Azuma T, Miyashita Y, Mori H, Imanishi K, Takeda N, Ochi T, Otsubo M, Asahina D, Miyakawa A (2016) Characteristics of the surface ruptures associated with the 2016 Kumamoto earthquake sequence, central Kyushu, Japan, *Earth, Planets and Space*, Springer Berlin Heidelberg, 68(1), pp. 1–12. doi: 10.1186/s40623-016-0559-1.
- Skempton AW (1953) The colloidal activity of clay, *Proceedings of the third international conference on soil mechanics and foundation engineering, Zurich*, 1, pp. 57–61.
- Singer A, Zarei M, Lange FM, Stahr K (2004) Halloysite characteristics and formation in the northern Golan Heights, *Geoderma*, 123(3–4), pp. 279–295. doi: 10.1016/j.geoderma.2004.02.012.
- SIO, NOAA, U.S. Navy, NGA, GEBCO. (2020) Copernicus,

<http://www.earth.google.com>. Accessed December 2020

- Smalley I, Ross CW, Whitton J (1980) Clays from New Zealand support the inactive particle theory of soil sensitivity, *Nature*, 288, pp. 576–577. doi: 10.1038/288576a0.
- Smith KL, Milnes AR, Eggleton RA (1987) Weathering of basalt: formation of iddingsite, *Clays & Clay Minerals*, 35(6), pp. 418–428. doi: 10.1346/CCMN.1987.0350602.
- Smith VC, Shane P, Nairn IA (2005) Trends in rhyolite geochemistry, mineralogy, and magma storage during the last 50 kyr at Okataina and Taupo volcanic centres, Taupo Volcanic Zone, New Zealand, *Journal of Volcanology and Geothermal Research*, 148(3–4), pp. 372–406. doi: 10.1016/j.jvolgeores.2005.05.005.
- Smith VC, Shane P, Nairn IA, Williams CM (2006) Geochemistry and magmatic properties of eruption episodes from Haroharo linear vent zone, Okataina Volcanic Centre, New Zealand during the last 10 kyr, *Bulletin of Volcanology*, 69(1), pp. 57–88. doi: 10.1007/s00445-006-0056-7.
- Song K, Wang F, Dai Z, Iio A, Osaka O, Sakata S (2017) Geological characteristics of landslides triggered by the 2016 Kumamoto earthquake in Mt. Aso volcano, Japan, *Bull Eng Geol Environ*, 78(1), pp. 167–176.
- Soya T, Sato H (1980) Geology of the Chitose District Quadrangle Series 1: 50,000, *Geol. Surv. Japan*, pp. 92. (in Japanese with English abstract)
- Sudo T, Shimoda S (1978) Clays and clay minerals of Japan, *Elsevier, Amsterdam*, pp. 326, In: Adamo, P., Violante, P. and Wilson, M. J. (2001) Tubular and spheroidal halloysite in pyroclastic deposits in the area of the Roccamonfina volcano (Southern Italy), *Geoderma*, 99(3–4), pp. 295–316. doi: 10.1016/S0016-7061(00)00076-8.
- Suzuki M (1994) Holocene tephro-stratigraphy of Yukanboshi E9 ruin at Eniwa city, Ruin excavation report of Eniwa city, In: In: https://gbank.gsj.jp/volcano/Act_Vol/tarumae/text/exp15-2.html. Accessed November 2020. (in Japanese)
- Taskey RD (1997) Relationships of clay mineralogy to landscape stability in Western Oregon, *Doctoral dissertation, Oregon State University*.
- The Japanese Geotechnical Society (2015) Japanese geotechnical society standards laboratory testing standards of geomaterials Vol. 1.
- Tokunaga S, Goto S (2017) Study on measurement of strength discontinuity by digitized Yamanaka soil hardness tester for shallow landslide site at Aso volcano, *52nd Japan Society for Geotechnical Nagoya, July 2017*, pp. 1935–1936. (in Japanese)
- Turner MB, Cronin SJ, Bebbington MS, Platz T (2008) Developing probabilistic eruption forecasts for dormant volcanoes: A case study from Mt Taranaki, New Zealand, *Bulletin of Volcanology*, 70(4), pp. 507–515. doi: 10.1007/s00445-007-0151-4.
- Turner MB, Bebbington MS, Cronin SJ, Stewart RB (2009) Merging eruption datasets: Building an integrated Holocene eruptive record for Mt Taranaki, New Zealand, *Bulletin of Volcanology*, 71(8), pp. 903–918. doi: 10.1007/s00445-009-0274-x.
- US Geological Survey (2001) A laboratory manual for X-ray powder diffraction. <https://pubs.usgs.gov/of/2001/of01-041/index.htm>. Accessed July 2020

- Wada K (1989) Allophane and Imogolite. In: Dixon, G. B., Weed, S. B. (Eds.), *Minerals in Soil Environments*. S. S. S. A, Madison, WI, pp. 1051–1081.
- Wang F, Fan X, Yunus AP, Subramanian SS, Alonso-Rodriguez A, Dai L, Xu Q, Huang R (2019) Coseismic landslides triggered by the 2018 Hokkaido, Japan (Mw 6.6), earthquake: spatial distribution, controlling factors, and possible failure mechanism, *Landslides*, 16(8), pp. 1551–1566. doi: 10.1007/s10346-019-01187-7.
- Weaver CE (1989) Clays, muds and shales, *Developments in sedimentology 44*, Elsevier, Amsterdam.
- Wen BP, Aydin A (2003) Microstructural study of a natural slip zone: Quantification and deformation history, *Engineering Geology*, 68(3–4), pp. 289–317. doi: 10.1016/S0013-7952(02)00234-X.
- Wildman WE, Jackson ML, Whittig LD (1968) Serpentinite rock dissolution as a function of carbon dioxide pressure in aqueous solution, *American Mineralogist: Journal of Earth and Planetary Materials*, 53(7–8), pp. 1252–1263. Available at: <https://pubs.geoscienceworld.org/msa/ammin/article-abstract/53/7-8/1252/542460>.
- Wilson CJN, Hildreth W (1997) The Bishop Tuff: New insights from eruptive stratigraphy, *The Journal of Geology*, 105, pp. 407–439.
- Yabakei landslide investigation committee (2018) Final summary report about landslide in Yabakei-cho, Nakatsu city that occurred in April 2018, http://www.pref.oita.jp/uploaded/life/2045589_2349104_misc.pdf. Accessed July 2020. (in Japanese)
- Yamagishi H, Yamazaki F (2018) Landslides by the 2018 Hokkaido Iburi-Tobu Earthquake on September 6, *Landslides*. *Landslides*, 15(12), pp. 2521–2524. doi: 10.1007/s10346-018-1092-z.
- Yamao M, Sidle RC, Gomi T, Imaizumi F (2016) Characteristics of landslides in unwelded pyroclastic flow deposits, southern Kyushu, Japan, *Natural Hazards and Earth System Sciences*, 16(2), pp. 617–627. doi: 10.5194/nhess-16-617-2016.
- Zhang S, Li R, Wang F, Iio A (2019) Characteristics of landslides triggered by the 2018 Hokkaido Eastern Iburi earthquake, Northern Japan, *Landslides*, 16(9), pp. 1691–1708. doi: 10.1007/s10346-019-01207-6.

List of Publications

- Istiyanti ML, Goto S (2017) Clay minerals effects in shallow landslide at Takadake area, Aso Mountain, Kumamoto, Japan, *Proceedings of the First JTCl Workshop Advances in Landslide Understanding, Barcelona, Spain*, pp. 89–92.
- Sato G, Goto S, Kimura T, Hayashi S, Istiyanti ML, Komori J (2017) Gravitational deformation as a precursor of shallow landslide within tephra-covered slope deposits in the Aso caldera, Japan, *Journal of the Japan Landslide Society*, 54(5), pp. 199–204. doi: 10.3313/jls.54.199. (in Japanese with English abstract)
- Istiyanti ML, Goto S (2018) Physical and chemical properties of slip surface in landslides triggered by heavy rainfall at Hita, Oita, Japan, *Proceedings of the 9th Symposium on Sediment-Related Disasters*, pp. 67–71.
- Istiyanti ML, Goto S, Ochiai H (2019) A characterization of the physical properties and the effects of clay on soil material at landslide in Yabakei, Oita, Japan, *Proceedings of the Technical Forum on Mitigation of Geo-disasters in Asia, Kumamoto, Japan*, pp. 51–55.
- Okada K, Goto S, Istiyanti ML (2019) Cyclic behavior of volcanic soil in earthquake-induced slope failure, *Proceedings of the Technical Forum on Mitigation of Geo-disasters in Asia, Kumamoto, Japan*, pp. 152–155.
- Istiyanti ML, Goto S (2020) Differences of physical properties between tephra and tuff breccia-andesite on sliding layer and surrounding layers of landslides, *Proceedings of the 10th Symposium on Sediment-Related Disasters*, pp. 31–36.
- Istiyanti ML, Goto S, Kimura T, Sato G, Hayashi S, Wakai A, Higaki D (2020) Sliding layer estimation of shallow landslides on Aso volcanic mountains in Japan based on tephra layer-physical properties of soil, *Geoenvironmental Disasters*. *Geoenvironmental Disasters*, 7(1). doi: 10.1186/s40677-020-00163-x.
- Istiyanti ML, Goto S, Ochiai H (2021) Characteristics of tuff breccia-andesite in diverse mechanisms of landslides in Oita Prefecture, Kyushu, Japan, *Geoenvironmental Disasters*. *Geoenvironmental Disasters*, 8(4). doi: 10.1186/s40677-021-00176-0.

List of Conferences

- Istiyanti ML, Goto S, Tokunaga S (2016) Characteristics of clay minerals in Kuroboku on shallow landslides at Aso Mountain, Kumamoto, Japan, *Japanese Geotechnical Society Annual Meeting 13th Kanto Branch (Geokanto2016)*, Tokyo, pp. 399–402.
- Istiyanti ML, Goto S, Kimura T, Sato G, Wakai A, Doshida S, Hayashi S, Higaki D (2017) Characteristics of soil layers on shallow landslides triggered by rainfall at Izu Oshima, Japan, *Slope Tectonic Conference, Kyoto*.
- Istiyanti ML, Goto S (2017) Soil plasticity effect in shallow landslide at Takadake area, Aso Mountain, Kumamoto, Japan, *Japanese Geotechnical Society 52nd Japan National Conference on Geotechnical Engineering, Nagoya*, pp. 1933-1934.
- Istiyanti ML, Goto S, Kimura T, Sato G, Wakai A, Doshida S, Hayashi S, Higaki D (2017) Slippage plane characteristics on shallow landslides triggered by rainfall at Aso Volcano, Kumamoto, Japan, *56th Japan Landslide Society Annual Meeting, Nagano*, P-43, pp. 241-242.
- Istiyanti ML, Goto S, Kimura T, Sato G, Wakai A (2017) Soil plasticity effects on shallow landslides triggered by rainfall at volcano areas, *Japanese Geotechnical Society Annual Meeting 14th Kanto Branch (Geokanto2017)*, Utsunomiya, pp. 219-222.
- Istiyanti M.L, Goto S (2018) Physical properties of weathered tuff breccia on the landslide triggered by rainfall in Ono, Hita, Oita Prefecture, *Japan Society of Civil Engineering Annual Meeting 45th Kanto Branch, Kofu*, III-59.
- Istiyanti ML, Goto S (2018) Relation between physical and chemical properties of tuff breccia on the landslide in Ono, Hita, Oita Prefecture, *Japanese Geotechnical Society 53rd Japan National Conference on Geotechnical Engineering, Takamatsu*, pp. 523-524.
- Istiyanti ML, Goto S (2018) Comparative characteristics on soil properties in different volcanic materials related with the slip surface on the landslides in Japan, *57th Japan Landslide Society Annual Meeting, Niigata*, pp. 265-266.
- Istiyanti ML, Goto S (2018) Soil physical properties of igneous rock stratigraphy in landslide induced by rainfall in Ohtsuru site, Hita, Oita prefecture, *Japan Society of Civil Engineering 73rd Japan National Conference on Civil Engineering, Hokkaido*, III-174, pp. 347-348.

- Istiyanti ML, Goto S, Ochiai H (2019) Landslide induced by geological formation and soil characteristics in Yabakei Area, Oita, Japan, *Japanese Geotechnical Society 54th Japan National Conference on Geotechnical Engineering, Saitama*, pp. 1943-1944.
- Istiyanti ML, Goto S, Ochiai H, Fujiwara T, Shibasaki N (2019) Influence of smectite on soil material at landslide in Yabakei, Oita, Japan, *58th Japan Landslide Society Annual Meeting, Kumamoto*, pp. 200-201.
- Istiyanti ML, Goto S (2019) The relation between fine fraction and plasticity index in several cases of a landslide at Kyushu, Japan, *Japanese Geotechnical Society Annual Meeting 16th Kanto Branch (Geokanto2019)*.
- Istiyanti ML, Goto S (2020) Soil physical properties and clay mineral contents of tuff breccia on landslide materials, *59th Japan Landslide Society Annual Meeting*, pp. 51-52.

APPENDIX

Table A.1 Soil hardness in Takadake 1, Aso volcanic mountain

Depth (cm)	Soil hardness (mm)	Depth (cm)	Soil hardness (mm)
2	12.0	50	21.9
2	7.5	50	23.0
2	16.3	70	11.6
2	13.4	70	23.9
8	8.4	70	24.8
8	17.2	70	10.5
8	11.5	70	28.3
8	16.4	83	19.3
14	11.5	83	17.8
14	9.1	83	16.1
14	15.6	83	14.7
14	17.0	89	10.0
21	8.7	89	14.4
21	13.7	89	15.0
21	11.4	89	16.3
25	14.1	95	11.7
25	17.3	95	14.2
25	18.9	95	16.9
25	19.9	95	17.8
30	12.1	107	16.4
30	13.7	107	17.0
30	17.6	107	18.6
30	18.3	107	20.6
38	20.0	116	14.6
38	17.7	116	14.0
38	17.2	116	16.2
38	15.5	116	17.0
50	5.1	125	17.0
50	13.2	125	16.5
50	20.4	125	11.0
50		125	9.7

Table A.2 Soil hardness in Takadake 2, Aso volcanic mountain

Depth (cm)	Soil hardness (mm)	Depth (cm)	Soil hardness (mm)
80	15.5	38	20
80	22.0	38	20
80	22.5	38	18.5
80	11	38	19
80	18	118	19
85	15	50	19
85	21	50	19
85	22	50	21
85	21.5	118	19
85	22	50	18
93	17.5	123	25
14	25	70	25
21	23	70	27
21	16	70	27
21	13	70	27
103	18	83	27
25	16	83	27
25	16	133	27
25	16.5	133	24
30	16	89	25
30	16	89	26
113	22	89	26
30	19	89	26

Table A.3 Soil hardness in Izu Oshima, Tokyo

Depth (cm)	Soil hardness (mm)	Depth (cm)	Soil hardness (mm)
5	14.0	90	19.2
10	15.3	95	18.2
20	15.6	100	14.8
25	18.8	105	17.5
30	18.7	110	21.0
35	20.6	115	23.5
40	22.2	120	22.4
45	19.2	125	16.6
50	15.3	130	15.6
55	13.5	135	15.8
60	18.1	140	14.4
65	19.5	145	14.4
70	24.5	150	13.6
75	20.7	155	13.7
80	18.5	160	16.4
85	21.2	165	18.9

Table A.4 Soil hardness in Takanodai, Aso volcanic mountain

Depth (cm)	Soil hardness (mm)	Depth (cm)	Soil hardness (mm)
770	20.5	815	23.0
770	18.0	815	24.5
770	21.0	815	24.5
770	22.5	815	23.0
770	22.0	815	25.0
770	22.0	815	24.5
780	22.5	820	22.0
780	22.5	820	24.0
780	22.5	820	25.0
780	22.5	820	23.5
780	22.0	820	22.0
780	22.0	820	24.0
795	23.0	820.25	24.0
795	23.0	820.25	22.0

795	23.5	820.25	20.0
795	24.5	820.25	25.0
795	24.0	820.25	21.0
795	23.0	820.25	19.0
800	23.5	825.25	21.0
800	23.0	825.25	19.5
800	23.5	825.25	20.0
800	23.0	825.25	21.0
800	24.5	825.25	22.0
800	23.0	825.25	20.5
805	23.0	835.25	21.0
805	22.5	835.25	23.5
805	23.0	835.25	21.0
805	23.5	835.25	22.0
805	24.5	835.25	20.5
805	24.5	835.25	20.0
810	24.0	845.25	23.5
810	24.0	845.25	23.5
810	25.0	845.25	23.5
810	23.5	845.25	22.5
810	26.5	845.25	20.0
810	25.5	845.25	21.5

Table A.5 Soil hardness in Towa, Hokkaido

Depth (cm)	Soil hardness (mm)	Depth (cm)	Soil hardness (mm)
5	10.5	115	17.0
5	11.0	115	15.5
5	15.5	115	13.0
5	13.8	115	17.0
5	14.0	115	16.5
15	13.0	125	21.0
15	12.0	125	16.8
15	10.8	125	19.0
15	11.0	125	15.0

15	10.0	125	15.2
25	9.2	135	17.5
25	10.8	135	17.2
25	11.0	135	19.0
25	10.5	135	17.0
25	11.5	135	18.9
35	10.5	145	19.2
35	9.0	145	15.3
35	11.2	145	18.8
35	10.8	145	18.0
35	11.8	145	16.0
45	11.0	155	17.0
45	11.0	155	14.2
45	10.8	155	13.5
45	11.8	155	17.8
45	16.0	155	21.5
55	8.0	165	16.8
55	15.0	165	17.0
55	15.0	165	16.0
55	14.0	165	21.8
55	10.8	165	20.8
65	15.0	175	12.3
65	14.5	175	14.5
65	15.0	175	13.8
65	13.0	175	14.0
65	11.8	175	14.0
75	12.0	190	15.0
75	14.8	190	15.0
75	12.8	190	15.0
75	13.8	190	14.0
75	13.0	190	15.3
85	17.8	200	10.0
85	15.0	200	13.9

85	19.0	200	13.0
85	13.8	200	14.0
85	14.8	200	11.0
95	19.0	210	14.0
95	16.0	210	14.8
95	19.8	210	14.2
95	16.0	210	12.0
95	14.3	210	15.0
105	17.5	220	11.9
105	17.0	220	11.9
105	16.0	220	11.8
105	16.0	220	12.8
105	18.8	220	12.2

Table A.6 Soil hardness in Mizuho, Hokkaido

Depth (cm)	Soil hardness (mm)	Depth (cm)	Soil hardness (mm)
19.5	10.0	139.5	15.0
19.5	11.0	139.5	12.0
19.5	11.5	139.5	15.5
19.5	12.5	139.5	15.0
19.5	12.0	139.5	15.5
29.5	13.5	149.5	17.0
29.5	15.0	149.5	18.0
29.5	12.0	149.5	17.5
29.5	13.5	149.5	19.5
29.5	14.0	149.5	18.0
39.5	13.0	159.5	19.0
39.5	10.0	159.5	17.0
39.5	18.0	159.5	18.5
39.5	17.0	159.5	15.5
39.5	14.0	159.5	17.5
49.5	10.0	169.5	17.0
49.5	14.0	169.5	18.0
49.5	16.0	169.5	17.0

49.5	15.0	169.5	17.0
49.5	16.0	169.5	20.5
59.5	21.0	174	12.5
59.5	20.0	174	11.5
59.5	19.5	174	14.5
59.5	18.0	174	13.5
59.5	18.0	174	11.5
69.5	15.0	178	14.0
69.5	17.5	178	13.0
69.5	19.0	178	13.0
69.5	14.0	178	13.0
69.5	18.5	178	12.0
79.5	15.5	188	15.5
79.5	10.5	188	12.0
79.5	15.5	188	14.0
79.5	13.5	188	14.0
79.5	16.0	188	11.0
89.5	14.0	198	15.0
89.5	12.0	198	15.0
89.5	16.5	198	16.5
89.5	11.5	198	12.5
89.5	11.0	198	18.0
99.5	9.0	208	17.0
99.5	12.0	208	13.0
99.5	13.0	208	12.0
99.5	10.5	208	11.5
99.5	12.5	208	16.0
109.5	17.0	218	9.0
109.5	13.0	218	11.5
109.5	14.0	218	10.0
109.5	13.0	218	8.0
109.5	15.5	218	8.0
119.5	13.0	228	17.0

119.5	14.0	228	18.5
119.5	16.0	228	18.5
119.5	14.0	228	19.0
119.5	10.0	228	15.0
129.5	16.5	238	20.0
129.5	17.5	238	23.5
129.5	19.0	238	21.5
129.5	15.0	238	19.5
129.5	15.5	238	22.0

Table A.7 Soil hardness in Ohtsuru, Oita Prefecture

Depth (cm)	Soil hardness (mm)	Depth (cm)	Soil hardness (mm)
120	11.0	350	14.5
120	12.5	350	14.0
120	14.0	550	18.0
120	17.0	550	20.0
120	17.0	550	20.0
350	10.0	550	23.0
350	11.0	550	28.0
350	13.5		

Table A.8 Soil hardness in Ono, Oita Prefecture

Sample	Soil hardness (mm)	Depth (cm)	Soil hardness (mm)
Weathered andesite	23.5	Weathered tuff breccia	18.5
Weathered andesite	24.5	Weathered tuff breccia	20.6
Weathered andesite	25.0	Tuff breccia	28.0
Weathered andesite	28.0	Tuff breccia	31.0
Weathered andesite	28.0	Tuff breccia	31.0
Weathered tuff breccia	22.5	Tuff breccia	35.0

Weathered tuff breccia	21.0	Tuff breccia	35.0
Weathered tuff breccia	20.0		

Table A.9 Soil hardness in Yabakei, Oita Prefecture

Depth (cm)	Soil hardness (mm)	Depth (cm)	Soil hardness (mm)
10	15.5	60	20.0
10	21.0	60	21.0
20	18.0	70	22.0
20	18.5	70	22.5
30	18.5	80	21.0
30	18.5	80	24.0
40	22.0	90	20.0
40	24.0	90	21.5
50	20.0	100	18.0
50	23.5	100	25.0

Table B.1 Plasticity index and activity values in Takadake 1, Aso volcanic mountain

Sample	Plastic Limit (%)	Liquid Limit (%)	Plasticity Index	Activity
N1 kuroboku	69.96	98.0	28.04	14.02
N2 scoria	44.36	46.41	2.05	0.45
N3-4 kuroboku U	62.44	87.23	24.79	24.79
N3-4 kuroboku L	84.75	118.78	34.03	34.03
OJS scoria	77.40	95.44	18.04	6.01

Table B.2 Plasticity index and activity values in Takadake 2, Aso volcanic mountain

Sample	Plastic Limit (%)	Liquid Limit (%)	Plasticity Index	Activity
N1 kuroboku	51.33	76.61	25.28	8.43
N2 kuroboku	37.67	59.18	21.51	10.75
N2 scoria	27.01	35.17	8.16	2.72
N3-4 kuroboku U	39.37	53.25	13.88	4.21
N3-4 kuroboku L	51.36	77.76	26.40	6.60
OJS scoria	40.0	51.29	11.29	3.76

Table B.3 Plasticity index and activity values in Izu Oshima, Tokyo

Sample	Plastic Limit (%)	Liquid Limit (%)	Plasticity Index	Activity
Y1.0	20.63	22.10	1.47	0.27
Loess	27.81	28.87	1.06	0.26
Y4.0	20.15	20.93	0.78	0.12

Table B.4 Plasticity index and activity values in Takanodai, Aso volcanic mountain

Sample	Plastic Limit (%)	Liquid Limit (%)	Plasticity Index	Activity
Brown Kusasenrigahama	-	-	NP	-
Orange Kusasenrigahama	-	-	NP	-
Dark brown tephra	48.37	66.80	18.43	3.07

Table B.5 Plasticity index and activity values in Towa, Hokkaido

Sample	Plastic Limit (%)	Liquid Limit (%)	Plasticity Index	Activity
Kuroboku	33.57	45.90	12.33	4.11
Ta-c U	-	-	NP	-
Ta-c L	43.14	48.0	4.86	0.97
Weathered Ta-d	88.49	128.80	40.31	1.85
Ta-d U	80.16	100.50	20.34	1.36
Ta-d L	-	-	NP	-
Loam	46.38	63.15	16.77	2.39

Table B.6 Plasticity index and activity values in Mizuho, Hokkaido

Sample	Plastic Limit (%)	Liquid Limit (%)	Plasticity Index	Activity
Weathered Ta-d	60.21	89.80	29.59	-
Loam (En-a) U	29.70	39.50	9.80	1.63
Loam (En-a) L	27.78	38.0	10.22	2.49
Weathered En-a	-	-	NP	-
En-a	-	-	NP	-
Loam (Spfa-1)	-	-	NP	-

Table B.7 Plasticity index and activity values in Ohtsuru, Oita Prefecture

Sample	Plastic Limit (%)	Liquid Limit (%)	Plasticity Index	Activity
Highly weathered andesite	35.80	47.50	11.70	1.62
Weathered andesite	40.72	49.65	8.93	1.39
Tuff breccia	36.59	48.0	11.41	1.11

Table B.8 Plasticity index and activity values in Ono, Oita Prefecture

Sample	Plastic Limit (%)	Liquid Limit (%)	Plasticity Index	Activity
Weathered andesite	59.12	68.84	9.72	1.46
Weathered tuff breccia	51.60	63.45	11.85	1.19
Tuff breccia	46.01	53.81	7.80	1.46

Table B.9 Plasticity index and activity values in Yabakei, Oita Prefecture

Sample	Plastic Limit (%)	Liquid Limit (%)	Plasticity Index	Activity
Highly weathered tuff breccia	51.50	97.30	45.80	3.82

Table C.1 Grain size distribution properties in Takadake 1, Aso volcanic mountain

Sample	0.002 mm (%)	0.075 mm (%)	D ₁₀	D ₃₀	D ₆₀	U _c	U _c '
N1 kuroboku	2.0	21.93	0.065	0.10	0.27	4.15	0.57
N2 scoria	4.5	12.24	0.038	0.150	0.35	9.21	1.69
N3-4 kuroboku U	1.0	35.99	0.025	0.050	0.15	6.0	0.67
N3-4 kuroboku L	1.0	40.88	0.030	0.058	0.17	5.67	0.66
OJS scoria	3.0	13.12	0.040	0.20	0.60	15.0	1.67

Table C.2 Grain size distribution properties in Takadake 2, Aso volcanic mountain

Sample	0.002 mm (%)	0.075 mm (%)	D ₁₀	D ₃₀	D ₆₀	U _c	U _c '
N1 kuroboku	3.0	44.49	0.019	0.060	0.09	4.74	2.10
N2 kuroboku	2.0	31.67	0.029	0.070	0.14	4.83	1.21
N2 scoria	3.0	23.0	0.020	0.10	0.23	11.50	2.17
N3-4 kuroboku U	3.3	44.31	0.019	0.048	0.12	6.31	1.01
N3-4 kuroboku L	4.0	44.25	0.012	0.039	0.12	10.0	1.06
OJS scoria	3.0	27.85	0.030	0.080	0.19	6.33	1.12

Table C.3 Grain size distribution properties in Izu Oshima, Tokyo

Sample	0.002 mm (%)	0.075 mm (%)	D ₁₀	D ₃₀	D ₆₀	U _c	U _c '
Y1.0	5.5	32.78	0.048	0.070	0.22	4.58	0.46
Loess	4.0	46.91	0.048	0.060	0.13	2.71	0.58
Y4.0	6.5	43.95	0.017	0.052	0.15	8.82	1.06

Table C.4 Grain size distribution properties in Takanodai, Aso volcanic mountain

Sample	0.002 mm (%)	0.075 mm (%)	D ₁₀	D ₃₀	D ₆₀	U _c	U _c '
Kusasenrigahama U	4.5	13.57	0.020	0.50	1.60	80.0	7.81
Kusasenrigahama L	4.0	11.12	0.060	0.480	1.0	16.67	3.84
Dark brown tephra	6.0	25.83	0.008	0.10	0.37	46.25	3.38

Table C.5 Grain size distribution properties in Towa, Hokkaido

Sample	0.002 mm (%)	0.075 mm (%)	D ₁₀	D ₃₀	D ₆₀	U _c	U _c '
Kuroboku	3.0	26.97	0.012	0.106	0.38	31.67	2.46
Ta-c U	3.5	14.30	0.020	0.30	0.48	24.0	9.37
Ta-c L	5.0	44.49	0.007	0.03	0.16	22.86	0.80
Weathered Ta-d	17.0	79.56	-	0.010	0.02	-	-
Ta-d U	15.0	55.96	-	0.010	0.15	-	-
Ta-d L	4.0	6.84	0.290	0.630	1.35	4.65	1.01
Loam	7.0	40.40	0.003	0.020	0.21	70.0	0.63

Table C.6 Grain size distribution properties in Mizuho, Hokkaido

Sample	0.002 mm (%)	0.075 mm (%)	D ₁₀	D ₃₀	D ₆₀	U _c	U _c '
Weathered Ta-d	-	32.57	-	-	0.45	-	-
Loam (En-a) U	6.0	42.92	0.004	0.022	0.20	50.0	0.60
Loam (En-a) L	4.1	32.03	0.006	0.040	0.32	53.33	0.83
En-a U	0.3	2.76	0.40	0.70	1.80	4.50	0.68
En-a L	-	0.40	3.0	7.0	10.30	3.43	1.58
Loam (Spfa-1)	10.3	74.90	0.002	0.009	0.05	25.79	0.85

Table C.7 Grain size distribution properties in Ohtsuru, Oita Prefecture

Sample	0.002 mm (%)	0.075 mm (%)	D ₁₀	D ₃₀	D ₆₀	U _c	U _c '
Highly weathered andesite	8.0	40.27	0.003	0.035	0.25	83.33	1.63
Weathered andesite	7.5	32.04	0.005	0.070	0.39	78.0	2.51
Tuff breccia	7.8	43.40	0.004	0.050	0.25	62.50	2.50

Table C.8 Grain size distribution properties in Ono, Oita Prefecture

Sample	0.002 mm (%)	0.075 mm (%)	D ₁₀	D ₃₀	D ₆₀	U _c	U _c '
Weathered andesite	6.0	46.68	0.005	0.039	0.25	50.0	1.22
Weathered tuff breccia	8.5	26.46	0.004	0.100	0.45	118.42	5.85
Tuff breccia	7.0	19.60	0.004	0.140	0.50	111.11	8.71

Table C.9 Grain size distribution properties in Yabakei, Oita Prefecture

Sample	0.002 mm (%)	0.075 mm (%)	D ₁₀	D ₃₀	D ₆₀	U _c	U _c '
Highly weathered tuff breccia	12.0	51.24	0.002	0.014	0.12	70.59	0.96

Table D.1 Density of soil particles in Takadake 1, Aso volcanic mountain

Sample	Density of soil particles (g/cm ³)
N1 kuroboku	2.602
N2 scoria	2.689
N3-4 kuroboku U	2.585
N3-4 kuroboku L	2.449
OJS scoria	2.644

Table D.2 Density of soil particles in Takadake 2, Aso volcanic mountain

Sample	Density of soil particles (g/cm ³)
N1 kuroboku	2.684
N2 kuroboku	2.705
N2 scoria	2.806
N3-4 kuroboku U	2.727
N3-4 kuroboku L	2.646
OJS scoria	2.767

Table D.3 Density of soil particles in Izu Oshima, Tokyo

Sample	Density of soil particles (g/cm ³)
Y1.0	2.798
Loess	2.862
Y4.0	2.897

Table D.4 Density of soil particles in Takanodai, Aso volcanic mountain

Sample	Density of soil particles (g/cm ³)
Kusasenrigahama U	2.425
Kusasenrigahama L	2.541
Dark brown tephra	2.713

Table D.5 Density of soil particles in Towa, Hokkaido

Sample	Density of soil particles (g/cm ³)
Kuroboku	2.558
Ta-c U	2.645
Ta-c L	2.590
Weathered Ta-d	2.421
Ta-d U	2.605

Ta-d L	2.523
Loam	2.729

Table D.6 Density of soil particles in Mizuho, Hokkaido

Sample	Density of soil particles (g/cm ³)
Weathered Ta-d	2.717
Loam (En-a) U	2.845
Loam (En-a) L	2.884
Weathered En-a	-
En-a U	2.802
En-a L	2.612
Loam (Spfa-1)	2.635

Table D.7 Density of soil particles in Ohtsuru, Oita Prefecture

Sample	Density of soil particles (g/cm ³)
Highly weathered andesite	2.745
Weathered andesite	2.754
Tuff breccia	2.717

Table D.8 Density of soil particles in Ono, Oita Prefecture

Sample	Density of soil particles (g/cm ³)
Weathered andesite	2.717
Weathered tuff breccia	2.807
Tuff breccia	2.752

Table D.9 Density of soil particles in Yabakei, Oita Prefecture

Sample	Density of soil particles (g/cm ³)
Highly weathered tuff breccia	2.438

Table E.1 Saturated permeability properties in Takadake 1, Aso volcanic mountain

Sample	Water content (%)	Coefficient of saturated permeability (m/s)	Degree of saturation (%)	Void ratio	Dry density (g/cm ³)
N1 kuroboku	89.57	2.65E-06	87.41	2.67	0.709
	90.32	5.97E-05	87.80	2.68	0.707
N2 scoria	34.17	3.07E-04	66.27	1.39	1.126
	64.35	3.04E-04	86.64	2.00	0.897
N3-4 kuroboku U	95.68	2.58E-04	93.06	2.62	0.704
	102.41	1.10E-04	32.24	2.83	0.665
	79.72	3.15E-05	89.44	2.27	0.779
N3-4 kuroboku L	102.07	2.96E-05	94.55	2.66	0.673
	117.71	8.12E-05	90.50	3.20	0.586
	108.21	1.84E-04	95.45	2.79	0.649
OJS scoria	103.45	8.96E-06	96.21	2.64	0.675
	104.55	7.89E-06	96.56	2.66	0.671
	119.34	7.48E-06	99.45	2.95	0.622

Table E.2 Saturated permeability properties in Takadake 2, Aso volcanic mountain

Sample	Water content (%)	Coefficient of saturated permeability (m/s)	Degree of saturation (%)	Void ratio	Dry density (g/cm ³)
N2 scoria	29.69	2.80E-04	56.50	1.48	1.135
	31.60	2.65E-06	61.68	1.44	1.152
N3-4 kuroboku U	60.08	4.04E-05	77.90	2.10	0.879
	62.49	6.37E-05	58.65	2.91	0.698
N3-4 kuroboku L	70.76	1.40E-07	87.18	2.15	0.841
	73.61	2.74E-06	80.78	2.41	0.776
OJS scoria	51.52	7.33E-06	70.50	2.02	0.915
	44.28	2.15E-04	79.35	1.54	1.087

Table E.3 Saturated permeability properties in Izu Oshima, Tokyo

Sample	Water content (%)	Coefficient of saturated permeability (m/s)	Degree of saturation (%)	Void ratio	Dry density (g/cm ³)
Y1.0	22.0	4.36E-05	48.20	1.28	1.233
	22.10	1.02E-04	44.20	1.43	1.177
	20.90	4.63E-05	48.70	1.23	1.284
Loess	37.80	3.15E-05	66.10	1.63	1.083
Y4.0	23.40	6.82E-05	50.10	1.29	1.207
	29.0	3.53E-05	60.70	1.33	1.193
	25.10	4.61E-06	69.60	1.05	1.422
	30.0	2.92E-06	84.10	1.0	1.399
	23.40	1.28E-05	69.90	0.97	1.468

Table E.4 Saturated permeability properties in Takanodai, Aso volcanic mountain

Sample	Water content (%)	Coefficient of saturated permeability (m/s)	Degree of saturation (%)	Void ratio	Dry density (g/cm ³)
Kusasenrigahama U	110.12	1.41E-04	73.73	3.62	0.505
	107.76	2.51E-04	72.75	3.59	0.528
	108.19	1.24E-04	72.47	3.62	0.525
	118.95	7.59E-05	80.96	3.56	0.531
Kusasenrigahama L	103.54	4.18E-04	70.45	3.73	0.537
	100.35	2.48E-04	68.88	3.70	0.540
	89.27	1.72E-04	65.25	3.48	0.568
	103.21	9.84E-05	75.88	3.45	0.570
Dark brown tephra	133.94	4.11E-08	97.23	3.29	0.557
	131.25	1.13E-07	97.94	3.20	0.569
	128.56	2.98E-08	100.32	3.06	0.588
	137.28	1.47E-06	94.77	3.46	0.536

Table E.5 Saturated permeability properties in Towa, Hokkaido

Sample	Water content (%)	Coefficient of saturated permeability (m/s)	Degree of saturation (%)	Void ratio	Dry density (g/cm ³)
Ta-c U	35.81	1.67E-04	43.29	2.19	0.830
	41.86	1.99E-04	51.38	2.15	0.838
	40.15	3.07E-04	43.73	2.43	0.771
Ta-c L	78.11	2.46E-04	59.38	3.41	0.588
	57.87	1.59E-04	55.07	2.72	0.696
	41.76	2.51E-04	46.90	2.31	0.783
Weathered Ta-d	121.60	8.53E-05	73.87	3.99	0.486
	103.61	2.15E-04	71.48	3.51	0.537
	110.72	1.63E-04	67.64	3.96	0.488
Ta-d U	209.26	3.60E-03	60.52	9.01	0.260
	202.99	4.31E-03	55.51	9.53	0.248
	217.0	3.40E-03	64.88	8.71	0.268
Ta-d L	77.02	4.43E-04	58.34	3.33	0.583
	67.87	4.84E-05	60.64	2.82	0.660
	94.18	2.96E-04	63.79	3.72	0.534
Loam	77.42	4.80E-05	71.11	2.97	0.687
	42.19	3.15E-05	53.21	2.16	0.863
	79.07	5.05E-05	74.03	2.91	0.697

Table E.6 Saturated permeability properties in Mizuho, Hokkaido

Sample	Water content (%)	Coefficient of saturated permeability (m/s)	Degree of saturation (%)	Void ratio	Dry density (g/cm ³)
En-a U	43.08	3.61E-03	42.13	2.86	0.725
	40.26	3.86E-03	40.93	2.76	0.746
	41.21	3.97E-03	42.75	2.70	0.757
En-a L	64.87	3.66E-03	41.15	4.12	0.510
		4.21E-03			
		4.53E-03			

Loam (Spfa-1)	91.57	8.96E-05	108.70	2.22	0.818
		7.90E-05			
		7.82E-05			

Table E.7 Saturated permeability properties in Ohtsuru, Oita Prefecture

Sample	Water content (%)	Coefficient of saturated permeability (m/s)	Degree of saturation (%)	Void ratio	Dry density (g/cm ³)
Highly weathered andesite	54.90	2.40E-05	80.20	1.86	0.949
	48.20	3.10E-05	79.20	1.65	1.023
	57.50	1.70E-05	86.20	1.81	0.966
Weathered andesite	66.97	1.18E-05	92.45	1.99	0.920
	87.14	5.32E-05	101.82	2.36	0.820
	72.27	1.71E-06	95.23	2.09	0.891
Tuff breccia	42.24	8.51E-05	65.30	1.76	0.985
	32.01	6.09E-05	55.79	1.56	1.062
	43.67	7.48E-06	66.47	1.78	0.976

Table E.8 Saturated permeability properties in Ono, Oita Prefecture

Sample	Water content (%)	Coefficient of saturated permeability (m/s)	Degree of saturation (%)	Void ratio	Dry density (g/cm ³)
Weathered andesite	59.20	1.10E-04	111.50	1.44	1.112
	33.40	2.80E-04	71.50	1.27	1.197
	44.70	9.80E-05	99.80	1.22	1.226
Weathered tuff breccia	42.0	1.20E-04	92.70	1.27	1.235
	49.70	1.90E-04	91.10	1.53	1.109
	47.10	2.50E-04	96.10	1.38	1.182
	46.40	1.70E-05	94.30	1.38	1.178
	49.0	2.00E-04	95.70	1.44	1.151
	47.20	2.70E-05	92.30	1.44	1.152

Table E.9 Saturated permeability properties in Yabakei, Oita Prefecture

Sample	Water content (%)	Coefficient of saturated permeability (m/s)	Degree of saturation (%)	Void ratio	Dry density (g/cm ³)
Highly weathered tuff breccia	43.35	4.30E-05	104.07	1.03	1.219
	54.0	1.34E-04	102.0	1.31	1.072
	51.53	3.33E-05	107.91	1.16	1.127